ANALYSIS OF SOLAR HEAT GAIN AND THERMAL TRANSMISSION FOR WINDOWS WITH LOUVERED SHADE SYSTEMS

by

MICHAEL R COLLINS

A thesis submitted to the Department of Mechanical Engineering in conformity with the requirements for the degree of Doctor of Philosophy (Engineering)

Queen's University
Kingston, Ontario, Canada
December, 2001

0-612-65668-3

ABSTRACT

A numerical study of heat transfer through a sunlit glazing unit with internal louvered shade has been performed. The two-dimensional model was developed to approximate the system as an isothermal vertical flat plate with adjacent heated, horizontal, and rotateable louvers, and includes the effects of convection, radiation, and conduction. Six variables were identified for examination of their effects on heat transfer in the system: slat angle, slat nominal distance, slat emissivity, absorbed heat flux in the slats, plate temperature, and plate emissivity.

An experimental model of the system was constructed to validate the numerical model using a Mach-Zehnder Interferometer. The interferometer allows examination of convective heat transfer in the system. Experiments were performed which examined the effects of blind placement and angle, and glass temperature. Convective heat flux rates measured at the plate's surface, measured blind slat temperatures, and isotherms were found to be in excellent agreement with numerically obtained results.

A parametric analysis was conducted to aid in designing an investigative numerical series. Results suggested that heat flux from the glass surface exhibited a 2nd order response. Subsequently, a three level factorial parametric series was performed numerically, and the results were examined using statistical methods. As a result of this analysis, an estimator equation was derived which predicts heat flux at the indoor window surface as a function of the investigative variables.

The estimator equation was subsequently used to predict *SHGC* and *U*-factor for a number of conditions, and compared to data obtained experimentally with a solar calorimeter. Calculated and measured data were found to be in excellent agreement.

ACKNOWLEDGEMENTS

I wish to express my gratitude to my research advisor, Dr. Stephen J. Harrison of the Department of Mechanical Engineering at Queen's University, for his support and guidance.

I would also like to express my appreciation to Dr. Pat Oosthuizen of the Department of Mechanical Engineering at Queen's University, and Dr. Dave Naylor of the Department of Mechanical, Aerospace and Industrial Engineering at Ryerson University, for their invaluable support.

My thanks also goes to Jeff Phillips, Alan Machin, Nuno Duarte, and Ping Ye for laying the groundwork for this research. Special thanks are given to Alan Machin for his input and guidance concerning all things interferometric.

I would also like to express my appreciation to the following:

To NSERC and OGS for financial support;

To Queen's University Department of Mechanical Engineering for the use of their facilities;

To all the members of the Solar Lab for their assistance, encouragement, and friendship;

To my wife, Lora Feltham, for her love, support, patience, and understanding;

To my parents, Ron and Genevieve, and my sisters, Lynn and Jeannine, for their love and support;

Finally, to my friends at the Domino Theater, for helping preserve my sanity.

TABLE OF CONTENTS

TITLE PAGE
ABSTRACT ... i
ACKNOWLEDGEMENTS ... ii
TABLE OF CONTENTS ... iii
LIST OF TABLES ... vi
LIST OF FIGURES ... ix
NOMENCLATURE ... xiv

1.0 INTRODUCTION ... 1
  1.1 Introduction ... 1
  1.2 Literature Review ... 5
    1.2.1 Previous Investigations on the Effects of Venetian Blinds on Window Thermal and Solar Performance ... 5
    1.2.2 Current Investigations on the Effects of Venetian Blinds on Window Thermal and Solar Performance ... 12
  1.3 Present Research Objectives ... 14
  1.4 Thesis Format ... 17

2.0 NUMERICAL MODEL DEVELOPMENT ... 19
  2.1 Introduction ... 19
  2.2 Physical Description of Model ... 19
  2.3 Governing Equations ... 22
    2.3.1 Assumptions ... 22
    2.3.2 Dimensional Equations ... 22
    2.3.3 Non-Dimensionalization ... 24
    2.3.4 Boundary Conditions ... 27
    2.3.5 Solution ... 29
  2.4 Data Analysis ... 32
    2.4.1 Convective Flux ... 32
    2.4.2 Radiative Post Processing ... 32
  2.5 Model Checks ... 33
    2.5.1 Grid Sensitivity ... 34
    2.5.2 Far Field Boundary Tests ... 37
    2.5.3 Comparison with Ostrach's (1953) Boundary Layer Solution ... 40
    2.5.4 Comparison to Phillips (1999) Solution ... 41

3.0 EXPERIMENTAL VALIDATION OF NUMERICAL MODEL ... 43
  3.1 Introduction ... 43
  3.2 Description of Mach-Zehnder Interferometer ... 44
  3.3 Interferogram Analysis ... 46
    3.3.1 Infinite Fringe Method ... 48
    3.3.2 Wedge Fringe Method ... 52
    3.3.3 Local and Average Convective Heat Flux ... 55
  3.4 Experimental Model ... 55

3.5 Test Conditions 60
3.6 Experimental Procedure 61
3.7 Results and Discussion 63
3.8 Conclusions 79

4.0 PARAMETRIC ANALYSIS 81
4.1 Introduction 81
4.2 Investigative Parametrics 81
4.2.1 Procedure 81
4.2.2 Results and Discussion 85
4.2.3 Conclusions 95
4.3 Three-Level Parametric Series 97
4.3.1 Procedure 97
4.3.2 Results and Discussion 102
4.3.3 Conclusions 109

5.0 DISCUSSION OF RESULTS 111
5.1 Introduction 111
5.2 Summary of Previous Discussion 111
5.2.1 Validation 111
5.2.2 Parametric Analysis 115
5.3 *U*-Factor and *SHGC* Prediction 119
5.3.1 Procedure 120
5.3.1.1 *U*-Factor Calculation 121
5.3.1.2 *SHGC* Calculation 122
5.3.2 Results and Discussion 124

6.0 CONCLUSIONS AND RECOMMENDATIONS 127
7.1 Conclusions 127
7.2 Recommendations 131

REFERENCES 134

Appendix A: NUMERICAL FILES 139
A.1 Introduction 139
A.2 FIDAP Files 139
A.2.1 FIDAP Input File 139
A.2.2 FIDAP Output Files 143
A.3 Post Processing 143
A.3.1 Convection Analysis 143
A.3.2 Radiation Analysis Code 146

Appendix B: INTERFEROMETRY: UNCERTAINTY AND SAMPLE CALCULATIONS 150
B.1 Introduction 150
B.2 Uncertainty 150

B.2.1 Infinite Fringe Method 151
B.2.2 Wedge Fringe Method 153
B.2.3 Convective Heat Flux 154
B.3 Sample Calculation 155
B.3.1 Infinite Fringe Method 160
B.3.2 Wedge Fringe Method 163
B.3.3 Uncertainty 164

Appendix C: INTERFEROMETER / NUMERICAL OUTPUT 166
C.1 Introduction 166
C.2 Isothermal Vertical Flat Plate Solution 166
C.3 Validation Cases 170
C.3.1 Photos 170
C.3.2 Sample Data 176

Appendix D: PARAMETRIC RESULTS 179
D.1 Introduction 179
D.2 Investigative Parametric 179
D.3 Full Parametric 187

Appendix E: SOLAR CALORIMETRY AND *SHGC* MEASUREMENT 200
E.1 Introduction 200
E.2 Experimental Procedure 200
E.2.1 Calorimetry 200
E.2.2 Experimental Series 205
E.2.3 Experimental Results 206
E.3 Sample *U*-Factor and *SHGC* Prediction 207
E.3.1 Sample *U*-Factor Calculation 208
E.3.2 Sample SHGC Calculation 210
E.3.3 Results 213

VITA 214

LIST OF TABLES

Table 2-1: Constant numerical model parameters 20

Table 3-1: Sequence of experimental/numerical conditions for model validation. Experimental target is in brackets 60

Table 3-2: Parameters used for validation of the numerical model. All fluid properties except k_p are evaluated at $T = 300$ K 62

Table 3-3: Comparison of predicted and measured convective heat flux and predicted radiative heat flux from the plate for all validation cases. Results for the middle third of the plate are presented in brackets 72

Table 3-4: Comparison of predicted and measured blind slat temperatures for all validation cases. M and E denote modeled and experimental results respectively. Experimental measurement accuracy is ± 0.2 K 75

Table 4-1: Numerical conditions of investigative parametric series 82

Table 4-2: Numerical conditions of secondary investigative parametric series. All parametrics performed at $\phi = 0^{\circ}$. Base conditions indicated in bold 83

Table 4-3: Numerical parameters used in investigative parametric. Fluid properties are evaluated at $T_f = 300$ K 83

Table 4-4: Numerically predicted average convective and radiative heat flux from the center-of-glass region of the plate as a function of plate temperature, slat position, and slat angle. Results are for tests indicated in Table 4-1. Models executed at $\varepsilon_b = \varepsilon_p = 0.6$, $q_b = 60$ W/m^2 88

Table 4-5: Numerically predicted average convective and radiative heat flux from the center-of-glass region of the plate as a function of slat emissivity. Results are for tests indicated in Table 4-2. Models executed at $\phi = 0^{\circ}$, $b = 30$ mm, $\varepsilon_p = 0.6$, $q_b = 60$ W/m^2 91

Table 4-6: Numerically predicted average convective and radiative heat flux from the center-of-glass region of the plate as a function of plate emissivity. Results are for tests indicated in Table 4-2. Models executed at $\phi = 0^{\circ}$, $b = 30$ mm, $\varepsilon_b = 0.6$, $q_b = 60$ W/m^2 92

Table 4-7: Numerically predicted average convective and radiative heat flux from the center-of-glass region of the plate as a function of nominal spacing. Results are for tests indicated in Table 4-2. Models executed at $\phi = 0^{\circ}$, $\varepsilon_b = \varepsilon_p = 0.6$, $q_b = 60$ W/m^2 94

Table 4-8: Numerically predicted average convective and radiative heat flux from the center-of-glass region of the plate as a function of absorbed solar energy in the shade. Results are for tests indicated in Table 4-2. Models executed at $\phi = 0^{\circ}$, $b = 30$ mm, $\varepsilon_b = \varepsilon_p = 0.6$.....94

Table 4-9: Numerical conditions of parametric series 97

Table 4-10: Relative quality of statistical data fits....................104

Table 4-11: Estimated model parameters and quality of fit indicators for parametric case using $\cos\phi$. Parameters are presented in uncoded form. 99% confidence interval of parameters are provided. Note that b is in mm, T is in °C 104

Table 4-12: Estimated model parameters when blind and glass emissivity are 0.76 and 0.84 respectively. Parameters are presented in uncoded form. 99% confidence interval of parameters are provided. Note that b is in mm, T is in °C 109

Table 4-13: Total heat transfer at indoor window surface. Positive values are towards room. Blind and glass emissivity are 0.76 and 0.84 respectively. Values determined at $T_i = 297$ K. If $b > 40$ mm then use $b = 40$ mm....................110

Table 5-1: Comparison of measured and predicted solar heat gain coefficients....................124

Table B-1: Interferometric measurement uncertainties....................164

Table C-1: Sample analysis of numerical and interferometric data for no-blind case. Ostrach (1953) results are also included for comparison....................168

Table C-2: Sample analysis of selected interferometric data for validation case 2....................178

Table D-1: Heat flux at inside glass surface for all parametric cases where b = 20 mm....................188

Table D-2: Heat flux at inside glass surface for all parametric cases where b = 30 mm....................190

Table D-3: Heat flux at inside glass surface for all parametric cases where b = 40 mm 192

Table D-4: Estimated model parameters and quality of fit indicators for parametric case using $\cos\phi$. Parameters are presented in coded form. 99% confidence interval of parameters are in brackets. Note that b is in mm, T is in °C 194

Table D-5: Estimated model parameters and quality of fit indicators for parametric case using ϕ and $\sin\phi$. Parameters are presented in coded form. 99% confidence interval of parameters are in brackets. Note that b is in mm, T is in °C. 196

Table D-6: Estimated model parameters and quality of fit indicators for parametric case using n. Parameters are presented in coded form. 99% confidence interval of parameters are in brackets. Note that b is in mm, T is in °C 198

Table E-1: Calorimetric results of solar performance for a window and shade system with b = 30 mm. Fenestration is double glazed clear 3 mm glass (both lites). Measured *SHGC* uncertainty is ±0.02. *U*-factor uncertainty is ±1.4 W/m^2·K 206

Table E-2: Layer specific optical properties used in data analysis. For the current investigation, optical properties apply to both sides of each glazing 208

Table E-3: Comparison of measured and predicted solar heat gain coefficients 213

LIST OF FIGURES

Figure 1-1: Thermal resistance circuit for a window and venetian blind combination. (A) shows a circuit with no blind, while (B) shows the modifications necessary when a blind is added 4

Figure 1-2: Scope of research 16

Figure 2-1: System geometry (left), and photo of experimental model (right) 21

Figure 2-2: System computational domain and boundary conditions 28

Figure 2-3: Computation mesh used in the current study 31

Figure 2-4: Comparison of radiative and convective Nusselt numbers from the isothermal plate obtained using a full and reduced mesh 36

Figure 2-5: Comparison of radiative and convective Nusselt numbers from the isothermal plate obtained from an examination of boundary placement 39

Figure 2-6: Comparison of the local convection Nusselt number results for the "no blind" case with the boundary layer solution of Ostrach (1953). $Ra_l = 10^6, 10^7, 10^8$ 41

Figure 2-7: Comparison of the local convection and radiation Nusselt number results for the unheated blind case with the solution of Phillips (1999). $Ra_l = 10^7$ 42

Figure 3-1: Plan view of the Ryerson Mach-Zehnder interferometer. Reprinted with permission from Machin (1997) 44

Figure 3-2: Comparison of infinite fringe (left) and wedge fringe (right) interferograms 47

Figure 3-3: Schematic of isothermal plate 57

Figure 3-4: Schematic and photograph of plate and blind assembly 58

Figure 3-5: Convective and radiative heat flux for validation case 1: b = 15.4 mm, $\phi = 0^{o,}$ T_p = 283 K. Points represent interferometric results with associated experimental uncertainty. Solid line represents numerical results. Slat positions are superimposed on graphs for clarity. 64

Figure 3-6: Convective and radiative heat flux for validation case 2: b = 15.4 mm, $\phi = 0^{o\cdot}$ T_p = 298 K. Points represent interferometric results with associated experimental uncertainty. Solid line represents numerical results. Slat positions are superimposed on graphs for clarity. 65

Figure 3-7: Convective and radiative heat flux for validation case 3: b = 20.0 mm, $\phi = 0^{o\cdot}$ T_p = 283 K. Points represent interferometric results with associated experimental uncertainty. Solid line represents numerical results. Slat positions are superimposed on graphs for clarity. 66

Figure 3-8: Convective and radiative heat flux for validation case 4: b = 20.0 mm, $\phi = 0^{o\cdot}$ T_p = 298 K. Points represent interferometric results with associated experimental uncertainty. Solid line represents numerical results. Slat positions are superimposed on graphs for clarity. 67

Figure 3-9: Convective and radiative heat flux for validation case 5: b = 15.4 mm, $\phi = 45^{o\cdot}$ T_p = 283 K. Points represent interferometric results with associated experimental uncertainty. Solid line represents numerical results. Slat positions are superimposed on graphs for clarity. 68

Figure 3-10: Convective and radiative heat flux for validation case 6: b = 15.4 mm, $\phi = 45^{o\cdot}$ T_p = 298 K. Points represent interferometric results with associated experimental uncertainty. Solid line represents numerical results. Slat positions are superimposed on graphs for clarity. 69

Figure 3-11: Convective and radiative heat flux for validation case 7: b = 15.4 mm, $\phi = -45^{o\cdot}$ T_p = 283 K. Points represent interferometric results with associated experimental uncertainty. Solid line represents numerical results. Slat positions are superimposed on graphs for clarity. 70

Figure 3-12: Convective and radiative heat flux for validation case 8: b = 15.4 mm, $\phi = -45^{o\cdot}$ T_p = 298 K. Points represent interferometric results with associated experimental uncertainty. Solid line represents numerical results. Slat positions are superimposed on graphs for clarity. 71

Figure 3-13: Comparison of isotherms for validation case 2. Interferometric (left) and numerical (right)........76

Figure 4-1: Local convective and radiative heat flux in the center-of-glass region with changing glass temperature ($\phi = 0^{\circ}$, b = 30 mm, $\varepsilon_b = \varepsilon_p = 0.6$, q_b = 60 W/m^2). Slat positions are shown in gray......................86

Figure 4-2: Average convective and radiative heat flux from the center-of-glass region of the plate for the plate temperatures presented in Table 4-1. Models executed at $\phi = 0^{\circ}$, b = 30 mm, $\varepsilon_b = \varepsilon_p = 0.6$, q_b = 60 W/m^2......................88

Figure 4-3: Average convective and radiative heat flux from the center-of-glass region of the plate for the plate temperatures presented in Table 4-1. Models executed at $\phi = 0^{\circ}$, n = 18 mm, $\varepsilon_b = \varepsilon_p = 0.6$, q_b = 60 W/m^2......................89

Figure 4-4: Average convective and radiative heat flux from the center-of-glass region of the plate for the slat emissivities presented in Table 4-2. Models executed at $\phi = 0^{\circ}$, b = 30 mm, $\varepsilon_p = 0.6$, q_b = 60 W/m^2......................90

Figure 4-5: Average convective and radiative heat flux from the center-of-glass region of the plate for the plate emissivities presented in Table 4-2. Models executed at $\phi = 0^{\circ}$, b = 30 mm, $\varepsilon_b = 0.6$, q_b = 60 W/m^2......................92

Figure 4-6: Average convective and radiative heat flux from the center-of-glass region of the plate for the nominal spacings presented in Table 4-2. Models executed at $\phi = 0^{\circ}$, $\varepsilon_b = \varepsilon_p = 0.6$, q_b = 60 W/m^2......................93

Figure 4-7: Average convective and radiative heat flux from the center-of-glass region of the plate for the absorbed solar flux as presented in Table 4-2. Models executed at $\phi = 0^{\circ}$, b = 30 mm, $\varepsilon_b = \varepsilon_p = 0.6$......................95

Figure 4-8: Predicted and residuals verses modeled convective radiative and total heat flux......................103

Figure 4-9: Residuals verses model parameters......................107

Figure B-1: Sample infinite (left) and wedge (right) fringe interferograms for validation case 2 (b = 15.4 mm, $\phi = 0^{\circ}$)......................156

Figure B-2: Close-up infinite (left) and wedge (right) fringe interferograms for validation case 2 (b = 15.4 mm, $\phi = 0^{\circ}$)......................157

Figure C-1: Infinite fringe interferogram for no blind case with test conditions......................167

Figure C-2: Comparison of the local convection Nusselt number results for the "no blind" case with the similarity solution of Ostrach (1953), Ra_l=10^8 169

Figure C-3: Numerically and experimentally determined isotherms for ϕ = 0°, b = 15.4 mm 171

Figure C-4: Numerically and experimentally determined isotherms for ϕ = 0°, b = 20.0 mm 172

Figure C-5: Numerically and experimentally determined isotherms for ϕ = 45°, b = 15.4 mm 173

Figure C-6: Numerically and experimentally determined isotherms for ϕ = -45°, b = 15.4 mm 174

Figure C-7: Experimentally determined wedge fringe interferograms for validation cases 2, 4, 6, and 8 175

Figure C-8: Infinite fringe interferogram for validation case 2 with test conditions 177

Figure D-1: Local convective and radiative heat flux in the center-of-glass region with changing glass temperature (ϕ = -45°, b = 30 mm, ε_b = ε_p = 0.6, q_b = 60 W/m^2). Slat positions are shown in gray 180

Figure D-2: Local convective and radiative heat flux in the center-of-glass region with changing glass temperature (ϕ = 0°, b = 30 mm, ε_b = ε_p = 0.6, q_b = 60 W/m^2). Slat positions are shown in gray 181

Figure D-3: Local convective and radiative heat flux in the center-of-glass region with changing glass temperature (ϕ = 45°, b = 30 mm, ε_b = ε_p = 0.6, q_b = 60 W/m^2). Slat positions are shown in gray 182

Figure D-4: Local convective and radiative heat flux in the center-of-glass region with changing plate emissivity and glass temperature (ϕ = 0°, T_p = 287 K, 307 K, b = 30 mm, ε_b = 0.6, q_b = 60 W/m^2). Slat positions are shown in gray. Arrows indicate direction of increasing plate emissivity 183

Figure D-5: Local convective and radiative heat flux in the center-of-glass region with changing blind emissivity and glass temperature (ϕ = 0°, T_p = 287 K, 307 K, b = 30 mm, ε_p = 0.6, q_b = 60 W/m^2). Slat positions are shown in gray. Arrows indicate direction of increasing blind emissivity 184

Figure D-6: Local convective and radiative heat flux in the center-of-glass region with changing absorbed solar flux and glass temperature ($\phi = 0^o$, T_p = 287 K, 307 K, b = 30 mm, $\varepsilon_b = \varepsilon_p = 0.6$). Slat positions are shown in gray. Arrows indicate direction of increasing absorbed solar flux 185

Figure D-7: Local convective and radiative heat flux in the center-of-glass region with changing blind position and glass temperature (ϕ = 0^o, T_p = 287 K, 307 K, $\varepsilon_b = \varepsilon_p = 0.6$, q_b = 60 W/m^2). Slat positions are shown in gray. Arrows indicate direction of increasing nominal blind spacing 186

Figure D-8: Predicted verses calculated heat flux for case of cosϕ 195

Figure D-9: Predicted verses calculated heat flux for case of ϕ and sinϕ 197

Figure D-10: Predicted verses calculated heat flux for case of n 199

Figure E-1: Queen's University Solar Calorimeter in operation 201

Figure E-2: Queen's Solar Calorimeter. Cross-sectional schematic 202

Figure E-3: Calorimeter energy balance for standard test procedures 202

Figure E-4: Example of thermal efficiency verses $\Delta T/I$. The slope represents the U-factor, and the y-intercept is the solar heat gain coefficient 204

NOMENCLATURE

b	nominal louver spacing, mm
c	speed of light, m/s
C_p	specific heat, J/kg·K
d	fringe spacing, m
F	radiation shape factor, dimensionless, or Solar Heat Gain Coefficient, dimensionless
g	gravity, m/s^2
G	Gladstone-Dale Constant, m^3/kg
h	heat transfer coefficient, W/m^2·K
I	solar irradiation, W/m^2
k	conductivity, W/m·K
K	conductivity, dimensionless
l	plate height, mm
MSE	Mean Square Error, dimensionless
MSR	Mean Square Regression, dimensionless
n	louver tip to plate spacing, mm, or index of refraction, dimensionless, or
N	normal vector, or inward-flowing fraction, dimensionless, or number of points in data fit, or number of wavelengths
N_{RC}	radiation-to-conduction interaction parameter, dimensionless
Nu	Nusselt number, dimensionless
p	pressure, Pa
P	pressure, dimensionless, or number of parameters in data fit
Pr	Prandtl number, dimensionless
ps	louver pitch spacing, mm
q	heat flux, W/m^2
Q	heat flux, W
r	specific refractivity, m^3/kg
R	gas constant, Pa·m^3/kg·K
Ra	Raleigh number, dimensionless
rc	louver radius of curvature, mm
SC	Shading Coefficient, dimensionless
SHG	Solar Heat Gain, W/m^2
$SHGC$	Solar Heat Gain Coefficient, dimensionless
t	louver thickness, mm
T	temperature, K
TSS	Total Sum of Squares, dimensionless
u, v	velocity, m/s
U, V	velocity, dimensionless
U	Thermal transmission, W/m^2·K
w	louver width, mm

X	variable (matrix form)
x,y	coordinate axis, mm
X,Y	coordinate axis, dimensionless
y	response, W/m^2
Y	response (matrix form)
Z	model width, m

Symbols

α	fringe angle, rad, or absorptivity, dimensionless
β	volume expansion coefficient, 1/K, or parameter estimate
δ	Kronecker delta, dimensionless
Δ	change/difference
ε	emissivity, dimensionless
ϕ	louver angle, deg, or
η	fringe shift, dimensionless
λ	wavelength, m
μ	dynamic viscosity, kg/m·s
θ	solar azimuth angle, deg
ν	kinematic viscosity, m^2/s
ρ	density, kg/m^3, or reflectivity, dimensionless
σ	Stefan-Boltzmann Constant, W/m^2·K^4, or standard deviation, W/m^2
τ	transmissivity, dimensionless
ψ	solar altitude angle, deg

Subscripts

b	blind
c	inner glass to blind air space
C	convective
COG	center of glass
com	common window glass
d	diffuse
D	direct
f	fluid
fan	calorimeter fan
fen	fenestration
$flow$	calorimeter flow loop
g	glass
i	indoor/ambient
$input$	calorimeter input
l	fenestration layer indicator
$mask$	calorimeter mask

o	outdoor
o	vacuum
p	plate
pump	calorimeter pump
R	radiative
ref	reference
s	glazing cavity space
walls	calorimeter walls

Superscripts

T	transpose

Other

*	alternative dimensionless notation
—	average

CHAPTER 1
INTRODUCTION

1.1 Introduction

In order to evaluate the energy performance of buildings, estimate peak electrical loads, and assess occupant comfort in buildings, it is necessary to determine the Solar Heat Gain (*SHG*) through fenestration systems. *SHG* is the energy that enters a room through directly transmitted solar radiation and the inward flow of absorbed solar radiation. It may be shown that it is the product of the Solar Heat Gain Coefficient (*SHGC*), F, and the intensity of the incident solar irradiation, I, i.e.,

$$SHG = F \cdot I \tag{1.1}$$

F is usually quoted on a per unit area basis under specified conditions of wind speed and direction, interior and exterior temperature, and solar radiation. The *SHGC* of a particular fenestration system can be calculated as the sum of solar energy transmitted by the system, and the inward flow of absorbed solar energy in each layer of the system. Therefore

$$F = \tau + \sum_{l=1}^{n} N_l \cdot \alpha_l \tag{1.2}$$

where τ is the effective solar transmission, α is the effective solar absorption of a layer of the system, and N is the inward-flowing fraction of absorbed solar radiation. The subscript l denotes a fenestration layer where, for example, an individual glazing or shading device constitutes a layer in the system. The term "effective" is used to indicate that multiple reflections are considered between fenestration layers using the layer specific optical properties, which are in turn largely based on the material optical properties. The rate of energy transfer through a fenestration is then calculated using

$$q_{fen} = SHG - U(\Delta T_{i,o}) \tag{1.3}$$

where q_{fen} is the energy flux through a fenestration system, U is the window thermal transmissivity or U-factor, and $\Delta T_{i,o}$ is the indoor to outdoor air temperature difference.

It is common to mount a louvered shading device, such as a Venetian blind, adjacent to the indoor surface of a window to provide privacy and to control daylighting. The presence of these shading devices, however, will affect natural convection and radiant heat transfer from the window. Consequently, this will bring about a change in the U-factor and SHG of a window system. Collectively, combined window and shade systems are referred to as "complex fenestration."

In the past, calculation of SHG was mainly undertaken using tables contained in the ASHRAE Handbook of Fundamentals (2001). More recently, computer simulation (Wright 1994, Finlayson et al. 1993) has been used in the same way to estimate the thermal and solar performance of fenestrations consisting of combinations of glazings. Both methods are based on a one-dimensional analysis of the radiative, conductive, and convective heat transfer through a window, where convection from the indoor surface is obtained using accepted correlations for an isothermal vertical flat plate.

While software and tables handle many simple systems adequately, the methods have been limited in applicability and usage. Improved methods for predicting SHG values for complex fenestration systems need to be developed. While this task has been accomplished in the past, this was largely due to an inability to calculate the thermal performance of the shade layer, i.e., the inward-flowing fraction. While complexities in calculating the layer specific solar-optical properties are apparent, it is not as difficult to analyze as the thermal aspects of the problem. In fact, when examining previous investigations, methods of determining the layer specific optical properties are consistent; the data used was either obtained experimentally, or from a mathematical model developed by Parmelee et al. (1952, 1953b). The ways in which various researchers have attempted to determine the inward-flowing fraction is much more varied.

Inward-flowing fraction for most fenestration systems is easily quantified. For each layer of the fenestration, N_l can be determined based on the U-factor of the system, and the convective and radiative heat transfer coefficients found on and between the glazings (Vild 1964). For each fenestration layer in a double glazing, N_l is given by

$$N_{go} = \frac{U}{h_o} \tag{1.4}$$

$$N_{gi} = \frac{U}{h_o} + \frac{U}{h_s} \tag{1.5}$$

where h_o is the combined exterior radiative and convective heat transfer coefficient, h_s is the combined glazing cavity radiative and convective film coefficient, and *go* and *gi* refer to the outdoor and indoor glazings, respectively. For single glazings, Eq. (1.4) can be applied alone to determine the inward-flowing fraction. Unfortunately, the inward-flowing fraction of an interior blind cannot currently be determined using a method similar to that given in Eqs. (1.4) and (1.5). In an unshaded system, convection and radiation only occur between adjacent layers. In a shaded system, the interaction between the inner glazing, shade, and room is much more complex, and the inward-flowing fraction for the shade cannot be solved directly. Two thermal resistance networks comparing a double glazing with and without an interior shade are presented in Fig. 1-1.

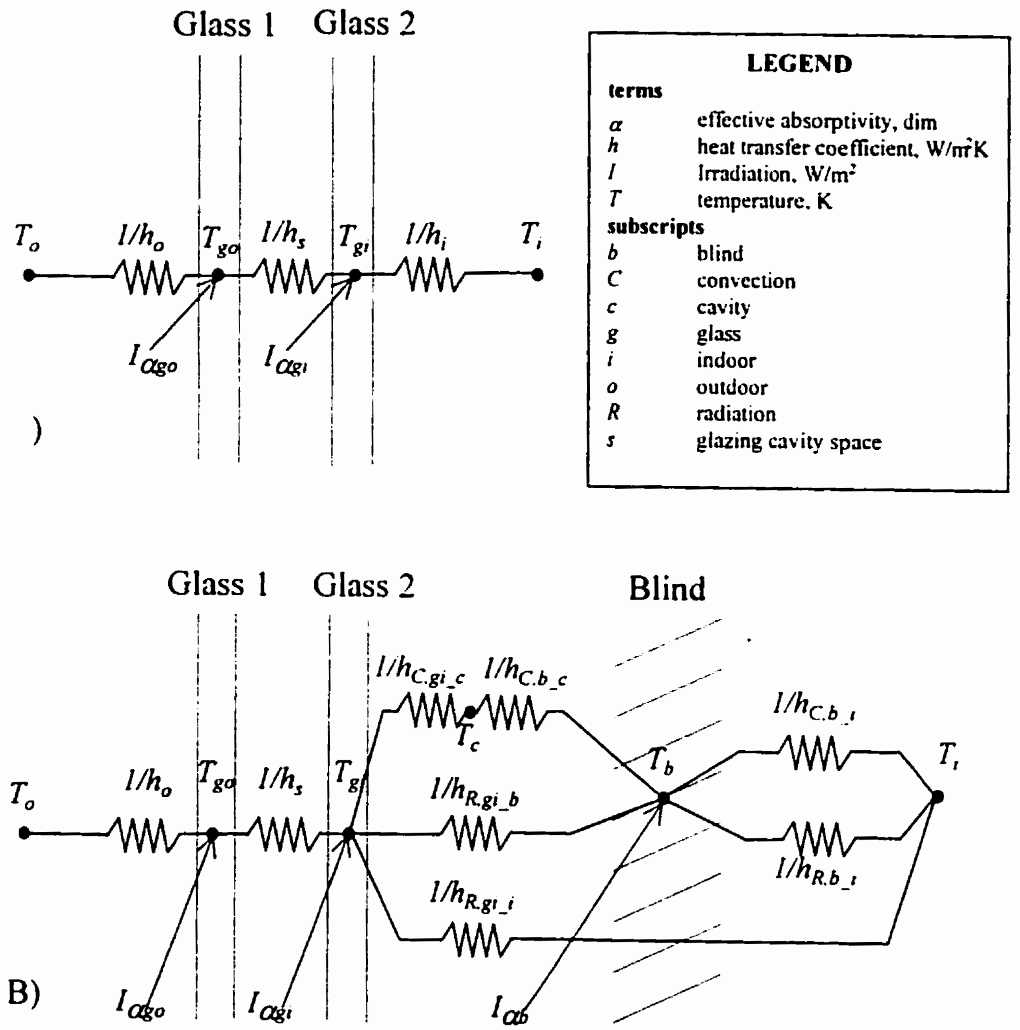

LEGEND

terms	
α	effective absorptivity, dim
h	heat transfer coefficient, W/m²K
I	Irradiation, W/m²
T	temperature, K
subscripts	
b	blind
C	convection
c	cavity
g	glass
i	indoor
o	outdoor
R	radiation
s	glazing cavity space

Figure 1-1: Thermal resistance circuit for a window and venetian blind combination. (A) shows a circuit with no blind, while (B) shows the modifications necessary when a blind is added.

1.2 Literature Review

1.2.1 Previous Investigations on the Effects of Venetian Blinds on Window Thermal and Solar Performance

The development of complex fenestration models is not a new endeavor. Since the early 1950's, researchers have attempted to quantify the effects of a shading layer on the solar and thermal performance of a window. Due to limitations in the scope of research, or the complexity of the analysis, none of these methods has become widely accepted.

The earliest investigation of horizontal louvered sun-shades was performed by Parmelee et al. (1952, 1953a, 1953b), in an attempt to determine the effectiveness of interior and exterior slat-type sun-shades for reducing heat gain through a single pane of sunlit glazing. Test samples were specially chosen to cover a broad range of cases including color, reflection characteristics, and geometry. A number of solar conditions were also investigated. The first of these studies presented a mathematical analysis (Parmelee and Aubele 1952) for the determination of layer specific absorptance, reflectance, and transmission for the shade layer. These properties were determined as a function of solar position with respect to the glazing system, the optical properties of the shade material, and slat geometry (slat width, angle, and pitch ratio), and results were presented for both direct and diffuse light. It was assumed in that analysis that the slats were flat and diffuse reflecting. The second paper (Parmelee et al. 1953a) presented an experimental verification of the fenestration system's layer specific optical properties. While the experimental results compared favorably with computed values for direct radiation, they did not for the case of diffuse radiation. The authors claimed that this was due to the uncertainty in predicting the distribution of diffuse sources. In a final work (Parmelee and Vild 1953b), tables of design data for use in predicting the Shading Coefficient (*SC*) for venetian blinds and sun-screens used in combination with several types of single flat glass are presented. *SC* is the ratio of *SHG* for a fenestration to the *SHG* of a single glazing. Expressions were obtained for the total heat gain and *SC* in terms of the transmittance and absorptance of the system, and an experimentally determined factor, *n*, used to account for the percent of absorbed solar energy that enters the room.

$$SC = \frac{\tau_{fen,D} \cdot I_D + \tau_{fen,d} \cdot I_d + n[(\alpha_{fen,D} - \alpha_{g,D})I_D + (\alpha_{fen,d} - \alpha_{g,d})I_d]}{\tau_{com,D} \cdot I_D + \tau_{com,d} \cdot I_d} \qquad (1.6)$$

where I_d and I_D are the diffuse and direct solar irradiation respectively, *fen* refers to the fenestration system, and *g*, *com* are the glass considered and common window glass respectively. The factor, *n*, was determined based on where the blind was situated in relation to the glazing. They concluded that the value, *n*, was constant for all similar systems, and contended that under most situations, incidence angle could be accurately represented by profile angle. *n* was held constant for the single glazing and shade systems considered in their study, however, a constant value of *n* may not suitably represent the complexity of a multiple glazing and shade combination (Farber et al. 1963).

Farber et al. (1963) and Pennington et al. (1964) presented a mathematical derivation and experimental verification of a *SHG* model for a double glass barrier with louvered shades or drapes. They expressed *SC* as

$$SC = \frac{(\tau_{fen,D} \cdot I_D + \tau_{fen,d} \cdot I_d) + (N_D \cdot \alpha_{fen,D} \cdot I_D + N_d \cdot \alpha_{fen,d} \cdot I_d)}{U_{com} / h_o(\alpha_{com,D} \cdot I_D + \alpha_{com,d} \cdot I_d) + \tau_{com,D} \cdot I_D + \tau_{com,d} \cdot I_d} \qquad (1.7)$$

where layer specific system optical properties were determined using the results given by Parmelee and Aubele (1952). Farber et al. (1963) attempted to develop a thermal resistance network to determine the convective and radiative gain (i.e., inward-flowing fraction) despite complex geometries such as blinds or pleated drapes, and multiple glazings. Unfortunately, a lack of a reliable predictor of convective heat transfer coefficients complicated the analysis of this thermal network. For example, they provided an equation for predicting convective heat transfer coefficients assuming convection from the inner glazing could be represented as occurring from a simple planer surface without interference from the slats on the outer edge of the boundary layer. Convective flow from the blind was calculated using the same equation, accounting only for the increase in total surface area. Pennington et al. (1964) in a later publication showed that the model had reasonable success in replicating experimentally obtained results.

Owens (1974) completed a mathematical analysis of blind optical performance. A matrix technique was used to find the optical properties of the shading layer based on the properties of the material. An energy balance was then used to determine the heat flow and effective absorption in each layer. Owens' model was applicable to a wide spectrum of fenestration incorporating multiple glazings, coatings, and various types of shades. Unfortunately, while trying to deal with the complexity of the problem, the analysis was oversimplified. Specifically, solar irradiation was considered only at normal incidence, diffuse sources were disregarded, and convective effects at the inside window surface were considered inconsequential, i.e., it was assumed that the system was dominated by the transmitted and reflected-through component of the direct solar radiation. More importantly, Owens avoided the problem of determining the inward-flowing fraction of the shade by assuming all absorbed energy was conducted to the interior, i.e., $N = 100\%$. Interestingly, even with these simplifications, Owens' model is too large to repeat here, and the reader is referred to Owens (1974) for details of his calculation method.

Van Dyck and Konen (1982) developed a mathematical method to analyze single glazing and shade combinations. Based on experimentally determined solar optical properties of the shade layer, they performed an optical balance to determine the effective transmittance and absorbed energy within each layer. Inward-flowing fraction of the glazing was then calculated using Eq. (1.4). For the blind, they postulated that all energy absorbed by any interior shading layer (blind, roller shade, or drape) would remain in the room, i.e., $N = 100\%$. They then produced the following equation for single glazings with internal shading

$$SC = \frac{1}{0.87}\left[\frac{(1-\rho_b)\tau_{go}}{(1-\rho_{go}\cdot\rho_b)} + N_{go}\cdot\alpha_{go}\left(1+\frac{\rho_b\cdot\tau_{go}}{(1-\rho_{go}\cdot\rho_b)}\right)\right] \tag{1.8}$$

where ρ is the reflectivity, and 0.87 is the *SHG* of a reference glazing. This work was extended to give predictive equations for single glazings with other types of shading layers. Thus, for any shading layer and single glazing combination, they proposed

$$SC = \frac{1}{0.87}\left[\frac{\tau_b\cdot\tau_{go}}{(1-\rho_{go}\cdot\rho_b)} + N_b\frac{\alpha_b\cdot\tau_{go}}{(1-\rho_{go}\cdot\rho_b)} + N_{go}\cdot\alpha_{go}\left(1+\frac{\rho_b\cdot\tau_{go}}{(1-\rho_{go}\cdot\rho_b)}\right)\right] \tag{1.9}$$

The interior blind analysis was completed for single glazings only. The adaptation of such a model to a double glazing scenario would have to be completed to provide a reasonable range of application.

A number of studies have also been performed to determine the thermal and solar characteristics of fenestration systems with a shading layer between the glazings. The treatment of these systems may provide useful information for the current analysis, and will therefore be reviewed here.

Ozisik and Schutrum (1960) attempted to determine *SHG* for the case where blinds were installed between the glazings of a double glazed window. Layer specific optical properties were determined using the method presented in Parmelee at al. (1952), while thermal properties were calculated from the heat balance equations assuming steady-state conditions. As with other models, the total *SHG* was then given as the sum of the transmitted solar energy, and some fraction of the energy absorbed by the fenestration. Data for use in the equations was limited in scope and availability. Multiple geometries or different types of glass were never considered, and only three types of slats were tested at two different slat angles. Their model results did, however, agree with calorimetric data, and was later validated experimentally by Smith and Pennington (1964).

Rheault and Bilgen (1989, 1990) investigated the overall heat transfer rates of a window system with Venetian-type blinds sealed between two panes of glass in an insulated glazing unit. The study was both analytical (1989) and experimental (1990), and used climatic conditions for a typical Canadian winter and summer. In the analytical work, the temperature variation across the slats and over the thickness of each glazing was assumed to be minimal, and therefore conduction effects were neglected within the blind slats. Furthermore, the distance between slat tips and the window glazings was relatively large. Therefore, it was assumed that the presence of the slats did not interfere with the cavity flow when the slats were all in positions other than the vertical angle. When the slats were placed vertically, the problem was treated as two side-by-side cavities with the slats as a dividing wall. Only radiation and convection transfer rates across the window system were considered, i.e., conduction was neglected. The numerical work concluded that the presence of louvers between the glazings could reduce heating and cooling loads. The analytical results were later verified by the results obtained in the experimental study.

Garnet et al. (1995) conducted an experimental investigation similar to that of Rhealt and Bilgen (1989, 1990). In that study, aluminum Venetian blinds similar to those available commercially were placed between the glazings at a closer tip-to-window spacing. These blinds could be raised and lowered so that comparisons of the *U*-factors with and without the venetian blinds could be made. It was observed that when the louvers were in the horizontal position the overall *U*-factor was greater than in the no-blind case. As the blind angle was increased. the *U*-factor would drop below that of the no blind case. It was speculated that, in the horizontal position. conduction effects in the aluminum blinds would outweigh convection suppression. Furthermore. as the angle increased, the louvers would block long-wave radiation leading to a decreased overall *U*-factor for the system.

A more recent experimental study was conducted by Fang and Ge (1993). This study considered Venetian blinds adjacent to the inside glazing of a single and double glazed window. The change in temperature across the fenestration system was varied along with blind angle. Only one blind spacing was considered. Furthermore, the louvers were large slats that were covered with aluminum foil. The results of this study showed that the overall heat transfer coefficient varied with blind angle and temperature difference.

Klems et al. (1992, 1994a, 1994b, 1995, 1996a, 1996b, 1997) developed a comprehensive mathematical analysis that was applicable to all shading devices, with all types and numbers of glazings, and in any combination or order. By assuming transmissivity and absorptance to be purely optical properties, values measured using a scanning radiometer were used. Similarly, if N was considered to be purely a thermal property, it was proposed that a calorimetric test would suffice for any particular geometry, regardless of material properties. Called "Solar-Thermal Separation", the method allows the calculation of *SHGC* for a complex fenestration for any orientation, irradiation direction, or surroundings. Accounting for the angular dependence of the optical properties

$$F(\psi,\theta) = \tau(\psi,\theta) + \sum_{l=1}^{n} N_l \cdot \alpha_l(\psi,\theta) \qquad (1.10)$$

where ψ is the solar incident angle, and θ is the azimuth angle. Application of this approach could permit the accurate and repeatable characterization of optically complex fenestration systems, accounting for the spectral and directional dependent properties of individual fenestration components. Unfortunately, the method is overly complex, and is currently not useful due to a lack of accurate input data. A large electronic data base of experimentally determined thermal and optical properties would be needed before this method could be widely applied. Such a data base would take many years to compile, and to date, no researcher has been willing to perform this task.

1.2.2 Current Investigations on the Effects of Venetian Blinds on Window Thermal and Solar Performance

At present, advances are being made that demonstrate the complex thermal interaction between a shade and a window in the absence of solar irradiation. Several studies have examined the effect of a Venetian blind on the free convective heat transfer at an indoor glazing surface when there is no solar irradiance, i.e., for "nighttime" conditions. All of these studies have been performed under an NSERC strategic project involving Queen's University, Ryerson University, and the University of Waterloo.

Machin (1997) performed interferometric and flow visualization studies to examine the effect of a Venetian blind on the free convective heat transfer at an indoor glazing surface when there is no solar irradiance. His experiment used a Mach-Zehnder Interferometer to examine the local and overall convection coefficients from the surface of an isothermal plate at various blind to plate spacings and louver angles. The results showed that Venetian blinds have a strong influence on the local heat transfer coefficients over the length of the plate. When an aluminum blind was placed close to the plate surface, the slats caused a strong periodic variation in the local Nusselt number distribution. In general, however, the average convective heat transfer rate was only slightly lower than that of an isolated vertical plate, indicating that a blind would only slightly lower a fenestration system *U*-factor.

A numerical study at Queen's University by Ye (1997) was undertaken in conjunction with Machin's work. A two-dimensional finite element examination was conducted of the local and average convective heat transfer rates at the indoor window glazing in the presence of a Venetian Blind. In that study, the effects of thermal radiation were neglected and the blind slats were modeled as zero thickness, flat, non-conducting, no-slip, impermeable surfaces. The work involved a study of the effect of blind angle and plate-to-blind spacing on the free convective heat transfer from an isothermal flat plate, and was compared to the results from Machin (1997). It was found that the numerical results were lower than the experimental results. Ye (1997) concluded that the conduction in the Venetian blind likely caused this difference.

A subsequent numerical study was performed by Phillips (1999). This study included the effect of heat conduction, and the curvature and thickness of the blind slats. Initially, radiative heat exchange was neglected, and agreement with the experimental data of Machin (1997) was poor except when the blind slat temperatures were fixed at the measured experimental values. It was concluded that the effect of radiation was significant and needed to be included in the model. Phillips (1999) then examined the effects of horizontal louvers on the coupled convective and radiative heat transfer at an indoor window glazing. The improved model showed excellent correlation with interferometric data.

With good agreement between experimental and numerical simulation of a window and interior Venetian blind under "nighttime" conditions, the investigation moved to a "daytime" situation that included the effects of incident solar energy. Daytime conditions were examined using the concept of solar-thermal separation, which works on the assumption that long and short wave radiation do not interfere with one another, and can be examined independently. Therefore, the effects of solar irradiation are considered from a thermal perspective by heating the shade layer as a representation of absorbed solar energy. The amount of absorbed energy would be determined by an optical analysis of the system.

In a recent experimental study, Duarte (2000) performed interferometry and flow visualization to examine the effect of a heated Venetian blind on the free convective heat transfer at an indoor glazing surface. His experiment used a Mach-Zehnder Interferometer to consider the effects of blind slat angle, blind-to-window spacing and blind irradiation on heat transfer from an isothermal plate maintained at 15 K above the ambient temperature. His investigation also focused on the plate leading edge and six blind louvers. The results show that Venetian blinds have a strong influence on the local heat transfer coefficients in the region investigated.

1.3 Present Research Objectives

The present work was specifically aimed at developing an understanding of the thermal aspects of a sunlit window and Venetian blind combination. It was intended that a two-dimensional numerical model of the radiative and convective heat transfer from an vertical isothermal surface (representing a window) with adjacent heated louvers (representing irradiated blind slats) would be developed. This numerical model would be validated using the experimental model and apparatus (Mach-Zehnder Interferometer) located at Ryerson University (Machin 1997, Duarte 2000). Once validated, the numerical model would be used to investigate the effects of a number of factors on the heat transfer in the system. These factors include blind location and slat angle, blind and glass emissivity, glass temperature, and the level of solar radiation absorbed in the blind slats. The ultimate goal would be to produce a correlation useful in predicting the *U*-

factor and solar heat gain coefficient of a sunlit fenestration and interior Venetian blind combination. It was hoped that this work will provide the methodology and data necessary for predicting the *U*-factor and solar gain of a sunlit fenestration and interior Venetian blind combination. Figure 1-2 indicates the scope of research.

The present analysis expands the previously described work in a number of ways. It numerically examines the influence of heated horizontal louvers on the convective and radiative heat transfer from a vertical isothermal surface. In addition, the effects of a cool plate were examined. All previous studies have only examined warm plate surfaces. Finally, the entire plate was examined. Past investigations have only examined a small section of fenestration model.

In reference to Fig. 1-1, two possible paths of investigation are possible; a modified inside glazing heat transfer coefficient (Fig. 1-1a), and a comprehensive thermal analysis of individual paths of heat transfer (Fig. 1-1b). For this study, it was decided to examine heat transfer at the interior glass surface rather than determining the heat transfer relations between the glass and shade layers. While it is understood that the mechanisms of heat transfer in this system can be described in traditional terms using the second option, the results would not be useful unless used in conjunction with a numerical solution. It is more desirable, in the author's opinion, to provide data usable by a semi-skilled end user. The success of the present analysis will determine if a more detailed and complex analysis is required.

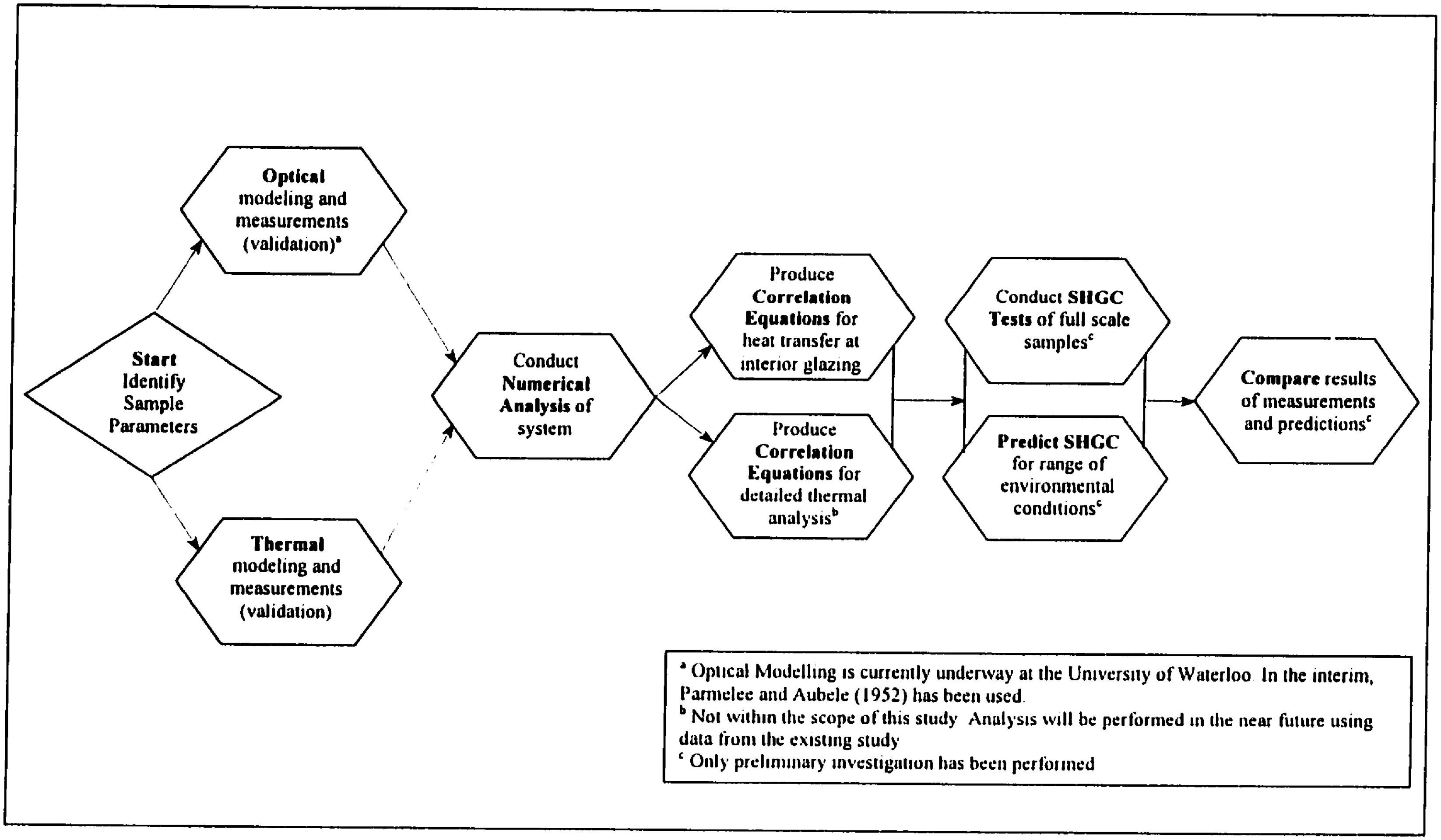

[a] Optical Modelling is currently underway at the University of Waterloo In the interim, Parmelee and Aubele (1952) has been used.
[b] Not within the scope of this study Analysis will be performed in the near future using data from the existing study
[c] Only preliminary investigation has been performed

Figure 1-2: Scope of research.

1.4 Thesis Format

It was originally intended to write this thesis in manuscript format as outlined by the School of Graduate Studies and Research. In that form, the chapters of the thesis would consist of published and publishable manuscripts followed by a general discussion of the results. It was the author's opinion, however, that this format ultimately caused excessive redundancy in the thesis, and that the traditional thesis format was required.

In that regard, Chapters 2 through 4 are largely composed of manuscripts. The information presented in Chapters 2 and 3 has been published in two parts at the American Society of Mechanical Engineers, International Mechanical Exposition (Collins et al. 2000, 2001) and are currently submitted for publication in the ASME Journal of Heat Transfer. The first part of Chapter 4 has been accepted for publication in ASHRAE Transactions (Collins et al. 2002). The second part of Chapter 4 has also been prepared, but at the time of submission, this section of the thesis had not yet been submitted to a Journal.

The information presented in the aforementioned publications has been reformatted to suit a traditional form of thesis. The numerical development, which is important to each of the sub-studies, is presented in detail as Chapter 2. Chapter 3 details the validation of the numerical determined convective heat transfer using the Mach-Zehnder interferometer located at Ryerson University. It also presents an analysis of the local radiative and convective heat flux from the interior glazing surface. The first part of Chapter 4 details the investigation of parameters which are expected to affect heat transfer in the system using the numerical model. It is intended to aid in the development of a comprehensive parametric analysis. The second part of Chapter 4 is a comprehensive parametric analysis of the system using the numerical model. A general discussion, and conclusions and recommendation sections will summarize the discussions and conclusions presented in Chapters 3 and 4, in addition to presenting some new material. Specifically, these sections include the development and application of new correlation equations to the determination of *U*-factor and *SHG* in a windows and shade systems.

Detailed results and supporting documentation in the experimental and numerical methods used are presented in the Appendices.

CHAPTER 2
NUMERICAL MODEL DEVELOPMENT

2.1 Introduction

This chapter describes how a conjugate conduction/convection/radiation numerical model was developed using the finite element method. The non-dimensionalization scheme has been outlined and applied to the governing partial differential equations and boundary conditions.

A number of tests were performed to provide confidence in the finite element solution. The grid selected for the computational domain was tested through a grid sensitivity study, and boundaries were examined carefully to ensure that their locations were suitable. Comparison of numerical model results to comparable accepted solutions was also performed.

2.2 Physical Description of Model

Numerical development was performed in conjunction with the development of an experimental model. In that regard, previous numerical developments (Ye 1997, Phillips 1999) were intended to mimic the experimental model located at Ryerson University (Machin 1997, Duarte 2000). In those studies, the system was idealized as a vertical isothermal surface (to represent the interior surface of a window) with adjacent louvers (to represent blind slats). In the case of Duarte (2000), the louvers were heated (to represent irradiated blind slats).

The current numerical model was also developed to approximate the experimental model. As such, the system geometry was determined from an isothermal plate and seventeen horizontal louvers from a commercially available aluminum Venetian blind. The indoor glazing surface was idealized as an isothermal vertical flat plate of height (l) and emissivity (ε_p), that was heated or cooled to a temperature (T_p) with respect to the ambient room temperature (T_i). A Venetian blind was positioned at a nominal distance (b) from the plate surface and the individual slats were inclined at an angle with respect to the horizontal (ϕ). The slats had a width (w), thickness (t), an arc length and a radius of curvature (rc), and a pitch (ps) which provided a slat pitch ratio (ps/w = 7/8) that was typical of commercially available Venetian blinds. The slats had an emissivity (ε_b), and slat thermal conductivity (k_b) (Machin 1997). To facilitate future analysis the blind tip-to-glass spacing (n) was also defined. A heat flux (q_b) was applied to one side of each slat to simulate the solar radiation absorbed by the blind. Finally, the room was considered a black body for all investigations, i.e., the room emissivity (ε_i) was 1. Parameters that remained constant for all simulations are given in Table 2-1. Figure 2-1 shows the system geometry and the experimental setup.

Table 2-1: Constant numerical model parameters.

l (mm)	ps (mm)	w (mm)	t (mm)	rc (mm,deg)	T_i (K)	ε_i	k_b (W/m·K)
379.6	22.2	25.4	0.17	52.3 , 27.3	297	1.00	120

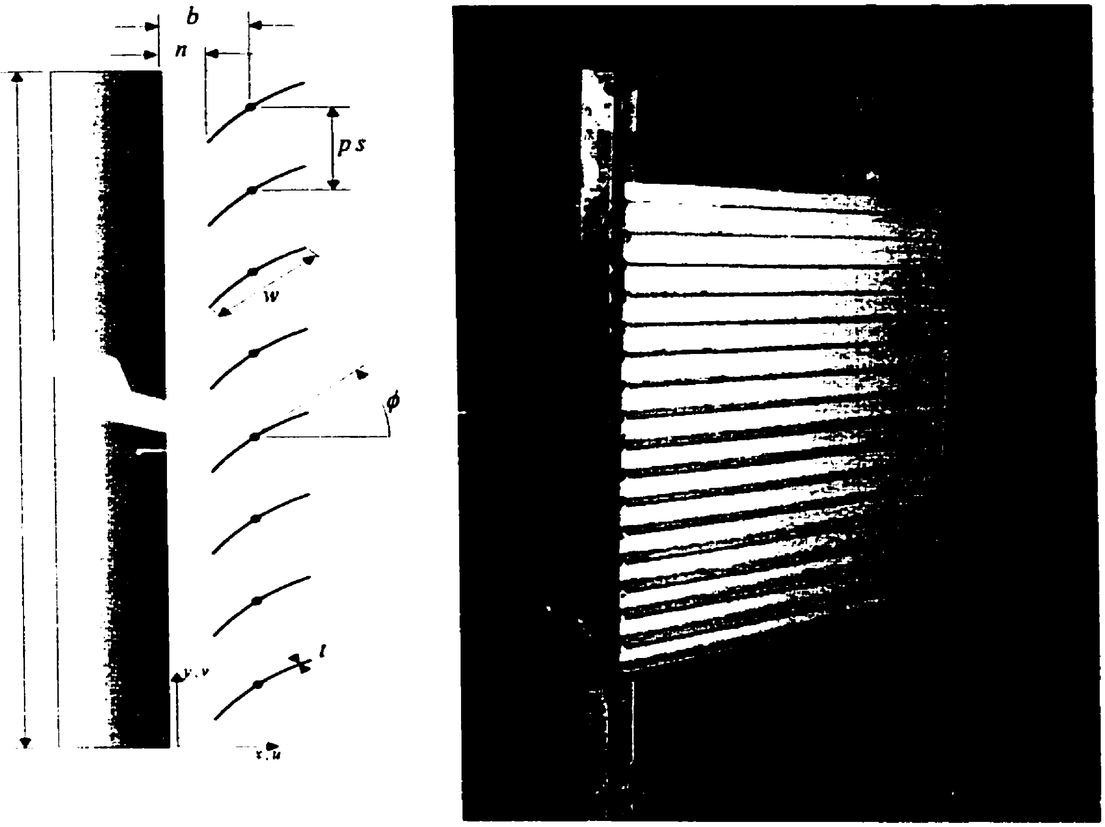

Figure 2-1: System geometry (left), and photo of experimental model (right).

The numerical model is an idealized representation of a real fenestration. For an actual window, there will be frame effects, and only the center-of-glass region will be nearly isothermal. Also, the actual indoor glazing temperature will increase with the solar irradiance, rather than being constant. These simplifications do, however, eliminate several secondary parameters, such as the frame geometry and the glazing external thermal boundary conditions.

Six variables were identified for further examination, i.e., the slat angle (ϕ) and nominal distance (b), slat emissivity (ε_b) and absorbed heat flux (q_b), and plate temperature (T_p) and emissivity (ε_p).

2.3 Governing Equations

In order to obtain a numerical solution, the physical problem must be described in mathematical terms. This involves defining the assumptions and governing equations that apply over the computational domain, reducing these equations to an appropriate form, and then imposing boundary conditions.

2.3.1 Assumptions

In developing the present numerical model, a number of assumptions have been made. These include:

- the flow is steady, laminar, incompressible and two-dimensional;
- the thermo-physical properties are constant, except for fluid density, which is treated by means of the Boussinesq approximation;
- the effects of viscous dissipation have been neglected; and
- grey diffuse radiation exchange exists between the window, blind and room, and the fluid is a non-participating medium. Individual surfaces are uniform in temperature.

2.3.2 Dimensional Equations

Free convective motion is due to differences in fluid density acted upon by a body force. In the case of this study, the body force is gravitational and differences in density are due to temperature variations within the flow field. To describe natural convective heat transfer, the continuity, momentum, and energy equations are required. These equations result from applying the laws of conservation of mass, momentum and energy.

Using the assumptions discussed above, the continuity, x and y momentum equations and the energy equations are as given in Eqs. (2.1), (2.2), (2.3), and (2.4) respectively.

$$\frac{\partial u}{\partial x}+\frac{\partial v}{\partial y}=0 \tag{2.1}$$

$$\rho\left(u\frac{\partial u}{\partial x}+v\frac{\partial u}{\partial y}\right)=-\frac{\partial p}{\partial x}+\mu\left(\frac{\partial^2 u}{\partial x^2}+\frac{\partial^2 u}{\partial y^2}\right) \tag{2.2}$$

$$\rho\left(u\frac{\partial v}{\partial x}+v\frac{\partial v}{\partial y}\right)=-\frac{\partial p}{\partial y}+\mu\left(\frac{\partial^2 v}{\partial x^2}+\frac{\partial^2 v}{\partial y^2}\right)+g\rho\beta(T-T_i) \tag{2.3}$$

$$u\frac{\partial T}{\partial x}+v\frac{\partial T}{\partial y}=\alpha\left(\frac{\partial^2 T}{\partial x^2}+\frac{\partial^2 T}{\partial y^2}\right) \tag{2.4}$$

here, u and v are velocities in the x and y directions respectively, p is the pressure, μ is the dynamic viscosity, α is the thermal diffusivity, ρ is the density, β is the volume expansion coefficient and equals $1/T$, and g is the gravitational acceleration. A detailed derivation of the above equations can be found in Schlicting (1970).

Conduction through the louvers is an important factor in the heat loss from a window glazing. This is especially true when the louver tips are in close proximity to the surface of the window. Conduction through each louver is described by Fourier's equation assuming steady-state conditions with no internal heat generation and isotropic conductivity.

$$\frac{\partial^2 T}{\partial x^2}+\frac{\partial^2 T}{\partial y^2}=0 \tag{2.5}$$

The final mode of heat transfer that requires numerical description is radiation. The radiation model employed in this study is the net radiation method outlined in Siegel and Howell (1970). This method is based on an enclosure that completely surrounds the computational domain. All solid surfaces within the computational domain have been treated as diffuse, hemispherical emitters of thermal radiation. Furthermore, the grey assumption has been implemented so that the emissivity of all solid surfaces are independent of thermal radiation wavelength. The final assumption in the net radiation method is that all surfaces have uniform temperature. Radiation exchange between all solid surfaces within the computational domain is governed by

$$\sum_{j=1}^{N}\left(\frac{\delta_{kj}}{\varepsilon_j} - F_{k-j}\frac{1-\varepsilon_j}{\varepsilon_j}\right) q_j = \sigma\sum_{j=1}^{N}\left(\delta_{kj} - F_{k-j}\right)\left(T_j\right)^4 \qquad (2.6)$$

In Eq. (2.6), ε_j is the emissivity of the j^{th} surface, σ is the Stefan-Boltzmann constant, and δ is the Kroniker delta which equals 1 when $j = k$ and 0 when $k \neq j$. F is the view factor. and q is the radiative heat flux associated with the jth surface. A complete derivation of Eq. (2.6) is given in Siegel and Howell (1970).

2.3.3 Non-Dimensionalization

The present study utilized a non-dimensional scheme which allowed radiation to be incorporated into the solution process. Radiation heat transfer is dependent on the absolute temperature while convection and conduction are governed by temperature differences. This non-dimensionalization scheme allowed for the solution of all modes of heat transfer. An in-depth description of this scheme was obtained from Phillips et al. (1999). The following dimensionless variables were used

$$X = \frac{x}{l} \qquad Y = \frac{y}{l}$$

$$U_{ref} = \frac{\alpha_f}{l} \qquad U = \frac{u}{U_{ref}} \qquad V = \frac{v}{U_{ref}} \tag{2.7}$$

$$P = \frac{pl}{\mu_f U_{ref}} \qquad T^* = \frac{T}{T_i}$$

The subscript f is used to denote the fluid. By substituting the dimensionless variables (2.7) into the continuity Eq. (2.1), the x and y momentum Eqs. (2.2) and (2.3), and the energy Eq. (2.4), the following dimensionless equations result

$$\frac{\partial U}{\partial X} + \frac{\partial V}{\partial Y} = 0 \tag{2.8}$$

$$\frac{1}{\mathrm{Pr}}\left(U\frac{\partial U}{\partial X} + V\frac{\partial V}{\partial Y}\right) = -\frac{\partial P}{\partial X} + \left(\frac{\partial^2 U}{\partial X^2} + \frac{\partial^2 U}{\partial Y^2}\right) \tag{2.9}$$

$$\frac{1}{\mathrm{Pr}}\left(U\frac{\partial V}{\partial X} + V\frac{\partial V}{\partial Y}\right) = -\frac{\partial P}{\partial Y} + \left(\frac{\partial^2 V}{\partial X^2} + \frac{\partial^2 V}{\partial Y^2}\right) + Ra_R\left(T^* - 1\right) \tag{2.10}$$

$$U\frac{\partial T^*}{\partial X} + V\frac{\partial T^*}{\partial Y} = \frac{\partial^2 T^*}{\partial X^2} + \frac{\partial^2 T^*}{\partial Y^2} \tag{2.11}$$

where the "modified" Rayleigh number Ra_R and the Prandtl number Pr are defined by

$$Ra_R = \frac{g\beta_f T_i l^3}{\alpha_f \nu_f} \qquad \mathrm{Pr} = \frac{\nu_f}{\alpha_f} \tag{2.12}$$

where ν_f is the kinematic viscosity of the fluid.

The dimensionless variables (2.7) may also be substituted into the conduction Eq. (2.5) to obtain the following dimensionless conduction equation

$$\frac{\partial^2 T^*}{\partial X^2} + \frac{\partial^2 T^*}{\partial Y^2} = 0 \tag{2.13}$$

Finally, Eq. (2.6) governing radiation heat transfer may be cast into dimensionless form by first introducing a dimensionless radiation heat flux as follows

$$q^* = \frac{ql}{k_f T_i} \tag{2.14}$$

By substituting this dimensionless heat flux into Eq. (2.6), the following dimensionless governing equation for radiation is obtained

$$\sum_{j=1}^{N}\left(\frac{\delta_{kj}}{\varepsilon_j} - F_{k-j}\frac{1-\varepsilon_j}{\varepsilon_j}\right) q_j^* = N_{RC}\sum_{j=1}^{N}\left(\delta_{kj} - F_{k-j}\right)\left(T_j^*\right)^4 \tag{2.15}$$

where $$N_{RC} = \frac{\sigma T_i^3 l}{k_f}$$

N_{RC} is a dimensionless variable resulting from the use of the non-dimensionalization scheme introduced above. This variable is called the Radiation-to-Conduction Interaction Parameter. Physically, it can be thought of as the ratio of the potential to radiate over the potential to conduct heat from a surface.

For most of this study a more traditional convection Rayleigh number will be used as follows

$$Ra_l = \frac{g\beta_f\left(T_p - T_i\right) l^3}{\alpha_f \nu_f} \tag{2.16}$$

The Rayleigh number Ra_l is the ratio of the strength of the buoyancy forces to viscous forces. Another quantity in the non-dimensionalization scheme is Ra_R, the "Modified" Rayleigh number, where the relationship between Ra_R and Ra_l is

$$Ra_l = Ra_R\left(T_p^* - 1\right) \tag{2.17}$$

Therefore, by defining a dimensionless surface temperature and a "Modified" Rayleigh number the traditional Rayleigh number can be found. In effect, they can be combined to form one convection parameter, and either Ra_l or Ra_R can be used.

For reasons that will be explained later, it is most convenient to present results in the form of dimensional heat transfer rate. The local and average convective heat transfer from the window, however, will sometimes be presented as a dimensionless convection Nusselt number. The local and average Nusselt numbers are defined by

$$Nu_C = \frac{q_C l}{k_f (T_p - T_i)} \qquad \overline{Nu_C} = \int_{Y=0}^{1} Nu_C \cdot dY \tag{2.18}$$

Similarly, the local and average radiation heat flux from the window has been expressed as local and average Nusselt numbers as follows

$$Nu_R = \frac{q_R l}{k_f (T_p - T_i)} \qquad \overline{Nu_R} = \int_{Y=0}^{1} Nu_R \cdot dY \tag{2.19}$$

2.3.4 Boundary Conditions

To obtain a solution, the boundary conditions must be specified. Considering Fig. 2-2, the boundary G-H represents the window, along which a no-slip boundary condition has been applied. To approximate an isothermal window, a constant temperature has also been applied to this boundary. Sections A-H and G-F are similar in that they are also isothermal wall sections, however, they are assumed to be at the ambient temperature. The room is represented by section B-E. Along this boundary, there are no buoyancy induced flows (i.e., no flow in the *y*-direction), and air entrained through the boundary

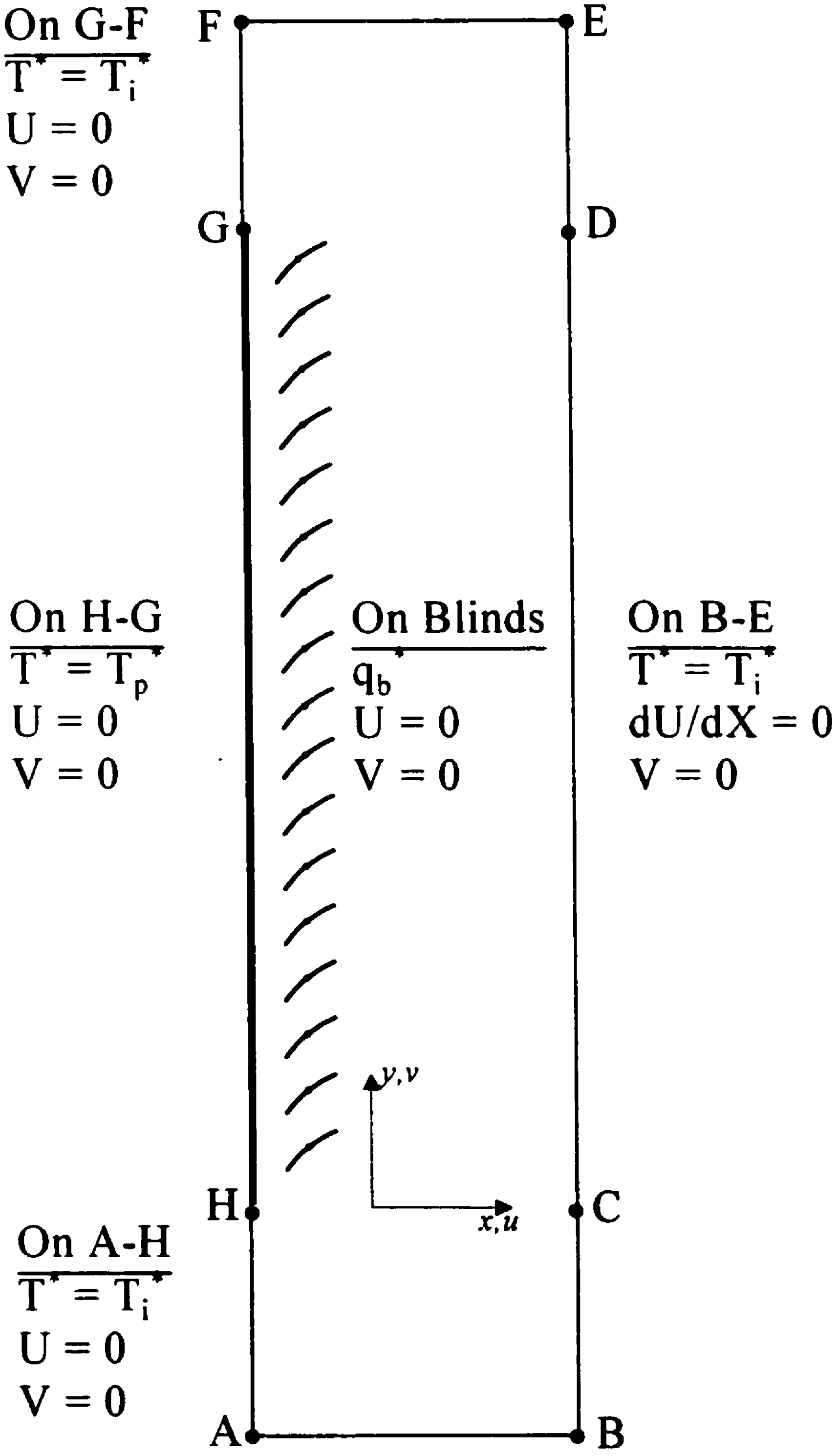

Figure 2-2: System computational domain and boundary conditions.

must be moving horizontally. The temperature of all entrained air has been set to the ambient temperature. Finally, sections A-B and E-F represent the upper and lower entrance regions respectively. Due to the possibility of both rising and falling flows occurring simultaneously, no temperature or velocity boundary was put on these sections.

The dimensional form of these boundaries are

$u = v = 0$ on A-F
$v = du/dx = 0$ on B-E
$T = T_p$ on H-G
$T = T_i$ on A-H, G-F, B-E

by substituting the dimensionless variables, these conditions become

$U = V = 0$ on A-F
$V = dU/dX = 0$ on B-E
$T = T_p^*$ on H-G
$T = T_i^* = 1$ on A-H, G-F, B-E

At the surface of the slats, no-slip and impermeability conditions apply ($U = V = 0$). Continuity conditions for temperature and heat flux also apply at this solid-fluid interface. These can be expressed in dimensionless form as

$$K_{bf} \left. \frac{\partial T^*}{\partial N} \right|_{solid} = \left. \frac{\partial T^*}{\partial N} \right|_{fluid} + \frac{q_b l}{k_f T_i} - \frac{q_j l}{k_f T_i} \tag{2.20}$$

where N is the normal vector, K_{bf} is the blind-to-fluid conductivity ratio, q_b is the absorbed flux in the blind slat, and q_j is the net radiative heat transfer from slat surface j, as determined using Eq (2.15).

2.3.5 Solution

Equations (2.8) through (2.15) have been solved subject to the specified boundary conditions using the finite element method. Fluid properties were evaluated at an estimated film temperature of 300 K and were taken from Touloukian et al. (1970a, 1970b, 1975). This approach was taken because the inclusion of a hot blind between the glass and the ambient would cause an under-prediction of the film temperature using the traditional method.

To produce a solution, the computational domain of a problem must first be broken into a number of elements (Fig. 2-3). The variables are then assumed to vary across the elements according to chosen interpolation functions. In this study, nine-node quadratic elements with biquadratic interpolation functions were used for temperature and velocity. These elements allow quadratic variations over the element. The complex governing equations are reduced from non-linear, partial differential equations, which apply continuously over the entire computational domain, to a system of non-linear algebraic expressions that apply over each element. These algebraic equations are then solved simultaneously to obtain temperature and velocity at each node. Pressure has been eliminated from the problem using a penalty function method (Fluent 2001). Specific values of pressure at any node may be recovered from the velocity field in the post-processing stage. The discretized equations were solved using successive substition, with incremental loading and under-relaxation to assist convergence.

The numerical model was developed and solved using the commercial software FIDAP 8.5.2 (Fluent 2001). An example input file (FDREAD) for this software is presented in Appendix A.

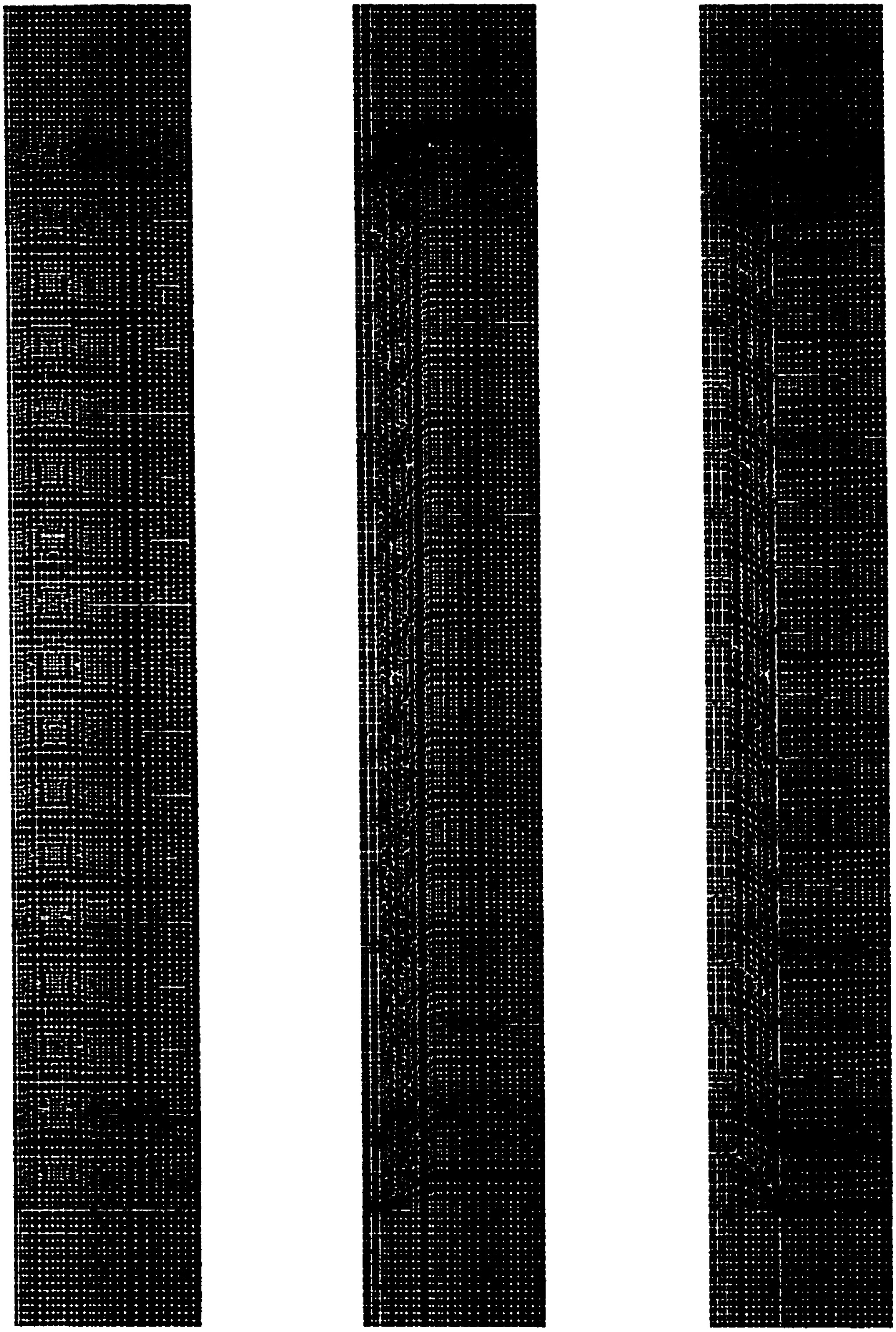

Figure 2-3: Computation mesh used in the current study.

2.4 Data Analysis

Data was collected in order to examine the convective and radiative flux from the window. The methodology of each analysis is described in the following sections.

2.4.1 Convective Flux

Convective flux is directly calculated by FIDAP using the conductivity of the fluid and the temperature gradient at the surface of a selected boundary. The FLUX command can be used to compute heat fluxes using the TEMPERATURE keyword. The heat flux normal to the requested boundary is defined and computed by

$$q = k_f \frac{dT}{dx} \tag{2.21}$$

The quantity q is referred to, by FIDAP, as the diffusive heat flux.

A sample output (FIOUT) file, which presents the results of the FLUX command, is given in Appendix A.

2.4.2 Radiation Post-Processing

During the solution process, FIDAP determines the net radiative flux from each surface using Eq. (2.15). Unfortunately, the radiation portion of the program is a recent addition, and as of yet, no method exists to output the results of the radiation analysis. FIDAP does provide a temperature profile of all surfaces, and the view factors calculated by the program for input into the radiation model. With this information, plus the surface emissivities, it is possible to recalculate radiative heat flux in the model.

The view factors calculated in FIDAP are determined using the VIEWFACTOR command. It does this calculation based on line integration and double area integration. To validate these, a number of individual view factors were confirmed using Hottel's cross string method. There was excellent agreement between the results given by the two methods.

To determine radiative heat transfer, it was necessary to develop software capable of reading the temperature and viewfactor data from FIDAP, and reproducing the results of FIDAP's solution routine. To do this, the radiation post processing code forms the matrix described by the Eq. (2.15). The matrix is then directly solved using Gauss-Jordan Matrix Inversion. The radiation post processor performs internal checks to confirm the calculated energy balance. Validation of this software has been performed by comparison to the results of Phillips (1999) in Section 2.5.4. The program listing is provided in Appendix A.

2.5 Model Checks

Before the model was used, a number of tests were performed to test the adequacy of the chosen parameters, and to compare solutions to similar established solutions. These tests include far field boundary tests, and grid sensitivity checks, comparison to a boundary layer solution (Ostrach 1953), and comparison to the work of Phillips (1999). Details of the validation are presented in Chapter 3.

2.5.1 Grid Sensitivity

The grid density is important in numerical analysis. A coarse grid may lead to numerical error and convergence problems, while a fine grid may require excessive amounts of computational power and time to obtain a solution.

To ensure grid independence, the grid density given by Phillips (1999) was used as a starting point. It was expected that this mesh density was suitable. For the sake of completeness, however, a grid-dependence analysis was performed. Increasing nodal density would increase solution accuracy and aid in convergence, at a cost of increased solution time. As a rule of thumb, doubling the nodal density increases the solution time by a factor of 4. This estimate does not include computational and software limitations. For example, if the solution becomes sufficiently large that it uses the entire RAM of the computer, additional information will be stored in virtual memory. The constant reading and writing to the hard drive is very slow in comparison to the computer processing speed, and will slow the solution considerably.

To test the effect of mesh density, it was intended that the nodal spacing would be both doubled and halved, using the original mesh density presented by Phillips (1999) as a base condition. Considering the expanded size of this model over the previous version (17 slats verses 10), it translated to approximately 28000 nodes in the base case. Consequently, doubling the nodal density would have produced a model that was beyond the computational abilities of the software and computer. Halving the nodal spacing produced a mesh consisting of approximately 9500 nodes.

As such, base parameters of the model are as presented as follows

$$b = 20 \text{ mm}$$
$$\phi = 0^{\circ}$$
$$q_b = 125 \text{ W/m}^2$$
$$T_p = 30\ ^{\circ}\text{C}$$
$$\varepsilon_b = \varepsilon_p = 0.81$$
$$Ra_R = 10^8,\ Ra_l = 20^6$$

and. referring to Fig. 2-2

Domain Width (A-B) = 60 mm
Entrance Height (A-H, G-F) = 40 mm

Additional parameters are as previously noted in Table 2-1.

A comparison of the results for both radiative and convective heat flux from the plate are presented in Fig. 2-4 using Nusselt numbers as calculated using Eqs. (2.18) and (2.19). The average value of Nu_R drops from 18.4 using the full mesh to 18.3 using the reduced mesh. Nu_C increases from 33.3 to 34.7 between those same models. The maximum local difference was 0.9 for Nu_R, and 2.4 for Nu_C.

Based on these results, it was decided to use the mesh density of the base case. To handle changing blind geometry, when the blind is moved, the nodal spacing between the blind tips and isothermal surface has been maintained, i.e., additional nodes were added. The mesh density on the room-side of the blind did not change. The room boundary was adjusted to keep a constant blind-to-room distance independent of blind angle and position.

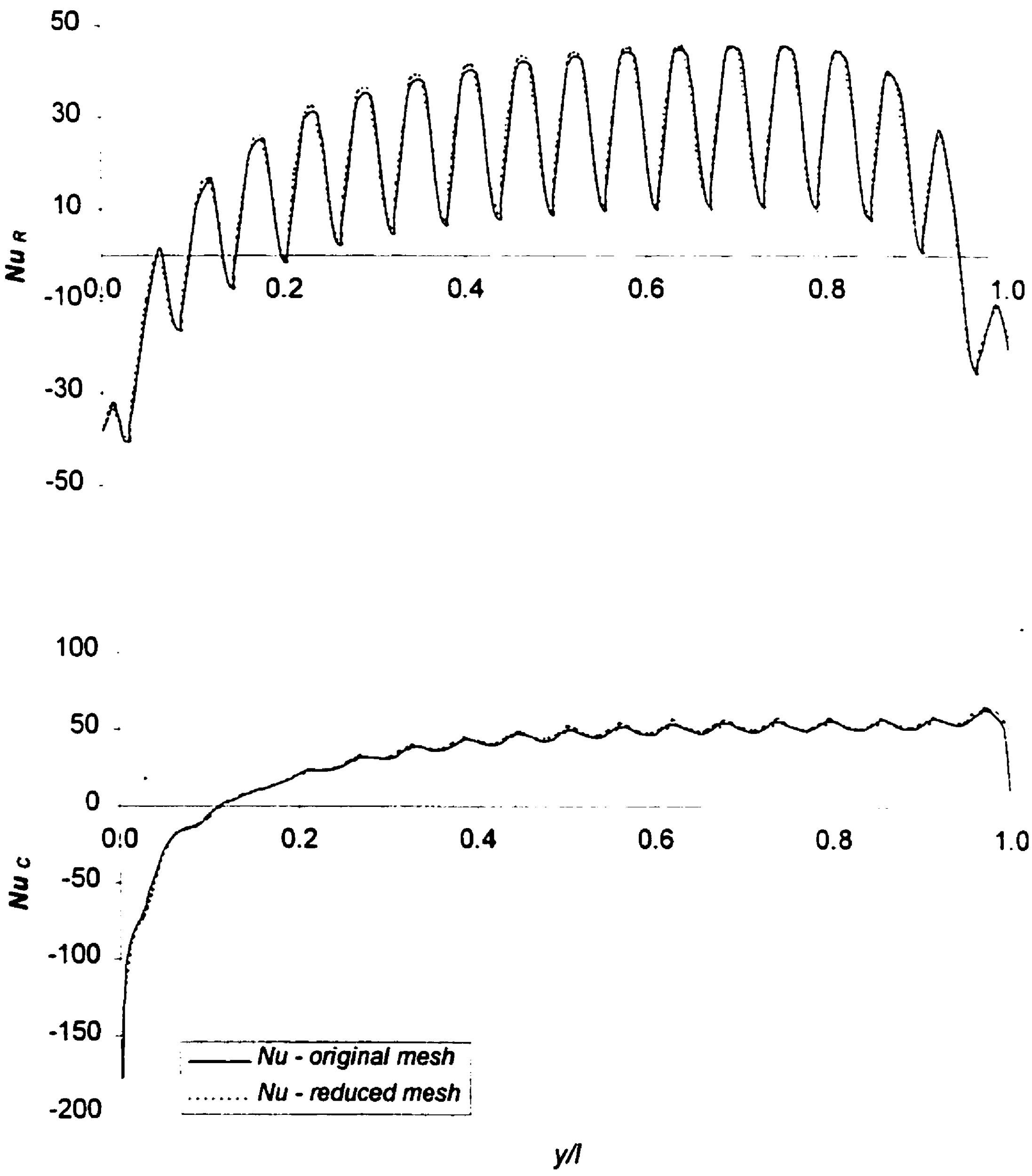

Figure 2-4: Comparison of radiative and convective Nusselt numbers from the isothermal plate obtained using a full and reduced mesh.

2.5.2 Far Field Boundary Tests

Boundary conditions placed on the upper and lower entrance regions, as well as the room, could potentially influence the results if these boundaries are placed within the flow field. For example, although air entrained from the room will have no vertical velocity component, a buoyancy induced vertical component does develop in proximity to the heated blind. If the room boundary is located within this buoyant flow, the no-vertical-motion boundary condition will influence the results such that both conditions are met. It is necessary to ensure that the results obtained are not influenced by the boundary conditions.

The work of Phillips (1999) was again used as a starting point. The boundary study conducted on the computational domain involved moving the inlet, outlet, and room boundaries away from the isothermal window. The results of this analysis were then compared quantitatively by examining the radiative and convective flux at the window surface, and qualitatively by examination of streamline plots.

The parameters of the model are as presented as follows

$$
\begin{gathered}
b = 20 \text{ mm} \\
\phi = 0^{\circ} \\
q_b = 125 \text{ W/m}^2 \\
Tp = 30\ ^{\circ}\text{C} \\
\varepsilon_b = \varepsilon_p = 0.81 \\
Ra_R = 10^8,\ Ra_l = 20^6
\end{gathered}
$$

and, referring to Fig. 2-2

Domain Width (A-B) = 50 mm, 60 mm, 70mm
Entrance Height (A-H, G-F) = 40 mm, 50 mm, 60 mm

Additional parameters are as previously noted in Table 2-1.

A comparison of the results for both radiative and convective heat flux from the plate are presented in Fig. 2-5 using Nusselt numbers as calculated using Eqs. (2.18) and (2.19). Consider the radiative Nusselt number, it is seen that there is little change due to the placement of the boundaries. The average value of Nu_R changes from 18.5 by less than 0.5% for any case. Similarly, the average value of Nu_C changes from an average of 33.4 by less than 0.3% for any case.

While these results suggest that a width of 50 mm would be sufficient, it was observed that increasing the distance of the room boundary did not significantly increase the solution time (the coarse nature of the far field grid did not significantly increase the number of nodes). As such, it was decided that models would have a width of 65 mm when the blind was at a 20 mm nominal spacing. Additionally, this boundary would be extended as the blind was moved. Therefore, for a nominal spacing of 30 mm, the width of the solution domain would be set at 75 mm.

An entrance region height of 40 mm would be sufficient for all models.

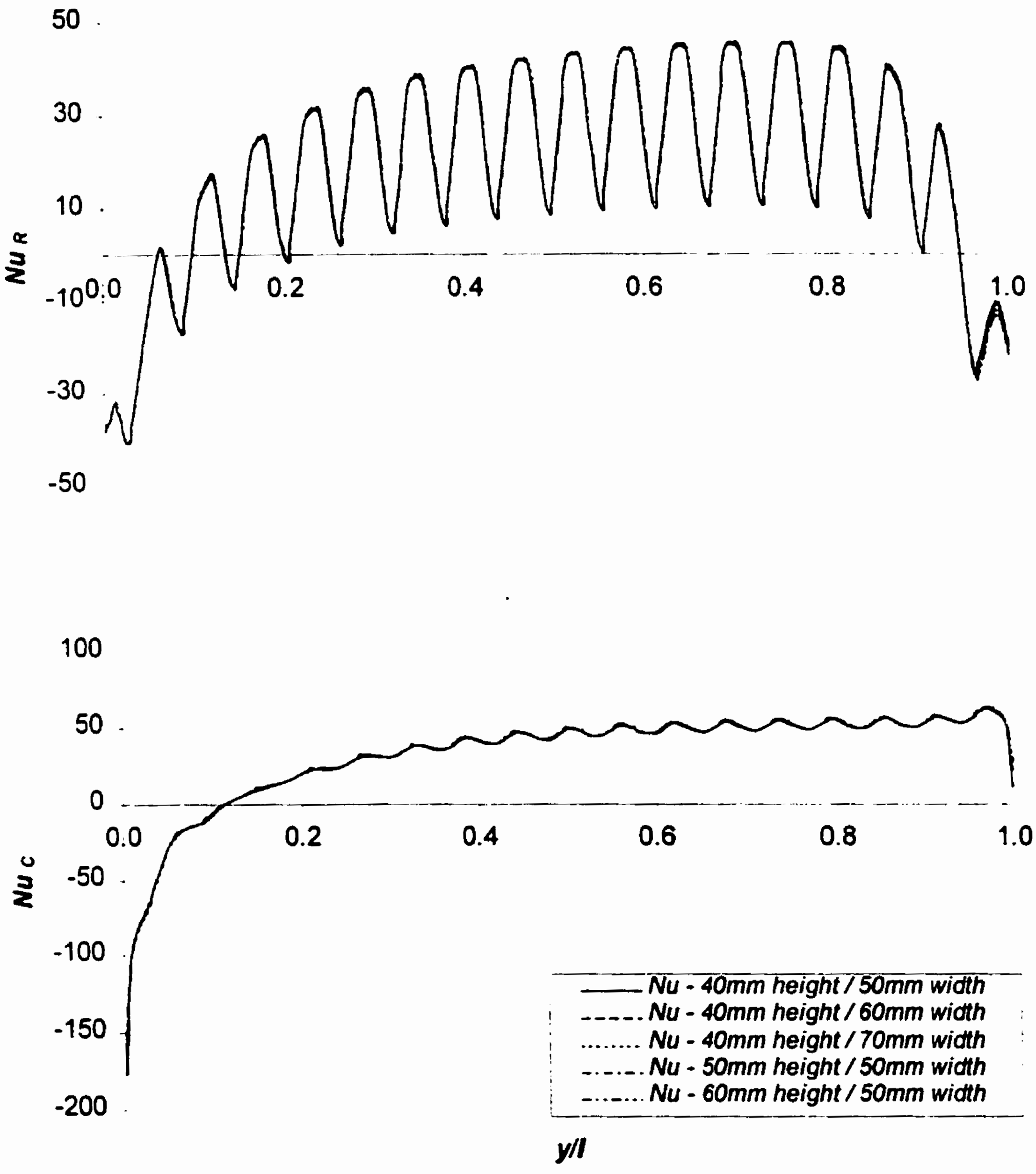

Figure 2-5: Comparison of radiative and convective Nusselt numbers from the isothermal plate obtained from an examination of boundary placement.

2.5.3 Comparison with Ostrach's (1953) Boundary Layer Solution

To establish a baseline for comparison, Ostrach's (1953) boundary layer solution for convection from a vertical flat plate with no blind was chosen. From this solution, the local and average convective Nusselt numbers are given by

$$Nu = 0.368 Ra_l^{1/4} \left(\frac{y}{l} \right)^{-1/4} \qquad (2.22)$$

$$\overline{Nu} = 0.515 Ra_l^{1/4} \qquad (2.23)$$

where the local and average convection Nusselt numbers are defined as follows

$$Nu = \frac{hl}{k_f} = \frac{ql}{k_f (T_p - T_i)} \qquad \overline{Nu} = \int_{y/l=0}^{1} Nu \, d\left(\frac{y}{l} \right) \qquad (2.24)$$

and the Rayleigh number is given using Eq. (2.16).

To make this comparison, the numerical model needed modification. The blind slats and the radiation model were removed from the system.

Ostrach's (1953) solution for the local heat transfer coefficient distribution is shown in Fig. 2-6, together with numerically determined data. It can be seen that the numerical results are in close agreement with this well validated boundary layer solution. The average convective Nusselt number for the "no blind" case differs by 4.1%, 1.4%, and 0.8% from Ostrach's (1953) solution at $Ra_l = 10^6$, 10^7, and 10^8 respectively.

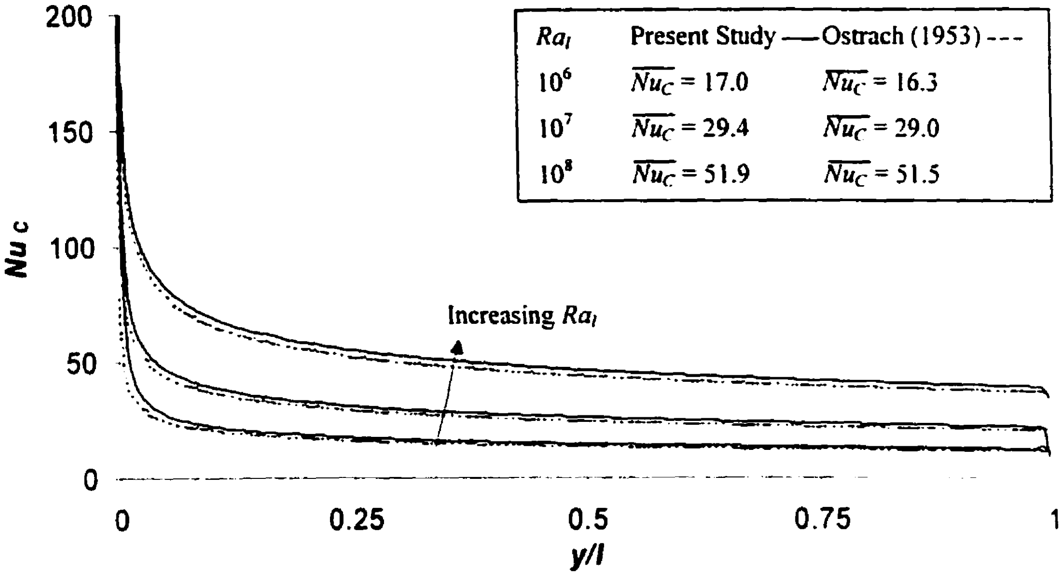

Figure 2-6: Comparison of the local convection Nusselt number results for the "no blind" case with the boundary layer solution of Ostrach (1953), $Ra_l = 10^6, 10^7, 10^8$.

2.5.4 Comparison to Phillips (1999) Solution

Numerical results obtained here for natural convection and radiation from an isothermal, heated vertical plate with unheated louvers was also compared to results for this case obtained by Phillips (1999). Because that model consisted of only 10 blind slats, results from the present model have been normalized to that size in order to facilitate a comparison.

The parameters of the model used for comparison were

$b = 15.4$ mm
$\phi = 0°$
$q_b = 0$ W/m^2
$T_p = 30$ °C
$\varepsilon_b = \varepsilon_p = 0.81$
$Ra_R = 5^9, Ra_l = 10^7$

Figure 2-7 shows the comparison of numerically obtained local convective and radiative Nusselt numbers from Phillips (1999) and from the present model. The results show excellent agreement. Between the models, there is a difference of 2.1% in the average convective Nusselt numbers, and 4.2% in the average radiation Nusselt numbers. This difference is primarily due to a slight divergence of the results near the tenth blind slat. The 10th slat of the model by Phillips (1999) was the topmost slat, and therefore subject to different radiation and convective exchange than those slats located in the middle of the model. The 10th slat of the present model is located near the middle of the blind.

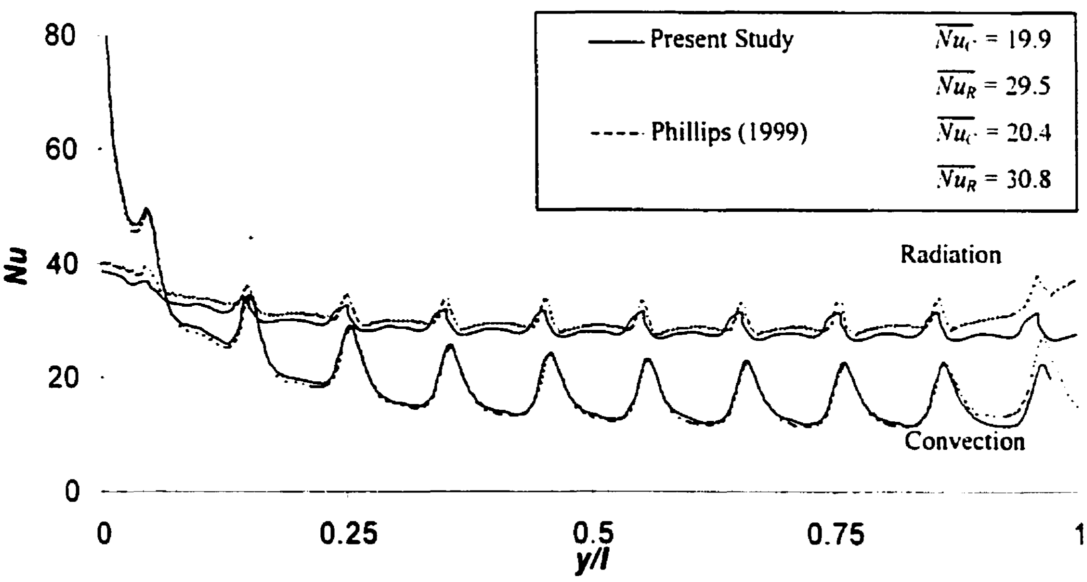

Figure 2-7: Comparison of the local convection and radiation Nusselt number results for the unheated blind case with the solution of Phillips (1999). $Ra_l = 10^7$.

CHAPTER 3
EXPERIMENTAL VALIDATION OF NUMERICAL MODEL

3.1 Introduction

It was deemed necessary to experimentally validate the numerical models in order to gain confidence in the accuracy of the results. In the current Chapter, the numerical model is compared to results obtained from an experimental model of a nearly identical system.

A Mach-Zehnder Interferometer was employed to obtain the experimental results needed to verify the numerically obtained results. The Mach-Zehnder Interferometer used for this comparison was located at Ryerson University. It provided the basis for a qualitative comparison of numerically and experimentally obtained isotherms in the air surrounding the shade layer. More importantly, a quantitative comparison of convective heat transfer coefficient at the plate surface can be made.

Temperature measurements of the blind slats were also obtained and compared to numerically predicted temperatures. This comparison was intended to give confidence in the numerically predicted radiation heat transfer from the plate surface.

3.2 Description of Mach-Zehnder Interferometer

Due to the large amount of information available concerning Ryerson's Mach-Zehnder interferometer, the physical system will only be described in general terms. The Ryerson Mach-Zehnder interferometer was based on a design that was built and operated at the University of Saskatchewan in 1968 (Tarasuk 1968). Specific details of the interferometer can be found in Von Bistram (1995).

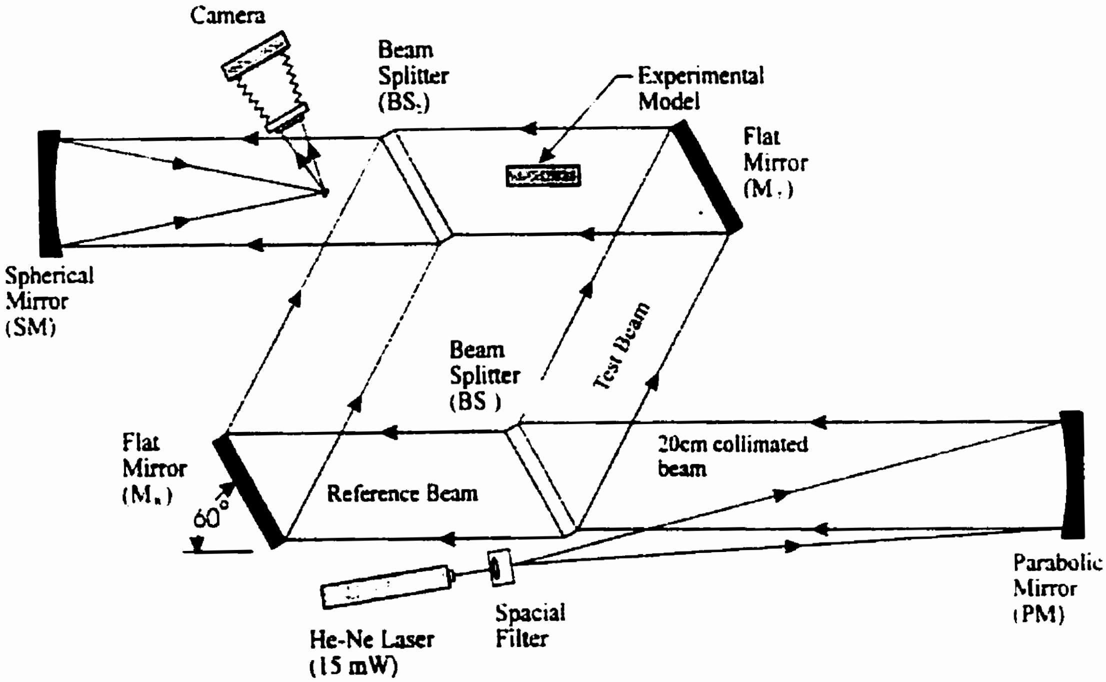

Figure 3-1: Plan view of the Ryerson Mach-Zehnder interferometer. Reprinted with permission from Machin (1997).

Figure 3-1 shows a plan view of the interferometer layout at Ryerson University. The light source was a 15 mW He-Ne laser fitted with a spatial filter which eliminated any high frequency “noise” in the beam and expanded the beam to a 200 mm diameter at the parabolic mirror (PM). The virtual origin of the expanding beam was located at the focal point of this parabolic mirror and the reflected elliptical beam was highly collimated. The beam was split by the first half-silvered beam splitter (BS_1) into two identical beams of almost equal length; the reference beam and the test beam. Each beam was half the intensity of the original. The reference beam reflected off the first flat mirror (M_R) to the second beam splitter (BS_2). The test beam reflected off the flat mirror (M_T) and recombined with the reference beam at (BS_2). This recombined beam was focused by a spherical mirror (SM) onto a small flat mirror and then to a camera to record an image.

If the paths of the beams pass through exactly the same conditions and if the beams were perfectly parallel to each other, then the output would appear either totally bright or totally dark. This depends on whether the difference in path lengths is an even or odd multiple of half wavelengths respectively. That is, an even number of half wavelengths produces constructive interference and an odd number of half wavelengths produce destructive interference. Thus, if a heated object were placed in the test section, the ray of the test beam that would pass near the model and would experience a decrease in the refractive index and "speed up". This causes a phase shift with respect to the reference beam and the result is an interferogram pattern representing lines of constant density. Since air can be considered to behave as an ideal gas, density and temperature are related by the ideal gas law and the lines of constant density can be interpreted as lines of constant temperature or isotherms.

This apparatus is an excellent choice for the present project for a number of reasons. Interferometry in general is non-intrusive, and unlike hot and cold wire techniques or thermocouple probes, an interferometer measures the entire field simultaneously. The system being investigated also lends itself to interferometry. The flow field can be considered two-dimensional and at steady-state with a constant pressure field, and the fluid in the intended application is air. Air is the perfect fluid for interferometers because it is homogenous and transparent to radiation so that only the convective heat transfer component is measured. Air can also be considered to be an ideal gas, directly relating the optically integrated refractive index field to the density field, and therefore, the temperature field. In comparison to other interferometers, the Mach-Zehnder interferometer, has a large displacement of the test beam from the reference beam. This allows the reference beam to pass through a uniform field, resulting in more sensitive and accurate interference.

3.3 Interferogram Analysis

It should be noted that a substantial portion of the theory presented here has been taken with permission from the work of Machin (1997) and Duarte (1999). An extensive analysis of fundamental interferometry theory, and a discussion of some of the optical considerations and techniques are given in Eckert and Goldstein (1976) and Hauf and Grigull (1970). Further details of the uncertainty and sample calculations have been included as Appendix B. The uncertainty has been determined using the method of Kline and McClintock (1953).

A Mach-Zehnder Interferometer can be used to obtain both infinite fringe and wedge fringe interferograms. In the infinite fringe mode, the optics are adjusted so that no fringes exist in the x or y directions when the experimental model is unheated. Heating the experimental model changes the index of refraction in the surrounding air, and the two light beams are no longer in phase when they are recombined. The resulting constructive and destructive interference fringes are isotherms. In the wedge fringe mode, the optics are adjusted to produce a constant fringe gradient in the y-direction, which is superimposed on the fringe field caused by temperature variations. In the latter case, the local convective heat transfer coefficient can be obtained by measuring the angle of intersection of a line of constant fringe shift with the plate. An example of an infinite and a wedge fringe interferogram is given in Fig. 3-2.

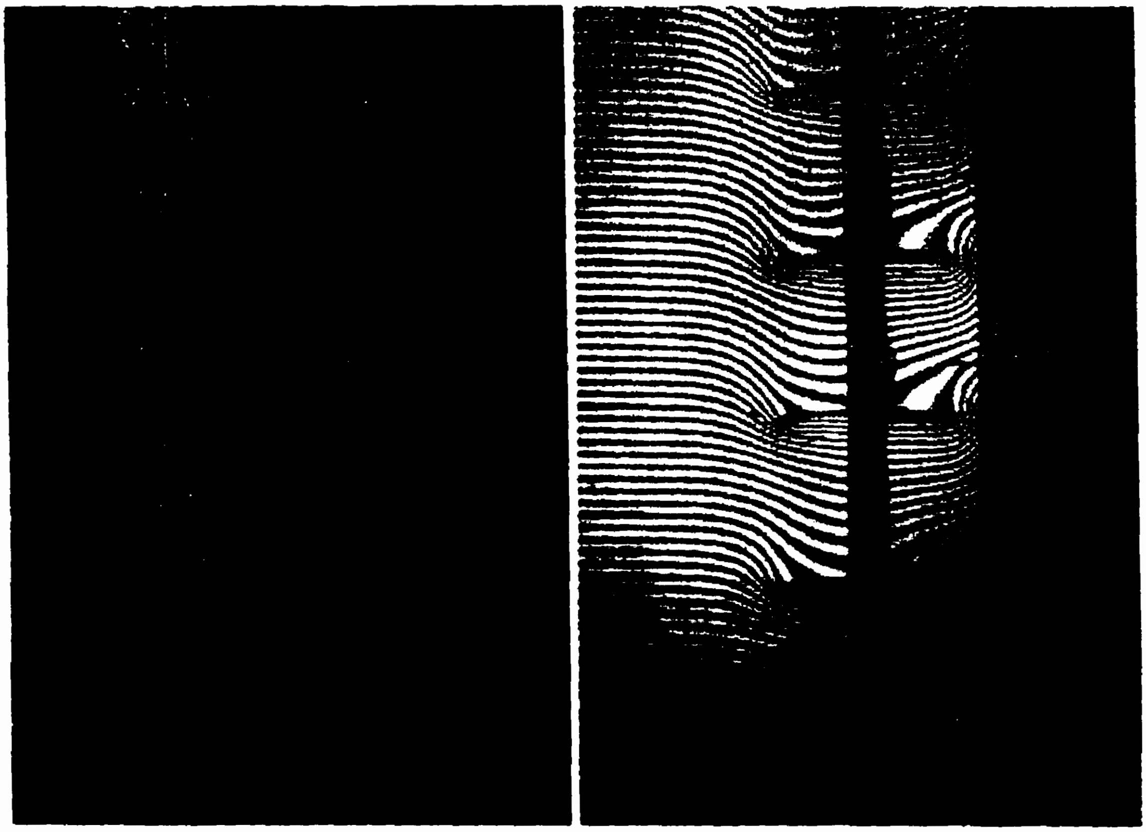

Figure 3-2: Comparison of infinite fringe (left) and wedge fringe (right) interferograms.

3.3.1 Infinite Fringe Method

In this study, the temperature of the experimental model was adjusted with respect to the ambient temperature, thus changing the density of the air surrounding the model. Light passing through this region of varying temperature tends to speed up or slow down due to decreases or increases in the index of refraction. The wave theory of light predicts that a fringe shift, η, or complete interference fringe will occur when the test beam is 180° out of phase with the reference beam. This will occur when the number of wavelengths (N) in the direction of the reference beam differs by an integer amount. Using the plate surface as the reference (N_p), it follows that

$$\eta = N_p - N = \text{integer} \tag{3.1}$$

The index of refraction (n) of a material is the ratio of the speed of light in a vacuum (c_o) to the speed of light in a material (c). In optical terms, it may better expressed by the ratio of light wavelength (λ_o) in a vacuum to the corresponding wavelength (λ) in the test medium. For the air very close to the plate surface

$$n_p = \frac{c_o}{c_p} = \frac{\lambda_o}{\lambda_p} = \frac{N_p}{N_o} \tag{3.2}$$

where p denotes variables at the plate surface. For the air near the test section

$$n = \frac{c_o}{c} = \frac{\lambda_o}{\lambda} = \frac{N}{N_o} \tag{3.3}$$

Therefore, a fringe shift is defined as

$$\eta = N - N_p = N_o(n - n_p) \tag{3.4}$$

Knowing the length of the model in the beam direction (Z), the number of wavelengths in that test section can be determined for a given wavelength by

$$N = \frac{Z}{\lambda} \tag{3.5}$$

The Lorenze-Lorenze equation gives the relationship between the index of refraction and material density (ρ).

$$\frac{(n^2 - 1)}{(n^2 + 2)\rho} = G \tag{3.6}$$

where G is a measure of the specific refractivity of the test medium for a given wavelength of light and is called the Gladstone-Dale constant. For air and a He-Ne laser ($\lambda = 6.328\text{X}10^{-7}$ m), $G = 1.504\text{x}10^{-4}$ m^3/kg (Hauf and Grigull 1970).

Since air has a refractive index very near unity (n = 1.0002716 at standard temperature and pressure (Hauf and Grigull 1970)), Eq. (3.6) can be reduced to approximate the Gladstone-Dale equation.

$$\frac{2(n-1)}{3\rho} = G \tag{3.7}$$

Thus, for the air at the plate surface

$$n_p = \frac{3}{2} G \rho_p + 1 \tag{3.8}$$

and for air near the test section

$$n = \frac{3}{2} G \rho + 1 \tag{3.9}$$

Substituting Eqs. (3.5), (3.8), and (3.9) into Eq. (3.4) gives

$$\eta = \frac{3}{2} \frac{Z}{\lambda} G(\rho - \rho_p) \tag{3.10}$$

where η is the fringe shift.

For the purpose of this study, air was considered to behave as an ideal gas. Therefore, for a given pressure (p), the following relationships can be used

$$\frac{\rho}{\rho_p} = \frac{T_p}{T} \qquad \rho_p = \frac{p}{RT_p} \tag{3.11}$$

where R is the gas constant for air (R = 287.096 Pa·m^3/kg·K) and T is the local temperature. Substituting Eqs. (3.11) into (3.10) yields

$$\eta = \frac{3}{2}\frac{Z}{\lambda}\frac{Gp}{R}\left(\frac{1}{T} - \frac{1}{T_p}\right) \tag{3.12}$$

This is a useful equation for determining the number of fringe shifts for a known temperature difference. A more practical form of Eq. (3.12), however, can be derived by solving for the fringe temperature for a given fringe, T_i, and a known reference temperature, T_p. This gives

$$T_i = \frac{T_p}{\frac{2\eta_i R\lambda T_p}{3GpZ} + 1} \tag{3.13}$$

When the temperature gradient in the air at the plate surface was sufficiently high (approx. dT/dy = 1500 K/m), the gradient was calculated by linear extrapolation using the first two clearly visible destructive interference fringes on a scan perpendicular to the surface. Equating the heat transferred by convection to the heat transferred by conduction at the wall gives an expression for the local heat transfer coefficient (h)

$$-k_p \left.\frac{dT}{dy}\right|_{wall} = h\left(T_p - T_i\right) \tag{3.14}$$

$$h = \frac{-k_p \left.\frac{dT}{dy}\right|_{wall}}{\left(T_p - T_i\right)} \tag{3.15}$$

where k_p is the thermal conductivity of air evaluated at the wall temperature based on property tables (Touloukian et al. 1970a), and T_i is the ambient temperature.

For determining the temperature gradient at the wall in a flat plate geometry, linear extrapolation has successfully been used by Eckert and Soehngen (1948). The experimental convection coefficient is therefore

$$h = \frac{k_p\left(\frac{T_2 - T_3}{y_3 - y_2}\right)}{\left(T_p - T_i\right)} \tag{3.16}$$

here the temperature gradient dT/dx at the surface has been replaced by the linear extrapolation of the temperature profile. In most cases, the first fringe (η_1) does not represent a full fringe shift from the surface. Linear extrapolation of the first two clear destructive interference fringes closest to the model was instead used to calculate the fractional fringe shift. The term (T_2 - T_3) is the optically measured temperature difference between the first and second fringes and (y_3 - y_2) is the first and second fringe spacing. From Eq. (3.13), the optically measured temperature difference can be calculated as

$$T_2 - T_3 = \frac{T_p}{\frac{2\eta_2 R\lambda T_p}{3GZp} + 1} - \frac{T_p}{\frac{2\left(\eta_2 + 1\right)R\lambda T_p}{3GZp} + 1} \tag{3.17}$$

where

$$\eta_2 = \frac{y_2}{y_{2+1} - y_2} \tag{3.18}$$

and where y is the distance of the fringe perpendicular to the plate. In Eq. (3.17), consecutive fringes from the first are represented by this fractional shift plus an integer amount. Therefore, η_3 has been substituted by $\eta_2 + 1$.

3.3.2 Wedge Fringe Method

When temperature data are obtained only at fringe centers, several fringes are needed near the surface in order to get an accurate gradient from the extrapolation procedure. Unfortunately, due to the large variation in local heat transfer rates that may be encountered in a single experimental model, this is not always possible. Regions of low heat transfer rates (approx. $dT/dy < 1500$ K/m) result in insufficient fringe shift close to the surface of the plate, making it difficult to get the necessary data for temperature profile extrapolation. Recently, to overcome this problem, a new interferometric technique has been developed by Naylor and Duarte (1999). They have shown that the surface temperature gradient can be measured directly from the interference fringe field, i.e., a wedge field interferogram.

The formulae presented in the previous section apply to both infinite and wedge fringe interferogram calculations. To apply the current analysis technique, however, the interferometer must be operated in the wedge fringe mode in which the test and reference beams are not parallel upon recombination. The test and reference beams are intentionally misaligned by a small angle θ in order to produce a wedge fringe pattern in the y-direction with spacing (d)

$$d = \frac{\lambda}{2\sin\left(\frac{\theta}{2}\right)} \approx \frac{\lambda}{\theta} \tag{3.19}$$

When analyzing a wedge fringe interferogram, the fringe spacing must be measured parallel to the fringe angle in the ambient surroundings. It is common, but not necessary to set the fringes perpendicular to the surface, as it facilitates the scanning process.

Rewriting Eq. (3.12), the fringe image is related to the temperature field by the following expression

$$\eta = \frac{3GZp}{2R\lambda}\left(\frac{1}{T_i} - \frac{1}{T}\right) \tag{3.20}$$

where fringe shift η is now expressed relative to the ambient, where $\eta = 0$. With the superimposed wedge fringe pattern in the y-direction, the fringe shift is related to the temperature field as follows

$$\eta = \frac{3GZp}{2R\lambda}\left(\frac{1}{T_i} - \frac{1}{T}\right) \pm \frac{y\theta}{\lambda} \tag{3.21}$$

For generality, the last term in this equation is shown as plus or minus. The sign depends upon whether the test beam is angled upward or downward relative to the reference beam. For this setting, the wedge fringes will be perpendicular to the vertical isothermal plate in the ambient and a negative temperature gradient in the x-direction will cause the wedge fringes to bend downward near the surface.

Differentiating Eq. (3.21) with respect to x gives

$$\frac{\partial\eta}{\partial x} = \frac{3GZp}{2R\lambda T^2}\frac{\partial T}{\partial x} \tag{3.22}$$

Rearranging Eq. (3.22) and applying it at the surface ($x = 0$) gives an expression for the fluid side temperature in terms of the fringe gradient

$$\left.\frac{\partial T}{\partial x}\right|_{x=0} = \frac{2R\lambda T_p^2}{3GZp}\frac{\partial \eta}{\partial x} \tag{3.23}$$

The fringe shift gradient along the surface was obtained by differentiating Eq. (3.21) with respect to y

$$\frac{\partial \eta}{\partial y} = \frac{3GZp}{2R\lambda T^2}\frac{\partial T}{\partial y} + \frac{1}{d} \tag{3.24}$$

Consider an incremental fringe shift along a line in the x-direction, and applying Eq. (3.22) for an isothermal surface ($dT/dy = 0$), the incremental fringe shift will be $d\eta = +dy/d$. Noting that $tan\alpha = -dx/dy$, the fringe shift gradient in the x-direction can be expressed as

$$\left.\frac{\partial \eta}{\partial x}\right|_{x=0} = \frac{-1}{d\tan\alpha} \quad . \tag{3.25}$$

where α is the angle between a line of constant fringe shift and the surface at $x = 0$.

Again we can equate the local convective heat transfer rate to the conduction heat transfer rate into the fluid at the surface. From Eq. (3.15) and using Eqs. (3.23) and (3.25) gives an expression for the local heat transfer coefficient (h)

$$h = \frac{2R\lambda T_p^2 k_p}{3GZp\left(T_p - T_i\right) d\tan\alpha} \tag{3.26}$$

Using Eq. (3.26), the local convective heat transfer coefficient can be derived by measuring the angle, α, between a line of constant fringe shift and an isothermal surface.

3.3.3 Local and Average Convective Heat Flux

The local convective heat flux is defined as

$$q = h(T_p - T_i) \tag{3.27}$$

The location of the local heat transfer data obtained from an interferogram is non-uniform. Therefore, the average coefficients were obtained by integrating the local h variation using the trapezoidal rule. The average convective heat flux is defined as

$$\bar{q} = \bar{h}(T_p - T_i) \tag{3.28}$$

3.4 Experimental Model

The indoor glazing surface was idealized as an isothermal vertical flat plate that was maintained at a temperature above or below the ambient temperature. A commercially available Venetian blind consisting of seventeen horizontal louvers, was positioned at a specific distance from the plate surface and the individual slats were inclined at an angle with respect to the horizontal. A heat flux was applied to one side of each slat using surface mounted thin foil heaters to simulate the solar radiation absorbed by the blind. Figure 2-1 shows the system geometry and a photo of the experimental model.

To facilitate the simulation of a warm or cool window surface, it was necessary to replace the heated isothermal plate built by Machin (1997). The plate constructed for the present experimental work was machined from two sheets of aluminum. Figure 3-3 presents an illustration of the plates. The main sheet (19.1 mm thick x 381.0 mm high x

355.6 mm wide) had flow channels (6.4 mm deep x 12.7 mm wide) milled into the back surface, while the front surface of the plate (the experimental surface) was precision flat milled. The flatness of the plate was important in the horizontal direction. Surface roughness and curvature in that direction would cause scatter in the laser sheet as it passed the experimental model. Testing on a coordinate mapping machine showed the plate to be flat to within ±0.046 mm of the average height. Pins place in precisely located holes drilled into the front of the plate aided in leveling the experimental model and in the examination of the resulting interferograms. Leveling pins were positioned at heights of 63.5, 190.5, and 317.5 mm along both sides of the plate, and scale pins were located 25.4 mm above and below the leveling pins on one side of the plate. Both the top and bottom edges of the front plate angled back to create a sharp edge at the upper and lower entrance regions. The second aluminum sheet (6.4 mm thick x 355.6 mm high x 355.6 mm wide) became the backing plate and sealed the flow channels with the aid of an O-ring. Liquid gasketing prevented leaks between flow channels. Machine screws located every 44.5 mm around the perimeter ensured a tight seal between the plates.

The assembled plate was backed with insulation and mounted on an aluminum stand. The insulation (25.4 mm thick polystyrene) served two purposes. It ensured that heat would ideally flow from the liquid to and from the experimental isothermal surface. Additionally, it prevented convective heat loss from areas that could interfere with the Mach-Zehnder interferometer. Support stands were constructed from 25.4 mm x 50.8 mm aluminum angle and connected the isothermal plate to a base plate. Four machine screws connected the supports to the plate, through the insulating layer, using the same holes

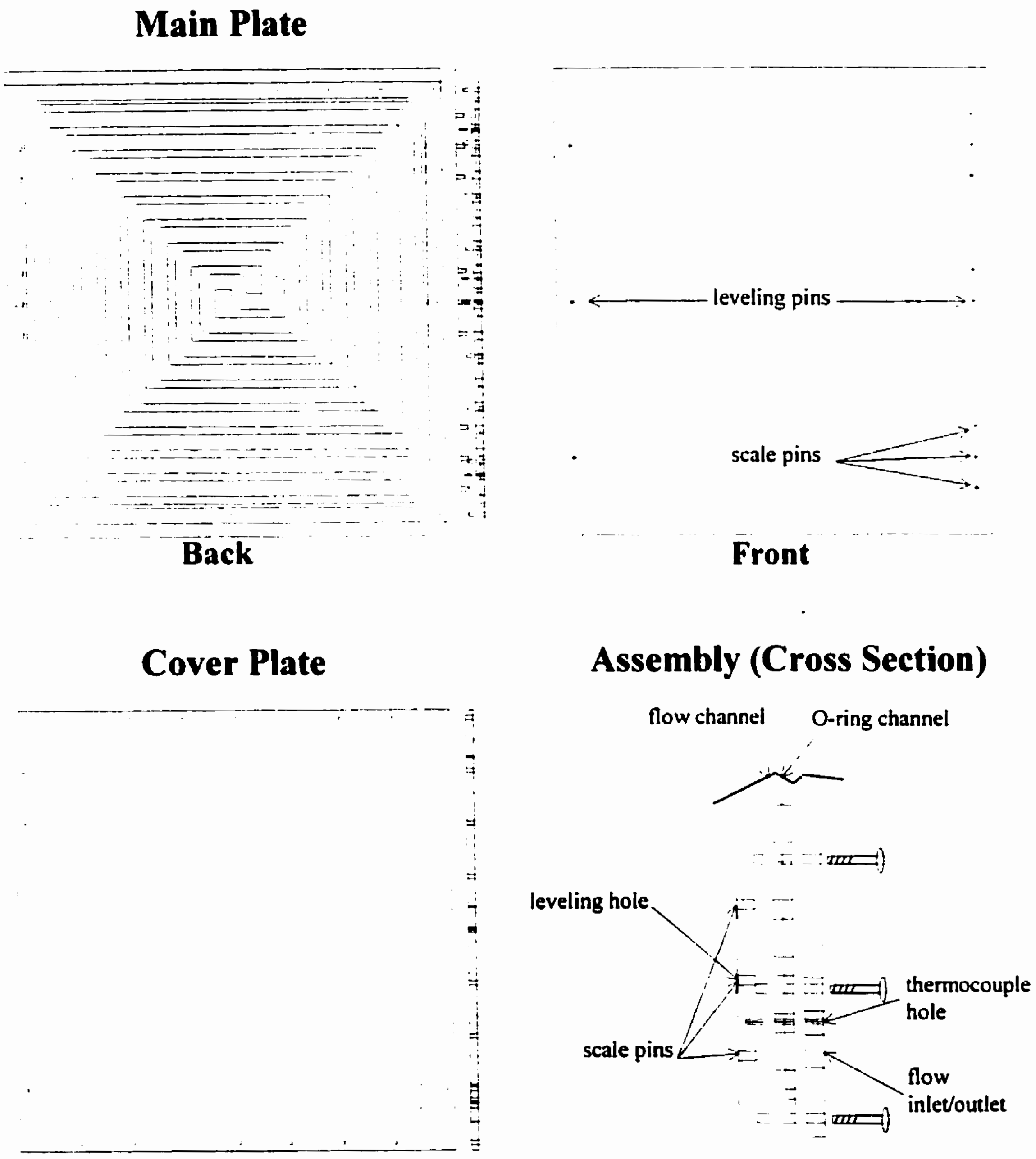

Main Plate

Back

Front

Cover Plate

Assembly (Cross Section)

Figure 3-3: Schematic of isothermal plate.

intended to connect the back and front plates. The support stands also served as a mounting point for the blind assembly. The base plate was located 152 mm below the bottom edge of the plate to prevent it from interfering with the convective flow. It had three adjustable legs in a tripod formation to allow leveling of the experimental model. Figure 3-4 shows the assembly of the plate and mounting system, and the blind mount.

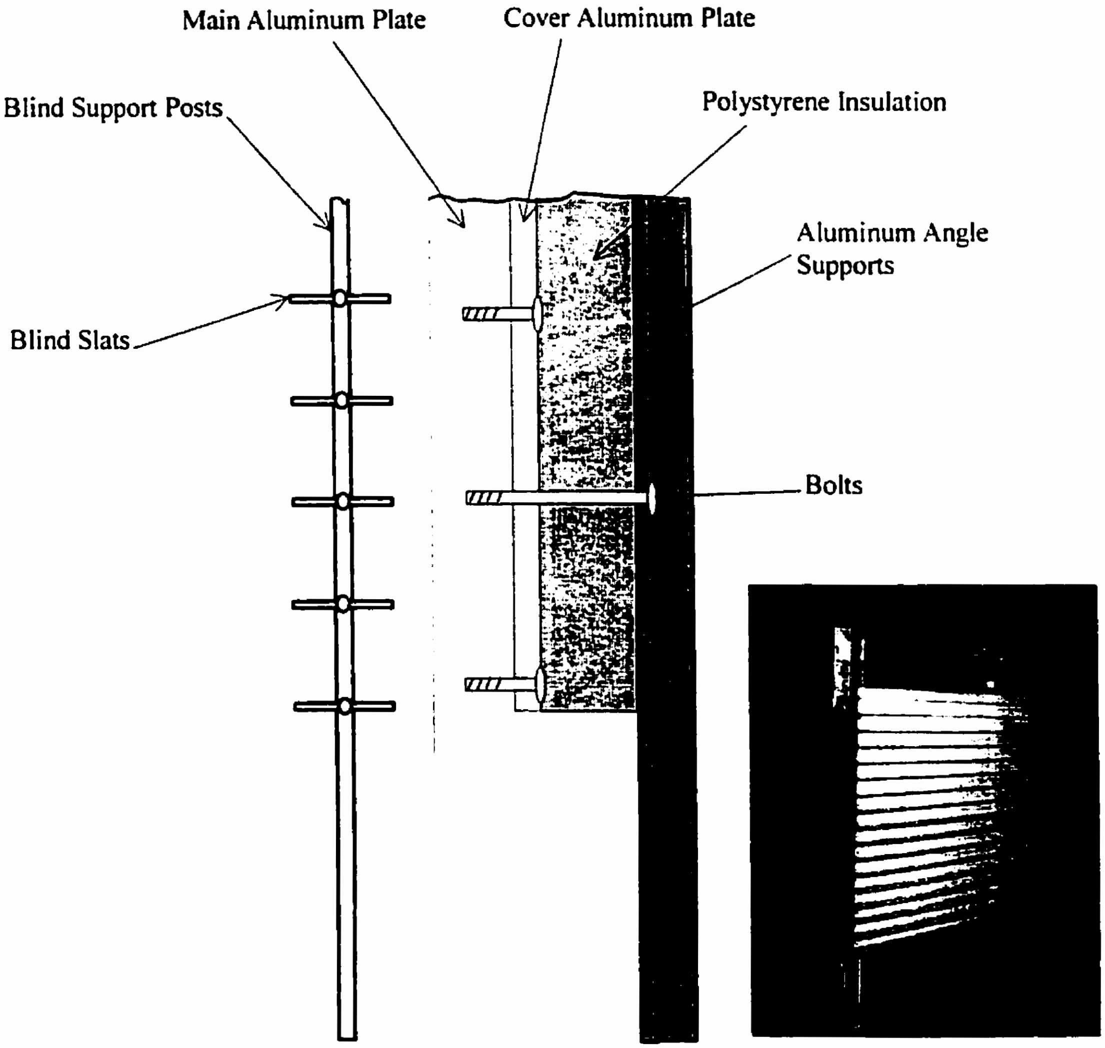

Figure 3-4: Schematic and photograph of plate and blind assembly.

The plate was heated and cooled using a Fisher Scientific - ISOTEMP 1016D precision temperature bath. It was intended that the flow channel configuration, in which the inlet and outlet flow channels coil inward side by side, would make the plate essentially isothermal. Ten precision drilled holes were made into the plate back so that thermocouples could be inserted to 2 mm below the test surface of the experimental setup. Testing showed that the plate remained isothermal to within 0.1 ±0.06 K from the average over the entire surface at 10 K above or below ambient temperature.

Slats from a commercially available Venetian blind were used for this experiment. The slats had a width, thickness, an arc length and a radius of curvature typical of many commercially available products. The slats were held at a pitch that is typical of commercially available Venetian blinds (ps = 22.2 mm) using slits cut into 4-40 nylon rod that was threaded through two precision machined steel posts (4.76 mm square). The vertical position of the blind relative to the plate was such that the lower tip of the first slat was in line with the plate leading edge when the blind was fully closed. To simulate solar loading, two thin foil electric heaters (with dimensions 167 mm x 14 mm x 0.15 mm) were bonded to the concave side of each slat. After the heaters were bonded to the slats, they were sprayed with paint to give a uniform hemispherical emissivity ($\varepsilon_p = \varepsilon_b =$ 0.81). The slat thermal conductivity (k_b) was also measured (Machin 1997). Fine T type thermocouples (40 gauge) were bonded to the top surface of the slats using high conductivity epoxy. The thermocouple tips were placed one third the way along the length of the slat and in the center of the slat profile. A complete description of the blind mounting system can be found in Machin (1997) and Duarte (2000). Figure 3-4 gives a photograph and schematic of the blind mount in relation to the isothermal plate.

All temperatures and the power to the blind were monitored using a Sciemetrics model 641 data acquisition system (Sciemetrics 1991) with QMON software (SCL 1993). Instruments were calibrated using the same system.

3.5 Test Conditions

For validation purposes, it was decided that two plate temperatures, one level of irradiation, one nominal blind spacing, and three blind angles would be examined. An additional set of test experiments at a 0 deg slat angle, with an increased nominal distance, was also taken. This allowed for an examination of the effects of plate-to-blind leading edge distance, *n* (i.e., 7.3 mm tip-to-plate spacing can be examined despite the fact that the louver angle changes). The plate temperatures and irradiation levels examined were considered to be near the extreme limits of what would be encountered in nature, and it was expected that these cases would pose the largest problem for the numerical model. The cases examined experimentally and numerically are presented in Table 3-1.

Table 3-1: Sequence of experimental/numerical conditions for model validation. Experimental target is in brackets.

Case	q_b (W/m^2)	T_i (K)	T_p (K)	ϕ (deg)	b (mm)	n (mm)
1	123.9 (125)	296.7 (297)	283.3 (283)	0	15.4	3.0
2	151.5 (150)	296.2 (297)	298.3 (298)	0	15.4	3.0
3	124.5 (125)	296.2 (297)	283.3 (283)	0	20.0	7.3
4	151.5 (150)	296.7 (297)	298.3 (298)	0	20.0	7.3
5	124.0 (125)	296.5 (297)	283.3 (283)	45	15.4	7.3
6	151.1 (150)	296.2 (297)	297.8 (298)	45	15.4	7.3
7	124.4 (125)	296.7 (297)	283.3 (283)	-45	15.4	7.3
8	151.3 (150)	296.7 (297)	298.3 (298)	-45	15.4	7.3

3.6 Experimental Procedure

The procedure for setting up and using the interferometer can be found in Machin (1997) and Duarte (1999). Machin (1997) provides instructions on focusing the interferometer, aligning the experimental model, and positioning the camera. Consequently, in the interest of brevity, only details specific to this investigation will be presented here.

For each experiment, the blind slats were adjusted to the desired slat angle using a jig. The blind tip-to-plate spacing was subsequently adjusted using gauge blocks. Consequently, the inner slat tip-to-plate spacing was carefully controlled, and the slat angle varied slightly from slat to slat because of small dimensional imperfections. This approach was taken because previous experimental and numerical studies with an unheated blind have shown that it is more important to control the slat tip-to-plate spacing than slat angle or nominal spacing (Machin 1997, Phillips 1999).

An optical window mounted in a sheet of acrylic was placed on each end of the model. This assembly prevented entrainment of air into the sides of the model, promoting a more two-dimensional flow and temperature field. To reduce the effect of air currents within the laboratory, the interferometer was located inside a large unventilated enclosure.

Due to optical restrictions, the maximum interferogram size could only be 200 mm in diameter, whereas the experimental model was 380 mm high. As a result, accounting for some picture overlap, and the loss of some information at the top and bottom of the circular interferogram, it was decided to examine the plate as three distinct sections. The plate and blind were mounted on a table that allowed control of the experimental model's vertical position. Interferograms were then taken at the bottom, middle, and top of the experimental model.

Experimental and numerical parameters have been summarized in Table 3-2. Fluid properties were evaluated at an estimated film temperature of 300 K and were taken from Touloukian et al. (1970a, 1970b, 1975). Film temperatures predicted by the numerical model after the present analysis showed that the average fluid temperature was between 297 K and 302 K for all validation cases. The numerical model described in Chapter 2 was executed to duplicate the exact conditions of the interferometer experiments, as presented in those tables.

Data was collected every 60 seconds over a period of approximately 30 min for each experimental case. This data was used to ensure that steady-state operation was obtained at each experimental case.

Table 3-2: Parameters used for validation of the numerical model. All fluid properties except k_p are evaluated at $T = 300$ K.

c_p (J/kg·K)	ρ_f (kg/m^3)	β_f (1/K)	ν_f (m^2/s)	μ_f (kg/m·s)	k_f (W/m·K)	ε_i	k_p (283 K) (W/m·K)
1006.3	1.1656	0.0033	1.590E-5	1.853E-5	0.026	1.00	0.024

l (mm)	ps (mm)	w (mm)	t (mm)	rc (mm,deg)	T_i (K)	k_b (W/m·K)	k_p (298 K) (W/m·K)
379.6	22.2	25.4	0.17	52.3 , 27.3	297	120	0.026

3.7 Results and Discussion

For clairity in presenting the results, the dimensional flux is presented instead of the Nusselt number. Due to the fact that the isothermal plate can be either hot or cold, negative and positive Nusselt numbers will result, where the sign is not indicative of the direction of heat flow. Using this convention, positive flux is from the plate, while negative is into the plate.

Numerically and experimentally obtained average convective heat flux rates are presented in Table 3-3, and local convective heat flux rates are presented in Figs. 3-5 to 3-12, where slat positions and experimental uncertainty are shown in gray. Numerically obtained local and average radiative heat flux rates are also presented in Table 3-3 and Figs. 3-5 to 3-12.

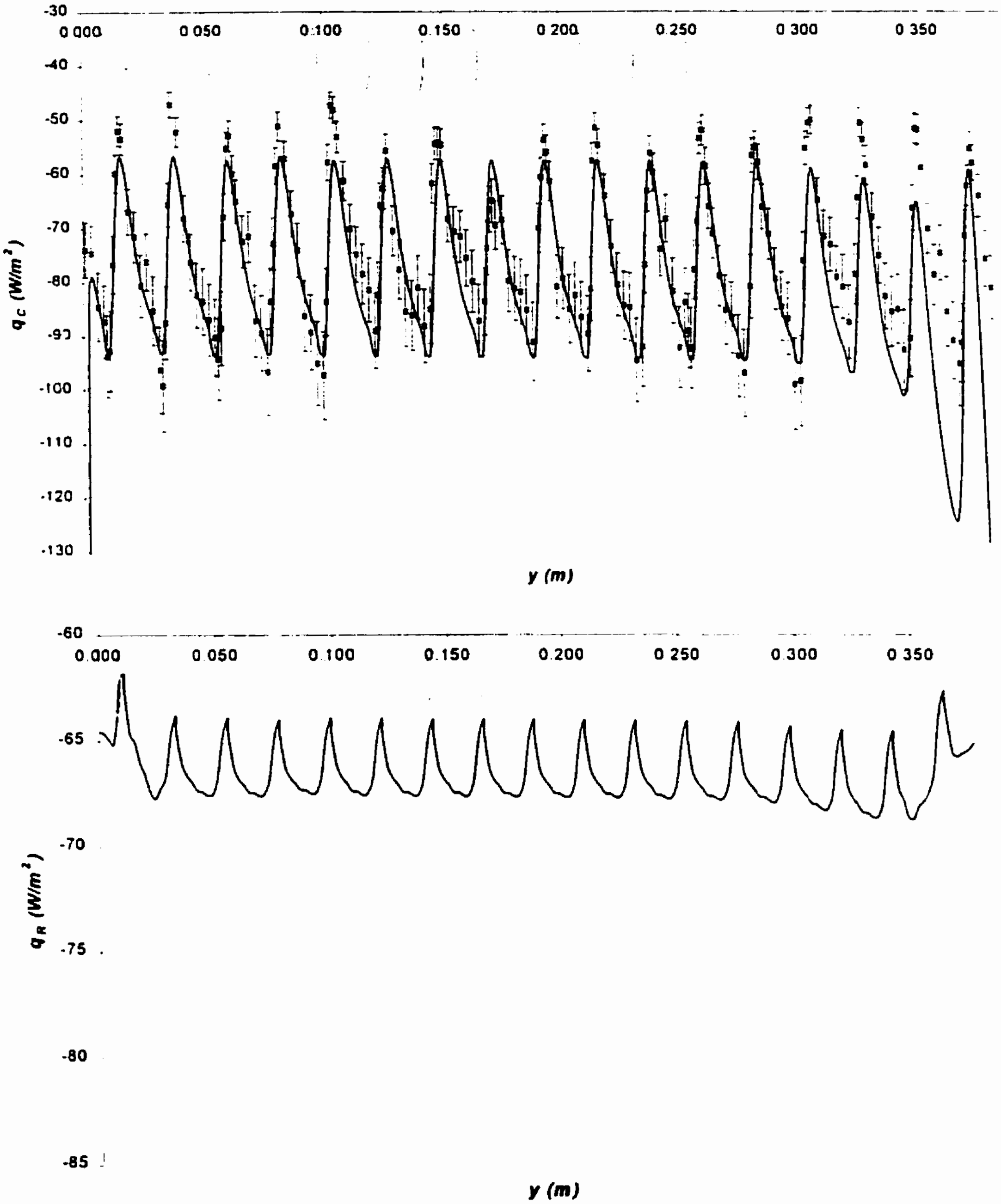

Figure 3-5: Convective and radiative heat flux for validation case 1: b = 15.4 mm, $\phi = 0°$· T_p = 283 K. Points represent interferometric results with associated experimental uncertainty. Solid line represents numerical results. Slat positions are superimposed on graphs for clarity.

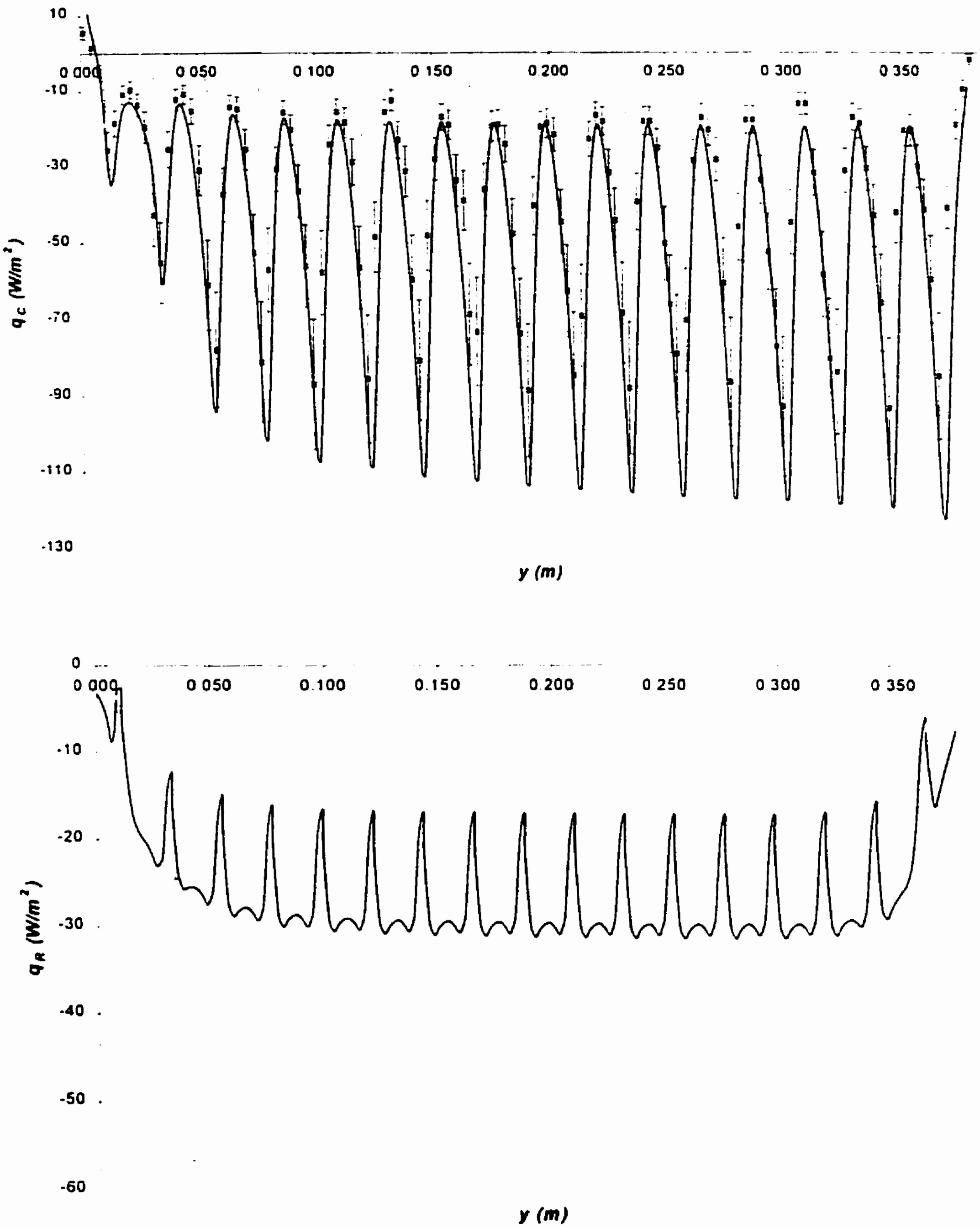

Figure 3-6: Convective and radiative heat flux for validation case 2: b = 15.4 mm, ϕ = 0°, T_p = 298 K. Points represent interferometric results with associated experimental uncertainty. Solid line represents numerical results. Slat positions are superimposed on graphs for clarity.

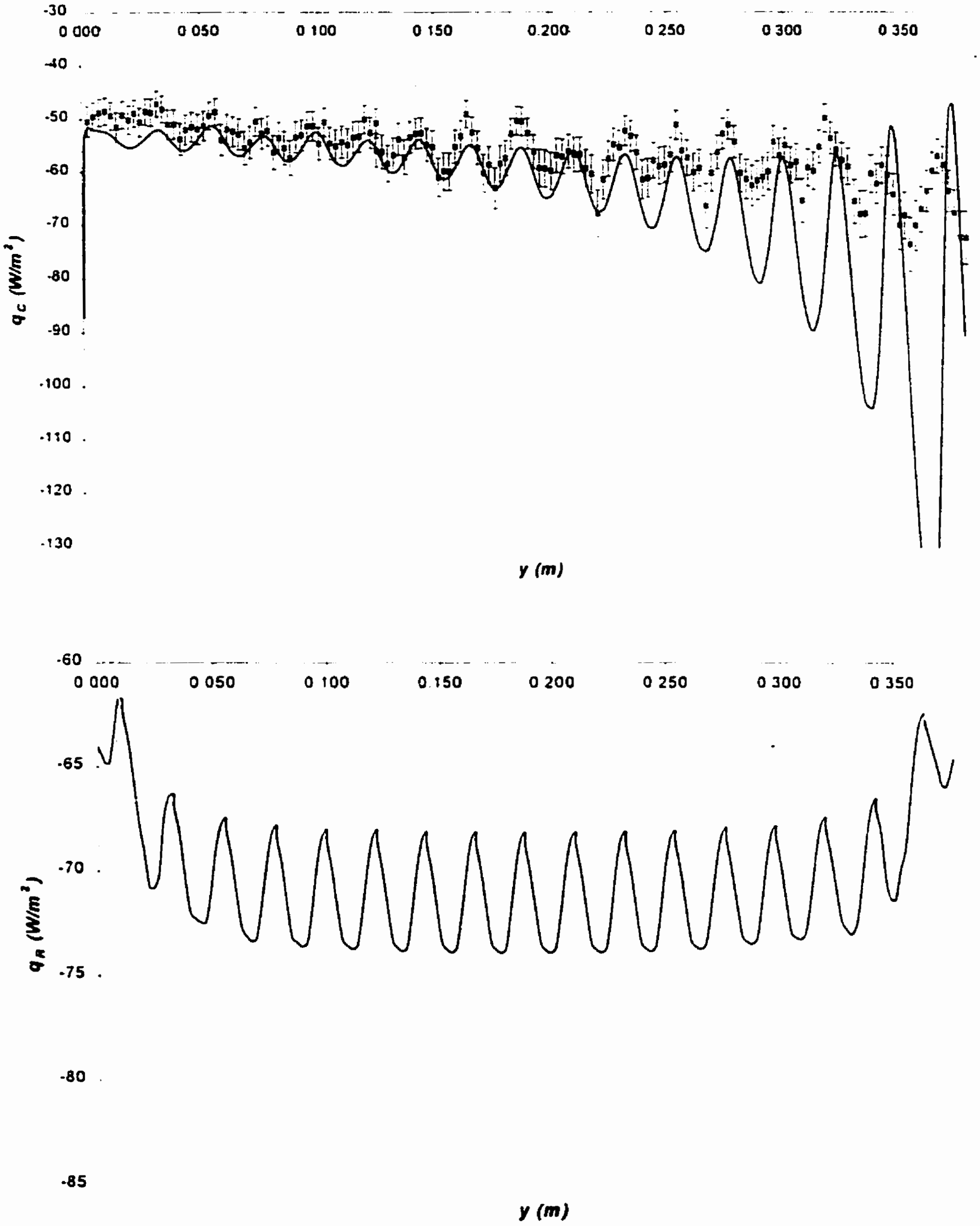

Figure 3-7: Convective and radiative heat flux for validation case 3: $b = 20.0$ mm, $\phi = 0^{\circ}$· $T_p = 283$ K. Points represent interferometric results with associated experimental uncertainty. Solid line represents numerical results. Slat positions are superimposed on graphs for clarity.

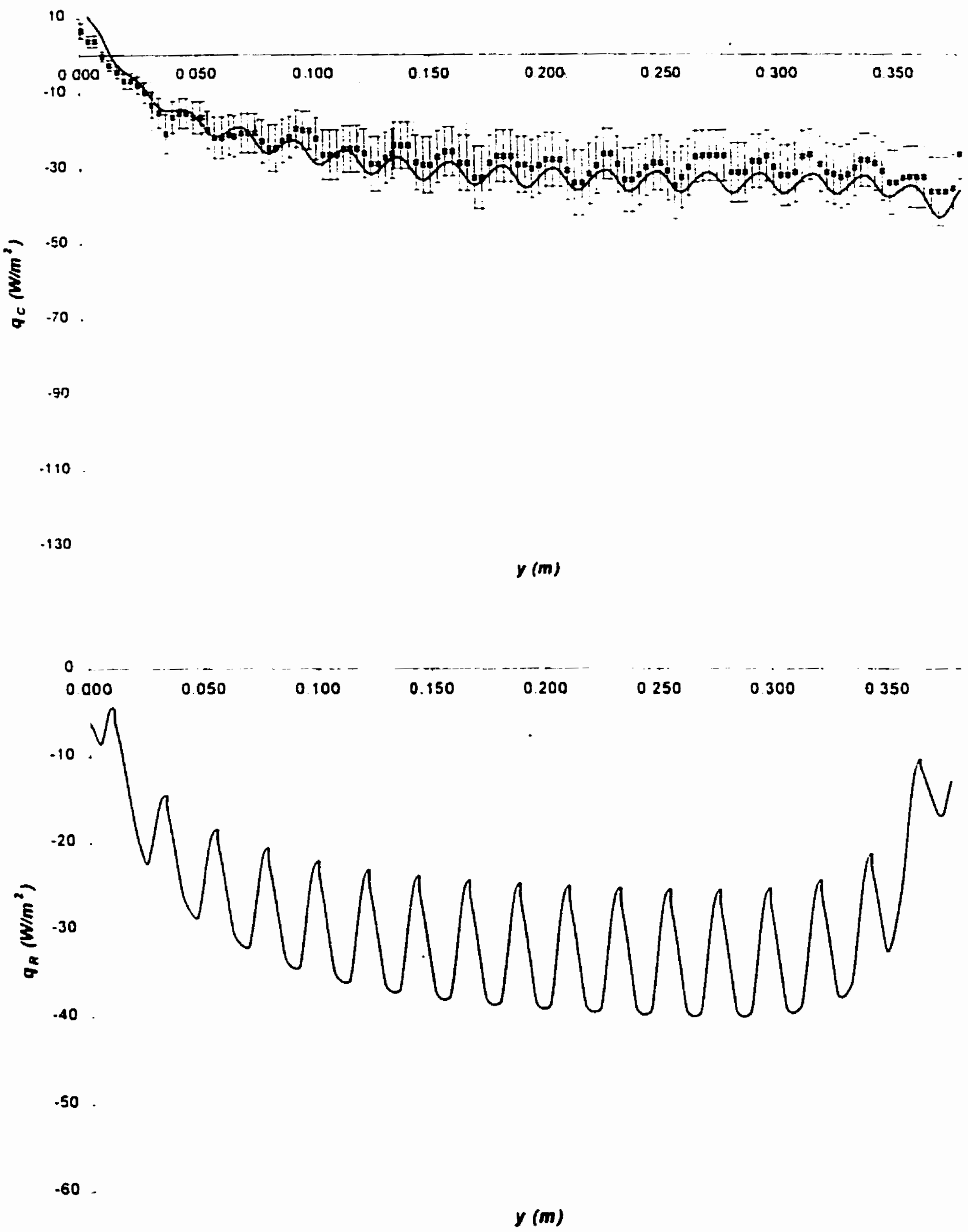

Figure 3-8: Convective and radiative heat flux for validation case 4: b = 20.0 mm, $\phi = 0°$· T_p = 298 K. Points represent interferometric results with associated experimental uncertainty. Solid line represents numerical results. Slat positions are superimposed on graphs for clarity.

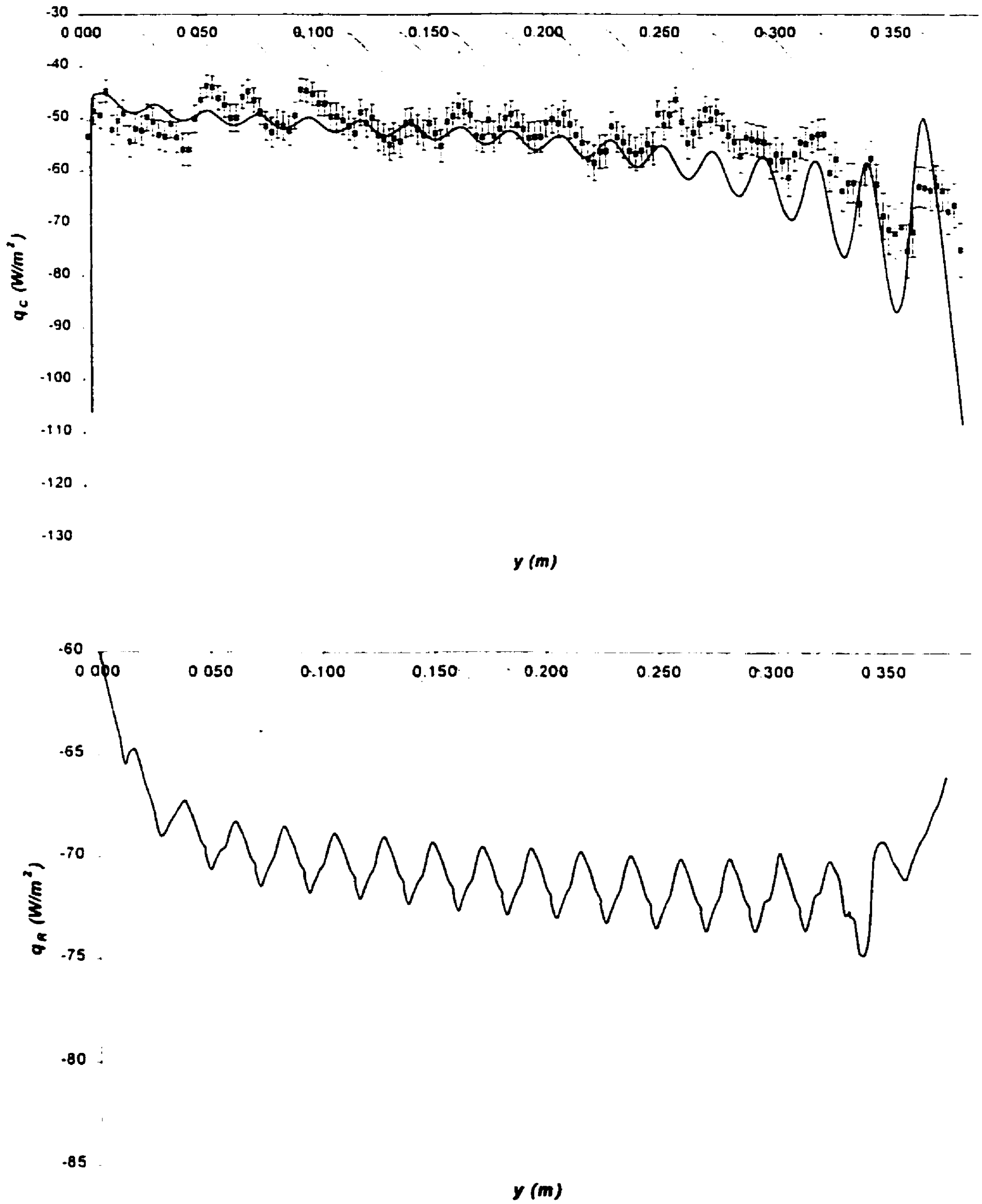

Figure 3-9: Convective and radiative heat flux for validation case 5: b = 15.4 mm, ϕ= 45°· T_p = 283 K. Points represent interferometric results with associated experimental uncertainty. Solid line represents numerical results. Slat positions are superimposed on graphs for clarity.

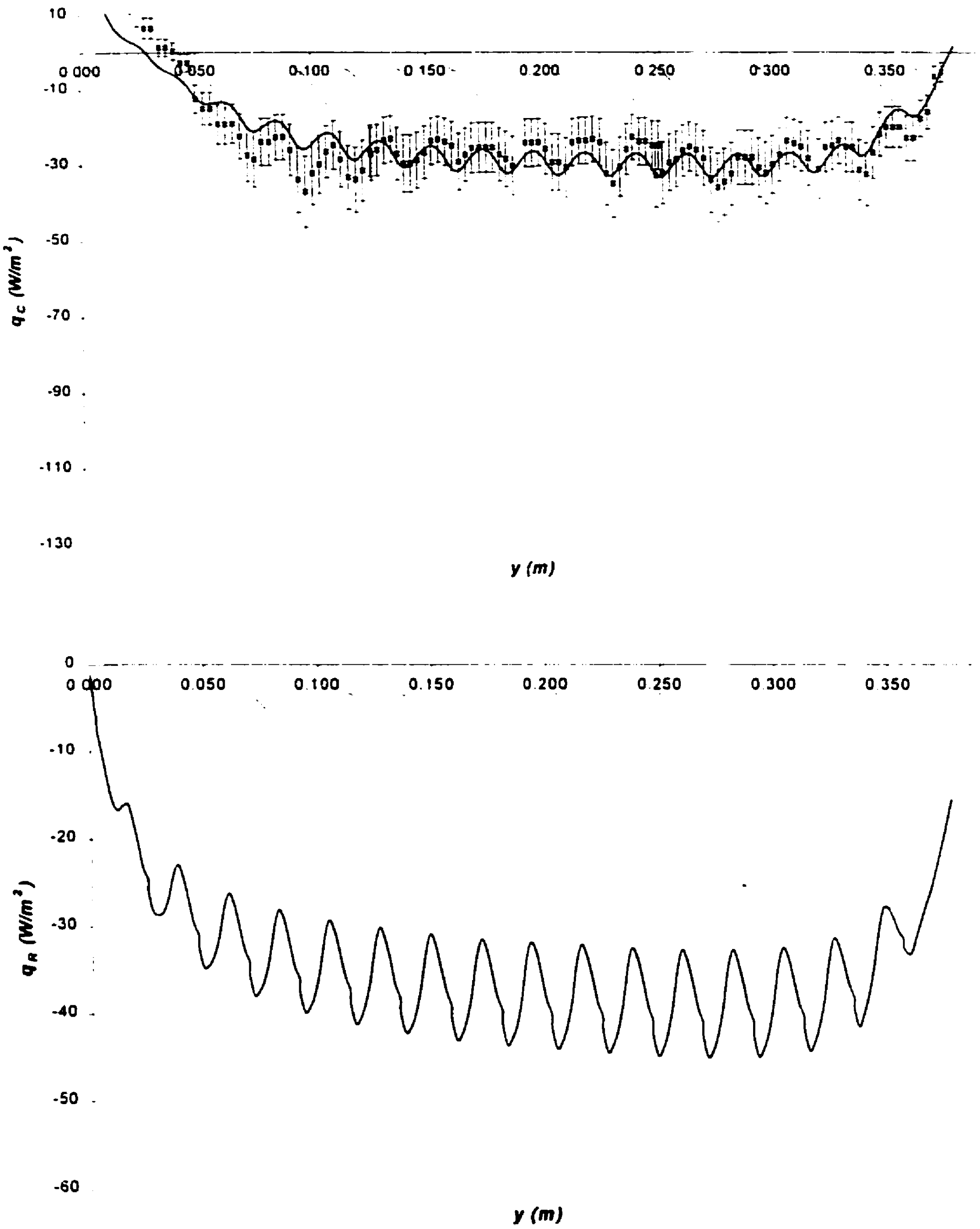

Figure 3-10: Convective and radiative heat flux for validation case 6: b = 15.4 mm, ϕ= 45°, T_p = 298 K. Points represent interferometric results with associated experimental uncertainty. Solid line represents numerical results. Slat positions are superimposed on graphs for clarity.

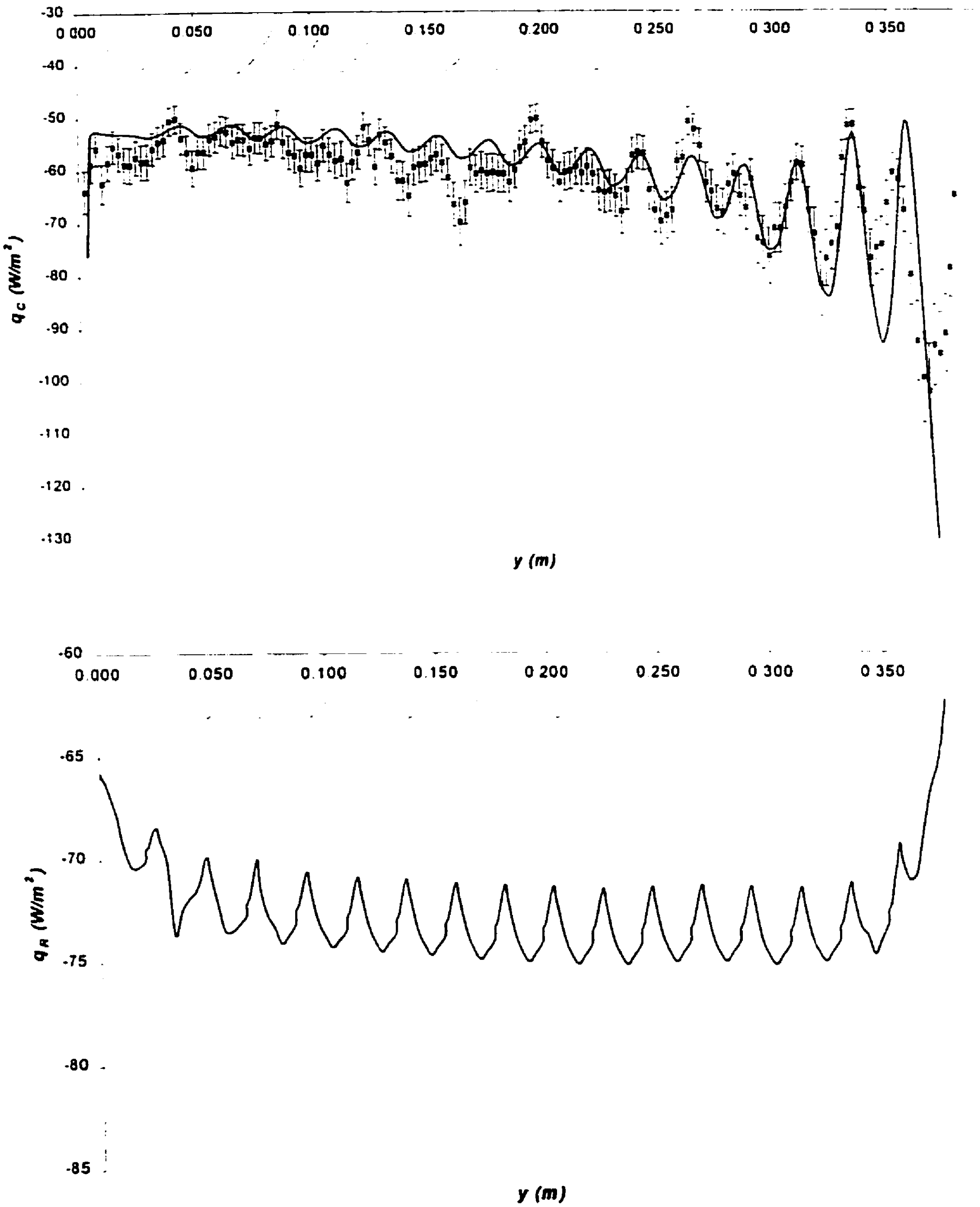

Figure 3-11: Convective and radiative heat flux for validation case 7: $b = 15.4$ mm, $\phi = -45^{\circ}$, $T_p = 283$ K. Points represent interferometric results with associated experimental uncertainty. Solid line represents numerical results. Slat positions are superimposed on graphs for clarity.

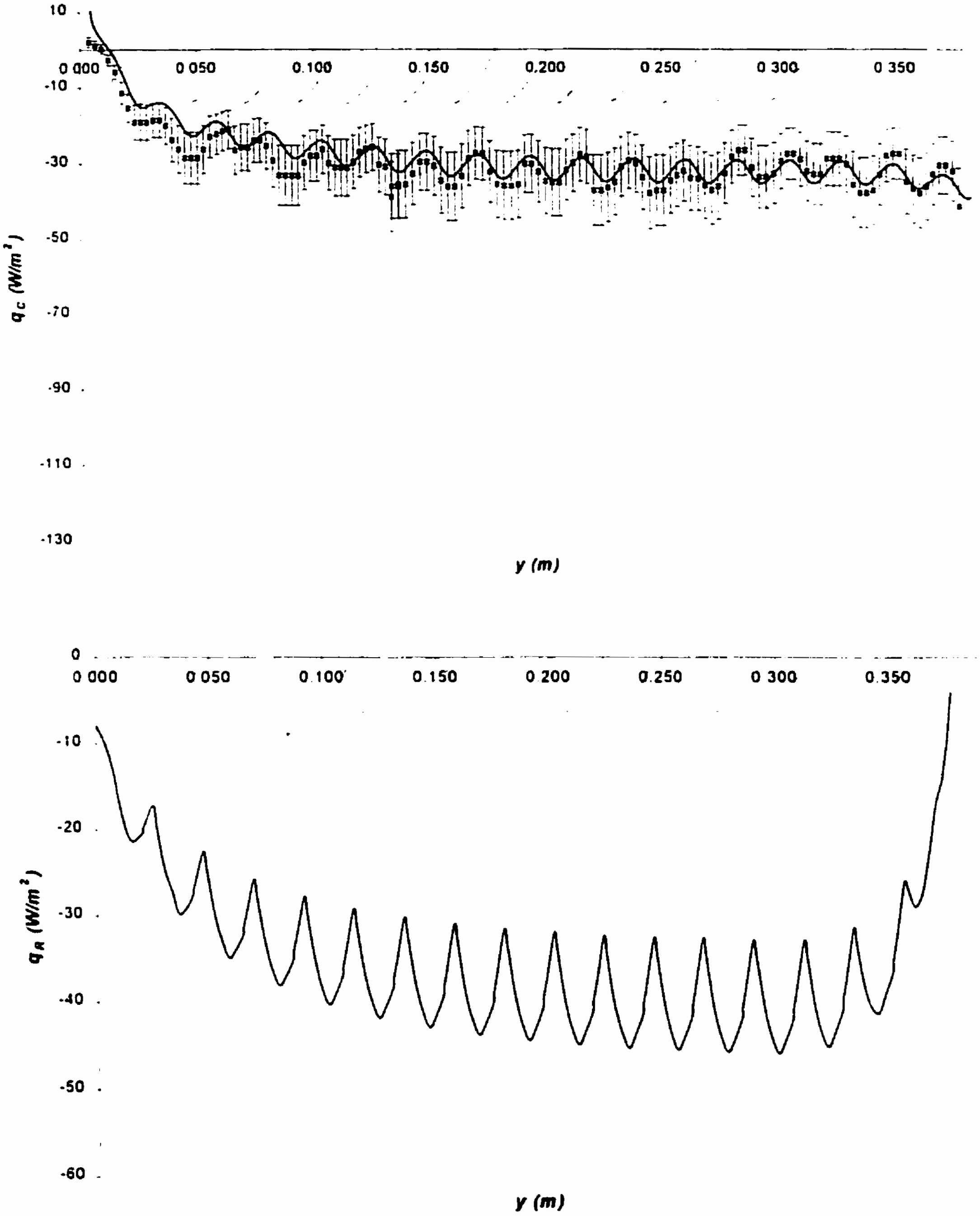

Figure 3-12: Convective and radiative heat flux for validation case 8: b = 15.4 mm, ϕ= -45°· T_p = 298 K. Points represent interferometric results with associated experimental uncertainty. Solid line represents numerical results. Slat positions are superimposed on graphs for clarity.

Table 3-3: Comparison of predicted and measured convective heat flux and predicted radiative heat flux from the plate for all validation cases. Results for the middle third of the plate are presented in brackets.

Case	$\bar{q}_C$ Model (W/m^2)	$\bar{q}_C$ Experiment (W/m^2)	$\bar{q}_R$ Model (W/m^2)
1	-79.2 (-79.0)	-75.1 (-76.1)	-66.6 (-66.7)
2	-52.2 (-57.1)	-39.2 (-43.4)	-25.4 (-27.9)
3	-64.0 (-60.8)	-55.8 (-56.7)	-70.4 (-71.6)
4	-27.5 (-32.0)	-25.1 (-28.9)	-28.9 (-33.2)
5	-56.1 (-56.1)	-53.1 (-53.4)	-70.3 (-72.6)
6	-21.3 (-29.7)	-20.6 (-27.0)	-34.0 (-38.7)
7	-62.4 (-59.5)	-61.3 (-60.5)	-72.6 (-75.7)
8	-27.6 (-31.8)	-28.9 (-33.4)	-34.9 (-40.3)

The experimental data correlated well with numerical results. For the majority of cases, the error is within the uncertainty of the experimentally determined results. More importantly, the local flux rates obtained experimentally agree with numerically obtained data both in trend and magnitude.

While the quality of the experimental/numerical comparison is good, a number of discrepancies are evident in the experimental data. It is advantageous, at this point, to identify these discrepancies and discuss their significance. They include aspects of modeled verses experimental inlet and outlet conditions, as well as limitations with the experimental method.

As indicated in Table 3-3, the experimentally measured average heat flux for case 2 was found to be 25% lower than the numerically predicted results, even though the results shown in Fig. 3-6 appear to be accurate. The descrepancy is a result of the wedge fringe method of analyzing interferometric data. In this particular case, the fringe angle can only be measured on the fringes themselves, which are spaced by a distance *d*. With this spacing, the extreme peaks demonstrated by the numerical results have been missed, resulting in an underprediction of the average heat flux.

It was expected that the top and bottom slats in each case would be affected by the radiative heat transfer conditions set in the numerical model. The temperature was not set as a boundary condition on the top and bottom sections of the numerical model because those could either be regions of inflow or outflow. The radiation model, however, must use the temperature of these sections to calculate radiant exchange between the slats and the room in the direction of the inlet and outlet. As a result, the bottom and top slats are largely radiating to the fluid temperature at the inlet and outlet, as opposed to the T_i. It can be seen in Figs. 3-5 through 3-12 that this did not have any noticable effect on the end slats.

One significant difference between the numerical model and the experiment existed at the bottom and top edges of the plate. In the experiment, flow was entrained around the sharp edge of the plate. In the numerical model, an adiabatic wall continues above and below the plate. While this difference has no identifiable effect on cases where the plate was warmer than the ambient (i.e., cases 2, 4, 6, and 8), it did have an effect on the cases where the plate was cooler than ambient (i.e., cases 1, 3, 5, and 7). In particular, the top portion of data from case 3 does not follow the experimental results as well as any of the other cases. During the experiment, air flowing downward from the cold plate is entrained around the sharp lead edge of the plate, while hot air from the blind rises and is guided away from the plate by the momentum of the air flow which was developed on the room-side of the blind. This allows the boundary layer on the plate to grow unhindered to the topmost slat as if no blind was present. By contrast, because the numerical model assumes that the unheated wall continues above the heated plate, flow from the blind is pulled back towards the wall by downward flow entrained by the cold plate, thereby increasing the air temperature and heat flux in that area. This effect is less significant in the three other cold cases due to the proximity of the blind to the plate in case 1, and the slat angle in cases 5 and 7. These conditions provide added stability to the flow, which quickly removes the effect of a downward developing boundary layer. This problem was not apparent in the warm plate cases (2, 4, 6, and 8) because no counter flow is produced.

Due to optical restrictions, the experimental data in Figs. 3-5 through 3-12 were obtained from three individual photographs. As a result of environmental changes occuring between the times at which these photos were taken, some step discontinuities are evident in all of the data. The flux measured in the top 1/3rd of case 5 demonstrates the problem clearly. This reduction is due to a small change (> 0.2 K) in the ambient temperature at the time that the final interferometer picture was taken. This was acknowledged as a limitation of the current experimental setup.

Although these discrepancies have been identified, they are not considered to be a weakness of the numerical model. In fact, the continuing unheated portion of wall present in the numerical analysis, is closer to a realistic window situation than the experimental setup. More importantly, if the blind can be shown to suppress the growth of convective heat transfer from the plate surface, the center portion of the model can then be used as a center of glass heat transfer rate for other window sizes. In this respect, the top and bottom portions of the model would be disregarded.

An example comparison of numerically and experimentally obtained isotherms is given in Fig 3-13. Visibly, the surrounding temperature field shows excellent agreement. A complete summary of numerically and experimentally obtained isotherms is given in Appendix C. In all cases, the location and trends of isotherms are similar.

Although the experimental setup is unable to directly validate the radiative heat transfer calculated by the numerical model, blind temperatures measured during the experiments can confirm that predicted blind slat temperatures are correct. Table 3-4 shows a comparison of this data for selected louvers where the average difference between the modeled and experimental results is only 0.64 K. As can be seen, the experimental results are in excellent agreement with the numerically obtained temperatures. In this way, additional confidence was gained in the numerical results, especially when considering the predicted radiation exchange.

Table 3-4: Comparison of predicted and measured blind slat temperatures for all validation cases. M and E denote modeled and experimental results respectively. Experimental measurement accuracy is ± 0.2 K.

Case	*T* Slat 4 (K)		*T* Slat 6 (K)		*T* Slat 8 (K)		*T* Slat 10 (K)		*T* Slat 12 (K)		*T* Slat 14 (K)	
	M	E	M	E	M	E	M	E	M	E	M	E
1	299.9	301.0	300.0	301.1	300.0	301.2	300.0	301.5	300.0	301.7	300.1	301.0
2	309.4	309.3	309.6	309.2	309.7	309.2	309.8	309.7	309.8	309.8	309.8	309.6
3	303.1	303.3	303.1	303.2	303.1	303.2	303.1	303.8	303.1	303.7	303.0	303.8
4	309.8	309.7	310.7	310.0	311.1	310.2	311.4	311.0	311.6	311.1	311.7	310.9
5	302.3	301.5	302.4	301.9	302.6	302.0	302.6	302.5	302.8	302.7	302.8	303.1
6	308.7	308.7	309.3	308.7	309.8	308.4	310.0	309.3	310.2	309.4	310.3	308.7
7	302.5	302.4	302.6	302.3	302.7	302.2	302.7	302.7	302.7	302.5	302.8	302.5
8	308.9	308.6	309.9	308.8	310.4	308.6	310.7	309.4	310.8	309.7	311.0	309.5

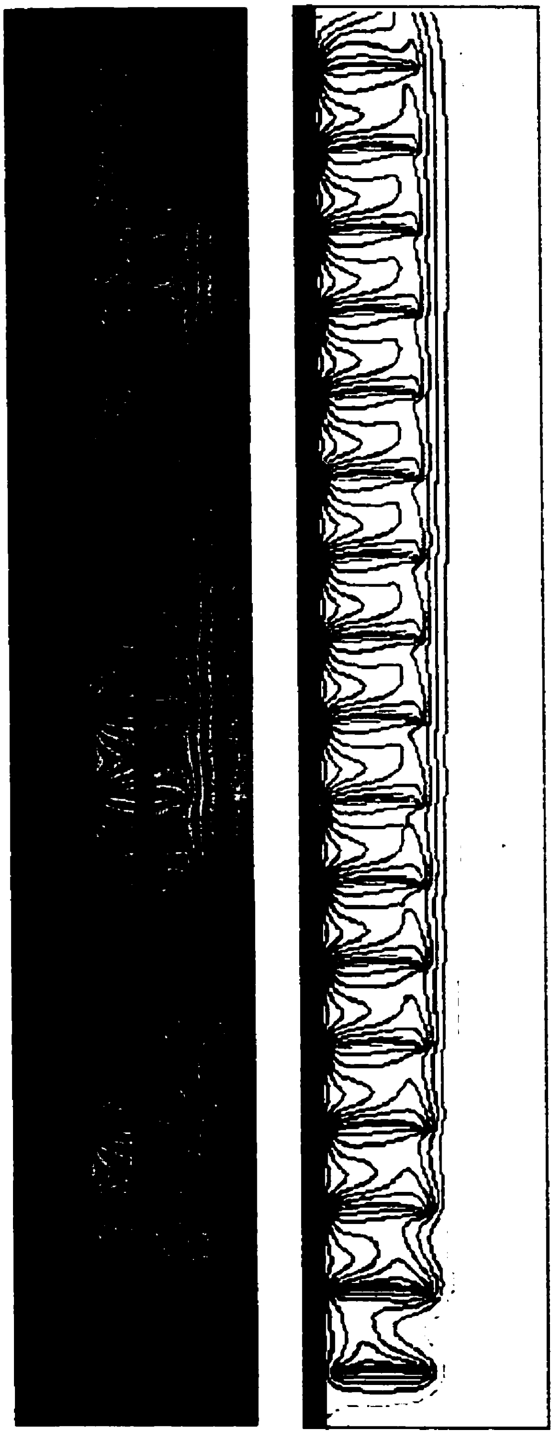

Figure 3-13: Comparison of isotherms for validation case 2. Interferometric (left) and numerical (right).

Other information can be obtained through observation of the numerically obtained convective and radiative heat transfer rates. Trends obtained from the data presented in Figs. 3-5 through 3-12 are discussed in the following paragraphs.

The convective and radiative flux for the cold plate was consistently larger in magnitude than that for the warm plate when considering cases involving identical geometry. For example, the convective flux for the cold plate was 52% larger in magnitude than that for the warm plate when considering cases 1 and 2. The remaining cases show an increase of 141% between the cold and hot plate results. The average radiative heat flux for the cold plate was 162% larger than that for the warm plate when considering 0° slat tilt, i.e., cases 1 verses 2, and 3 verses 4. The +45° and –45° tilt angles show an increase of 108% between the cold and hot plate results, i.e., cases 5 verses 6, and 7 verses 8. In all cases, the average heat transfer occured in the direction of the plate surface. This is a significant point. Conceivably, heat transfer at the window surface may occur when no plate-to-air temperature difference exists due to heating of the shade layer. As such, a modified interior heat transfer coefficient may be indeterminate. It does not, however, prevent analysis of the heat transfer at the inner glass, or analysis of a fenestration from that perspective.

A more significant result is apparent when considering the effects of system geometry. In Fig. 3-5 and 3-6, for cases 1 and 2, the proximity of the slat leading edges and the plate produce a significant periodic effect on the convection from the plate, where an increase in the local convective flux occurs when the leading edge and plate are positioned close together. For cases 3 to 8, when the slat leading edge was furthest from the plate, the blind angle was observed to have little effect on the convective heat flux.

Considering radiative heat flux, for cases 1 and 2, when the slat leading edge was closest to the plate, peaks in the local heat transfer rate were sharper and more distinct than in the other models. In this case, a decrease in the local radiative flux occured when the leading edge and plate were close together. As the blind was moved away from the plate. the "view" from the plate becomes largely independent of vertical location and slat angle. In Figures 3-7 to 3-12, while some periodicity is evident in both the radiative and convective heat flux, the results of cases 3, 5, and 7 and cases 4, 6, and 8 are not significantly different.

The final trend evident from this data is the steady and periodic nature of the data. If the first five slats from the bottom and top of each model are disregarded, q_C and q_R do not change significantly with location. Previous investigations (Machin 1997, Phillips 1999) have also suggested that the blind may suppress boundary layer growth. Together, these points give confidence in using the model to predict center-of-glass heat transfer for larger window and shade systems. Unfortunately, this did not hold true for all of the validation cases. In cases 4, 6 and 8, the viewfactor between the plate and the louvers was large, and the blind slat temperature continued to rise with increased distance up the plate, thereby producing a gradual increase in q_R. Likewise, an increase was noted in the level of convective flux from the plate when the blind was further away and counterflow existed (cases 3, 5, and 7). While some of this increase was due to boundary layer growth, the majority was undoubtably a result of end effects. Even though the cases represented extreme conditions, the increase in radiative and convective flux was not significant, and should not prevent a center-of-glass analysis with the data.

It is important to note that a single experiment was performed at b = 30 mm, T_p = 283 K, ϕ - 0 deg, and q_b = 150 W/m^2. The results of that experiment have not been presented because the unsteady conditions produced prevent any useful analysis of the data. It is not known if the unsteady flow was due to laminar/turbulent transition, or some other effect. While the experiment did represent an exteme condition, it did demonstrate an important point. The bounds of the validation experiment are near the point where the initial assumptions become invalid. As well, it was difficult to obtain convergence numerically using those conditions.

3.8 Conclusions

Experimentally determined natural convective and radiative heat transfer from a horizontal Venetian blind adjacent to an indoor window glazing has been obtained and compared to the results produced with a conjugate heat transfer numerical model of the system. With the exception of some readily explained departures between the experimental and numerical results, the local and average convective heat transfer coefficients were found to agree closely both in magnitudes and trends. Furthermore, experimentally obtained blind temperatures and isotherms were in close agreement with those obtained from the numerical model. This provides additional confidence in the numerical results.

The following conclusions were drawn from the numerically obtained results.

- For the cases examined, convective and radiative heat flux was found to be into the plate, despite the fact that for cases 2, 4, 6 and 8, the plate temperature was higher than the ambient room temperature. This prevents the determination of an equivalent air film coefficient for the inside glazing, i.e., the hot blind layer would result in negative and indeterminate heat transfer coefficients. Total heat flux at that boundary, however, may still be used.

- The effect of louver tip to plate spacing was clearly demonstrated. As the louver is moved away from the plate, the local convective and radiative heat flux were less affected by individual louvers. There was little difference between the results of cases 3, 5 and 7, and 4, 6, and 8, despite the fact that the louver angle changed. At a certain spacing, the dimension *b* was no longer needed to determine heat transfer from the system.
- For the majority of cases, in the middle section of the plate, the local convective and radiative heat flux results tended to be periodic with very little increase in magnitude. Slight increases in the radiative flux, however, could be seen under specific conditions. While this growth could conceivably become significant, it was unavoidable. Future analysis may be needed on a larger system to determine under what conditions this growth occurs.
- The onset of unsteady flow was observed both numerically and experimentally. This occurred under conditions of large and opposing convective flow, i.e., large blind heat flux, low blind emissivity, and cold plate temperatures. While the occurrence of these conditions would be rare, the limits of the model need further investigation.

CHAPTER 4
PARAMETRIC ANALYSIS

4.1 Introduction

The present chapter describes the statistical analysis of the radiative and convective heat transfer from the interior surface of a window to the surrounding environment with respect to six variables, using the numerical model described and validated in the preceding Chapters. An investigative parametric analysis was performed to determine the effects of the variables on the heat transfer from the inner glazing surface. The results of this analysis were subsequently used to aid in the design of a comprehensive three-level factorial parametric analysis (Montgomery and Runger 1999) of the system. Finally, correlation equations were produced using this data.

4.2 Investigative Parametrics

4.2.1 Procedure

To develop a comprehensive parametric analysis of a window and shade system, it was first necessary to observe the effects each variable has on the convective and radiative heat flux from the plate surface. In this way, it could be determined if the response of a given variable could be treated as linear or quadratic, or if some other treatment was necessary.

To facilitate this analysis, an investigative parametric was performed on each of the six variables which were expected to have an affect on heat transfer from the inner glazing surface. By changing one variable while holding the remaining five constant, it is possible to formulate the effect that variable had on the system. For each of three slat angles (-45, 0, 45 deg), an analysis of the effects of glass temperature was performed for a base case of b = 30 mm and n = 18 mm, with $\varepsilon_b = \varepsilon_p$ = 0.6, and q_b = 60 W/m^2. Previous investigations (Machin 1997, Phillips 1999) have suggested that convective heat transfer from the window was more strongly influenced by tip spacing (n) as opposed to nominal spacing (b). The authors were not certain if this trend also applied to radiative heat transfer. Secondary investigations were subsequently performed using two base cases consisting of 0 deg slat angle with glass temperatures of 287 K and 307 K (10 K above and below ambient). It was known, however, that the interaction between the heated blind and the heated or cooled glass could produce situations where convective boundaries developing on the blind and glass may or may not be moving in the same direction. The differences between these two cases were considered to be important enough to justify performing the investigation for each case. The effects of blind flux, glass and blind emissivity, and nominal spacing were each examined independently at four additional levels around the conditions of each base case. Tables 4-1 and 4-2 present the numerical model conditions considered in this study.

Table 4-1: Numerical conditions of investigative parametric series.

ϕ (deg)	b (mm)	n (mm)	ε_b	ε_p	q_b (W/m^2)	T_p (K)
-45	30	20	0.6	0.6	60	277, 287, 297, 307, 317
0	30	18	0.6	0.6	60	277, 287, 297, 307, 317
45	30	22	0.6	0.6	60	277, 287, 297, 307, 317
-45	27	18	0.6	0.6	60	277, 287, 297, 307, 317
45	25	18	0.6	0.6	60	277, 287, 297, 307, 317

Table 4-2: Numerical conditions of secondary investigative parametric series. All parametrics performed at ϕ = 0°. Base conditions indicated in bold.

b (mm)	ε_b	ε_p	q_b (W/m^2)	T_p (K)
20, 25, **30**, 35, 40	**0.6**	**0.6**	**60**	**287, 307**
20, 25, **30**, 35, 40	**0.6**	**0.6**	**60**	**287, 307**
30	0.2, 0.4, **0.6**, 0.8, 1.0	**0.6**	**60**	**287, 307**
30	0.2, 0.4, **0.6**, 0.8, 1.0	**0.6**	**60**	**287, 307**
30	**0.6**	0.2, 0.4, **0.6**, 0.8, 1.0	**60**	**287, 307**
30	**0.6**	0.2, 0.4, **0.6**, 0.8, 1.0	**60**	**287, 307**
30	**0.6**	**0.6**	0, 30, **60**, 90, 120	**287, 307**
30	**0.6**	**0.6**	0, 30, **60**, 90, 120	**287, 307**

The analysis was performed using the numerical model described in Chapter 2. Fluid properties were evaluated at an estimated film temperature of 300 K (i.e., constant Ra_l) and were taken from Touloukian et al. (1970a, 1970b, 1975). Fluid properties and miscellaneous model parameters are given in Table 4-3.

Table 4-3: Numerical parameters used in the investigative parametrics. Fluid properties are evaluated at T_f=300 K.

c_p (J/kg·K)	ρ_f (kg/m^3)	β_f (1/K)	ν_f (m^2/s)	μ_f kg/m·s)	k_f (W/m·K)	ε_i
1006.3	1.1656	0.0033	1.590E-5	1.853E-5	0.026	1.00

l (mm)	ps (mm)	w (mm)	t (mm)	rc (mm,deg)	T_i (K)	k_b (W/m·K)
379.6	22.2	25.4	0.17	52.3 , 27.3	297	120

Results were examined using trendlines fit using polynomial regression (Devore 1987). By that method, a linear fit was obtained by solving the simultaneous equations, i.e.,

$$b_o n + b_1 \sum x_i = \sum y_i \tag{4.1}$$

$$b_o \sum x_i + b_1 \sum x_i^2 = \sum x_i y_i \tag{4.2}$$

where b is the parameter estimate, and x and y are the variables being fit. A quadratic fit was determined by solving

$$b_o n + b_1 \sum x_i + b_2 \sum x_i^2 = \sum y_i \tag{4.3}$$

$$b_o \sum x_i + b_1 \sum x_i^2 + b_2 \sum x_i^3 = \sum x_i y_i \tag{4.4}$$

$$b_o \sum x_i^2 + b_1 \sum x_i^3 + b_2 \sum x_i^4 = \sum x_i^2 y_i \tag{4.5}$$

The resulting trendline for a linear fit was of the form

$$b_o + b_1 x = y \tag{4.6}$$

and for a quadratic fit

$$b_o + b_1 x + b_2 x^2 = y \tag{4.7}$$

To assess the quality of these data fits, the R^2 coefficient was calculated.

$$R^2 = 1 - \frac{\sum (y - \hat{y})^2}{\sum (y - \bar{y})^2} \tag{4.8}$$

where $\bar{y}$ and $\hat{y}$ are the average and predicted y parameters respectively. An R^2 value near 1 was deemed to represents an acceptable fit.

4.2.2 Results and Discussion

The ultimate intention of this research is to determine the effects of a sunlit shade on heat transfer in the center-of-glass region of a window. One conclusion presented in Chapter 3 was that the blind layer generally supressed significant changes in radiative and convective heat transfer, and allowed a center-of-glass analysis to be performed on the middle section of the window model. As such, average and local heat flux rates will only be presented for the glass region located between the midpoint of the 5th and 6th slats, to the midpoint of the 12th and 13th slats. This vertical section includes 7 blind slats, and 0.16 m of glass.

An example of local convective and radiative heat flux rates for the complete 0° slat angle temperature parametric can be seen in Fig. 4-1 where slat positions are shown in gray, and positive flux is from the plate. Local heat flux results from all the investigative parametrics are given in Appendix D. The local radiative heat flux is observed not to change with vertical location on the glass, indicating that only insignificant changes in blind slat temperature occurred. Conversely, local convective heat transfer rates do change with distance up the glass, indicating the effects of boundary layer growth. The magnitude of this change increased as the plate temperature deviated further from the ambient temperature. That is, the convective flux from the glass over a height of 0.16 m increased by only 1.8 W/m^2 at T_p = 297 K, while at T_p = 317 K the convective flux into the glass decreased by 17 W/m^2. Significant changes in local convective flux only occured at extreme glass temperatures, and are considered as a limitation of the analysis.

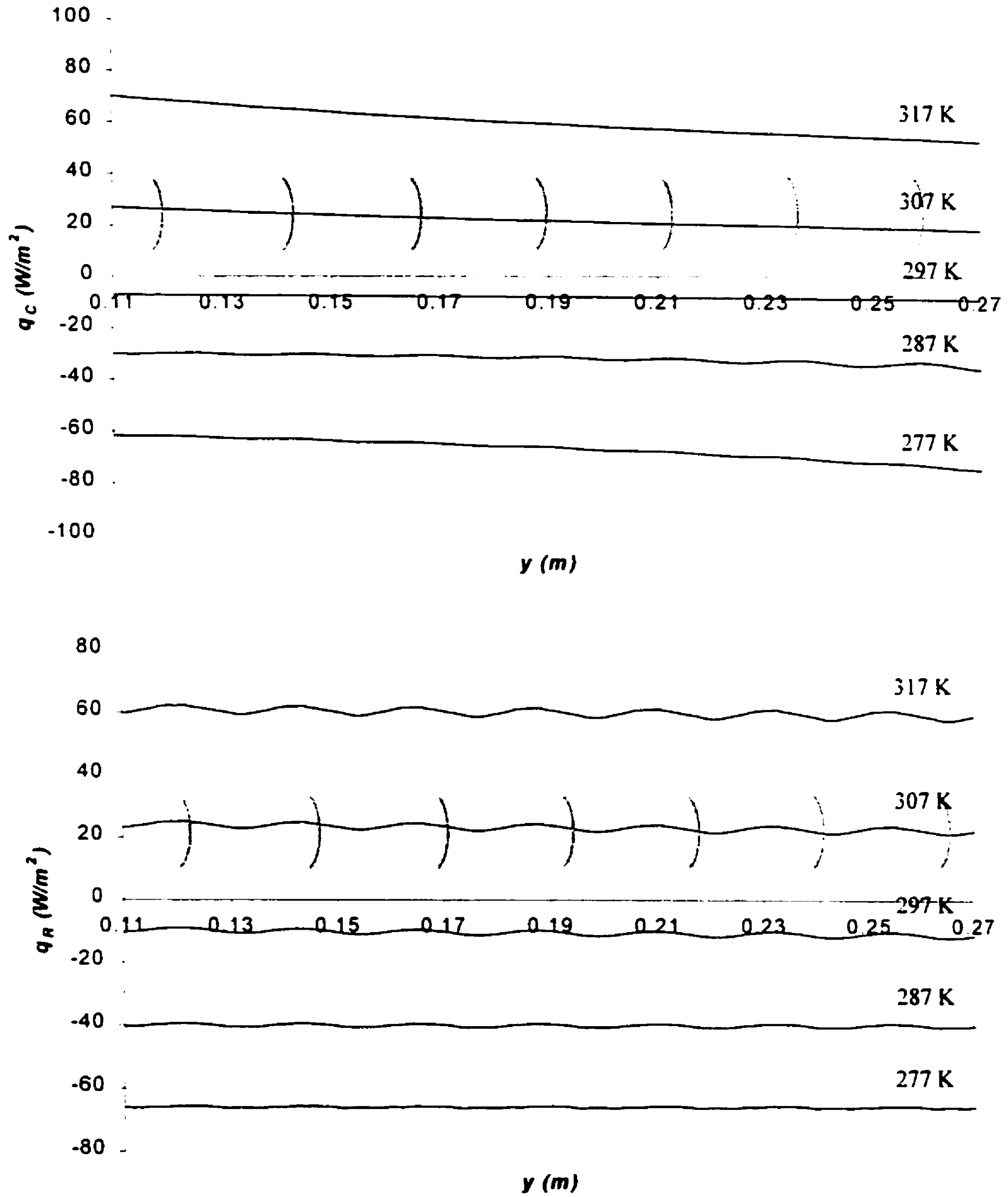

Figure 4-1: Local convective and radiative heat flux in the center-of-glass region with changing glass temperature ($\phi = 0°$, $b = 30$ mm, $\varepsilon_b = \varepsilon_p = 0.6$, $q_b = 60$ W/m^2). Slat positions are shown in gray.

The effect of glass temperature and slat angle on the average convective and radiative flux are presented in Figs. 4-2 and 4-3 and Table 4-4. Figures 4-2 and 4-3 present the effects of varying the glass temperature and slat angle at a constant nominal spacing and tip spacing, respectively. Both radiative and convective heat transfer rates indicated a linear relationship with temperature, whereby the average flux became increasingly positive with elevated glass temperature. At all three slat angles, linear trendlines fit to the convective data produced correlation coefficients of 0.992 or greater when $b = 30$ mm and 0.995 when $n = 18$ mm. Considering the radiative heat transfer results, linear trendlines fit to the data produced correlation coefficients of 0.995 when $b = 30$ mm and 0.994 when $n = 18$ mm. A more significant result can be found by examining the difference, or lack of difference, of the calculated heat flux with differing blind slat angle. By ignoring slat angle and adding a linear fit to the convective flux data, correlation coefficients of 0.993 for $b = 30$ mm and 0.995 for $n = 18$ mm are produced. This confirms the findings of Machin (1997) and Phillips (1999) who found that tip spacing was more important than slat angle when determining convective heat transfer from the glass. A slightly different result occurs when considering radiative heat transfer. As before, by ignoring slat angle and fitting a linear trendline to the radiative flux data, a correlation coefficient of 0.994 was obtained for $b = 30$ mm and 0.993 for $n = 18$ mm. It is therefore concluded that the radiative heat transfer rate was more dependent on nominal spacing than blind slat angle. These results suggests that slat angle can be omitted when determining radiative heat transfer, and need only be considered in calculating tip spacing for determining convective heat transfer. It is also interesting to note that for the cases chosen, average radiative and convective flux were found to be of the same magnitude.

Table 4-4: Numerically predicted average convective and radiative heat flux from the center-of-glass region of the plate as a function of plate temperature, slat position, and slat angle. Results are for tests indicated in Table 4-1. Models executed at $\varepsilon_b = \varepsilon_p = 0.6$, $q_b = 60$ W/m².

ϕ	blind spacing	Average flux (W/m²)					
		T_p (K)	277	287	297	307	317
-45	b = 30 mm	convective	-65.5	-31.3	-7.1	22.8	60.7
		radiative	-62.7	-38.6	-11.0	20.7	55.3
0	b = 30 mm n = 18 mm	convective	-66.7	-31.8	-8.0	22.0	59.8
		radiative	-65.9	-40.1	-10.5	23.2	60.0
45	b = 30 mm	convective	-65.1	-26.4	-4.4	24.5	62.4
		radiative	-61.7	-37.8	-10.6	20.6	54.3
-45	n = 18 mm	convective	-66.1	-32.0	-8.2	21.5	59.2
		radiative	-62.6	-38.8	-11.6	20.1	54.6
45	n = 18 mm	convective	-66.4	-30.9	-7.0	22.0	59.6
		radiative	-61.5	-38.3	-11.4	19.8	53.5

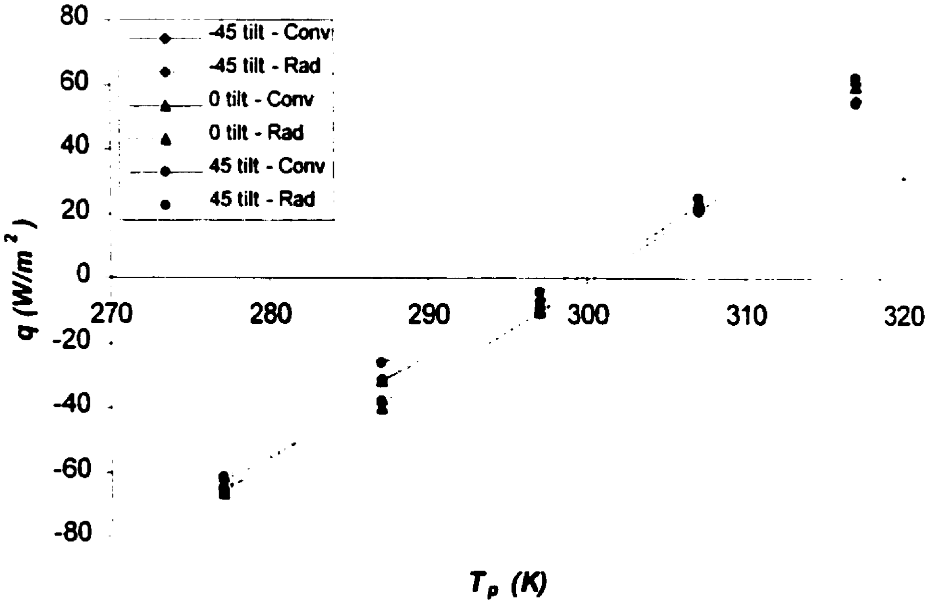

Figure 4-2: Average convective and radiative heat flux from the center-of-glass region of the plate for the plate temperatures presented in Table 4-1. Models executed at $\phi = 0$, $b = 30$ mm, $\varepsilon_b = \varepsilon_p = 0.6$, $q_b = 60$ W/m².

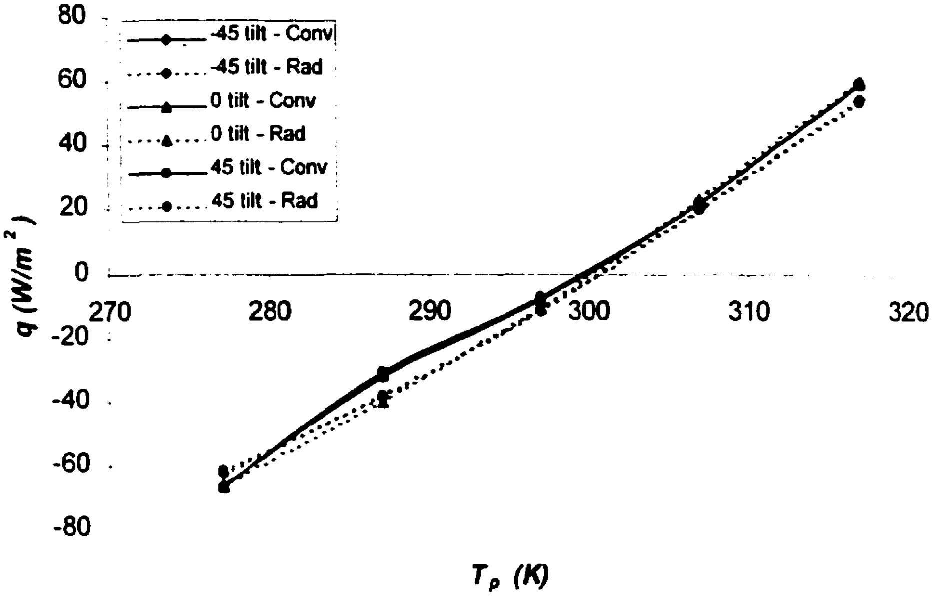

Figure 4-3: Average convective and radiative heat flux from the center-of-glass region of the plate for the plate temperatures presented in Table 4-1. Models executed at $\phi = 0°$, $n = 18$ mm, $\varepsilon_b = \varepsilon_p = 0.6$, $q_b = 60$ W/m^2.

The effect of blind emissivity on convective and radiative heat transfer from the glass is presented in Fig. 4-4 and Table 4-5. These results indicate that the average convective heat transfer coefficients are not significantly affected by changes in blind emissivity. The magnitude of the change in the convective heat transfer over the range of blind emissivities examined was not significant. As such, it may be possible to accurately predict convective heat transfer without using the blind emissivity as input. When considering the warm glass case, the convective flux changed by less than 1.2 W/m^2 or 5.6% over the entire range. The cold glass case was more significant at 5.0 W/m^2 or 14.5%. Quadratic trendline fits of the data produced correlation coefficients in excess of 0.990 in both cases while linear fits were slightly worse with correlation coefficients of 0.903 at $T_p = 287$ K and 0.947 and $T_p = 307$ K. When considering the radiative heat flux, changes in the slope of the trendline were more significant than observed in the convective data. Greater blind emissivities reduce the resistance of the blind to radiative heat flux to, and from, the glass. Therefore, radiative flux from the glass became more negative with increasing blind emissivity. Quadratic fits of the data produced correlation coefficients in excess of 0.992 in both cases. Correlation coefficients of 0.914 were obtained for the linear fits at $T_p = 287$ K and 0.866 at $T_p = 307$ K.

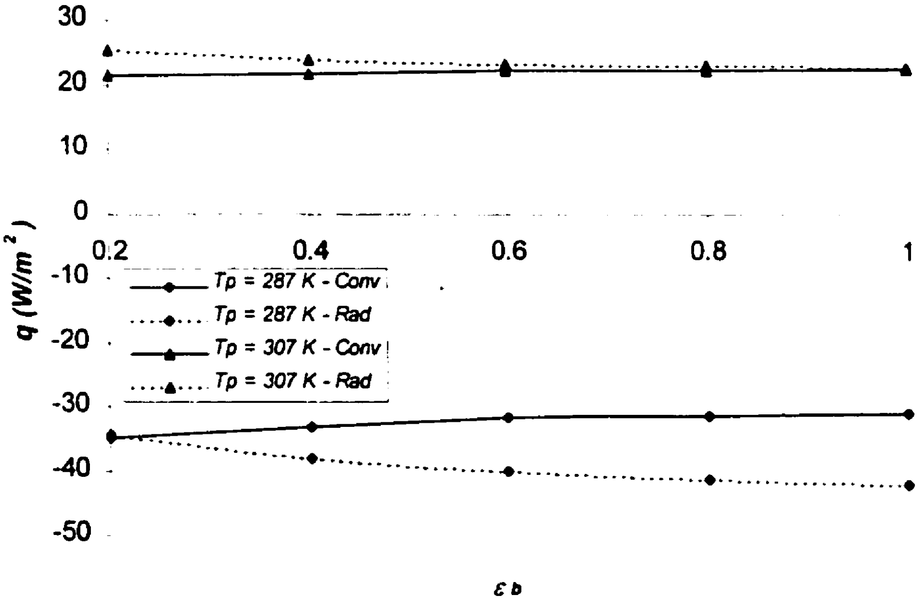

Figure 4-4: Average convective and radiative heat flux from the center-of-glass region of the plate for the slat emissivities presented in Table 4-2. Models executed at $\phi = 0°$, $b = 30$ mm, $\varepsilon_p = 0.6$, $q_b = 60$ W/m^2.

Table 4-5: Numerically predicted average convective and radiative heat flux from the center-of-glass region of the plate as a function of slat emissivity. Results are for tests indicated in Table 4-2. Models executed at $\phi = 0°$, $b = 30$ mm, $\varepsilon_p = 0.6$, $q_b = 60\ \mathrm{W/m^2}$.

T_p (K)	Average flux ($\mathrm{W/m^2}$)					
	ε_b	0.2	0.4	0.6	0.8	1.0
287	convective	-35.0	-33.1	-31.8	-31.4	-30.9
	radiative	-34.4	-38.2	-40.1	-41.4	-42.2
307	convective	21.3	21.7	22.0	22.1	22.3
	radiative	25.3	23.9	23.2	22.9	22.7

The effect of glass emissivity can be seen from the results given in Fig. 4-5 and Table 4-6. Convective heat flux from the glass was unaffected by the range of glass emissivity investigated. Convective flux reduced by only 1 $\mathrm{W/m^2}$ or 4.4% for the hot plate, and increased by 2.9 $\mathrm{W/m^2}$ or 8.7% over the entire range of emissivities examined. This result would support the argument that it may be possible to ignore glass emissivity when predicting convective heat transfer. A linear fit to the data works well in both cases with correlation coefficients of 0.975 at $T_p = 287$ K and 1.000 at $T_p = 307$ K. In contrast however, the radiative heat transfer changed significantly with glass emissivity, indicating that increased glass emissivity reduced the resistance of the glass to radiative heat transfer, and increased the magnitude of the flux emitted or absorbed at the plate surface. Both the convective and radiative heat flux results show excellent linearity with correlation coefficients of 0.997 for each glass temperature.

Table 4-6: Numerically predicted average convective and radiative heat flux from the center-of-glass region of the plate as a function of plate emissivity. Results are for tests indicated in Table 4-2. Models executed at $\phi = 0°$, b = 30 mm, ε_b = 0.6, q_b = 60 W/m^2.

T_p (K)	Average flux (W/m^2)					
	ε_p	0.2	0.4	0.6	0.8	1.0
287	convective	-33.3	-32.6	-31.8	-31.5	-31.0
	radiative	-14.6	-28.0	-40.1	-51.3	-61.5
307	convective	22.4	22.2	22.0	21.8	21.6
	radiative	8.4	16.2	23.2	29.7	35.8

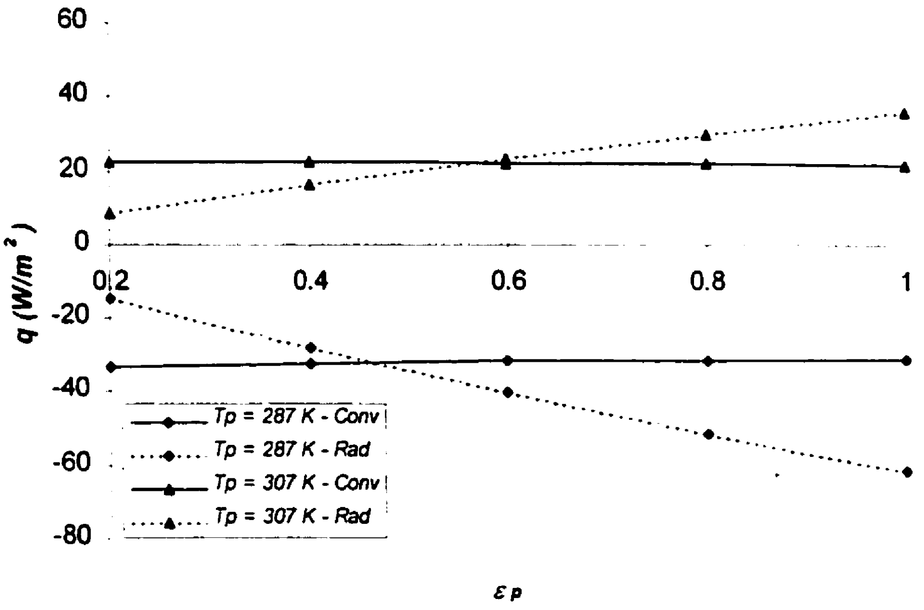

Figure 4-5: Average convective and radiative heat flux from the center-of-glass region of the plate for the plate emissivities presented in Table 4-2. Models executed at $\phi = 0°$, b = 30 mm, ε_b = 0.6, q_b = 60 W/m^2.

The effect of nominal blind spacing can be seen from the results given in Fig. 4-6 and Table 4-7. As the blind is moved closer to the glass, an increased affect is clearly visible. In the case of convection heat transfer, the results support the premise that closer spacing causes an increasingly negative shift in the direction of heat flux, i.e., heat lost from a warm plate is reduced, while heat gained by a cold plate increases. A 2nd order fit to the data produced a correlation coefficient of 0.985 for both of the glass temperatures considered. Changes in radiative heat flux with proximity were less pronounced, although a slight decrease in heat transfer was obtained as the blind gets closer to the glass. Such a change was most likely the result of an increase of the glass-to-ambient viewfactor and an associated decrease in the glass-to-blind viewfactor. As the ambient temperature was below the plate temperature, radiative exchange was reduced. Quadratic fits to this data produced correlation coefficients of 0.960 at $T_p = 287$ K and 0.990 at $T_p = 307$ K.

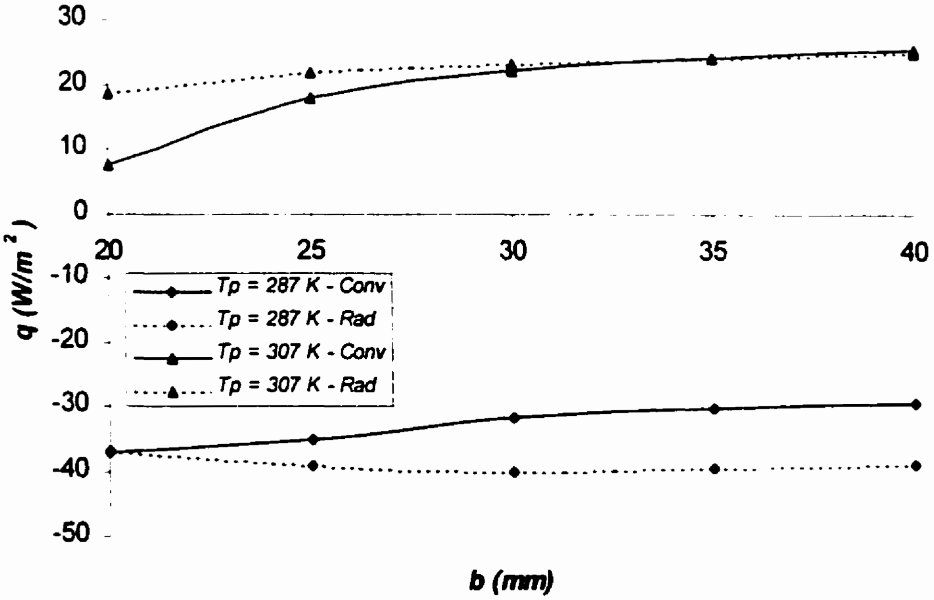

Figure 4-6: Average convective and radiative heat flux from the center-of-glass region of the plate for the nominal spacings presented in Table 4-2. Models executed at $\phi = 0°$, $\varepsilon_b = \varepsilon_p = 0.6$, $q_b = 60$ W/m^2.

Table 4-7: Numerically predicted average convective and radiative heat flux from the center-of-glass region of the plate as a function of nominal spacing. Results are for tests indicated in Table 4-2. Models executed at $\phi = 0°$, $\varepsilon_b = \varepsilon_p = 0.6$, $q_b = 60$ W/m^2.

T_p (K)	Average flux (W/m^2)					
	b (mm)	20	25	30	35	40
287	convective	-37.2	-35.1	-31.8	-30.2	-29.4
	radiative	-36.9	-39.1	-40.1	-39.5	-39.0
307	convective	7.5	17.9	22.0	24.0	25.4
	radiative	18.7	21.8	23.2	24.1	24.8

The final variable examined was the level of absorbed blind flux due to solar heating of the blind. Figure 4-7 and Table 4-8 show the effect of blind flux on heat transfer rate from the glass. A higher blind flux resulted in greater blind slat temperatures, which caused both the convective and radiative flux to become more negative. Linear trendlines fit to each data set produced correlation coefficients in excess of 0.997. A more important result was found by examining the slope of each trendline. The convective heat flux changed from –0.06 to –0.10 W/m^2 per W/m^2 of absorbed flux between $T_p = 287$ K and 307 K respectively. Between these same temperatures, the radiative heat flux varied from –0.15 to –0.17 W/m^2 per W/m^2 of absorbed flux. These small changes in slope with changing temperature suggest that q_b and T_p were not strongly coupled.

Table 4-8: Numerically predicted average convective and radiative heat flux from the center-of-glass region of the plate as a function of absorbed solar energy in the shade. Results are for tests indicated in Table 4-2. Models executed at $\phi = 0°$, $b = 30$ mm, $\varepsilon_b = \varepsilon_p = 0.6$.

T_p (K)	Average flux (W/m^2)					
	q_b	0	30	60	90	120
287	convective	-25.9	-28.6	-31.8	-35.0	-38.4
	radiative	-29.1	-34.4	-40.1	-45.3	-49.3
307	convective	26.0	23.9	22.0	20.1	18.3
	radiative	32.6	27.8	23.2	18.9	14.6

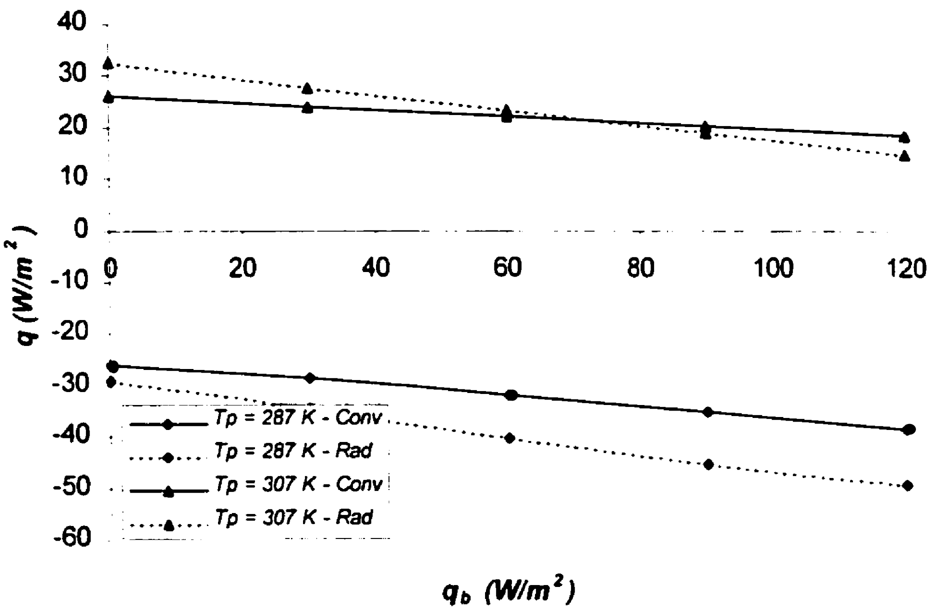

Figure 4-7: Average convective and radiative heat flux from the center-of-glass region of the plate for the absorbed solar flux as presented in Table 4-2. Models executed at $\phi = 0°$, b = 30 mm, $\varepsilon_b = \varepsilon_p = 0.6$.

4.2.3 Conclusions

Numerically determined values of radiative and convective heat transfer from an indoor window glazing with adjacent Venetian blind were obtained using a validated numerical model of the system. Results were obtained within the boundaries of an investigative parametric analysis. The following conclusions were drawn from these results, and can be applied within the range of the parameters investigated.

- Blind slat angle does not affect the average convective or radiative heat flux from the glass. Convective heat flux determined at different slat angles with equivalent tip-to-glass spacings (n = 18 mm), and radiative heat flux determined at different slat angles with equivalent nominal spacings (b = 30 mm), were similar.

- The average radiative and convective heat fluxes increased linearly with increased plate temperature. For the cases examined, radiative and convective fluxes were found to be of the same magnitude.
- The average convective flux from the plate was not significantly affected by either the plate or the blind emissivity, and may not be required in a predictive equation. The average radiative flux from the plate increased linearly in magnitude with increasing glass emissivity, and became more negative with increasing blind emissivity.
- Nominal blind distance had more influence on heat transfer as the blind got nearer to the glass surface. Average convective and radiative heat transfer rates were well represented by quadratic trendlines.
- Convective and radiative heat flux become increasingly negative with increased levels of absorbed blind flux, i.e., the flux from the blind to the plate increased in the direction of the plate. In addition, both fluxes changed linearly with q_b. More importantly, the rate of change of heat flux from the glass, with respect to changing glass temperature, suggests that these variables were not coupled.
- Local heat flux rates show that while the radiative flux was steady under all the conditions examined, the convective flux changed slightly with distance up the glass surface. These changes in convective flux have been accepted and noted as a limitation of this analysis.

While the present analysis has shown the effect of model parameters, it does not provide comprehensive information concerning parameter interactions. Inferences can be made, however, concerning the glass temperature/slat angle and glass temperature/blind flux interactions. A full factorial parametric will be required to assess those interactions.

4.3 Three-Level Parametric Series

4.3.1 Procedure

Heat flux rates at the plate were determined for conditions dictated by a three-level factorial design (Montgomery and Runger 1999). That design was required because the analysis performed in the previous section indicated that the effects of some variables on the results could be quadratic in nature. Under that method, each of the six investigative variables was represented at a high, low, and mid point value, where every possible combination was numerically modeled, producing 3^6 or 729 models. The factorial design allowed the first and second order effects of the variables to be estimated in addition to the effects of parameter interaction. Table 4-9 gives the parameters and values investigated. The full range of investigation for each variable was largely chosen from experience, and were thought to be representative of conditions that may occur in an actual window and shade installation.

Table 4-9: Numerical conditions of parametric series.

ϕ (deg)	b (mm)	T_p (K)	ε_b	ε_p	q_b (W/m^2)
-45	20	283	0.30	0.30[c]	25
0	30	297[a]	0.60	0.57	75
45	40	311[b]	0.90	0.84[d]	125[e]

[a]ambient temperature; [b]near experimentally observed high temperature; [c]emissivity of retrofit coating; [d]glass emissivity; [e]predicted high absorption level

The analysis was performed using the numerical model described in Chapter 2. Fluid properties were evaluated at an estimated film temperature of 300 K (i.e., constant Ra_l) and were taken from Touloukian et al. (1970a, 1970b, 1975). Fluid properties and miscellaneous model parameters are given in Table 4-3. The effect of using an estimated film temperature was examined after the numerical models were completed. The case of ϕ = 0 deg, b = 20 mm, T_p = 283 K, ε_b = 0.60, ε_p = 0.57, and q_b = 25 W/m^2 was found to have the lowest average fluid temperature at 295 K. The average flux rate obtained numerically changed by only 1.2% when using fluid properties determined at this temperature.

To fit the data, an equation was chosen which includes all linear and quadratic effects and two factor interactions. Third order terms were neglected. Since that equation contained 28 terms, the method of analysis will be described using a representative 3^2 data set with 6 terms, e.g.,

$$\hat{Y} = \hat{\beta}_o + \hat{\beta}_1 X_1 + \hat{\beta}_{1\_1} X_1^2 + \hat{\beta}_2 X_2 + \hat{\beta}_{2\_2} X_2^2 + \hat{\beta}_{1\_2} X_1 X_2 \qquad (4.9)$$

where $\hat{Y}$ and $\hat{\beta}$ are the predicted response and estimated parameter respectively. X represents each variable, in coded form, where

$$X = \frac{X_{uncoded} - X_{average}}{0.5 X_{range}} \qquad (4.10)$$

where X would normally be 1, 0, or -1.

For the above design, there would be 3^2 or 9 data points and 6 model parameters. The design matrixes X, β, and Y are therefore

$$
\begin{array}{ccc}
\begin{array}{cccccc} X_o & X_1 & X_2 & X_{1\_1} & X_{1\_2} & X_{2\_2} \end{array} & \beta & Y \\
\left|\begin{array}{cccccc}
1 & 1 & 1 & 1 & 1 & 1 \\
1 & 1 & 0 & 1 & 0 & 0 \\
1 & 1 & -1 & 1 & -1 & 1 \\
1 & 0 & 1 & 0 & 0 & 1 \\
1 & 0 & 0 & 0 & 0 & 0 \\
1 & 0 & -1 & 0 & 0 & 1 \\
1 & -1 & 1 & 1 & -1 & 1 \\
1 & -1 & 0 & 1 & 0 & 0 \\
1 & -1 & -1 & 1 & 1 & 1
\end{array}\right| \bullet
&
\left|\begin{array}{c}
\beta_o \\ \beta_1 \\ \beta_2 \\ \beta_{1\_1} \\ \beta_{1\_2} \\ \beta_{2\_2}
\end{array}\right| =
&
\left|\begin{array}{c}
Y_1 \\ Y_2 \\ Y_3 \\ Y_4 \\ Y_5 \\ Y_6 \\ Y_7 \\ Y_8 \\ Y_9
\end{array}\right|
\end{array}
$$

Data were fit using the sum of squared residuals, and by making the following assumptions:

- random noise components were independent for each variable;
- explanatory variables were known exactly;
- variance was constant over entire region; and
- the equation was an adequate representation of the data.

The first three assumptions could be made with certainty because the data came from a numerical model of the system. The final assumption was supported by the results of the investigative parametric presented in the previous sections, and could be confirmed after the analysis using quality of fit indicators.

The least squares parameter estimates are determined using matrix operation

$$\hat{\beta} = \left(X^T X\right)^{-1} X^T Y \tag{4.11}$$

For the data sets, the full model fit and the uncertainty of the parameters were examined. Parameters which could statistically be zero were removed, and the model was refit.

To determine the confidence intervals for parameter estimates, it was necessary to form the covariance matrix, Σ,

$$\Sigma = \hat{\sigma}^2 \left(X^T X\right)^{-1} \tag{4.12}$$

where the diagonal elements indicated the variance of each of the parameters, and the off-diagonal elements indicated covariance between parameters. In this case, there was no measure of pure error variance, $\hat{\sigma}$. Instead, variance was estimated by the sum of squared errors

$$\hat{\sigma}^2 \approx \frac{\sum (y - \hat{y})^2}{N - P} \tag{4.13}$$

where N is the number of test runs (728), P is the number of parameters, and N - P is the number of degrees of freedom of the variance estimate. y and $\hat{y}$ are the measured and predicted y parameters respectively. The confidence intervals for each parameter estimate was formed using the equation

$$\hat{\beta}_i \pm t_{N-P,0.005} \sqrt{Var(\hat{\beta}_i)} \tag{4.14}$$

where $t_{N-P,0.005}$ was the t-statistic with N-P degrees of freedom and 99% confidence, and was taken from a t-distribution table, and $Var(\beta_i)$ was the diagonal element of the covariance matrix taken from row/column i. Any of the intervals which could statistically be zero, were considered insignificant. The parameter estimates were checked each time because the estimate of pure error variance changed with each refit of the data. Variables showing significance after one iteration, were often found to be insignificant in the next.

Three forms of the coded model were examined. The first included the variable ϕ or $\sin\phi$ (in coded form, these variables are identical). This made each blind angle distinct within the model. The second included the blind angle in the form $\cos\phi$. In this form, blind slat angles of -45° and 45° were identical. Previous examinations have suggested that this was the best form for the radiation model. It should be noted that because $\cos\phi$ cannot be negative in the range examined, the $\cos\phi$ and $\cos^2\phi$ columns of the X matrix were identical, and consequently one had to be removed. The parameter associated with the remaining column was aliased, meaning that it included the effects of both terms. The final form of the model was formulated in terms of the tip spacing ($n = b - w \cdot (\cos\phi)/2$). Previous examinations suggested that this was the best form in the convection model.

To quantitatively test the quality of the fit, the *Mean Square Ratio* test was used. This test is appropriate for cases where no measure or estimate of pure error variance is available. For 99% confidence in the resulting data fit, if

$$\frac{MSR}{MSE} = \frac{\sum(\hat{y}-\bar{y})^2/(P-1)}{\sum(y-\hat{y})^2/(N-P)} = \frac{\left(\sum(y-\bar{y})^2 - \sum(y-\hat{y})^2\right)/(P-1)}{\sum(y-\hat{y})^2/(N-P)} > F_{P-1,N-P,0.01} \quad (4.15)$$

then there is no evidence of lack of fit. Here, *MSR* is the *Mean Square Regression* and *MSE* is the *Mean Square Error*. F is the F-statistic with P-1 and N-P degrees of freedom in the numerator and denominator respectively, and 0.01 denoted 99% confidence. $\bar{y}$ is the average measured value of y.

The adjusted R^2 coefficient may also be considered.

$$R^2_{adj} = 1 - \frac{MSE}{TSS/(N-1)} = 1 - \frac{\sum(y-\hat{y})^2/(N-P)}{\sum(y-\bar{y})^2/(N-1)} \quad (4.16)$$

where *TSS* is the *Total Sum of Squares*. An R^2_{adj} value near 1 represents an acceptable fit.

Finally, a graphical analysis of the data aided in determining the quality of the fit. Residuals were examined with respect to predicted response, and the explanatory variables. While statistical analyses of this sort often include an analysis of i^{th} vs $i^{th}+1$ residuals, and residuals verses sampling order, the fact that the data was obtained numerically made this unnecessary. Individual results could not have been influenced by the order of numerical model execution.

4.3.2 Results and Discussion

The quantity of data required for the statistical analysis prevented any convenient method of presenting the individual results of the parametric series, or the results of each data fit. Instead, the quality of fit and number of parameters are presented in Table 4-10. The estimated parameters for the best data fits are presented in Table 4-11, where the fit equation can be produced by multiplying each parameter by the associated variable presented in the left-most column of the table. Figure 4-8 presents plots of predicted response and residuals verses numerically obtained data. A complete summary of the data and individual fits are presented in Appendix D.

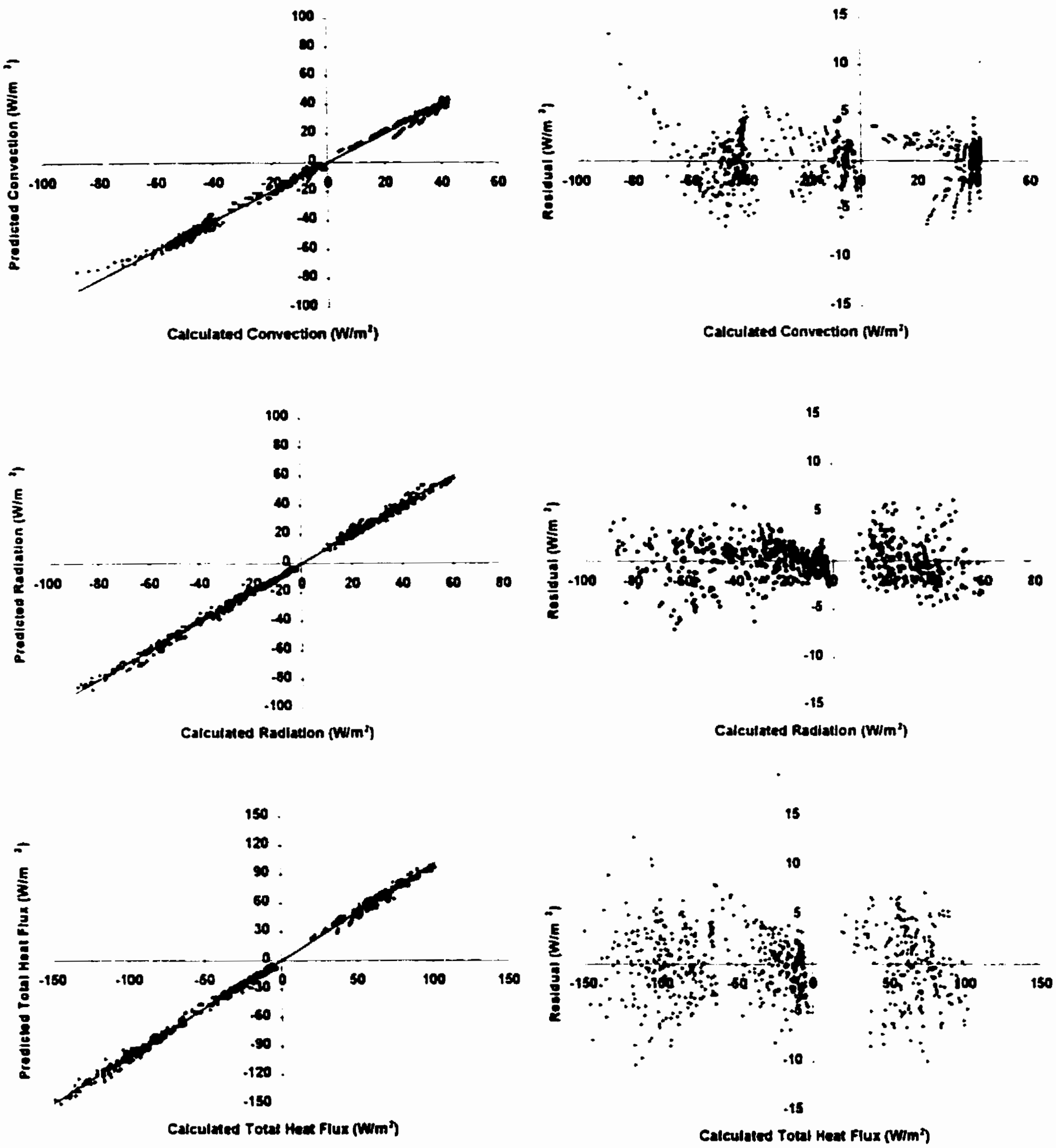

Figure 4-8: Predicted and residuals verses modeled convective, radiative, and total heat flux.

Table 4-10: Relative quality of statistical data fits.

Treatment of b and ϕ	Radiative		Convective	
	Terms	$\bar{\sigma}$ (W/m^2)	*Terms*	$\bar{\sigma}$ (W/m^2)
b and ϕ, or b and $sin\phi$	19	2.27	18	2.59
b and $cos\phi$	19	2.04	18	2.50
$n = (b\text{-}wcos\phi/2)$	17	2.48	15	2.51

Table 4-11: Estimated model parameters and quality of fit indicators for parametric case using cosϕ. Parameters are presented in uncoded form. 99% confidence interval of parameters are provided. Note that b is in mm, T is in °C.

	Convection (W/m^2)	Radiation (W/m^2)	Total Flux (W/m^2)
Constant	-77.761 ± 1.634	29.822 ± 9.574	-47.940 ± 9.712
b	1.309 ± 0.228	-0.434 ± 0.132	0.876 ± 0.263
T_{gi}	2.178 ± 0.157	-1.811 ± 0.128	0.367 ± 0.202
ε_b	16.170 ± 6.435	-15.422 ± 9.892	[a]0.748 ± 11.801
ε_{gi}	5.083 ± 2.271	-96.784 ± 7.998	-91.701 ± 8.315
q_b	-0.339 ± 0.004	-0.032 ± 0.047	-0.370 ± 0.047
$cos\phi$	-17.337 ± 11.461	-13.485 ± 1.550	-30.822 ± 11.521
b^2	-0.034 ± 0.005		-0.034 ± 0.005
bT_{gi}	0.012 ± 0.003	0.012 ± 0.002	0.024 ± 0.003
$b\varepsilon_b$	-0.393 ± 0.119		-0.393 ± 0.119
$b\varepsilon_{gi}$		0.228 ± 0.108	0.228 ± 0.108
bq_b	0.009 ± 0.001	0.002 ± 0.001	0.011 ± 0.001
$bcos\phi$	0.810 ± 0.211		0.810 ± 0.211
$T_{gi}{}^2$	0.014 ± 0.003	0.019 ± 0.002	0.033 ± 0.003
$T_{gi}\, \varepsilon_b$	-0.182 ± 0.085	0.563 ± 0.070	0.381 ± 0.110
$T_{gi}\, \varepsilon_p$	-0.212 ± 0.095	4.183 ± 0.077	3.971 ± 0.122
$T_{gi}\, q_b$	0.002 ± 0.001	0.001 ± 0.000	0.003 ± 0.001
$T_{gi}\, cos\phi$	-0.254 ± 0.151	0.654 ± 0.123	0.400 ± 0.195
$\varepsilon_b{}^2$		8.689 ± 4.587	8.689 ± 4.587
$\varepsilon_b\varepsilon_{gi}$		-13.458 ± 3.604	-13.458 ± 3.604
$\varepsilon_b q_b$	0.056 ± 0.024	-0.111 ± 0.019	-0.055 ± 0.031
$\varepsilon_b cos\phi$			
$\varepsilon_{gi}{}^2$			
$\varepsilon_{gi}\, q_b$		-0.221 ± 0.022	-0.221 ± 0.022
$\varepsilon_{gi}\, cos\phi$			
$q_b{}^2$			
$q_b cos\phi$	-0.160 ± 0.042		-0.160 ± 0.042
σ	2.50	2.04	3.43
$MSR/MSE > F_{P-1,N-P,0.01}$	8242>1.98 ∴ no evidence of lack of fit	11469>1.94 ∴ no evidence of lack of fit	12848>1.84 ∴ no evidence of lack of fit
R^2	0.995 ∴ strong fit	0.996 ∴ strong fit	0.997 ∴ strong fit

[a]upon combination, blind emissivity statistically becomes unimportant. As a significant term in both the radiation and conduction portions of heat transfer, however, the term will be retained.

The results of Section 4.2 and previous investigations (Machin 1997, Phillips 1999) suggested that convective heat transfer from the interior glazing was more strongly influenced by tip spacing (*n*) as opposed to nominal spacing (*b*). When considering radiation, treating -45 and 45 degree slat angles as identical situations (using *cosϕ*) produced a better data fit than those produced by considering each slat angle independently (using *ϕ* of *sinϕ*) or by considering the blind tip spacing (*n*). When considering convection, an excellent fit was produced by combining the nominal spacing and slat angle to obtain the louver tip spacing (*n*). The fit produced by considering *cosϕ* and *b*, however, was even better. This result allows the two flux rates to be combined in a relatively simple manner.

The final equations presented in Table 4-11 can be compared to the results of the investigative parametric. Both studies indicated that the quadratic effects of blind emissivity, glass emissivity, and blind flux were unimportant when considering convection, and the quadratic effects of plate emissivity and blind flux were unimportant when considering radiation. By comparison, the results of the full and investigative parametric studies disagree on a number of points. The investigative parametric incorrectly indicated that plate and blind emissivity and the quadratic effects of temperature were not important when considering convection, and the quadratic effect of temperature and the temperature/blind flux interaction were not important when considering radiation. Additionally, that parametric analysis mistakenly indicated that the blind spacing was quadratic in nature when considering radiation. These differences can be explained. The previous work never considered parameter interaction, or the expanded range of possible cases. For example, although the results from the investigative analysis suggest that emissivity of the blind and shade did not seem important in calculating convection, only a limited number of cases were examined, and parameter interaction could not be examined using this technique. Consequently, these effects were not observed within the investigative range. In defense of the exclusion of b^2 from the radiation equation, an anomaly may have been seen in the previous investigation which is not normally present.

The quality of the data fit presented in Table 4-11 is presented in Figs. 4-8 and 4-9. Figure 4-8 presents the predicted values and residuals verses modeled results for convection, radiation, and total heat flux. The quality of fit in each case was qualitatively and quantitatively excellent. R^2_{adj} and MSR tests showed good quality of fit and no evidence of lack of fit respectively. It was seen, however, that some slight trends were missed in the convective heat transfer model. The curvature seen at the far left of that fit is most noticeable in Fig. 4-8. Those data points, however, represent the onset of unsteady flow (and the limit of model capabilities). Each of these points occurs at the high blind flux rate, low glass temperature, and low emissivity on the blind or glass. Figure 4-9 presents the residuals verses the explanatory variables for the total heat flux. No evidence of missed trends were evident from those plots.

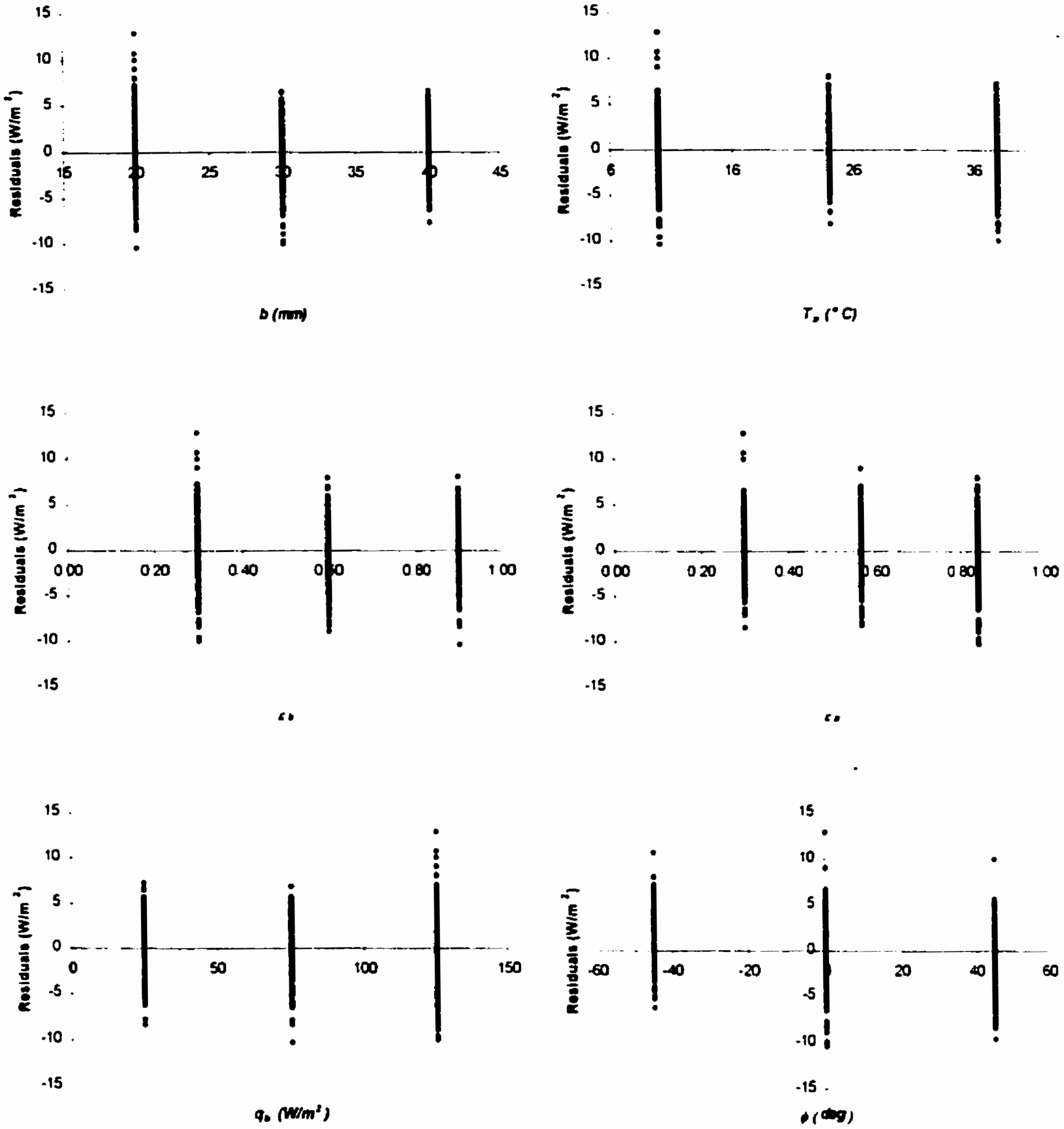

Figure 4-9: Residuals verses model parameters.

While the equations presented are suitable for use in software development, the size of the equations and data required as input prevent them from being easily used. As such, the data has been presented in tabular format by making a number of assumptions about the range of data likely to be encountered. White and off-white blind slat samples were tested at the University of Waterloo using a Gier Dunkle Infrared Reflectometer, and were found to have thermal emissivities of 0.77 and 0.75 respectively (Wright 1997). It was observed that blinds with similar coatings (regardless of color) would have similar emissivities in the thermal range. Additionally, it was assumed that the inner glazing surface would not have any special coatings, and the emissivity of window glass could be used. Therefore, ε_b and ε_{gi} were set as 0.76 and 0.84 respectively. Combining these values with the equations presented in Table 4-11 gives a reduced equation which is presented in Table 4-12. Table 4-13 gives the same data in tabular format, where the plate temperature T_p now becomes the inner glass temperature T_{gi} and is quoted relative to the ambient temperature, T_i. While values were determined for $T_i = 297$ K, analysis using different room temperatures are possible. Quoting the glass temperature relative to the ambient will not affect the calculated convection, and radiation will not be significantly affected if the room temperature does not change drastically from $T_i = 297$ K. Likewise, the plate emissivity ε_p, becomes ε_{gi}. The results of Ye (1997) and Machin (1997) showed that at distance, the nominal spacing, b, ceases to have an effect. From their analysis, this distance was approximately 30 mm. Analysis indicates, however, that this distance would be dependent on a particular set of conditions. Until this limit can be established, analysis of systems where $b > 40$ mm should be taken at $b = 40$ mm.

Table 4-12: Estimated model parameters when blind and glass emissivity are 0.76 and 0.84 respectively. Parameters are presented in uncoded form. 99% confidence interval of parameters are provided. Note that *b* is in mm, *T* is in °C.

	Convection (W/m^2)	Radiation (W/m^2)	Total Flux (W/m^2)
Constant	-61.202 ± 7.017	-66.770 ± 16.956	-127.972 ± 18.351
b	1.010 ± 0.257	-0.242 ± 0.170	0.768 ± 0.308
T_{gi}	1.862 ± 0.202	2.131 ± 0.165	3.993 ± 0.261
q_b	-0.296 ± 0.024	-0.302 ± 0.055	-0.598 ± 0.060
$\cos\phi$	-17.337 ± 11.461	-13.485 ± 1.550	-30.822 ± 11.521
b^2	-0.034 ± 0.005		-0.034 ± 0.005
bT_{gi}	0.012 ± 0.003	0.012 ± 0.002	0.024 ± 0.003
bq_b	0.009 ± 0.001	0.002 ± 0.001	0.011 ± 0.001
$b\cos\phi$	0.810 ± 0.211		0.810 ± 0.211
T_{gi}^2	0.014 ± 0.003	0.019 ± 0.002	0.033 ± 0.003
$T_{gi}q_b$	0.002 ± 0.001	0.001 ± 0.000	0.003 ± 0.001
$T_{gi}\cos\phi$	-0.254 ± 0.151	0.654 ± 0.123	0.400 ± 0.195
q_b^2			
$q_b\cos\phi$	-0.160 ± 0.042		-0.160 ± 0.042

4.3.3 Conclusions

Equations for predicting the radiative, convective, and total heat transfer from the interior surface of a window with an attached horizontal Venetian blind have been obtained. While some of the predictions presented in the investigative parametric were proven, others were not. That study, however, considered only a limited number of cases and never considered parameter interaction. Contrary to the prediction that convective heat transfer was dependent on blind tip distance, these results showed that nominal spacing provided a better quality data fit. This was a fortunate result in that it allowed easy combination of the radiative and convective predictor equations. While the resulting equations are complex, qualitative and quantitative indicators show that the data fit is very good. Based on a number of assumptions, an equation and table of flux from the interior glazing has been presented for simplified calculation purposes.

Table 4-13: Total heat transfer at indoor window surface. Positive values are towards room. Blind and glass emissivity are 0.76 and 0.84 respectively. Values determined at $T_i = 297$ K. If $b > 40$ mm then use $b = 40$ mm.

	ϕ	-45° / 45°			0°		
q_b (W/m^2)	T_{gi}-T_i (K)	b = 20 mm	b = 30 mm	b => 40 mm	b = 20 mm	b = 30 mm	b =>40 mm
0	-15	-91.0	-92.3	-100.4	-94.2	-93.2	-98.9
	-10	-63.4	-63.5	-70.4	-66.0	-63.8	-68.3
	-5	-34.1	-33.0	-38.7	-36.2	-32.7	-36.0
	0	-3.2	-0.9	-5.4	-4.6	0.0	-2.1
	5	29.4	32.9	29.6	28.5	34.4	33.5
	10	63.7	68.3	66.3	63.4	70.4	70.7
	15	99.6	105.5	104.6	99.9	108.1	109.6
25	-15	-102.4	-100.9	-106.2	-106.8	-102.9	-105.8
	-10	-74.5	-71.8	-75.8	-78.3	-73.2	-74.9
	-5	-44.8	-40.9	-43.8	-48.1	-41.8	-42.3
	0	-13.6	-8.4	-10.1	-16.2	-8.7	-8.0
	5	19.4	25.7	25.3	17.3	26.0	28.0
	10	54.0	61.5	62.3	52.5	62.4	65.5
	15	90.3	99.0	100.9	89.4	100.5	104.8
50	-15	-113.9	-109.5	-111.9	-119.4	-112.7	-112.8
	-10	-85.6	-80.0	-81.2	-90.5	-82.6	-81.5
	-5	-55.6	-48.8	-48.8	-60.0	-50.9	-48.5
	0	-23.9	-16.0	-14.8	-27.8	-17.4	-13.9
	5	9.4	18.5	20.9	6.1	17.7	22.4
	10	44.3	54.7	58.3	41.7	54.4	60.4
	15	80.9	92.5	97.3	78.9	92.8	100.0
75	-15	-125.3	-118.1	-117.7	-132.1	-122.5	-119.7
	-10	-96.7	-88.3	-86.6	-102.8	-92.1	-88.1
	-5	-66.3	-56.7	-53.9	-71.9	-59.9	-54.7
	0	-34.3	-23.5	-19.5	-39.3	-26.1	-19.7
	5	-0.7	11.3	16.6	-5.1	9.3	16.9
	10	34.6	47.8	54.3	30.8	46.4	55.2
	15	71.6	86.0	93.7	68.4	85.2	95.2
100	-15	-136.8	-126.8	-123.5	-144.7	-132.3	-126.7
	-10	-107.8	-96.5	-92.1	-115.1	-101.5	-94.6
	-5	-77.1	-64.6	-59.0	-83.8	-69.0	-61.0
	0	-44.7	-31.1	-24.2	-50.9	-34.9	-25.6
	5	-10.7	4.1	12.2	-16.3	0.9	11.4
	10	25.0	41.0	50.3	20.0	38.4	50.0
	15	62.3	79.5	90.0	57.9	77.5	90.4
125	-15	-148.2	-135.4	-129.3	-157.3	-142.1	-133.6
	-10	-118.9	-104.8	-97.5	-127.3	-110.9	-101.2
	-5	-87.8	-72.5	-64.0	-95.7	-78.1	-67.2
	0	-55.1	-38.6	-28.9	-62.4	-43.6	-31.5
	5	-20.7	-3.1	7.8	-27.5	-7.4	5.9
	10	15.3	34.2	46.3	9.2	30.4	44.9
	15	53.0	73.1	86.4	47.4	69.9	85.6
150	-15	-159.7	-144.0	-135.1	-169.9	-151.9	-140.6
	-10	-130.0	-113.1	-102.9	-139.6	-120.3	-107.8
	-5	-98.6	-80.4	-69.1	-107.6	-87.2	-73.4
	0	-65.5	-46.2	-33.6	-74.0	-52.3	-37.4
	5	-30.8	-10.3	3.5	-38.7	-15.8	0.3
	10	5.6	27.3	42.3	-1.7	22.4	39.7
	15	43.7	66.6	82.7	36.9	62.2	80.7

CHAPTER 5
DISCUSSION OF RESULTS

5.1 Introduction

The current Chapter presents a discussion of the numerical and experimental data obtained during the course of the present investigation. Discussion previously presented in Chapters 3 and 4 has been revisited as dictated by the School of Graduate Studies. Additional information and discussion concerning this project has also been presented.

5.2 Summary of Previous Discussion

5.2.1 Validation

Experimental validation of the numerical model using a Mach-Zehnder Interferometer was successful. The experimental data correlated well with numerical results, and for the majority of cases, the error was within the uncertainty of the experimentally determined results. More importantly, the instantaneous heat flux. agreed with numerically obtained data both in trend and magnitude. Local convective and radiative heat flux rates were presented in Figs. 3-5 to 3-12, and average heat flux rates were presented in Table 3-3. Experimentally obtained slat temperatures and isotherms were also in close agreement with experimentally obtained results. This gives additional confidence in the numerical results. A comparison of numerically and experimentally obtained isotherms was given in Appendix C, and a comparison of predicted and measured blind slat temperatures was presented in Table 3-4.

While the quality of the experimental/numerical comparison is good, a number of discrepancies are evident in the experimental data. These problems were identified and discussed in Chapter 3, and include aspects of modeled verses experimental inlet and outlet conditions, as well as deficiencies in the experimental method. Those discrepancies are summarized as follows:

- Using the wedge fringe method of analyzing interferometric data, the fringe angle can only be measured on the fringes themselves. Consequently, peaks demonstrated by the numerical results may have been missed, resulting in an underprediction of the average heat flux during the experimental analysis.
- In the experiment, flow was entrained around the sharp edge of the plate, while in the numerical model, an adiabatic wall continues above and below the plate. While this difference has no identifiable affect on cases where the plate was warmer than the ambient, it did have an affect on the cases where the plate was cooler than ambient. During the experiment, air flowing downward from the cold plate was entrained around the sharp lead edge of the plate, while hot air from the blind rose and was guided away from the plate by momentum of the air flow which has developed on the room-side of the blind. This allowed the boundary layer on the plate to grow unhindered to the topmost slat as if no blind was present. By contrast, because the numerical model assumed that unheated wall continued above the heated plate, flow from the blind was pulled back towards the wall by the downward flow entrained by the cold plate, which increased the air temperature and heat flux in that area.
- Due to optical limitations, the experimental data were obtained from three individual photographs. As a result of environmental changes occuring between the times at

which these photos were taken, some step discontinuities were evident in all of the data. Due to the difficulty in controlling environmental parameters to the tolerance needed to avoid this problem, over the duration of an experiment, it was decided to simply recognize the problem as a limitation of the experimental procedure.

Although these discrepancies have been identified, they are not considered a weakness of the numerical model. In fact, the continuing unheated portion of wall present in the numerical analysis, is closer to a realistic window situation than the experimental setup. More importantly, if the blind can be shown to suppress the growth of convective heat transfer from the plate surface, the center portion of the model can then be used to determine the center-of-glass heat transfer rate for other window sizes, and the top and bottom portions of the model will be disregarded.

Other information was obtained through observation of the numerically obtained convective and radiative heat transfer rates presented in Figs. 3-5 through 3-12. The trends include:

- The convective and radiative flux for the cold plate was consistently larger than that for the warm plate when considering cases with identical geometry. In all cases, the average heat transfer occurs in the direction of the plate surface. This is a significant point. Concievably, heat transfer at the window surface may occur when no air-to-air temperature difference exists due to heating of the shade layer. Therefore, a modified interior heat transfer coefficient may be indeterminant. It does not, however, prevent analysis of the heat transfer at the inner glass, or analysis of a fenestration from that perspective.

- A significant result is apparent when considering the effects of system geometry. An increase in the local convective flux occured when the leading edge of the slats and the plate were close together. When the slat leading edge was furthest from the plate, the blind angle had little effect on the convective heat flux. Considering radiative heat flux, when the slat leading edge was closest to the plate, peaks in the local heat transfer rate were sharper and more distinct than in the other cases. In that case, a decrease in the local radiative flux occured when the leading edge and plate were close together. As the blind is moved away from the plate. the "view" from the plate became largely independent of vertical location and slat angle. There was little difference between the further spaced shades despite differing slat angles.
- If the first five slats from the bottom and top of each case are disregarded, q_C and q_R did not change significantly with location. This result supports the use of the model for predicting center-of-glass heat transfer in larger window and shade systems. Even though the cases represent extreme conditions, however, increases in convective and radiative flux were not significant and should not prevent a center-of-glass analysis of the data.

5.2.2 Parametric Analysis

The investigative parametric analysis was designed to provide important information necessary for the development of a full numerical investigation of the system. In that regard, it was successful. An example of local convective and radiative heat flux rates is presented in Appendix D where slat positions are shown in gray, and positive flux is from the plate. The results of the parametrics have been summarized in Figs. 4-2 through 4-7 and Tables 4-4 through 4-8.

Local radiative heat flux will be seen not to change with vertical location on the glass, indicating insignificant changes in blind slat temperature. Local convective heat transfer rates do change with distance up the glass, however, indicating boundary layer growth. The magnitude of this change increased as the plate temperature became further from the ambient temperature. While this suggests that window height should be included in the analysis, software limitations prevent expansion of the model at this time. Significant changes in local convective flux only occured at extreme glass temperatures, and must be accepted as a limitation of the analysis.

The effect of glass temperature and slat angle on the average convective and radiative flux can be seen from the results given in Figs. 4-2 and 4-3 and Table 4-4. Both radiative and convective heat transfer rates demonstrate a linear relationship with temperature whereby the average flux became more positive with increasing glass temperature. A more significant result was found by examining the difference, or lack of difference, of calculated heat flux with differing blind slat angle. Tip spacing was more important than slat angle when determining convective heat transfer from the glass, while the radiative heat transfer rate is more dependent on nominal spacing than blind slat angle. It is also interesting to note that for the cases chosen, average radiative and convective flux are of the same magnitude.

The effect of blind emissivity on convective and radiative heat transfer from the glass can be seen in Fig. 4-4 and Table 4-5. The magnitude of change in convective heat transfer over the range of blind emissivities examined was not significant. It may be possible to accurately predict convective heat transfer without using the blind emissivity as input. When considering the radiative heat flux, changes in slope are more significant than seen in the convective data. Radiative flux from the glass becomes more negative with increasing blind emissivity, i.e., increased radiative flux from the blind to the glass. Quadratic fits of the data produce excellent correlation.

The effect of glass emissivity can be seen from the results given in Fig. 4-5 and Table 4-6. Convective heat flux from the glass did not seem to be influenced by the glass emissivity. As with the blind emissivity, it may be possible to ignore glass emissivity when predicting convective heat transfer. By contrast, the radiative heat transfer changed significantly with glass emissivity. Increasing glass emissivity increased the magnitude of flux emitted or absorbed at the plate surface. Both cases showed excellent linearity.

The effect of nominal blind spacing can be seen from the results given in Fig. 4-6 and Table 4-7. As the blind gets closer to the glass, an increased effect was clearly visible. When considering convection, closer spacing caused a more negative shift in the direction of heat flux. Heat lost from a warmer than ambient plate was reduced, while heat gained by a colder than ambient plate increased. Changes in radiative heat flux were less pronounced with blind proximity, although a slight decrease in heat transfer occurs as the plate was moved closer to the glass. Such a change is most likely caused by an increase in the glass-to-ambient viewfactor and an associated decrease in the glass-to-blind viewfactor. Because the ambient temperature was below the plate temperature, radiative exchange was reduced. Quadratic data fits produce good correlation for both cases.

The final variable examined was the level of absorbed blind flux. Fig. 4-7 and Table 4-8 show the effect of blind flux on heat transfer rate from the glass. Higher blind flux resulted in larger blind slat temperatures, which causes both the convective and radiative flux to become more negative. A more important result was found by examining the slope of each trend line. Small changes of slope with changing temperature suggest that that q_b and T_p were not strongly coupled.

Chapter 4 also presented a full three-level factorial examination of the system with respect to six variables: i.e., blind position and slat angle, glass temperature, blind and glass emissivity, and amount of energy absorbed by the blind. Individual results and the statistical analysis of the data have been presented in Appendix D.

The results given in the first section of Chapter 4 and previous investigations (Machin 1997, Phillips 1999) have suggested that convective heat transfer from the interior glazing is more strongly influenced by tip spacing (n) than by the blind nominal spacing (b). When considering radiation, treating -45 and 45 degree slat angles as identical situations (using $cos\phi$) produced a better data fit than those produced by considering each slat angle independently (using ϕ of $sin\phi$) or by considering the blind tip spacing (n). When considering convection, an excellent fit was produced by combining the nominal spacing and slat angle to obtain the louver tip spacing (n). The fit produced by considering $cos\phi$ and b, however, was slightly better. This allows the two flux rates to be combined in a relatively simple manner.

The equation parameters presented in Table 4-11 were compared to the results of the investigative parametric. While both studies agreed about the effects of a number of the variables on the radiative and convective heat transfer, there were some contradictory results. These differences can be explained. The investigative parametric never considered parameter interaction, or the expanded range of possible cases. For example, although the results from the investigative analysis suggest that the emissivity of the blind and shade did not seem important in calculating convection, only a limited number of cases were examined, and parameter interaction could not be evaluated.

The quality of the data fit presented in Table 4-10 can be examined in Figs. 4-8 and 4-9. Figure 4-8 presents the predicted values and residuals verses modelled results for convection, radiation, and total heat flux. The quality of fit in each case were qualitatively and quantitatively excellent. It was observed, however, that some slight trends were being missed in the convective heat transfer model. Those data points represent limits imposed by the onset of unsteady flow (and the numerical model capabilities). These cases occurred at the high blind flux rate, low glass temperature, and low emissivity on the blind or glass. Figure 4-9 presents the residuals verses the explanatory variables for the total heat flux. No evidence of missed trends is evident from those plots.

While the equations presented are suitable for use in software development, the size of the equations and data required as input prevent them from being easily used. As such, the data has been presented in tabular format by making a number of assumptions about the range of data likely to be encountered. Those users are not likely to know the blind emissivity, and are likely to be dealing with uncoated glass on the interior surface. It is also expected that blinds with similar coatings (regardless of color) would have similar emissivities. Therefore, ε_b and ε_{gi} were set as 0.76 and 0.84 respectively.

5.3 *U*-Factor and *SHGC* Prediction

Although the calculation of *SHGC* and *U*-factor was the logical next step in the progression of this research, important parts of the analysis were still missing. A reliable method of predicting blind layer optical properties needed to be developed, and experimental data needed to be produced to provide a comprehensive basis for validating calculated values of *SHGC* and *U*-factor. A preliminary comparison, however, was possible. While a method of predicting layer specific optical properties was being produced at the University of Waterloo, the method of Parmelee et al. (1952, 1953b) was used in the interim. Additionally, calorimetric testing of a limited number of window and shade systems was performed. Calorimetric evaluation, however, requires days of testing to determine *U*-factor and *SHGC* for a single fenestration system. Factoring in equipment maintenance, down time, the short testing season, and inclement weather, only a limited data comparison with a predictor method based on this analysis was performed.

5.3.1 Procedure

Predictions of *SHG* performance for complex fenestration systems cannot be made using the method currently used in the ASHRAE HOF (2001). By that method, the system equations are solved iteratively with respect to layer specific temperatures. In an unshaded system, convection and radiation only occur with adjacent layers, and therefore the layer specific inward-flowing fraction for the outer and inner glazings can be determined using Eqs. (1.4) and (1.5). The interaction between the inner glazing, shade, and room is much more complex. As a result, the inward-flowing fraction for the shade cannot be solved directly.

Mathematically, however, the system could be solved using an assumption commonly made during calorimetric *SHGC* and *U*-value testing (Harrison and Barakat 1983). That is, it was assumed that the *SHGC* and *U*-factor are uncoupled, and the relation between the instantaneous efficiency, η, and $\Delta T_{i,o}/I$ was linear. Assuming no irradiation, I, will allow calculation of the *U*-factor. Similarly, no temperature gradient, $\Delta T_{i,o}$, will allow calculation of the *SHGC*. To illustrate this, a predictor method of determining *U*-factor and *SHGC* was developed.

5.3.1.1 *U*-Factor Calculation

To calculate the *U*-factor of a window and shade system it was necessary to iterate on the glass temperatures. To begin, the inner and outer glass temperatures must be assumed.

Based on these temperatures, it is possible to determine the inner, outer, and air space heat transfer coefficients. The air-space heat transfer coefficient was determined from Table 4 in Chapter 29 of the ASHRAE HOF (2001), while the external heat transfer coefficient was taken from experiments or ASHRAE standard design conditions (ASHRAE HOF 2001). The interior heat transfer coefficient was solved using the flux equation in Table 4-11, 4-12, or 4-13, using the interior glass temperature with q_b = 0 W/m^2. Therefore, the interior radiative and convective heat transfer coefficient, h_i became

$$h_i = \frac{q_i}{(T_{gi} - T_i)} \tag{5.1}$$

The system *U*-factor was then calculated using

$$U = \frac{1}{1/h_o + R_{go} + 1/h_s + R_{gi} + 1/h_i} \tag{5.2}$$

Because there was no solar flux, the heat flux at the indoor surface was also the heat flux through the window. In this case, for the whole window, the heat flux was

$$q_{fen} = U(T_o - T_i) \tag{5.3}$$

Comparing q_{fen} to q_i determines if another iteration was required.

If $q_{fen} \neq q_i$ then it was necessary to recalculate the glass temperatures. Therefore

$$T_{go} = T_o - \frac{q_{fen}}{h_o} \tag{5.4}$$

$$T_{gi} = T_i + \frac{q_{fen}}{h_i} \tag{5.5}$$

Using these new temperatures, the process was repeated until $q_{fen} = q_i$ and the predicted glass temperatures converged.

5.3.1.2 *SHGC* Calculation

To calculate the *SHGC* of a fenestration system, it was first necessary to estimate the absorption in the glasses and blind for a specified solar incidence angle. Using layer specific optical properties, estimated from Parmelee and Aubele (1952), an optical balance could be used to find the effective absorption of each layer (Farber et al. 1963). Considering one inter-reflection, for the exterior glass

$$\alpha_{go} = \alpha_1 + \frac{\tau_{go}\rho_3\alpha_2}{(1-\rho_2\rho_3)} + \tau_{go}\tau_{gi}^2\rho_5\alpha_2 \tag{5.6}$$

the interior glass was

$$\alpha_{gi} = \frac{\tau_{go}\alpha_3}{(1-\rho_2\rho_3)} + \tau_{go}\tau_{gi}\rho_5\alpha_4(1+\rho_4\rho_5+\tau_{gi}\rho_2) \tag{5.7}$$

and, the blind absorption was

$$\alpha_b = \alpha_5\tau_{go}\tau_{gi}(1+\rho_3\rho_2)(1+\rho_5\rho_4) \tag{5.8}$$

The solar radiation absorbed then depended on the direct and diffuse irradiation levels. Therefore

$$I\alpha_{go} = I_D\alpha_{go,D} + I_d\alpha_{go,d} \tag{5.9}$$

$$I\alpha_{gi} = I_D\alpha_{gi,D} + I_d\alpha_{gi,d} \tag{5.10}$$

$$I\alpha_b = I_D\alpha_{b,D} + I_d\alpha_{b,d} \tag{5.11}$$

To determine the solar heat gain coefficient, it was necessary to iterate based on the interior glass temperature. The interior heat transfer coefficient (q_i) was solved using the flux equation in Tables 4-11, 4-12, or 4-13, for a given blind position, angle, and emissivity, glass emissivity, absorbed solar flux ($q_b = I\alpha_b$), and estimated interior glass temperature.

By performing an energy balance at the interior glazing, the exterior glazing temperature could be estimated using

$$q_s = q_i - I\alpha_{gi} \tag{5.12}$$

$$T_{go} = T_{gi} + \frac{q_s}{h_s} \tag{5.13}$$

where the air-space heat transfer coefficient was determined from Table 4 in Chapter 29 of the ASHRAE HOF (2001).

It was now possible to calculate the flux at the outdoor glazing by two methods: by the energy balance, and by using the exterior air film coefficient as determined from experiments or ASHRAE design conditions (ASHRAE HOF 2001).

$$q_{oA} = q_s - I\alpha_{go} \tag{5.14}$$

$$q_{oB} = h_o\left(T_o - T_{go}\right) \tag{5.15}$$

Finally, the estimate of the interior glass temperature, and the calculation procedure, must be iterated until $q_{oA} = q_{oB}$.

Once convergence was obtained, the solar heat gain coefficient could be calculated by performing an energy balance on the outer glazing, and adding the transmitted portion of radiation.

$$N_{sys}\alpha = \frac{(q_o + \sum I\alpha)}{I_D + I_d} \tag{5.16}$$

$$\tau = \tau_o(\tau_i + \rho_3\rho_2\tau_i)(\tau_b + \rho_5\rho_4\tau_b) \tag{5.17}$$

Equation (5.17) was solved using both direct and diffuse properties. The solar heat gain coefficient was then

$$SHGC = \frac{\tau_D I_D + \tau_d I_d}{I_D + I_d} + N_{sys}\alpha \tag{5.18}$$

5.3.2 Results and Discussion

A comparison of calorimetric and numerically determined solar heat gain and *U*-factor data have been presented in Table 5-1. Details of experiments, calculations, and data used in producing these results have been included as Appendix E.

Table 5-1: Comparison of measured and predicted solar heat gain coefficients.

α_b	ϕ (deg)	ψ (deg)	*U* (W/m·K)	τ_{sys}	$N\alpha_{sys}$	Predicted *SHGC*	Measured *SHGC*
no blind	no blind	45	[a]2.87 [b](2.84)	0.66	0.07	[a]0.73	0.71±0.02
0.32	0	30	2.81	0.35	0.26	0.61	0.59±0.02
0.32	0	45	2.81	0.21	0.32	0.53	0.56±0.02
0.32	45	30	2.77	0.13	0.31	0.44	0.46±0.02
0.32	45	45	2.77	0.13	0.29	0.42	0.44±0.02
0.90	0	30	2.82	0.23	0.45	0.68	0.66±0.02
0.90	0	45	2.82	0.06	0.57	0.63	NA[c]
0.90	45	30	2.78	0.05	0.60	0.65	0.64±0.02
0.90	45	45	2.78	0.04	0.58	0.63	0.64±0.02

[a] results predicted using standard ASHRAE calculations (ASHRAE HOF 2001)

[b] U_{cog} as reported by CSA tests (CSA 1992)

[c] Test not performed

As seen in Table 5-1, for the cases examined, predicted and experimental values of *SHGC* show excellent agreement. As a worst case, the results differ by 3%. Experimental uncertainty was determined using the method presented by Harrison and Dubrous (1993), and is ±2% for each measurement. Considering the predicted values, a number of assumptions were made during the calculation which would affect the accuracy of the calculated *SHGC*. For example, while the direct/diffuse irradiation split was known, the ground/sky diffuse split was estimated. Additionally, blind layer properties were estimated. The magnitude of those errors are not quantified here.

The shade layer reduced the *SHGC* for all cases. Considering the blind with the lower absorptivity, the *SHGC* was reduced by 26% to 42% between 0° and 45° slat angles at 45° solar incidence. In this case, the reduction was due to the interception of directly transmitted solar radiation. Even so, the average reduction was 32%. When considering the more absorbing blind, however, the benefits are less pronounced than with the less absorbing blind. In all cases, the *SHGC* was only reduced between 7% and 15%, where again, the lower reductions due to better alignment of the solar incident and slat angles. While a highly absorbing shade layer does have some benefit, it does not efficiently limit the transmission of solar heat to the space.

Calorimetric data provided window *U*-factors, but in the absence of data needed to predict the *U*-factor of the frame and edge of glazing, the center of glass *U*-factors could not be determined. In relation to the glazing *U*-factor, however, the predicted glazing and shade *U*-factor is only slightly lower. While a reduction in *U*-factor is beneficial in both a heating and cooling situation, the reduction observed here was small. This result agrees with the results presented by Machin (1997) and Ye (1997).

The implications of these results for shade design and placement are dependent on the designer's intentions. To reduce solar heat gain successfully, a design must meet two criteria: it must intercept the majority of incident solar radiation without absorbing it, i.e., the blind should be closed and reflective. Most importantly, if a shade is to be effective, the majority of solar radiation has to be intercepted by the shade layer. To increase solar heat gains, it is best not to use a blind as the shade layer will reduce *SHG*. If we factor in other concerns, however, (i.e., privacy and aesthetics) a highly absorbing blind would be preferable. Improvements in *U*-factor are not significant enough to be important.

The methodology used provides an unskilled end user with the ability to quickly calculate the center-of-glass *SHGC* and *U*-factor for a window and Venetian blind combination. As an added benefit, a solution can be obtained by iterating on the interior glass temperature only. The same method could be incorporated into software such as VISION (Wright 1994). A more theory based final product would most likely be more practical for use in software routines. The full resistance network, such as the one presented in Fig. 1-1b, would provide increased model versatility and information. Radiative exchange between surfaces could be easily determined based on well established theory. An examination of convection from the glass and both sides of the shade as a function of blind temperature and geometry is all that is required. Unfortunately, the solution procedure would have to iterate on the inside glass, blind, and channel temperatures. Even then, methods may be required to ensure stability in the solution routine. An analysis of the full resistance network will be performed in the future.

CHAPTER 6
CONCLUSIONS AND RECOMMENDATIONS

6.1 Conclusions

A numerical model of an interior glazing and shade combination has been developed using commercial finite element software. The model includes radiative, convective, and conductive heat transfer. Experimentally determined natural convective and radiative heat transfer from a horizontal Venetian blind adjacent to an indoor window glazing has been obtained and used to validate the numerical model. Using the validated numerical model, convective and radiative heat transfer from a horizontal Venetian blind adjacent to an indoor window glazing has been obtained to examine the sensitivity of heat transfer from the plate surface to various system variables. This data was used to design a full three level parametric analysis of the system, and equations for predicting the radiative, convective, and total heat transfer from the interior surface of a window with an attached horizontal Venetian blind have been obtained. Conclusions drawn from the experimental and numerical analysis are as follows

i) With the exception of some easily explained departures between the experimental and numerical results, the local and average convective heat transfer coefficients agreed closely both in magnitude and trend. Experimentally and numerically obtained blind temperatures and isotherms were also found to be in close agreement.

ii) Further information was obtained from the validation data. That information is summarized as follows:

- Due to the hot shade layer, the direction of heat transfer at the window surface is not dictated by the air-to-air temperature difference. Consequently, a modified interior film coefficient could be indeterminate. Determining *SHGC* must be approached from a rate of heat transfer approach.
- The validity of a center-of-glass analysis was supported. Even under the extreme conditions chosen for the validation experiments and models. insignificant increases in convective and radiative heat transfer rates were observed.
- The validation data indicates that at larger distances, heat transfer between the shade and plate ceases to be strongly coupled with blind slat angle.

iii) The onset of unsteady flow was observed both experimentally and numerically. It occurred under situations of high blind temperature and low glass temperatures.

iv) The sensitivity of heat transfer from the glass surface to various system variables was examined. Local flux rates show that while radiative flux is steady under all the conditions examined, convective flux does change slightly with distance up the glass surface. These changes in convective flux have been accepted and noted as a limitation of the analysis.

v) The following trends were identified during the investigative parametric analysis:

- Blind slat angle does not affect the average convective or radiative heat flux from the glass. Convective heat flux determined at different slat angles with equivalent tip to glass spacings, and radiative heat flux determined at different slat angles with equivalent nominal spacings were not dissimilar.
- The average radiative and convective heat flux increased linearly with increased plate temperature. For the cases examined, radiative and convective fluxes were also of the same magnitude.
- The average convective flux from the plate was not significantly affected by either the plate or the blind emissivity, and may not be required in a predictive equation. The average radiative flux from the plate increased linearly in magnitude with increased glass emissivity, and became more negative with increased blind emissivity.
- Nominal blind distance had more influence on heat transfer as the blind got nearer to the glass surface. Average convective and radiative heat transfer rates were well represented by quadratic relations.
- Convective and radiative heat flux became increasingly negative with increased levels of absorbed blind flux. In addition, both fluxes changed linearly with q_b. More importantly, insignificant changes in the rate of change in flux from the glass with changing glass temperature suggest that that q_b and T_p were not strongly coupled.

vi) From a full three-level parametric analysis of the system, equations for predicting the radiative, convective, and total heat transfer from the interior surface of a window with an attached horizontal Venetian blind were obtained. While the resulting equations are complex, qualitative and quantitative indicators show that the data fit is very good.

vii) Some of the conclusions found in the investigative parametric were further supported by the three level parametric analysis, while others were not. That initial study, however, only considered a limited number of cases, and never addressed parameter interaction. Contrary to the prediction that convective heat transfer was dependant on blind tip distance, these results showed that nominal spacing provided a better quality data fit. This allowed easy combination of the radiative and convective predictor equations.

viii) The present analysis was focused on presenting a method of examining the solar and thermal performance of a window and shade system that could be used by a semi-skilled end-user. In that regard, the results of this analysis have proven to be successful. A method has been presented for predicting *SHGC* and *U*-factor in a window and shade combination. Predicted verses experimental data show excellent agreement.

iv) This thermal model of the window and shade interaction could be represented by a resistance network as shown in Fig. 1-1b. Such an analysis would provide additional data about the system, and would be more firmly based in traditional heat transfer theory. This procedure has the disadvantage of being more difficult to solve mathematically.

6.2 Recommendations

i) The onset of unsteady flow was observed both numerically and experimentally. This occurred under conditions of large and opposing convective flow, i.e., large blind heat flux, low blind emissivity, and cold plate temperatures. While the occurrence of these conditions would be rare, the actual model limits need to be further investigated.

ii) It is not known at what nominal spacing the blind ceases to have an influence the heat transfer through the window. In the current analysis it was assumed, based on evidence presented by Machin (1997) and Ye (1997), that the nominal spacing, *b*, ceases to have an effect at a distance of about 30 mm. Their conclusion, however, was taken from a nighttime case where the blind layer was not heated. Furthermore, that distance will be dependent on a particular set of conditions. Until this limit can be established, analysis of systems where $b > 40$mm should be taken at $b = 40$ mm, as that was the limit of the present investigation.

iii) The increase in radiative and convective heat flux with increased distance up the plate surface indicates that boundary layer changes are a function of plate height. While this investigation has determined that under the range of investigative parameters, these changes are not significant, the conditions under which convective changes become significant, need to be determined.

iv) Due to the size of the parametric analysis, only a single shading product was examined. The results, therefore, only apply to products of similar geometry. Fortunately, the product chosen is by far the most popular Venetian shade used in residential applications. It was recognized that this would occur, and a decision was made early in this project to non-dimensionalize the system. The existing numerical model need only be rerun with adjusted system properties to account for the change in the plate height.

v) Testing limitations did not allow for the completion of calorimeter tests to fully examine the effects of changing nominal blind distance, or the interior glass emissivity. These cases need to be studied in order to verify the predictor equations.

vi) Insufficient optical data is available to fully test the performance of the predictor method. The author had originally collected calorimetric data for a total of twelve cases that included combinations of two solar incident angles, three blind slat angles, and two blinds with different optical properties. A reliable predictor of layer specific optical properties, however, is necessary to perform this analysis. Work is underway at the University of Waterloo to produce a reliable method of calculating the optical properties for other cases.

vii) The analysis of heat transfer, determined numerically, from the perspective of from the inner window surface has proven successful. A more stringent analysis, however, which examines heat transfer between the glass, blind, and room, from first principles, would be useful. Such an analysis is desirable for the use of this model into the window analysis software programs. It would allow a more grounded and explainable analysis of the system, include a mass transfer term that would allow windows of various heights, and allow determination of variables such as the blind temperature. This analysis would also allow inclusion of various product sizes.

REFERENCES

ASHRAE (2001). **ASHRAE HANDBOOK - FUNDAMENTALS.** American Society of Heating, Refrigeration, and Air Conditioning Engineers, Inc., Atlanta.

Collins, M.R., Harrison, S.J., Oosthuizen, P.H., and Naylor, D. (2000). "Numerical Modeling of Radiative and Convective Heat Transfer from an Irradiated Complex Window Assembly", **Proceedings of ASME Heat Transfer Division**, HTD. Vol. 366 (2), pp. 95-106.

Collins, M.R., Harrison, S.J., Oosthuizen, P.H., and Naylor, D. (2001). "An Interferometric Study of Convective Heat Transfer from an Irradiated Complex Window Assembly", **To be presented at ASME, ImecE 2001**, New York, New York, November 11-16.

Collins, M.R., Harrison, S.J., Oosthuizen, P.H., and Naylor, D. (2002). "Sensitivity Analysis of Heat Transfer from an Irradiated Window and Horizontal Louvered Blind Assembly", **To be presented at ASHRAE, Annual Winter Meeting**, Atlantic City, New Jersey, January.

CSA (1992). "Development of a Procedure for Total Window U-factor and SHGC", **Canadian Standards Association.**

Devore, J.L. (1987). **Probability and Statistics for Engineering and the Sciences**, Second Edition, Brooks/Cole Publishing Company.

Duarte, N. (2000). "An Experimental Study of Free Convective Heat Transfer from a Vertical Plate in the Presence of Heated Venetian Blinds", **MESc. Thesis, The University of Western Ontario**, London, Ontario, Canada.

Eckert, E.R.G., Goldstein, R.J. (1976). **Measurements in Heat Transfer**, Hemisphere Publishing Corp.

Eckert, E.R.G, and Soehngen, E.E. (1948). "Studies in Heat Transfer in Laminar Free Convection with the Zehnder-Mach Interferometer," AF Technical Report, 5747, A.T.I. No. 44, **United States Air Force Air Material Command**, Wright-Patterson Air Force Base, Ohio.

Fang, X., Ge, X. (1993). "Experimental Study of Overall Heat Transfer Coefficients of the Glass Window with a Venetian Blinds", **Journal of Solar Energy (Chinese)**, Vol. 14 (2), pp. 138-142.

Farber, E. A., Smith, W. A., Pennington, C. W., and Reed, J. C. (1963). "Theoretical Analysis of Solar Heat Gain Through Insulating Glass with Inside Shading", **ASHRAE Transactions**, Vol. 69, pp. 392-405.

Finlayson, E.U., Arasteh, D.K., Huizenga, C., Rubin, M.D., and Reilly, M.S. (1993). "WINDOW 4.0: Documentation of Calculation Procedures", **Energy and Environmental Division, Lawrence Berkeley Laboratory**, 1993.

Flack, R.D. (1987). "Mach-Zehnder Interferometer Errors Resulting from Test Section Misalignment," **Applied Optics**, Vol. 17 (7) , pp. 985-987.

Fluent (2001). "FIDAP 8.5.2 Documentation Suite", **Fluent Inc.**

Garnet, J.M., Frazer, R.A., Sullivan, H.F., Wright, J.L. (1995). "Effect of Internal Venetian Blinds on Window Center-Glass U-Values, Conference Proceedings", **Window Innovations 95**, Toronto, Ontario, Canada, pp. 273-279.

Harrison, S.J., and Barakat, S.A. (1983). "A Method of Comparing the Thermal Performance of Windows." **ASHRAE Transactions**, Vol. 89 (1).

Harrison, S. J., and Collins, M. R. (1999). "Queen's Solar Calorimeter – Design, Calibration, and Operating Procedure." **Presented at NORSUN'99, Solar Energy Society of Canada**, Edmonton, Canada.

Harrison, S.J,. and Dubrous, F.M. (1993). "Uncertainties in the Evaluation of Window SHGC and U-Values Measured Using an Indoor Solar Simulator Facility." **ASHRAE Transactions**, 98 (2), pp. 638-645.

Hauf, W., Grigull, U. (1970). "Optical Methods in Heat Transfer," **Advances in Heat Transfer**, Academic press, Inc., New York, N.Y., Vol. 6, pp. 133-366.

Klems, J. H. and Warner, J. L. (1992). "A New Method for Predicting the Solar Heat Gain of Complex Fenestration Systems", **Thermal Performance of the Exterior Envelope of Building Conference V**, Clearwater Beach, FL.

Klems, J. H. (1994a). "A New Method for Predicting the Solar Heat Gain of Complex Fenestration Systems - 1. Overview and Derivation of the Matrix Layer Calculation", **ASHRAE Transactions**, Vol. 100 (1), pp. 1065-1072.

Klems, J. H. (1994b). "A New Method for Predicting the Solar Heat Gain of Complex Fenestration Systems - 2. Detailed Description of the Matrix Layer Calculation", **ASHRAE Transactions**, Vol. 100 (1), pp. 1073-1086.

Klems, J. H. and Warner, J. L. (1995). "Measurement of Bi-directional Optical Properties of Complex Shading Devices", **ASHRAE Transactions**, Vol. 101 (1), pp. 791-801.

Klems, J. H., Warner, J. L. and Kelley, G. O. (1996a). "A Comparison Between Calculated and Measured SHGC for Complex Glazing Systems", **ASHRAE Transactions**, Vol. 102(1), pp. 931-939.

Klems, J. H. and Kelley, G. O. (1996b). "Calorimetric Measurements of Inward-Flowing Fraction for Complex Glazing and Shading Systems", **ASHRAE Transactions,** Vol. 102 (1), pp. 947-954.

Klems, J. H., and Warner, J. L. (1997). "Solar Heat Gain Coefficient of Complex Fenestrations with a Venetian Blind for Differing Slat Tilt Angles", **ASHRAE Transactions**, Vol. 103 (1), pp. 1026-1034.

Kline, S.J., and McClintock, F.A. (1953). "Describing Experimental Uncertainties in Single Sample Experiments." **Mechanical Engineering**, Vol. 73, pp. 3-8.

Machin, A.D. (1997). "An Experimental Study of free convection Heat Transfer from a Vertical Flat Plate in the Presence of Louvers", **MESc. Thesis, The University of Western Ontario**, London, Ontario, Canada.

Machin, A.D., Naylor, D., Oosthuizen, P.H., and Harrison, S.J. (1998). "Experimental Study of Free Convection at an Indoor Glazing Surface with a Venetian Blind", **International Journal of HVAC&R Research,** Vol. 4 (2), pp. 153-166.

Mehta, J.M., Black, W.Z. (1977). "Errors Associated with Interferometric Measurement of Convective Heat Transfer Coefficients", **Applied Optics**, Vol. 16 (6), pp. 1720-1726.

Montgomery, D.C., and Runger, G.C. (1999). **Applied Statistics and Probability for Engineers**, John Wiley and Sons, Inc., Toronto.

Naylor, D., and Duarte, N. (1999). "Direct Temperature Gradient Measurement Using Interferometry", **Experimental Heat Transfer**, Vol. 12, pp. 279-294.

Ostrach, S. (1953). "An Analysis of Laminar Free-Convection Flow and Heat Transfer about a Flat Plate Parallel to the Direction of the Generating Body Force", **NACA Technical Report 1111**.

Owens, P. G. T. (1974). "Solar Control Performance of Open and Translucent Louver Systems", **ASHRAE Transactions,** Vol. 80, pp. 324-341.

Ozisik, N. and Schutrum, L. F. (1960). "Solar Heat Gains Through Slat-Type Between Glass Shading Devices. **ASHRAE Transactions**, Vol. 66, pp. 359-373.

Parmelee, G. V. and Aubele, W. W. (1952). "The Shading of Sunlit Glass: An Analysis of the Effect of Uniformly Spaced Flat Opaque Slats", **ASHVE Transactions**, Vol. 58, pp. 377-398.

Parmelee, G. V. and Aubele, W. W. and Vild, D. J. (1953a). "The Shading of Sunlit Glass: An Experimental Study of Slat-Type Sun Shades", **ASHVE Transactions**, Vol. 59, pp. 221.

Parmelee, G. V. and Vild, D. J. (1953b). "Design Data for Slat Type Sun Shades for Use in Load Estimating", **ASHVE Transactions**, Vol. 59, pp. 403-434.

Pennington, C. W., Smith, W. A., Farber, E. A., and Reed, J. C. (1964). "Experimental Analysis of Solar Heat Gain Through Insulating Glass with Indoor Shading", **ASHRAE Journal**, Vol. 2, pp. 27-39.

Phillips, J. (1999). "A Numerical Study of the Effects of Venetian Blinds on Radiation and Convection Heat Transfer from a Window Glazing", **MESc. Thesis, The University of Western Ontario**, London, Ontario, Canada.

Phillips, J., Naylor, D., Harrison, S.J., and Oosthuizen, P.H. (1999). "Free Convection from a Window Glazing with a Venetian Blind: Numerical Model Development", **CSME Transactions**, Vol. 23, pp. 159-172.

Phillips, J., Naylor, D., Oosthuizen, P.H., and Harrison, S.J. (2000). "Modeling of the Conjugate Heat Transfer from a Window Adjacent to a Louvered Shade", **Sixth International Conference on Advanced Computational Methods in Heat Transfer**, Madrid, Spain, pp. 127-136.

Rhealt, S., and Bilgen, E. (1989). "Heat Transfer Analysis in an Automated Venetian Blind Window System", **Journal of Solar Energy Engineering**, Vol. 111, pp. 89-95.

Rhealt, S., and Bilgen, E. (1990). "Experimental Study of Full-Size Automated Venetian Blind Windows", **Solar Energy**, Vol. 44 (3), pp. 157-160.

Rubin, M. (1984). "Optical Constants and Bulk Optical Properties of Soda Lime Silica Glasses for Windows", **Lawrence Berkeley Laboratory**, Document LBL-13572.

Sciemetric Instruments (1991). **Data Acquisition and Control System - Hardware User Guide**. Sciemetric Instruments, Inc.

Siegel, R., and Howell, J.R. (1970). **Thermal Radiation Heat Transfer**, McGraw-Hill, Toronto.

Shlichting, H. (1970). **Boundary Layer Theory - 7th Edition**, McGraw Hill, Toronto.

Smith, W. A. and Pennington, C. W. (1964). "Solar Heat Gain Through Slat Type Between Between-Glass Shading Devices", **ASHRAE Journal**, Vol. 6 (10), pp. 50-53.

Solar Calorimetry Laboratory (1993). **QMON Manual**: Solar Calorimetry Laboratory, Queen's University at Kingston.

Tarasuk, J.D. (1968). "Theory, Design and Operation of the University of Saskatchewan 8-inch Mirror Mach-Zehnder Interferometer," Technical Report .C-3, Mechanical Engineering Department, **University of Saskatchewan**, June.

Touloukian. Y.S., Liley, P.E., and Saxena, S.C. (1970a). "Thermal Conductivity: Nonmetallic Liquids and Gases." **Thermophysical Properties of Matter**, Vol. 3, Thermophysical Properties Research Center (TPRC), Purdue University. Plenum Publishing.

Touloukian, Y.S., and Makita, T. (1970b). "Specific Heat: Nonmetallic Liquids and Gases." **Thermophysical Properties of Matter**, Vol. 6, Thermophysical Properties Research Center (TPRC), Purdue University, Plenum Publishing.

Touloukian, Saxena, S.C., and Hestermans, P. (1975). "Viscosity: Nonmetallic Liquids and Gases." **Thermophysical Properties of Matter,** Vol. 11, Thermophysical Properties Research Center (TPRC), Purdue University, Plenum Publishing, 1975.

Van Dyck, R. L. and Konen, T. P. (1982). "Energy Conservation Through Interior Shading of Windows: An Analysis, Test and Evaluation of Reflective Venetian Blinds". **Lawrence Berkeley Laboratory**, University of California.

Vild. D. J. (1964). "Solar Heat Gain Factors and Shading Coefficients". **ASHRAE Journal**, Vol. 10, pp. 47-50.

Von Bistram, P. (1995). "The Design, Development and Preliminary Testing of the Ryerson Mach-Zehnder Interferometer," **B.Eng. Thesis, Ryerson Polytechnic University**, Toronto, Ontario, Canada.

Window 4.1 (1998). "A PC Program for Analyzing Window Thermal Performance", **Windows and Daylighting Group, Lawrence Berkeley Laboratory**, University of California.

Wright, J. (1994). **VISION4, Glazing System Thermal Analysis Program**. Advanced Glazing System Laboratory, University of Waterloo, Waterloo, ON, Canada.

Wright, J. (1997). Personal Communication.

Ye, P. (1997). "Effect of Venetian Blinds on Overall Heat Transfer Through Window Systems: A Finite Element Numerical Solution", **MESc. Thesis, Queen's University**, Kingston, Ontario, Canada.

Ye, P., Harrison, S.J., Oosthuizen, P.H., and Naylor, D. (1999). "Convective Heat Transfer from a Window with Venetian Blind: Detailed Modeling", **ASHRAE Transactions,** Vol. 105 (2), pp. 1031-1037.

APPENDIX A
NUMERICAL FILES

A.1 Introduction

The commercial software used in the present study required a number of files both to define and solve the system and to analyze the output. Details of the procedure used and files required are presented here. A full description of the software is given in the FIDAP users manual (2001).

A.2 FIDAP Files

A.2.1 FIDAP Input File

While FIDAP has a graphical user interface (gui), it was executed using text based input or FDREAD files. This format was chosen for two reasons. Primarily, the use of a text input file allowed model files to be batch run. Using the gui would require the user to activate each model individually. More importantly, text input files are easier to manipulate. Using the gui, the model would need to be re-drawn and re-meshed for each new geometric case. Additionally, to change system parameters, old parameters would need to be removed and then replaced. With a text file, the geometry can be manipulated by inserting preformatted FIMESH geometry files. System parameters could be changed in a text editor.

An example of a FIDAP input file is provided below. The file is large, and sections have been abbreviated for spatial consideration. Complete input data files can be obtained from the Queen's University Solar Calorimetry Laboratory.

```
TITLE
Geom. (b=0.0154,b'=.0030,ang=0)
FIMESH(2-D,IMAX=15,JMAX=109,MXPOINT=450)
EXPI
1 0 7 0 13 0 19 0 25 0 31 0 45 0 59
EXPJ
1 0 33 0 41 0 47 0 49 0 59 0 69 0 71 0 81 0 91 0 93 0 103 0 113 0
115 0 125 0 135 0 137 0 147 0 157 0 159 0 169 0 179 0 181 0
191 0 201 0 203 0 213 0 223 0 225 0 235 0 245 0 247 0 257 0
267 0 269 0 279 0 289 0 291 0 301 0 311 0 313 0 323 0 333 0
335 0 345 0 355 0 357 0 367 0 377 0 379 0 389 0 399 0 401 0
417 0 449
POINT
/#   i    j    k     x     y
/ entrance region
   1    1    1    1 0.00000 -0.10537
   2    3    1    1 0.00801 -0.10537
   3    5    1    1 0.02417 -0.10537
   4    7    1    1 0.04056 -0.10537
   5    9    1    1 0.05695 -0.10537
   6   11    1    1 0.07311 -0.10537
   7   13    1    1 0.12217 -0.10537
   8   15    1    1 0.17123 -0.10537
   9    1    3    1 0.00000 0.00000
  10    3    3    1 0.00801 0.00000
  11    5    3    1 0.02417 0.00000
  12    7    3    1 0.04056 0.00000
  13    9    3    1 0.05695 0.00000
  14   11    3    1 0.07311 0.00000
  15   13    3    1 0.12217 0.00000
  16   15    3    1 0.17123 0.00000
/ first slat
  17    1    5    1 0.00000 0.01628
  18    3    5    1 0.00801 0.01628
......
 400   15   99    1 0.17123 0.90843
/ seventeenth slat
 401    1  101    1 0.00000 0.93577
 402    3  101    1 0.00801 0.93577
 403    5  101    1 0.02417 0.93577
 404    7  101    1 0.04056 0.93577
 405    9  101    1 0.05695 0.93577
 406   11  101    1 0.07311 0.93577
 407   13  101    1 0.12217 0.93577
 408   15  101    1 0.17123 0.93577
 409    1  103    1 0.00000 0.96525
 410    3  103    1 0.00801 0.96525
 411    5  103    1 0.02417 0.96817
 412    7  103    1 0.04056 0.96915
 413    9  103    1 0.05695 0.96817
 414   11  103    1 0.07311 0.96525
 415   13  103    1 0.12217 0.96525
 416   15  103    1 0.17123 0.96395
 417    1  105    1 0.00000 0.96567
 418    3  105    1 0.00801 0.96567
 419    5  105    1 0.02417 0.96859
 420    7  105    1 0.04056 0.96957
 421    9  105    1 0.05695 0.96859
 422   11  105    1 0.07311 0.96567
 423   13  105    1 0.12217 0.96567
 424   15  105    1 0.17123 0.96698
/ outlet
 425    1  107    1 0.00000 1.00000
 426    3  107    1 0.00801 1.00000
 427    5  107    1 0.02417 1.00000
 428    7  107    1 0.04056 1.00000
 429    9  107    1 0.05695 1.00000
 430   11  107    1 0.07311 1.00000
 431   13  107    1 0.12217 1.00000
 432   15  107    1 0.17123 1.00000
 433    1  109    1 0.00000 1.10537
 434    3  109    1 0.00801 1.10537
 435    5  109    1 0.02417 1.10537
 436    7  109    1 0.04056 1.10537
 437    9  109    1 0.05695 1.10537
 438   11  109    1 0.07311 1.10537
 439   13  109    1 0.12217 1.10537
 440   15  109    1 0.17123 1.10537
LINE
/ Horizontal Lines
    1    2
    2    3    3    3
    3    4
    4    5
    5    6    3    4
    6    7    3    3
    7    8
    9   10
   10   11    3    3
   11   12
   12   13
   13   14    3    4
   14   15    3    3
   15   16
   17   18
   18   19    3    3
   19   20
   20   21
   21   22    3    4
   22   23    3    3
   23   24
   25   26
   30   31    3    3
......
  431  432
  433  434
  434  435    3    3
  435  436
  436  437
  437  438    3    4
  438  439    3    3
  439  440
/ Vertical Lines
    1    9
    2   10
    3   11
    4   12
    5   13
```

```
   6    14
   7    15
   8    16
   9    17    3    3
...
  428   436
  429   437
  430   438
  431   439
  432   440
ARC
   26    28    0    3    3    27    3   0.5
   28    30    0    3    3    29    3   0.5
   34    36    0    3    3    35    3   0.5
   36    38    0    3    3    37    3   0.5
   50    52    0    3    3    51    3   0.5
   52    54    0    3    3    53    3   0.5
   58    60    0    3    3    59    3   0.5
..
   410   412    0    3    3   411    3   0.5
   412   414    0    3    3   413    3   0.5
   418   420    0    3    3   419    3   0.5
   420   422    0    3    3   421    3   0.5
SURFACE
   1   440
ELEMENTS(QUADRILATERAL.NODES=9.ENTITY="fluid")
   1   434
   2    30
  34    54
  58    78
  82   102
 106   126
 130   150
 154   174
 178   198
 202   222
 226   246
 250   270
 274   294
 298   318
 322   342
 346   366
 370   390
 394   414
 418   438
   6   440
ELEMENTS(BOUNDARY.FACE.ENTITY="inlet")
   1    8
ELEMENTS(BOUNDARY.FACE.ENTITY="outlet")
  433   440
ELEMENTS(BOUNDARY.FACE.ENTITY="room")
   8   440
ELEMENTS(BOUNDARY.FACE.ENTITY="wall")
   1    9
  425   433
ELEMENTS(BOUNDARY,FACE,ENTITY="glass")
   9   425
ELEMENTS(BOUNDARY,FACE,ENTITY="bot1")
   26    30
ELEMENTS(BOUNDARY,FACE,ENTITY="right1")
   30    38
ELEMENTS(BOUNDARY,FACE,ENTITY="top1")
   38    34
ELEMENTS(BOUNDARY,FACE,ENTITY="left1")
   34    26
...
ELEMENTS(BOUNDARY,FACE,ENTITY="left16")
   394   386
ELEMENTS(BOUNDARY,FACE,ENTITY="bot17")
   410   414
ELEMENTS(BOUNDARY.FACE.ENTITY="right17")
   414   422
ELEMENTS(BOUNDARY.FACE.ENTITY="top17")
   422   418
ELEMENTS(BOUNDARY.FACE.ENTITY="left17")
   418   410
ELEMENTS(QUADRILATERAL.NODES=9.ENTITY="solid")
   26    38
   50    62
   74    86
   98   110
  122   134
  146   158
  170   182
  194   206
  218   230
  242   254
  266   278
  290   302
  314   326
  338   350
  362   374
  386   398
  410   422
END
FIPREP
PROBLEM(NONLINEAR,BUOYANCY)
PRESSURE(PENALTY=1.E-8,DISCONTINUOUS)
$PR=.715
$RA=1591514019
$GR=$PR*$RA
SPECIFICHEAT(CONSTANT=$PR)
VISCOSITY(CONSTANT=1.0)
DENSITY(CONSTANT=1/$PR)
VOLUMEX(CONSTANT=$GR,REFTEMP=1.0)
GRAVITY(MAGNITUDE=1.0)
CONDUCTIVITY(SET=1,CONSTANT=1.0)
CONDUCTIVITY(SET=2,CONSTANT=4633.2)
EMISSIVITY(SET=1,CONSTANT=0.81,STEFB=21.583)
EMISSIVITY(SET=2,CONSTANT=0.81,STEFB=21.583)
EMISSIVITY(SET=3,CONSTANT=1.0,STEFB=21.583,REFTEM
P=1.0)
/EXECUTION(NEWJOB)
EXECUTION(RESTART)
SOLUTION(S.S.=100,VELCONV=.0001,RESCONV=.0001,ACC
F=0.6)
DATAPRINT(NORMAL,PAGE,NODES)
POSTPROCESS
RADIATION(NOPARTI,GREY)
ENTITY(FLUID,NAME="fluid",MCOND=1)
ENTITY(SOLID,NAME="solid",MCOND=2)
ENTITY(RADIATION,GREY,NAME="wall",MEMSV=3)
ENTITY(RADIATION,GREY,NAME="glass",MEMSV=2)
ENTITY(RADIATION,GREY,NAME="inlet",MEMSV=3)
ENTITY(RADIATION,GREY,NAME="outlet",MEMSV=3)
ENTITY(RADIATION,GREY,NAME="room",MEMSV=3)
ENTITY(RADIATION,GREY,NAME="top1",MEMSV=1,ATTA
CH="fluid")
ENTITY(RADIATION,GREY,NAME="bot1",MEMSV=1,ATTA
CH="fluid")
ENTITY(PLOT,NAME="left1",ATTACH="fluid")
ENTITY(PLOT,NAME="right1",ATTACH="fluid")
...
ENTITY(RADIATION,GREY,NAME="top17",MEMSV=1,ATT
ACH="fluid")
ENTITY(RADIATION,GREY,NAME="bot17",MEMSV=1,ATT
ACH="fluid")
ENTITY(PLOT,NAME="left17",ATTACH="fluid")
ENTITY(PLOT,NAME="right17",ATTACH="fluid")
RENUMBER(PROFILE)
```

```
BCFLUX(HEAT,ENTITY="top1",CONSTANT=7.50)
BCFLUX(HEAT,ENTITY="top2",CONSTANT=7.50)
...
BCFLUX(HEAT,ENTITY="top17",CONSTANT=7.50)
BCNODE(TEMPERATURE,CONSTANT=1.0,ENTITY="wall")
BCNODE(TEMPERATURE,CONSTANT=1.007,ENTITY="gla
ss")
BCNODE(TEMPERATURE,CONSTANT=1.0,ENTITY="room
")
BCNODE(TEMPERATURE,CONSTANT=1.0,ENTITY="inlet"
)
BCNODE(VELOCITY,ZERO,ENTITY="glass")
BCNODE(VELOCITY,ZERO,ENTITY="wall")
BCNODE(VELOCITY,ZERO,ENTITY="top1")
BCNODE(VELOCITY,ZERO,ENTITY="bot1")
BCNODE(VELOCITY,ZERO,ENTITY="left1")
BCNODE(VELOCITY,ZERO,ENTITY="right1")
...
BCNODE(VELOCITY,ZERO,ENTITY="top17")
BCNODE(VELOCITY,ZERO,ENTITY="bot17")
BCNODE(VELOCITY,ZERO,ENTITY="left17")
BCNODE(VELOCITY,ZERO,ENTITY="right17")
BCNODE(UY,ZERO,ENTITY="room")
RADSURFACE(ENTITY="glass",INDIVIDUAL)
RADSURFACE(ENTITY="wall",INDIVIDUAL)
RADSURFACE(ENTITY="inlet",ALL)
RADSURFACE(ENTITY="outlet",ALL)
RADSURFACE(ENTITY="room",INDIVIDUAL)
RADSURFACE(ENTITY="top1",INDIVIDUAL)
RADSURFACE(ENTITY="bot1",INDIVIDUAL)
...
RADSURFACE(ENTITY="top17",INDIVIDUAL)
RADSURFACE(ENTITY="bot17",INDIVIDUAL)
OBSTRUCTION(LIST)
"bot1","top1","bot2","top2","bot3","top3","bot4","top4","bot5","to
p5","bot6",
"top6","bot7","top7","bot8","top8","bot9","top9","bot10","top10",
"bot11",
"top11","bot12","top12","bot13","top13","bot14","top14","bot15",
"top15",
"bot16","top16","bot17","top17"
VIEWFACTOR(NOSMOOTH,XZONE=5,YZONE=5,DEBUG=0,
OUTPUTFILE,CODED)
RENUMBER(PROFILE)
END
CREATE(FISOLV)
RUN(FISOLV,FORE,COMP)
END
```

A.2.2 FIDAP Output Files

While FIDAP produces a number of output files, three files are of interest: the FDOUT, FIOUT, and FDVWFC files. The FDOUT file provides a large amount of information, and most importantly, gives nodal values of velocity and temperature. The FIOUT file gives additional information requested by the user. In this case, the convective flux values at the plate surface were located in that file. Finally, the FDVWFC gives the viewfactor matrix as calculated by FIDAP.

The size of the FDOUT and FDVWFC files is excessively large. Combined, they typically represent over 15MB of information in text form, and to present them here would not be useful. A sample of an FIOUT file has been provided in the next section. Complete output data files can be obtained from the Queen's University Solar Calorimetry Laboratory.

A.3 Post Processing

A.3.1 Convection Analysis

When requested in FIDAP, convection from the plate surface was given in the FIOUT file. An abbreviated example of output from that file is given below. The diffuse flux is the term of interest. As the system was analyzed in non-dimensional form, so is the flux. Results can be converted to dimensional form using Eq. (2.21).

```
LIST OF DEFINING GROUPS:
     26
1ELEMENT  SIDE              INTEGRATION POINT FLUXES/QUANTITIES    INTEGRATED HEAT FLOW

  257   4   DIFFUSIVE  NORMAL  -0.1023531E+02 -0.1517525E+02       -0.3038917E-01
                  X  0.1023531E+02  0.1517525E+02        0.3038917E-01
                  Y  0.1136868E-12 -0.2273737E-12       -0.1359611E-15
       CONVECTIVE  NORMAL   0.0000000E+00  0.0000000E+00        0.0000000E+00
                  X  0.0000000E+00  0.0000000E+00        0.0000000E+00
                  Y  0.0000000E+00  0.0000000E+00        0.0000000E+00
       TOTAL      NORMAL  -0.1023531E+02 -0.1517525E+02       -0.3038917E-01
                  X  0.1023531E+02  0.1517525E+02        0.3038917E-01
                  Y  0.1136868E-12 -0.2273737E-12       -0.1359611E-15
       COORDINATE  ARC LN   0.1886396E-02  0.5054582E-03        0.2391854E-02
                  X  0.0000000E+00  0.0000000E+00
                  Y  0.1886396E-02  0.5054582E-03
       NORMAL VEC      X  -0.1000000E+01 -0.1000000E+01
                  Y  0.0000000E+00  0.0000000E+00

  273   4   DIFFUSIVE  NORMAL  -0.7299778E+01 -0.8814922E+01       -0.2637832E-01
                  X  0.7299778E+01  0.8814922E+01        0.2637832E-01
                  Y  0.0000000E+00 -0.1136868E-12       -0.1860952E-15
       CONVECTIVE  NORMAL   0.0000000E+00  0.0000000E+00        0.0000000E+00
                  X  0.0000000E+00  0.0000000E+00        0.0000000E+00
                  Y  0.0000000E+00  0.0000000E+00        0.0000000E+00
       TOTAL      NORMAL  -0.7299778E+01 -0.8814922E+01       -0.2637832E-01
                  X  0.7299778E+01  0.8814922E+01        0.2637832E-01
                  Y  0.0000000E+00 -0.1136868E-12       -0 1860952E-15
       COORDINATE  ARC LN   0.4973835E-02  0.3083694E-02        0.3273821E-02
                  X  0.0000000E+00  0.0000000E+00
                  Y  0.4973835E-02  0.3083694E-02
       NORMAL VEC      X  -0.1000000E+01 -0.1000000E+01
                  Y  0.0000000E+00  0.0000000E+00

  289   4   DIFFUSIVE  NORMAL  -0.5970195E+01 -0.6672129E+01       -0.2832515E-01
                  X  0.5970195E+01  0.6672129E+01        0.2832515E-01
                  Y  0.0000000E+00 -0.1136868E-12       -0.2547156E-15
       CONVECTIVE  NORMAL   0.0000000E+00  0.0000000E+00        0.0000000E+00
                  X  0.0000000E+00  0.0000000E+00        0.0000000E+00
                  Y  0.0000000E+00  0.0000000E+00        0.0000000E+00
       TOTAL      NORMAL  -0.5970195E+01 -0.6672129E+01       -0.2832515E-01
                  X  0.5970195E+01  0.6672129E+01        0.2832515E-01
                  Y  0.0000000E+00 -0.1136868E-12       -0.2547156E-15
       COORDINATE  ARC LN   0.9199731E-02  0.6612623E-02        0.4481004E-02
                  X  0.0000000E+00  0.0000000E+00
                  Y  0.9199731E-02  0.6612623E-02
       NORMAL VEC      X  -0.1000000E+01 -0.1000000E+01
                  Y  0.0000000E+00  0.0000000E+00


.......

  3281   4   DIFFUSIVE  NORMAL  -0.1511075E+01 -0.1491587E+01       -0.7591044E-02
                  X  0.1511075E+01  0.1491587E+01        0.7591044E-02
                  Y  0.1136868E-12 -0.5684342E-13        0.1437061E-15
       CONVECTIVE  NORMAL   0.0000000E+00  0.0000000E+00        0.0000000E+00
                  X  0.0000000E+00  0.0000000E+00        0.0000000E+00
                  Y  0.0000000E+00  0.0000000E+00        0.0000000E+00
       TOTAL      NORMAL  -0.1511075E+01 -0.1491587E+01       -0.7591044E-02
                  X  0.1511075E+01  0.1491587E+01        0.7591044E-02
                  Y  0.1136868E-12 -0.5684342E-13        0.1437061E-15
       COORDINATE  ARC LN   0.9863003E+00  0.9833811E+00        0.5056209E-02
                  X  0.0000000E+00  0.0000000E+00
                  Y  0.9863003E+00  0.9833811E+00
       NORMAL VEC      X  -0.1000000E+01 -0.1000000E+01
                  Y  0.0000000E+00  0.0000000E+00

  3297   4   DIFFUSIVE  NORMAL  -0.1591664E+01 -0.1451471E+01       -0.8907018E-02
                  X  0.1591664E+01  0.1451471E+01        0.8907018E-02
                  Y  0.5684342E-13  0.0000000E+00        0.1663763E-15
       CONVECTIVE  NORMAL   0.0000000E+00  0.0000000E+00        0.0000000E+00
```

```
                 X   0.0000000E+00  0.0000000E+00        0.0000000E+00
                 Y   0.0000000E+00  0.0000000E+00        0.0000000E+00
       TOTAL      NORMAL  -0.1591664E+01 -0.1451471E+01       -0.8907018E-02
                 X   0.1591664E+01  0.1451471E+01        0.8907018E-02
                 Y   0.5684342E-13  0.0000000E+00        0.1663763E-15
       COORDINATE  ARC LN   0.9919856E+00  0.9886059E+00       0.5853844E-02
                 X   0.0000000E+00  0.0000000E+00
                 Y   0.9919856E+00  0.9886059E+00
       NORMAL VEC      X  -0.1000000E+01 -0.1000000E+01
                 Y   0.0000000E+00  0.0000000E+00

 3313   4   DIFFUSIVE  NORMAL  -0.2065468E+01 -0.1248889E+01       -0.1123121E-01
                 X   0.2065468E+01  0.1248889E+01        0.1123121E-01
                 Y   0.5684342E-13  0.0000000E+00        0.1926227E-15
       CONVECTIVE  NORMAL   0.0000000E+00  0.0000000E+00       0.0000000E+00
                 X   0.0000000E+00  0.0000000E+00        0.0000000E+00
                 Y   0.0000000E+00  0.0000000E+00        0.0000000E+00
       TOTAL      NORMAL  -0.2065468E+01 -0.1248889E+01       -0.1123121E-01
                 X   0.2065468E+01  0.1248889E+01        0.1123121E-01
                 Y   0.5684342E-13  0.0000000E+00        0.1926227E-15
       COORDINATE  ARC LN   0.9985678E+00  0.9946549E+00       0.6777310E-02
                 X   0.0000000E+00  0.0000000E+00
                 Y   0.9985678E+00  0.9946549E+00
       NORMAL VEC      X  -0.1000000E+01 -0.1000000E+01
                 Y   0.0000000E+00  0.0000000E+00


TOTAL HEAT FLOW:    DIFFUSIVE = -0.2160390E+01
                    CONVECTIVE =  0.0000000E+00
                    TOTAL      = -0.2160390E+01

TOTAL SIDE LENGTH:           0.1000000E+01


AVERAGE HEAT FLUX: DIFFUSIVE = -0.2160390E+01
                    CONVECTIVE =  0.0000000E+00
                    TOTAL      = -0.2160390E+01
```

A.3.2 Radiation Analysis Code

FIDAP has no mechanism to output calculated radiative heat flux between surfaces. The following FORTRAN program was necessary to determine that heat flux. It will read the formatted temperature output from the FDOUT and FDVWFC files, and then solve radiation exchange using the net enclosure method (Siegel and Howell 1970). The program is specific to the nodal assignments used in this analysis, but not the nodal placement, i.e., the software did not need to be changed if the slat angle under analysis was modified. In both cases, for example, the tips of the slats had the same nodal assignment even though their position changed. The matrix was solved using the Gauss-Jordan method. As the model is in non-dimensional form, so is the calculated flux. Results can be converted to dimensional form using Eq. (2.21).

A complete listing of the radiation post-processing code is as follows.

```
C
*************************************************
****************
C *
C *           FIDAP RADIATION DATA REDUCTION
C *           ******************************
C *
C * THIS PROGRAM WILL DETERMINE THE RADIATION
EXCHANGE FOR FIDAP FILES
C *  PRODUCED BY THE MODEL BY MIKE COLLINS
(WINDOW WITH BLIND)
C
*************************************************
****************
C
        COMMON                              /VARS/
NCOLS.F(1000,1000).S(2,100).E(1000),N(50),T(1000)
   REAL F.E.T
        INTEGER NCOLS.S.N
        WRITE(*.1)
   OPEN(2.FILE='output.dat')
        CALL VIEWFACTOR
        CALL SURFACES
        CALL MENUA
   CALL TEMPERATURE
        CALL SETMATRIX
        CLOSE(2)
C       FORMAT STATEMENTS
  1     FORMAT(/.'***PROGRAM INITIALIZATION***')
        END

        SUBROUTINE VIEWFACTOR
C
C       - This routine will read in a formatted viewfactor file
and form the
C    appropriate array. It will also allow the user to look at
specified
C    viewfactors.
C
C    - Data is formatted by reducing the column delimiter to a
number, and
C    placing the data in comma delimited form. Rename the file
to viewfact.dat.
C
        COMMON                              /VARS/
NCOLS.F(1000,1000),S(2,100),E(1000),N(50),T(1000)
   REAL F.E.T.sum
        INTEGER NCOLS,S,N,ROWS,REM
        CHARACTER*1 DUMMY
        WRITE(*,1)
        OPEN(1,FILE='viewfact.dat')
        READ(1,2) NCOLS
        ROWS=NCOLS/8
        REM=NCOLS-ROWS*8
        DO 109 j=1, NCOLS
   READ(1,*) DUMMY
        DO 100 i=1, ROWS*8, 8
        READ(1,*)
F(i,j),F(i+1,j),F(i+2,j),F(i+3,j),F(i+4,j),F(i+5,j),
  $F(i+6,j),F(i+7,j)
  100   CONTINUE
        i=ROWS*8+1
   IF (REM.EQ.1) GOTO 101
        IF (REM.EQ.2) GOTO 102
        IF (REM.EQ.3) GOTO 103
        IF (REM.EQ.4) GOTO 104
        IF (REM.EQ.5) GOTO 105
        IF (REM.EQ.6) GOTO 106
        IF (REM.EQ.7) GOTO 107
        GOTO 108
 101    READ(1,*) F(i,j)
        GOTO 108
 102    READ(1,*) F(i,j).F(i+1,j)
        GOTO 108
 103    READ(1,*) F(i,j),F(i+1,j),F(i+2,j)
        GOTO 108
 104    READ(1,*) F(i,j),F(i+1,j),F(i+2,j),F(i+3,j)
        GOTO 108
 105    READ(1,*) F(i,j),F(i+1,j),F(i+2,j),F(i+3,j),F(i+4,j)
        GOTO 108
 106    READ(1,*)
F(i,j),F(i+1,j),F(i+2,j),F(i+3,j),F(i+4,j),F(i+5,j)
        GOTO 108
 107    READ(1,*)
F(i,j),F(i+1,j),F(i+2,j),F(i+3,j),F(i+4,j),F(i+5,j),
  $F(i+6,j)
 108    CONTINUE
 109 CONTINUE
        CLOSE(1)
C       DATA CHECK - SUM ROWS
   WRITE(*,3)
   WRITE(2,4)
        DO 111 i=1, NCOLS
   sum=0
   DO 110 j=1, NCOLS
        sum=sum+F(i,j)
 110    CONTINUE
        IF (sum.LT.1.02) THEN
        IF (sum.GT.0.98) THEN
        GOTO 111
        END IF
        END IF
        WRITE(2,*) i, sum
 111    CONTINUE
C   FORMAT STATEMENTS
  1 FORMAT(/,' READING VIEWFACTOR DATA..........')
  2 FORMAT(/,I3)
  3 FORMAT(' PERFORMING DATA CHECKS...........')
  4 FORMAT(' ***Summating Rows (nonconforming rows
listed)')
   RETURN
   END

        SUBROUTINE SURFACES
C
C       - This routine will read in the i,j spacing of the
problem and check to
C       see if the matrix size is correct.
C
C    - Data is formatted by placing the data in a single row.
Rename the file to
C    surfaces.dat.
C
        COMMON                              /VARS/
NCOLS,F(1000,1000),S(2,100),E(1000),N(50),T(1000)
        REAL F,E,T
   INTEGER NCOLS,S,N,MSIZE
        WRITE(*,1)
        OPEN(1,FILE='surfaces.dat')
        DO 200 i=1, 8
   READ(1,*) S(1,i)
 200    CONTINUE
        DO 201 i=1,        55
        READ(1,*) S(2,i)
 201    CONTINUE
        CLOSE(1)
        WRITE(*,2)
        WRITE(2,3)
```

```
        MSIZE=0
        MSIZE=1+1+17*2*(S(1,6)-S(1,2))/2+2*(S(2,55)-1)/2
        WRITE(2,*) NCOLS, MSIZE
C   FORMAT STATEMENTS
  1 FORMAT(/,' READING SURFACES DATA............')
  2       FORMAT(/,'        PERFORMING        DATA
CHECKS...........')
  3 FORMAT(/,' ***Checking matrix size')
   RETURN
        END

        SUBROUTINE MENUA
C
C         - This routine will determine the surface numbers and
allow them to be
C         used to examine particular viewfactors, and assign
surface emissivities.
C
        COMMON                                    /VARS/
NCOLS,F(1000,1000),S(2,100),E(1000),N(50),T(1000)
        REAL F,E,T
   INTEGER NCOLS,S,N
   WRITE(*,1)
        N(1)=1
        N(2)=N(1)+1
        N(3)=N(2)+(S(2,55)-S(2,1))/2
        N(4)=N(3)+(S(2,2)-S(2,1))/2
        N(5)=N(4)+(S(2,55)-S(2,54))/2
        N(6)=N(5)+(S(2,54)-S(2,2))/2
        N(7)=N(6)+(S(1,6)-S(1,2))/2
        N(8)=N(7)+(S(1,6)-S(1,2))/2
        N(9)=N(8)+(S(1,6)-S(1,2))/2
        N(10)=N(9)+(S(1,6)-S(1,2))/2
        N(11)=N(10)+(S(1,6)-S(1,2))/2
        N(12)=N(11)+(S(1,6)-S(1,2))/2
        N(13)=N(12)+(S(1,6)-S(1,2))/2
        N(14)=N(13)+(S(1,6)-S(1,2))/2
        N(15)=N(14)+(S(1,6)-S(1,2))/2
        N(16)=N(15)+(S(1,6)-S(1,2))/2
        N(17)=N(16)+(S(1,6)-S(1,2))/2
        N(18)=N(17)+(S(1,6)-S(1,2))/2
        N(19)=N(18)+(S(1,6)-S(1,2))/2
        N(20)=N(19)+(S(1,6)-S(1,2))/2
        N(21)=N(20)+(S(1,6)-S(1,2))/2
        N(22)=N(21)+(S(1,6)-S(1,2))/2
        N(23)=N(22)+(S(1,6)-S(1,2))/2
        N(24)=N(23)+(S(1,6)-S(1,2))/2
        N(25)=N(24)+(S(1,6)-S(1,2))/2
        N(26)=N(25)+(S(1,6)-S(1,2))/2
        N(27)=N(26)+(S(1,6)-S(1,2))/2
        N(28)=N(27)+(S(1,6)-S(1,2))/2
        N(29)=N(28)+(S(1,6)-S(1,2))/2
        N(30)=N(29)+(S(1,6)-S(1,2))/2
        N(31)=N(30)+(S(1,6)-S(1,2))/2
        N(32)=N(31)+(S(1,6)-S(1,2))/2
        N(33)=N(32)+(S(1,6)-S(1,2))/2
        N(34)=N(33)+(S(1,6)-S(1,2))/2
        N(35)=N(34)+(S(1,6)-S(1,2))/2
        N(36)=N(35)+(S(1,6)-S(1,2))/2
        N(37)=N(36)+(S(1,6)-S(1,2))/2
        N(38)=N(37)+(S(1,6)-S(1,2))/2
        N(39)=N(38)+(S(1,6)-S(1,2))/2
        N(40)=N(39)+(S(1,6)-S(1,2))/2
        WRITE(*,20)
        DO 300 i=1, N(5)
        E(i)=1
 300    CONTINUE
        DO 301 j=N(5)+1, N(6)
 C      glass
        E(j)=0.84
 301    CONTINUE
        DO 302 j=N(6)+1, NCOLS
C       slats
        E(j)=0.81
 302    CONTINUE
        WRITE(2,5)
        WRITE(2,6)
        WRITE(2,7) N(2)+1,N(3),N(3)+1,N(4)
        WRITE(2,8) N(4)+1,N(5),N(5)+1,N(6)
        WRITE(2,9) N(6)+1,N(8),N(8)+1,N(10)
        WRITE(2,10) N(10)+1,N(12),N(12)+1,N(14)
        WRITE(2,11) N(14)+1,N(16),N(16)+1,N(18)
        WRITE(2,12) N(18)+1,N(20),N(20)+1,N(22)
        WRITE(2,13) N(22)+1,N(24),N(24)+1,N(26)
        WRITE(2,14) N(26)+1,N(28),N(28)+1,N(30)
        WRITE(2,15) N(30)+1,N(32),N(32)+1,N(34)
        WRITE(2,16) N(34)+1,N(36),N(36)+1,N(38)
        WRITE(2,17) N(38)+1,N(40)
C       FORMAT STATEMENTS
 1 FORMAT(/,' DETERMINING SURFACES...........')
 5 FORMAT(/,' ***Surface Key')
 6 FORMAT(' Inlet      1       Outlet      2')
 7 FORMAT(' Room      ',I3,'  ',I3,'   Bot. Wall   ',I3,' ',I3)
 8 FORMAT(' Top. Wall ',I3,'  ',I3,'   Glass       ',I3,' ',I3)
 9 FORMAT(' Slat 1    ',I3,'  ',I3,'   Slat 2      ',I3,' ',I3)
 10 FORMAT(' Slat 3    ',I3,'  ',I3,'   Slat 4      ',I3,' ',I3)
 11 FORMAT(' Slat 5    ',I3,'  ',I3,'   Slat 6      ',I3,' ',I3)
 12 FORMAT(' Slat 7    ',I3,'  ',I3,'   Slat 8      ',I3,' ',I3)
 13 FORMAT(' Slat 9    ',I3,'  ',I3,'   Slat 10     ',I3,' ',I3)
 14 FORMAT(' Slat 11   ',I3,'  ',I3,'   Slat 12     ',I3,' ',I3)
 15 FORMAT(' Slat 13   ',I3,'  ',I3,'   Slat 14     ',I3,' ',I3)
 16 FORMAT(' Slat 15   ',I3,'  ',I3,'   Slat 16     ',I3,' ',I3)
 17 FORMAT(' Slat 17   ',I3,'  ',I3)
. 20 FORMAT(/,' ASSIGNING EMISSIVITIES..........')
        RETURN
        END

   SUBROUTINE TEMPERATURE
C
C         - This routine will assign temperatures to the
surfaces.
C
        COMMON                                    /VARS/
NCOLS,F(1000,1000),S(2,100),E(1000),N(50),T(1000)
        REAL F,E,T,TEMP(50000)
   INTEGER NCOLS, S, N,NODES,NODE(50000),NODEST
        WRITE(*,1)
        OPEN(1,FILE='temps.dat')
        NODES=S(1,8)*S(2,55)
        DO 400 i=1,NODES
   READ(1,*) NODE(i),TEMP(i)
        WRITE(2,*) NODE(i),TEMP(i)
        T(i)=0
 400    CONTINUE
        DO 401 i=1,S(1,8)
        T(1)=T(1)+TEMP(i)
        WRITE(2,*) NODE(i),TEMP(i)
 401    CONTINUE
        T(1)=T(1)/S(1,8)
        DO 402 i=S(1,8)*(S(2,55)-1)+1,S(1,8)*S(2,55)
        T(2)=T(2)+TEMP(i)
 402    CONTINUE
        T(2)=T(2)/S(1,8)
C  ROOM AND WALLS SET TO T=1
        DO 403 i=N(2)+1,N(5)
        T(i)=1
 403    CONTINUE
C  SET GLASS USING SINGLE READ
        DO 404 i=N(5)+1,N(6)
        T(i)=TEMP(S(1,8)*(S(2,2)-1)+1)
```

```
 404      CONTINUE
C   SET SLAT SURFACE TEMPERATURES
          DO 405 j=1,17
          NODEST=S(1,8)*(S(2,3*j+1)-1)+S(1,2)
          DO 406 i=N(4+j*2)+1,N(5+j*2)
          T(i)=(TEMP(NODEST)+TEMP(NODEST+1)+TEMP
(NODEST+2))/3
          NODEST=NODEST+2
 406      CONTINUE
          NODEST=S(1,8)*(S(2,3*j+2)-1)+S(1,2)
          DO 407 k=N(5+j*2)+1,N(6+j*2)
          T(k)=(TEMP(NODEST)+TEMP(NODEST+1)+TEM
P(NODEST+2))/3
          NODEST=NODEST+2
 407      CONTINUE
 405      CONTINUE
C   FORMAT STATEMENTS
  1 FORMAT(/,' READING TEMPERATURE DATA.........'/)
          RETURN
          END

   SUBROUTINE SETMATRIX
C
C         - This routine will form the radiation matrix.
C
          COMMON                                   /VARS/
NCOLS,F(1000,1000),S(2,100),E(1000),N(50),T(1000)
          REAL
F,E,T,NRC,A(1000,1000),AA(1000,1000),C(1000),CC(1000),
   $B(1000),dummy
    INTEGER NCOLS, S, N
    WRITE(*,1)
          NRC=21.683
          DO 501 k=1,NCOLS
          C(k)=0
    DO 502 j=1,NCOLS
          CRON=0
    IF (k.EQ.j) CRON=1
          C(k)=C(k)+NRC*F(k,j)*(T(k)*T(k)*T(k)*T(k)-
T(j)*T(j)*T(j)*T(j))
          A(k,j)=CRON/E(j)-F(k,j)*(1-E(j))/E(j)
 502      CONTINUE
    CC(k)=C(k)
          AA(k,j)=A(k,j)
 501      CONTINUE
C         CALL MATRIX SOLVERS
C   INVERT A & MULTIPLY A(-1)C (using Gauss-Jorden)
          DO 503 k=1,NCOLS
          dummy=A(k,k)
          DO 504 j=1,NCOLS
          A(k,j)=A(k,j)/dummy
 504      CONTINUE
          C(k)=C(k)/dummy
          DO 505 i=1,NCOLS
          IF (i.EQ.k) GOTO 506
          dummy=A(i,k)
          DO 507 j=1,NCOLS
          A(i,j)=A(i,j)-dummy*A(k,j)
 507      CONTINUE
          C(i)=C(i)-dummy*C(k)
 506      CONTINUE
 505      CONTINUE
 503      CONTINUE
          WRITE(2,2)
          DO 508 i=1,NCOLS
          WRITE(2,*) i,T(i),C(i)
 508      CONTINUE
          WRITE(2,3)
          DO 509 i=N(5)+1,N(6)
          WRITE(2,*) i,T(i),C(i)
 509      CONTINUE
C         WRITE(2,4)
C         DO 510 i=1,NCOLS
C         B(i)=0
C    DO 511 j=1,NCOLS
C         B(i)=B(i)+AA(i,j)*C(j)
C 511     CONTINUE
C         WRITE(2,*) i,B(i),CC(i)
C 510     CONTINUE
C   FORMAT STATEMENTS
  1 FORMAT(' SETTING RADIATION MATRIX.........')
  2       FORMAT(/,' ***non-dimensional flux (node, T, q)')
  3       FORMAT(/,' ***non-dimensional flux (wall nodes)')
  4       FORMAT(/,' ***Matrix Check')
          RETURN
          END
```

APPENDIX B
INTERFEROMETRY: UNCERTAINTY AND SAMPLE CALCULATIONS

B.1 Introduction

In the present study, the Ryerson Mach-Zehnder interferometer (Tarasuk 1968, Von Bistram 1995, Machin 1997, Duarte 1999) was used to determine the temperature field produced by natural convective flow from a heated or cooled isothermal surface in the presence of heated louvers. This Appendix will briefly present the uncertainty of interferometer measurements, and provide a sample calculation.

B.2 Uncertainty

With any experimental investigation there is always a certain degree of unavoidable uncertainty. Since Mach-Zehnder interferometry is a widely used technique for quantitative heat transfer (and other) measurements, a considerable amount of attention (Eckert and Goldstein 1976, Hauf and Grigull 1970, Mehta and Black 1977, Flack 1987) has been directed towards the corrections that are recommended when deviation from when ideal two-dimensional conditions exist. A discussion of probable sources of error inherent in this type of study was done by Machin (1997) in his Thesis. The errors discussed were end effects, refraction, diffraction, misalignment, beam convergence/divergence, fringe center location and scale factor.

An uncertainty analysis based on the method of Kline and McClintock (1953) is presented which indicates the relative uncertainty in the various primary experimental measurements. Suppose that a set of measurements were taken to compute some desired result. The result would be a function of the individual variables $x_1, x_2, \ldots x_n$. Thus

$$R = R\{x_1, x_2, \ldots, x_n\} \tag{B.1}$$

If each independent variable was given the same odds, then the relation between the uncertainty for the variables δx_1, and the uncertainty for the result δR, would be

$$\delta R = \pm\sqrt{\left(\frac{\partial R}{\partial x_1}\delta x_1\right)^2 + \left(\frac{\partial R}{\partial x_2}\delta x_2\right)^2 + \cdots + \left(\frac{\partial R}{\partial x_n}\delta x_n\right)^2} \tag{B.2}$$

Attention should be drawn to relative magnitude of the uncertainties in this root-sum-squared technique. Very little would be accomplished in reducing the uncertainty of any of the smaller variables as the square of the larger variables dominate the total uncertainty in the final result. Thus, it would be advantageous for an investigator to perform such an analysis prior to designing an experiment.

B.2.1 Infinite Fringe Method

Assuming that each independent variable was given the same odds, then the relation between the uncertainty of the variables, and the magnitude of the uncertainty for the local heat transfer coefficient, would be

$$\delta h = \sqrt{\begin{aligned}&\left(\frac{\partial h}{\partial k_p}\delta k_p\right)^2 + \left(\frac{\partial h}{\partial p}\delta p\right)^2 + \left(\frac{\partial h}{\partial Z}\delta Z\right)^2 + \left(\frac{\partial h}{\partial T_i}\delta T_i\right)^2 \\ &+ \left(\frac{\partial h}{\partial T_p}\delta T_p\right)^2 + \left(\frac{\partial h}{\partial (y_2 - y_1)}\delta (y_2 - y_1)\right)^2\end{aligned}} \tag{B.3}$$

where the expression for h is given in Eq. (3.16). The uncertainties in the gas constant, specific refractivity, and the He-Ne laser wavelength have been neglected. The partial derivatives take the form

$$\frac{\partial h}{\partial k_p} = \left(T_p - T_i\right)^{-1}\left(y_2 - y_1\right)^{-1}\left(T_1 - T_2\right) \tag{B.4}$$

$$\frac{\partial h}{\partial T_i} = k_p\left(T_p - T_i\right)^{-2}\left(y_2 - y_1\right)^{-1}\left(T_1 - T_2\right) \tag{B.5}$$

$$\frac{\partial h}{\partial\left(y_2 - y_1\right)} = -k_p\left(T_p - T_i\right)^{-1}\left(y_2 - y_1\right)^{-2}\left(T_1 - T_2\right) \tag{B.6}$$

$$\frac{\partial h}{\partial Z} = k_p\left(T_p - T_i\right)^{-1}\left(y_2 - y_1\right)^{-1}\left(\frac{\partial\left(T_1 - T_2\right)}{\partial Z}\right) \tag{B.7}$$

$$\frac{\partial h}{\partial p} = k_p\left(T_p - T_i\right)^{-1}\left(y_2 - y_1\right)^{-1}\left(\frac{\partial\left(T_1 - T_2\right)}{\partial p}\right) \tag{B.8}$$

$$\frac{\partial h}{\partial T_p} = k_p\left(y_2 - y_1\right)^{-1}\left[\frac{\partial\left(T_1 - T_2\right)}{\partial T_p}\left(T_p - T_i\right)^{-1} - \left(T_1 - T_2\right)\left(T_p - T_i\right)^{-2}\right] \tag{B.9}$$

where

$$\begin{aligned}\frac{\partial\left(T_1 - T_2\right)}{\partial Z} = 3GpT_p\Big\{ &\left[\left(2\eta_1 R\lambda T_p + 3GZp\right)^{-1} - 3GZp\left(2\eta_1 R\lambda T_p + 3GZp\right)^{-2}\right] \\ &- \left[\left(2\left(\eta_1 + 1\right)R\lambda T_p + 3GZp\right)^{-1} - 3GZp\left(2\left(\eta_1 + 1\right)R\lambda T_p + 3GZp\right)^{-2}\right]\Big\}\end{aligned}$$

$$\begin{aligned}\frac{\partial\left(T_1 - T_2\right)}{\partial p} = 3GZT_p\Big\{ &\left[\left(2\eta_1 R\lambda T_p + 3GZp\right)^{-1} - 3GZp\left(2\eta_1 R\lambda T_p + 3GZp\right)^{-2}\right] \\ &- \left[\left(2\left(\eta_1 + 1\right)R\lambda T_p + 3GZp\right)^{-1} - 3GZp\left(2\left(\eta_1 + 1\right)R\lambda T_p + 3GZp\right)^{-2}\right]\Big\}\end{aligned}$$

$$\frac{\partial(T_1 - T_2)}{\partial T_p} = 3GZp\Big\{ \left[(2\eta_1 R\lambda T_p + 3GZp)^{-1} - 2T_p\eta_1 R\lambda(2\eta_1 R\lambda T_p + 3GZp)^{-2}\right] - \left[(2(\eta_1 + 1)R\lambda T_p + 3GZp)^{-1} - 2T_p(\eta_1 + 1)R\lambda(2(\eta_1 + 1)R\lambda T_p + 3GZp)^{-2}\right]\Big\}$$

B.2.2 Wedge Fringe Method

As before, assuming that each independent variable was given the same odds, then the relation between the uncertainty of the variables, and the magnitude of the uncertainty for the local heat transfer coefficient, would be

$$\delta h = \sqrt{\begin{gathered}\left(\frac{\partial h}{\partial k_p}\delta k_p\right)^2 + \left(\frac{\partial h}{\partial p}\delta p\right)^2 + \left(\frac{\partial h}{\partial Z}\delta Z\right)^2 + \left(\frac{\partial h}{\partial T_i}\delta T_i\right)^2 \\ + \left(\frac{\partial h}{\partial T_p}\delta T_p\right)^2 + \left(\frac{\partial h}{\partial d}\delta d\right)^2 + \left(\frac{\partial h}{\partial \alpha}\delta \alpha\right)^2\end{gathered}} \qquad \text{(B.10)}$$

where the expression for h is given in Eq. (3.26). Again, the uncertainties in the gas constant, specific refractivity, and the He-Ne laser wavelength have been neglected. The partial derivatives were computed with respect to the variables, are

$$\frac{\partial h}{\partial k_p} = \frac{2R\lambda T_p^2}{3GZp(T_p - T_i)d\tan\alpha} \qquad \text{(B.11)}$$

$$\frac{\partial h}{\partial p} = -\frac{2R\lambda T_p^2 k_p}{3GZp^2(T_p - T_i)d\tan\alpha} \qquad \text{(B.12)}$$

$$\frac{\partial h}{\partial Z} = -\frac{2R\lambda T_p^2 k_p}{3GZ^2 p(T_p - T_i)d\tan\alpha} \qquad \text{(B.13)}$$

$$\frac{\partial h}{\partial T_\infty} = \frac{2R\lambda T_p^2 k_p}{3GZp(T_p - T_i)^2 d\tan\alpha} \qquad \text{(B.14)}$$

$$\frac{\partial h}{\partial T_p} = \frac{2R\lambda T_p k_p}{3GZp(T_p - T_i)d\tan\alpha}\left(2 - \frac{T_p}{(T_p - T_i)}\right) \tag{B.15}$$

$$\frac{\partial h}{\partial d} = -\frac{2R\lambda T_p^2 k_p}{3GZp(T_p - T_i)d^2\tan\alpha} \tag{B.16}$$

$$\frac{\partial h}{\partial \alpha} = -\frac{2R\lambda T_p^2 k_p(1 + \tan^2\alpha)}{3GZp(T_p - T_i)d\tan^2\alpha} \tag{B.17}$$

B.2.3 Convective Heat Flux

Applying Eq. (B.2) to Eq. (3.27)

$$\delta q = \sqrt{\left(\frac{\partial q}{\partial T_i}\delta T_i\right)^2 + \left(\frac{\partial q}{\partial T_p}\delta T_p\right)^2 + \left(\frac{\partial q}{\partial h}\delta h\right)^2} \tag{B.18}$$

where

$$\frac{\partial q}{\partial T_i} = -h \tag{B.19}$$

$$\frac{\partial q}{\partial T_p} = h \tag{B.20}$$

$$\frac{\partial q}{\partial h} = (T_p - T_i) \tag{B.21}$$

It is important to realize that the uncertainty associated with $\bar{h}$ is not the same as the previously calculated uncertainty of the local *h*. By averaging the data, most of the "noise" is filtered out in the integration process. Logically, the more data points that are used to calculate the average, the more accurate the mean will become. Unfortunately, this no longer becomes a single sample uncertainty and the method of Kline and McClintock (1953) can not be applied.

B.3 Sample Calculation

To clarify the method of analysis, a typical sample calculation is presented for the interferograms shown in Fig. B-1 (b = 15.4 mm, $\theta = 0^{\circ}$). These interferograms were taken on the same system under identical conditions. For validation cases 2,4,6, and 8, wedge fringe interferograms were used in the quantitative analysis, while infinite fringe interferograms were used for isotherm comparison. In case 2, however, the heat flux near the slat tip is large enough that either method can be used. Figure B-2 shows a close up of the same system in the area around the lowest scale and lowest leveling pins. The louvers visible in the photograph are the second and third from the bottom of the model.

Pertinent Test Data

ambient temperature (T_i) = 296.16 K
average plate temperature (T_p) = 298.30 K
ambient pressure (p) = 100 898.3 Pa

Test Section Specifications

plate height (l) = 0.3810 m
plate length in direction of beam (Z) = 0.3556 m

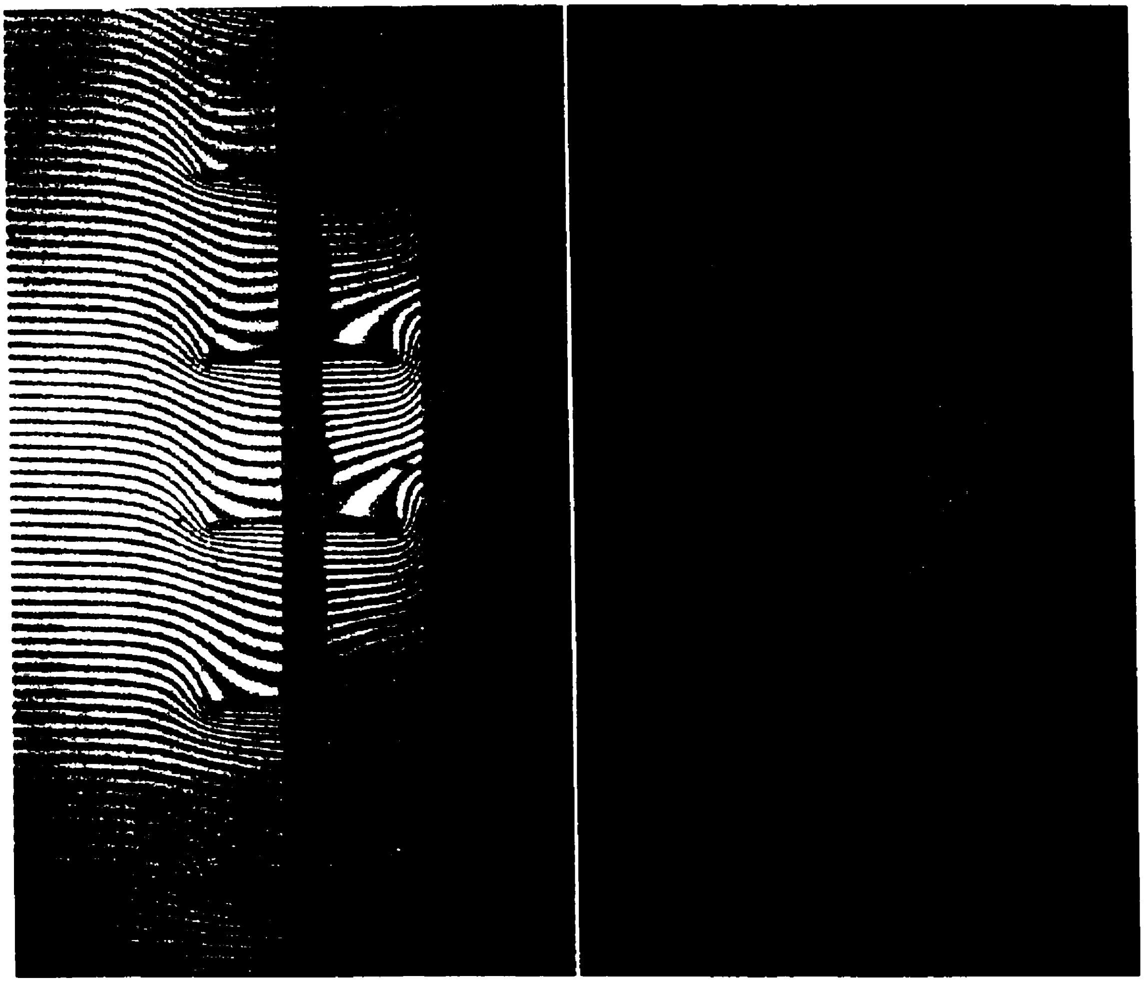

Figure B-1: Sample infinite (left) and wedge (right) fringe interferograms for validation case 2 (b = 15.4 mm, $\phi = 0^{\circ}$).

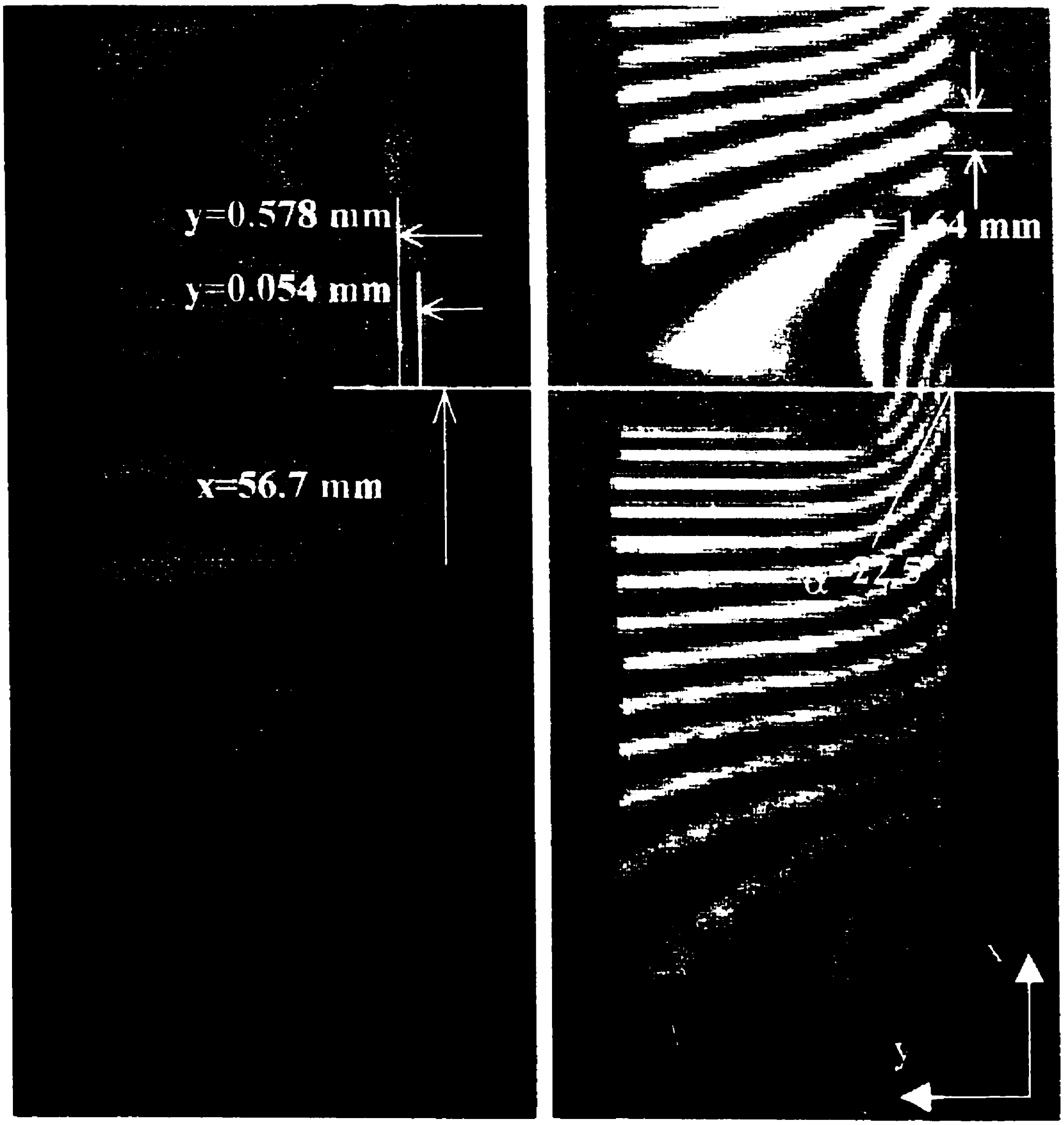

Figure B-2: Close-up infinite (left) and wedge (right) fringe interferograms for validation case 2 (b = 15.4 mm, $\phi = 0°$).

Scale factor specifications

The interferograms produced were not a 1:1 scale model, thus a scale factor was used with each fringe measurement. Small pins were strategically placed on the plate to serve as a reference of location along the plate and to function as a known spacing in order to determine a scale factor.

actual pin spacing on plate = 50.8 mm
pin spacing on scale photo = 40.2 mm

$$SF = \frac{actual\ pin\ distance}{measured\ pin\ distanance} \tag{B.22}$$

$$SF = \frac{50.8}{40.2} = 1.26$$

All properties of air were obtained from published data from the Thermophysical Properties Research Center, Purdue University (Touloukian et al. 1970a, 1970b, 1975). Recommended values for dynamic viscosity, thermal conductivity, and specific heat were compiled from an extensive collection of many independent experimental investigations (at standard pressure). All properties are considered to be a function of temperature only, with the exception of density. All of the air properties were evaluated at an estimated film temperature of 300 K.

Dynamic Viscosity (μ)

In the temperature range of this study, the values have an estimated accuracy of ±0.5%. At T_f= 300.00 K

$$\mu = 18.53 \times 10^{-6} \ kg/ms$$

Thermal Conductivity (k)

Linear interpolation of the data Touloukian, Liley, and Saxena (1970) was assumed. An extensive amount of research has been done around room temperature and the data is estimated to be accurate to ±1%. At T_f= 300.00 K

$$k_f = 26.14 \times 10^{-3} \ W/mK$$

At T_p = 298.30 K

$$k_p = 26.03 \times 10^{-3} \ W/mK$$

Specific Heat (C_p)

The following polynomial expression given by Touloukian and Makita (1970) was used and is valid for the temperature range of 260 K to 610 K, at standard pressure. The results are estimated to be accurate to ±0.25%. At T_f= 300.00 K

$$C_p = 1044.66 - 3.1597 \times 10^{-1}(T_f) + 7.07908 \times 10^{-4}(T_f)^2 - 2.7034 \times 10^{-7}(T_f)^3 \qquad \text{(B.23)}$$

$$= 1044.66 - 3.1597 \times 10^{-1}(300.00) + 7.07908 \times 10^{-4}(300.00)^2 - 2.7034 \times 10^{-7}(300.00)^3$$
$$= 1006.3 \ J/kgK$$

Density (ρ)

The density of air was calculated using the ideal gas law.

$$\rho = \frac{p}{RT_f} \tag{B.24}$$

$$= \frac{100898.3}{287.097 \times 300.00} = 1.169 \ kg/m^3$$

Coefficient of Thermal Expansion (β)

Since air is considered to behave as an ideal gas, the expression for the coefficient of thermal expansion can be simplified to

$$\beta = \frac{1}{T_f} \tag{B.25}$$

$$= \frac{1}{300.00} = 33.33 \times 10^{-4} \ \frac{1}{K}$$

B.3.1 Infinite Fringe Method

Fringe Shift, η

As outlined in Chapter 3, the first fringe represents a fractional fringe shift (η_1). Each successive fringe thus represents a shift of $\eta + 1$. Using a linear relationship between the wall and the first two clearly visible fringes (in this case the second and third fringes), the fractional shift is determined by

$$\eta_i = \frac{y_i}{y_{i+1} - y_i} \tag{B.26}$$

From Fig. B-2, at the position x_{photo}= 45.0 mm (x = 56.7 mm), the following information was obtained

$y_{1,photo} = ?$
$y_{2,photo} = 0.054$ mm
$y_{3,photo} = 0.578$ mm

$$\eta_2 = \frac{0.054}{0.578 - 0.054} = 0.103$$

Fringe Temperature Calculations

The temperature of each fringe was calculated using Eq. (3.13)

$$T_i = \frac{T_p}{\frac{2\eta_i R\lambda T_p}{3GZp} + 1} \tag{B.27}$$

Therefore

$$T_2 = \frac{298.30}{\frac{2(0.103)(287.097)(0.6328 \times 10^{-6})(298.30)}{3(0.1504 \times 10^{-3})(0.3556)(100898.3)} + 1} = 298.09\ K$$

and

$$T_3 = \frac{298.30}{\frac{2(1 + 0.103)(287.097)(0.6328 \times 10^{-6})(298.30)}{3(0.1504 \times 10^{-3})(0.3556)(100898.3)} + 1} = 296.11\ K$$

Temperature Gradient

By linear extrapolation, the temperature gradient is given by

$$\left.\frac{dT}{dy}\right|_{wall} \cong \frac{T_2 - T_3}{(y_2 - y_3)SF} \tag{B.28}$$

$$\cong \frac{298.09-296.11}{(0.000054-0.000578)1.26} = -2992.8\ \frac{K}{m}$$

Local Convection Coefficient, *h*

At a point 56.7 mm from the leading edge, the local convection coefficient was calculated from Eq. (3.15).

$$h = \frac{-k_p \left.\frac{dT}{dy}\right|_{wall}}{(T_p - T_t)}$$

$$h_{56.7} = \frac{-26.03\times10^{-3}(-2992.8)}{298.30-296.16} = 36.41\ \frac{W}{m^2K}$$

Local Heat Flux, *q*

From Eq. (3.27), the local convective heat flux is defined as

$$q = h(T_p - T_t)$$

thus, at the same location from the leading edge

$$q_{56.7} = 36.41(298.30-296.16) = 77.92\ \frac{W}{m^2}$$

B.3.2 Wedge Fringe Method

Local Convection Coefficient, *h*

From Fig. B-2, assuming that the ambient fringe is perpendicular to the plate surface, at the position $x_{photo} = 45.0$ mm ($x = 56.7$ mm), the following information was obtained

fringe angle $\alpha = 22.5^{\circ}$
fringe spacing in ambient = 1.62 mm

Therefore, from Eq. (3.26)

$$h = \frac{2R\lambda T_p^2 k_p}{3GZp\left(T_p - T_t\right)d \tan\alpha}$$

$$h_{56.7} = \frac{2(287.097)\left(0.6328\times10^{-6}\right)(298.30)^2\left(26.03\times10^{-3}\right)}{3\left(0.1504\times10^{-3}\right)(0.3556)(100898.3)(298.30-296.16)\left(1.62\times10^{-3}\right)\tan 22.5}\,.$$

$$= 36.20\ \frac{W}{m^2K}$$

Local Heat Flux, *q*

As before, using Eq. (3.27), the local convective heat flux at the same location from the leading edge

$$q_{56.7} = 36.20(298.30 - 296.16) = 77.47\ \frac{W}{m^2}$$

B.3.3 Uncertainty

The uncertainty in the measurements will only be summarized here. Table B-1 shows the uncertainty in the variables and for the entire calculation.

Table B-1: Interferometric measurement uncertainties.

	Infinite Fringe Method		Wedge Fringe Method	
Variable	δx_i (±)	$\frac{\partial R}{\partial x_i}\delta x_i$	δx_i (±)	$\frac{\partial R}{\partial x_i}\delta x_i$
k	0.0005 W/m·K	0.669 W/m^2·K	0.0005 W/m·K	0.760 W/m^2·K
p	30 Pa	0.011 W/m^2·K	30 Pa	0.012 W/m^2·K
Z	0.002 m	0.203 W/m^2·K	0.002 m	0.222 W/m^2·K
T_i	0.2 K	3.399 W/m^2·K	0.2 K	3.693 W/m^2·K
T_p	0.2 K	3.351 W/m^2·K	0.2 K	3.640 W/m^2·K
d			0.000025 m	0.666 W/m^2·K
$y_{2,1}$	0.000025 m			
y_2-y_1	0.000035 m	1.943 W/m^2·K		
α			2 deg	3.902 W/m^2·K
h	5.20 W/m^2·K	11.14 W/K	6.57 W/m^2·K	14.06 W/K
T_i	0.2 K	7.27 W/K	0.2 K	7.23 W/K
T_p	0.2 K	7.27 W/K	0.2 K	7.23 W/K
q	15.16 W/m^2		17.39 W/m^2	

All uncertainties are specified at a 95% confidence level (20 to 1 odds). The uncertainty in the thermal conductivity of air was estimated from scatter plots of data from a large number of independent measurements presented by Touloukian et al. (1970b). For the fringe angle measurement, the uncertainty was estimated by making several measurements of the same set of fringe angles. The ambient wedge fringe spacing (*d*) was obtained by measuring the distance between *n* fringes, where *n* was taken as large as possible on the interferogram. The main source of error in the measured fringe spacing was found to be imperfections in the optics. This uncertainty was estimated to be *d* = +/- 0.025 mm. With the current manual system, it was not possible to measure the fringe angle with an accuracy better than about 2 deg. Although calibrated, the uncertainty of temperature measurements has been conservatively estimated to account for non-uniform temperature distributions in the ambient air and in the plate surface. Other uncertainties were obtained from equipment specifications or measurement accuracy.

By inspection of Table B-1, when considering the infinite fringe measurement technique, the dominant sources of uncertainty in the convective heat transfer coefficient are the plate and ambient temperature measurements. As the plate to ambient temperature difference increases, this error becomes less. i.e., higher heat flux means that the infinite fringe technique becomes less uncertain. When considering the wedge fringe technique, the fringe angle also becomes important. As discussed by Naylor and Duarte (1999) this angle tends to be the dominant variable. As flux decreases, and α increases, the wedge fringe measurement becomes more accurate.

For this analysis, the chosen sample point was selected because both the infinite and wedge fringe methods were needed to analyze the interferogram. In the actual analysis, presented in Chapter 3, the infinite fringe technique was used to analyze this particular data point because of the relatively large heat flux in that area. Even so, the fringe shift is too small to give a good uncertainty. Unfortunately, the convective flux is large enough to give a small fringe angle, thereby making a wedge fringe interferogram even less accurate. This trade off between methods is discussed in detail by Naylor and Duarte (1999). When it was uncertain as to which technique should be used, both were performed and the less uncertain measurement was used.

APPENDIX C
INTERFEROMETER / NUMERICAL OUTPUT

C.1 Introduction

This Appendix presents additional data to support the validation of the numerical model presented in Chapter 3. A comparison of numerical and interferometric results has been made with the Ostrach's (1953) boundary layer solution. Additionally, the complete set of interferometric photographs are included, and combined with isothermal plots produced using the numerical model. The wedge fringe interferograms used in the analysis of cases 2, 4, 6, and 8 have also been included. Selected data for the analysis of case 2 has also been included for completeness. The complete data is available from the Queen's University Solar Calorimetry laboratory.

C.2 Isothermal Vertical Flat Plate Solution

Ostrach's (1953) boundary layer solution for the local heat transfer coefficient distribution along an isothermal vertical plate could be used as a comparison for the numerical and experimental results. Figure C-1 and Table C-1 present the input data and data analysis respectively. The final results of that comparison can be seen in Fig. C-2.

T_i	296.16 K
T_p	317.75 K
T_f	306.96 K
L	0.3810 m
Z	0.3556 m
Pin Act	0.0508 m
Pin Photo	0.0416 m
SF	1.22
p	100685 Pa
C_f	1006.55 J/kg·K
β_f	3.26E-03 K^{-1}
ρ_f	1.14E+00 kg/m^3
μ_f	1.89E-05 kg/m·s
k_f	2.66E-02 W/m·K
k_p	2.74E-02 W/m·K
Ra_l	9.97E+07

Figure C-1: Infinite fringe interferogram for no blind case with test conditions.

Table C-1: Sample analysis of numerical and interferometric data for no-blind case. Ostrach (1953) results are also included for comparison.

x_{photo}	x_{actual}	*fringe 1*	*fringe 2*	*e*	T_1	T_2	dT/dy	h_{IF}	h_{Ost}	h_{local}
0.001	0.001	0.781	0.959	4.388	308.09	305.97	-9746.73	12.38	11.64	
0.002	0.002	0.791	1.038	3.202	310.59	308.42	-7187.53	9.13	9.41	
0.003	0.003	0.822	1.084	3.137	310.73	308.56	-6782.21	8.62	8.40	
0.004	0.005	0.830	1.131	2.757	311.57	309.38	-5935.04	7.54	7.77	
0.005	0.006	0.857	1.160	2.828	311.41	309.23	-5889.99	7.48	7.32	
0.006	0.007	0.895	1.175	3.196	310.61	308.44	-6340.96	8.06	6.98	
0.007	0.008	0.930	1.230	3.100	310.82	308.64	-5926.24	7.53	6.71	
0.008	0.009	0.996	1.330	2.982	311.07	308.90	-5331.79	6.77	6.48	
0.009	0.011	1.001	1.350	2.868	311.32	309.14	-5110.79	6.49	6.29	
0.010	0.012	1.012	1.368	2.843	311.38	309.20	-5012.10	6.37	6.12	
0.011	0.013	1.032	1.401	2.797	311.48	309.30	-4838.64	6.15	5.97	
0.012	0.014	1.031	1.414	2.692	311.71	309.53	-4668.65	5.93	5.84	
0.013	0.016	1.044	1.422	2.762	311.56	309.37	-4725.75	6.00	5.72	
0.014	0.017	1.053	1.433	2.771	311.54	309.35	-4700.28	5.97	5.61	
0.015	0.018	1.056	1.448	2.694	311.71	309.52	-4561.34	5.79	5.52	
0.016	0.019	1.064	1.460	2.687	311.72	309.54	-4515.71	5.74	5.43	
0.017	0.020	1.073	1.496	2.537	312.05	309.86	-4236.42	5.38	5.34	
0.018	0.022	1.084	1.500	2.606	311.90	309.71	-4303.52	5.47	5.27	
0.019	0.023	1.086	1.519	2.508	312.12	309.93	-4140.25	5.26	5.19	
0.020	0.024	1.100	1.519	2.625	311.86	309.67	-4271.53	5.43	5.13	
0.021	0.025	1.118	1.546	2.612	311.89	309.70	-4182.48	5.31	5.06	
0.022	0.027	1.120	1.548	2.617	311.88	309.69	-4182.21	5.31	5.01	
0.023	0.028	1.128	1.555	2.642	311.82	309.64	-4190.53	5.32	4.95	
0.024	0.029	1.138	1.565	2.665	311.77	309.58	-4189.15	5.32	4.90	
0.025	0.030	1.153	1.580	2.700	311.69	309.51	-4187.08	5.32	4.85	
0.026	0.031	1.149	1.586	2.629	311.85	309.66	-4095.36	5.20	4.80	
0.027	0.033	1.143	1.579	2.622	311.87	309.68	-4105.20	5.22	4.75	
0.028	0.034	1.148	1.582	2.645	311.81	309.63	-4122.74	5.24	4.71	
0.029	0.035	1.148	1.596	2.563	312.00	309.81	-3998.56	5.08	4.67	
0.030	0.036	1.156	1.603	2.586	311.94	309.76	-4006.17	5.09	4.63	
0.031	0.038	1.156	1.628	2.449	312.25	310.05	-3801.31	4.83	4.59	
0.032	0.039	1.151	1.636	2.373	312.41	310.22	-3703.38	4.70	4.55	
0.033	0.040	1.155	1.630	2.432	312.29	310.09	-3778.24	4.80	4.52	
0.001	0.000									23.03
0.003	0.001									13.29
0.007	0.003									10.13
0.011	0.004									8.54
0.018	0.007									7.57
0.023	0.009									7.03
0.027	0.010									6.76
0.029	0.011									6.63
0.030	0.011									6.57
0.033	0.013									6.38
0.038	0.014									6.17
0.043	0.016									5.94
0.051	0.019									5.71
0.059	0.023									5.47
0.068	0.026									5.29
0.075	0.029									5.16
0.080	0.031									5.07
0.084	0.032									5.01
0.087	0.033									4.97
0.088	0.034									4.95
0.092	0.035									4.90
0.096	0.037									4.85
0.102	0.039									4.78

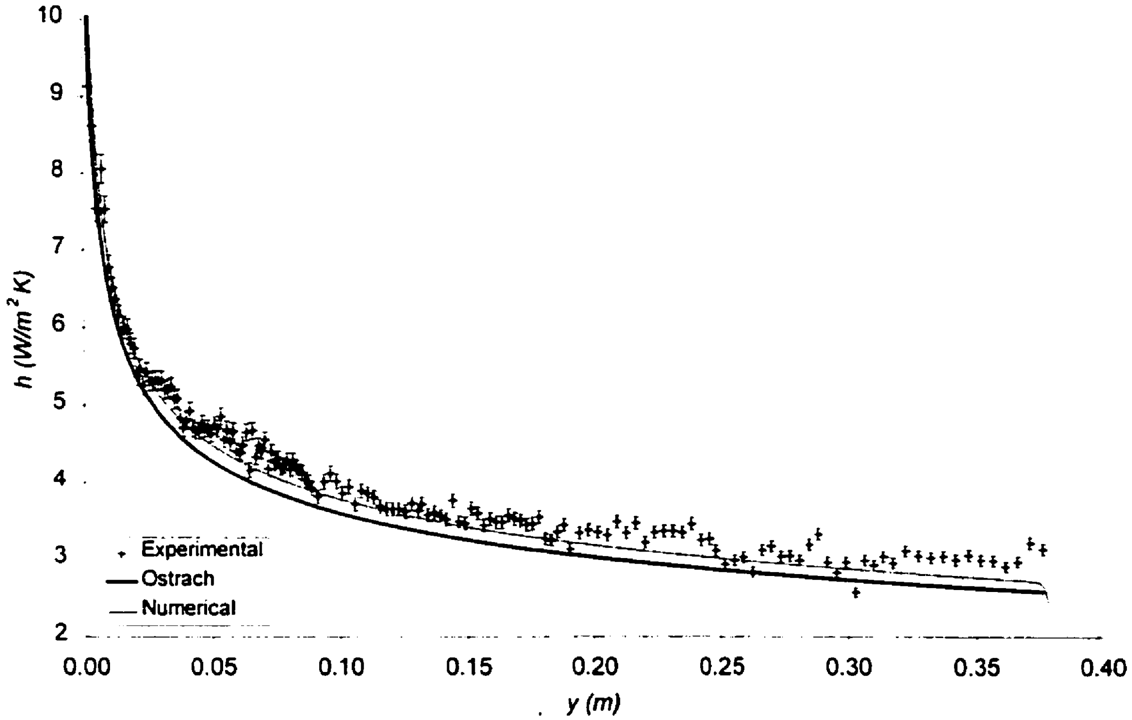

Figure C-2: Comparison of the local convection Nusselt number results for the "no blind" case with the similarity solution of Ostrach (1953), $Ra_l = 10^8$.

It can be seen that these results are in close agreement with this well validated boundary layer solution. The average convective heat transfer coefficient given by the experimental and numerical models differ by 3.6% and 1.1% respectively from Ostrach's solution at $Ra_l = 10^8$.

C.3 Validation Cases

C.3.1 Photos

The number of isotherms in the validation cases were determined as described by Machin (1997). By dividing the difference of the hottest and coldest experimental temperatures by 2.3 fringes/K, the theoretical number of fringes can be predicted. For the odd numbered cases (cold plate), this would be

$$number\ fringes = \frac{T_b - T_p}{2.3} \tag{C.1}$$

while for the even numbered cases (warm plate), this would be

$$number\ fringes = \frac{T_b - T_i}{2.3} \tag{C.2}$$

T_b, T_p, and T_i are the blind, plate, and ambient temperatures respectively. Interferograms and numerically obtained isotherms are presented in Figs. C-3 through C-6. Wedge fringe interferograms have also been presented as Figure C-7.

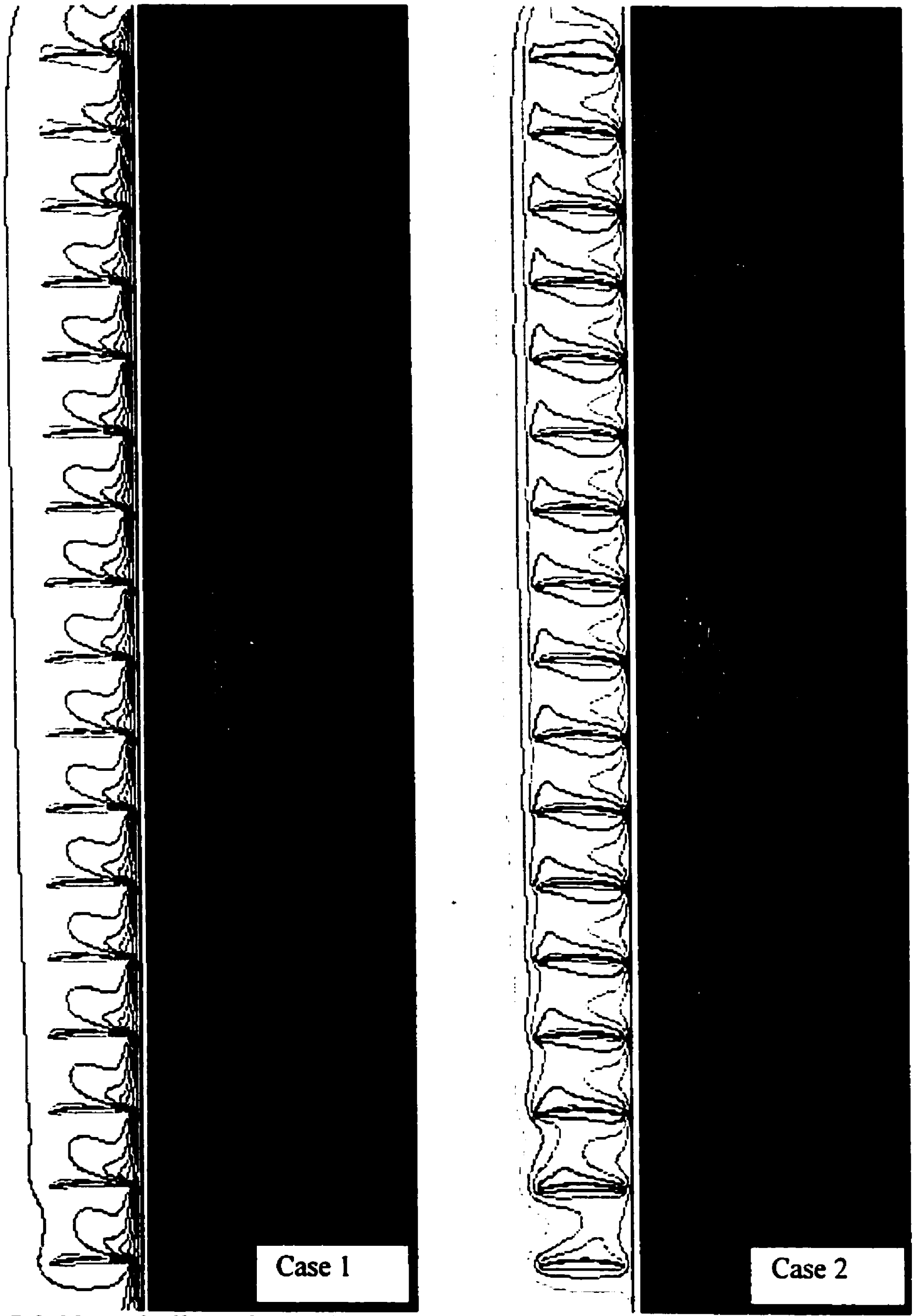

Figure C-3: Numerically and experimentally determined isotherms for $\phi = 0°$, b = 15.4 mm.

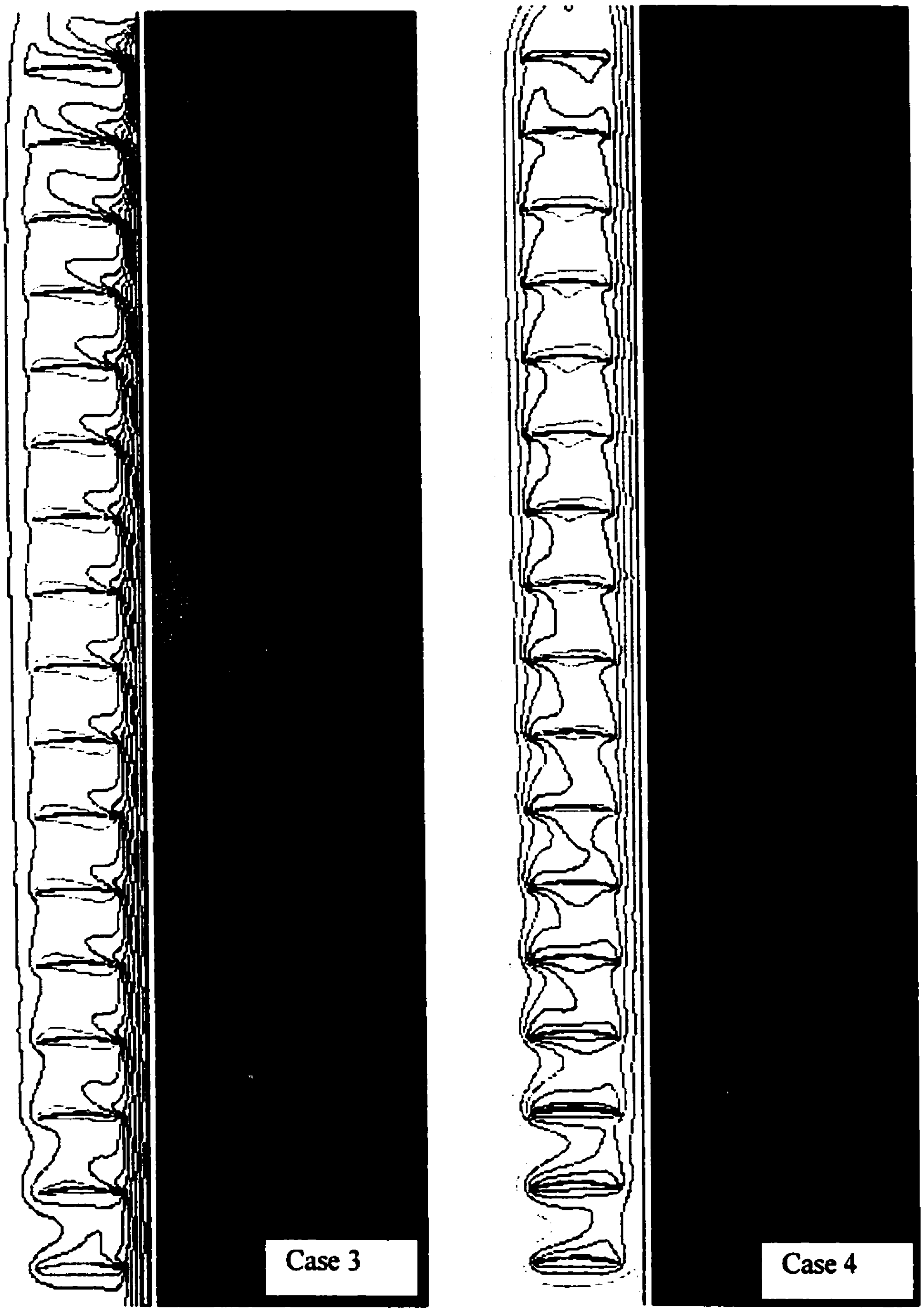

Figure C-4: Numerically and experimentally determined isotherms for $\phi = 0^\circ$, $b = 20.0$ mm.

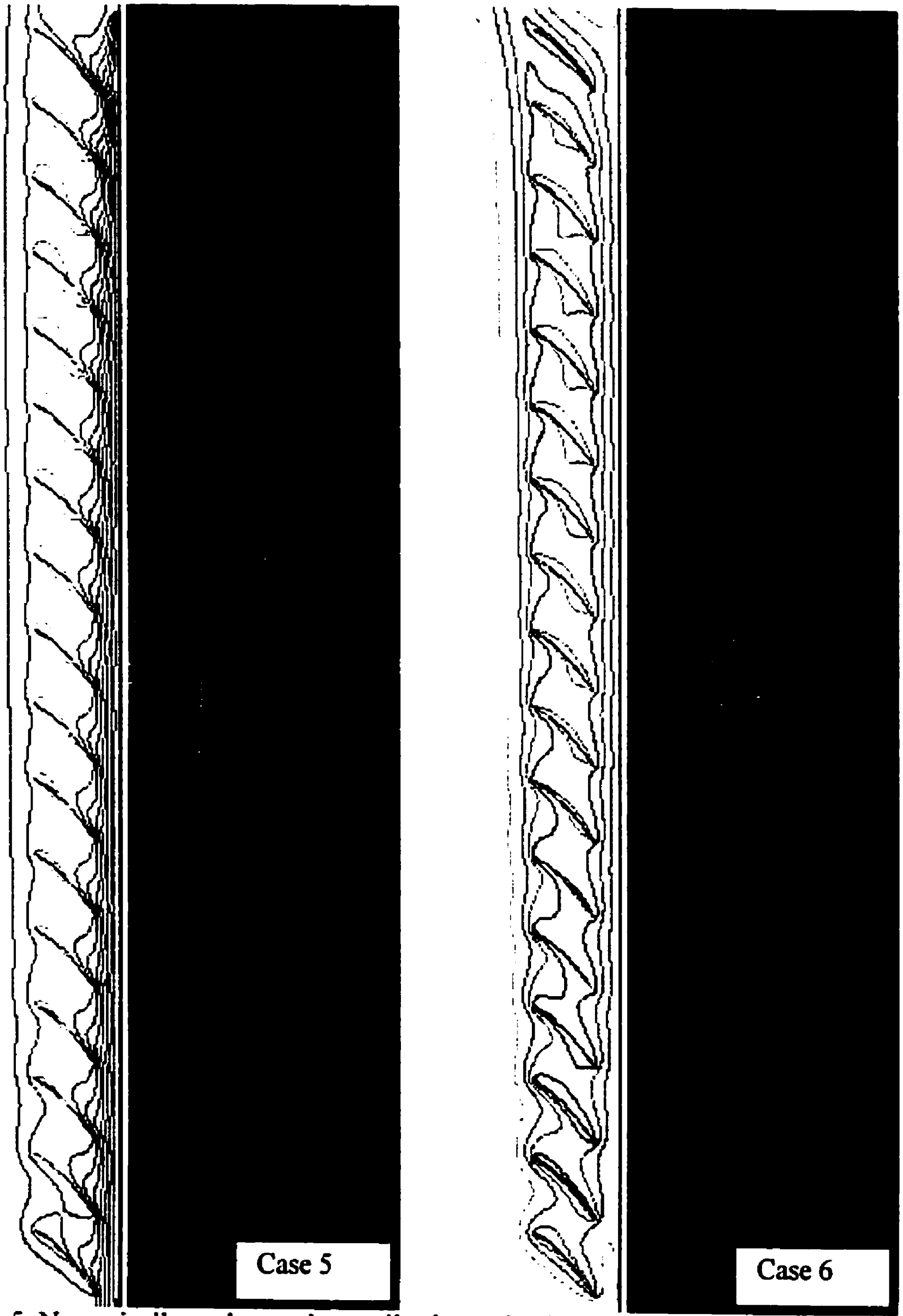

Figure C-5: Numerically and experimentally determined isotherms for $\phi = 45°$, b = 15.4 mm.

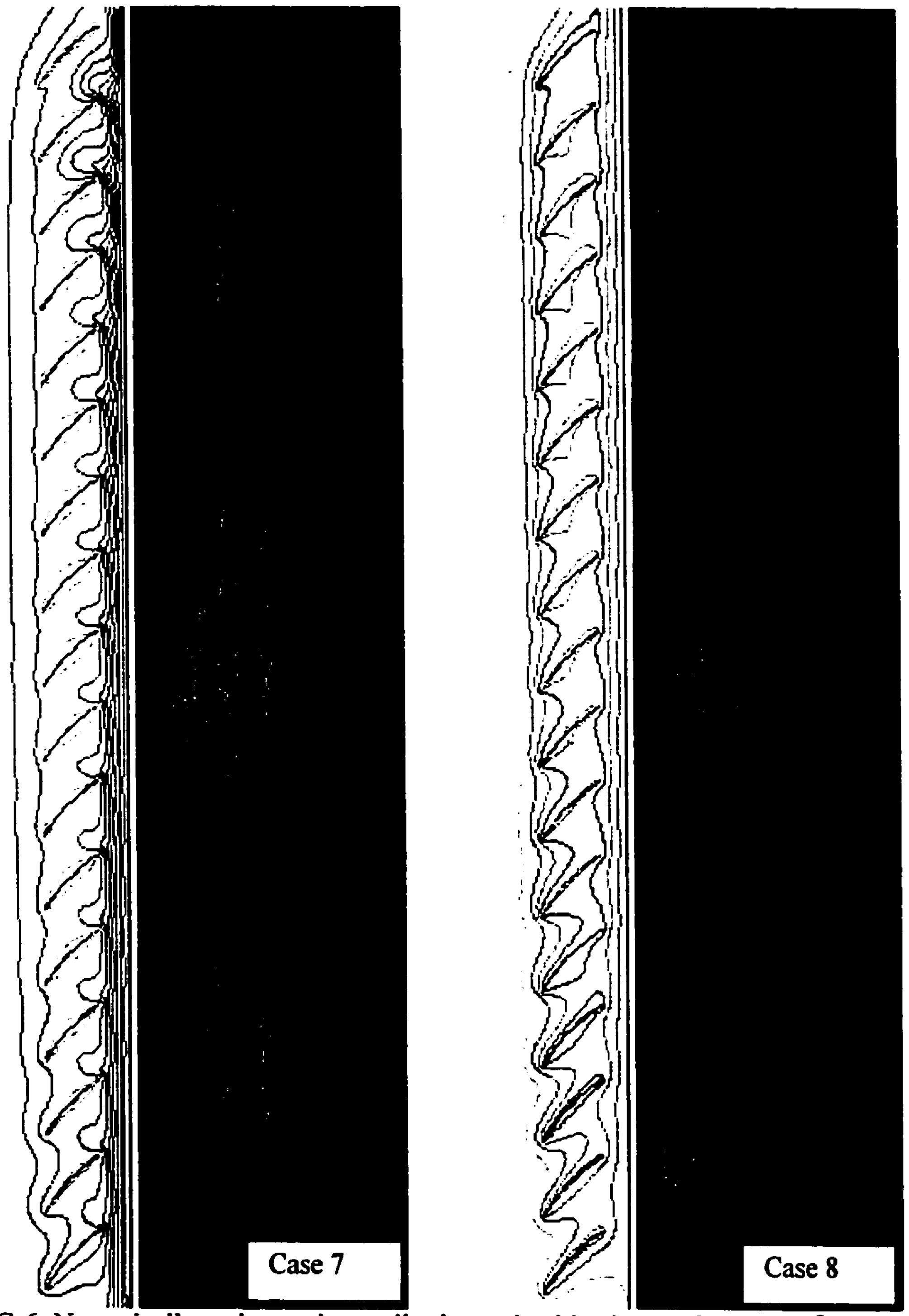

Figure C-6: Numerically and experimentally determined isotherms for $\phi = -45°$, $b = 15.4$ mm.

Figure C-7: Experimentally determined wedge fringe interferograms for validation cases 2, 4, 6, and 8.

C.3.2 Sample Data

As in Appendix B, sample data from case 2 will be presented. Although both an infinite and wedge fringe interferogram was taken for this model, only the wedge fringe photograph was used to perform the analysis. Figure C-8 shows the photograph of the system with the input variables while Table C-2 present the sample data analysis. A complete sample calculation for this model has been presented in Appendix B.

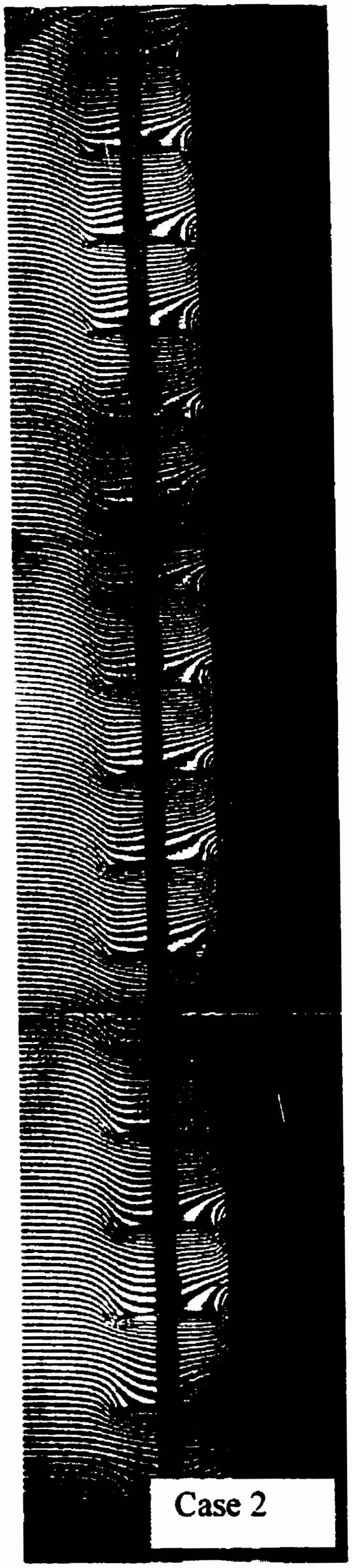

T_i	296.16 K
T_p	298.30 K
T_f	297.23 K
L	0.3810 m
Z	0.3556 m
Pin Act	0.0508 m
Pin Photo	0.0402 m
SF	1.26
p	100898 Pa
C_f	1006.19 J/kg·K
β_f	3.36E-03 K^{-1}
ρ_f	1.18E+00 kg/m^3
μ_f	1.84E-05 kg/m·s
k_f	2.59E-02 W/m·K
k_p	2.60E-02 W/m·K
Ra_l	1.15E+07

Figure C-8: Infinite fringe interferogram for validation case 2 with test conditions.

Table C-2: Sample analysis of selected interferometric data for validation case 2.

x_{photo}	x_{actual}	*Angle*	*fringe 1*	*fringe 2*	*e*	T_l	T_r	*dT/dy*	h_{IE}	h_{model}
0.001	0.0011	-99.67							2.55	
0.004	0.0044	-92.50							0.65	
0.006	0.0077	-82.00							-2.10	
0.009	0.0109	-56.33							-11.99	
0.011	0.0141		0.66	2.87	0.301	297.70	295.72	-709.35	-8.62	
0.014	0.0177	-71.33							-5.06	
0.017	0.0209	-73.33							-4.48	
0.019	0.0240	-67.00							-6.36	
0.022	0.0273	-58.67							-9.12	
0.024	0.0303		0.26	1.21	0.268	297.76	295.79	-1641.98	-19.95	
0.026	0.0335		0.17	0.91	0.229	297.84	295.86	-2118.56	-25.74	
0.029	0.0371		0.29	1.90	0.183	297.93	295.95	-975.45	-11.85	
0.032	0.0407	-69.17							-5.70	
0.035	0.0439	-71.33							-5.06	
0.037	0.0472	-64.50							-7.14	
0.040	0.0504	-46.00							-14.46	
0.042	0.0535		0.03	0.70	0.040	298.22	296.23	-2342.62	-28.47	
0.045	0.0567		0.05	0.58	0.103	298.09	296.11	-2992.83	-36.37	
0.048	0.0603		0.02	1.11	0.014	298.27	296.28	-1435.20	-17.44	
0.050	0.0635	-66.00							-6.67	
0.053	0.0668	-65.17							-6.93	
0.056	0.0701	-51.50							-11.91	
0.058	0.0733		0.13	0.90	0.165	297.97	295.99	-2021.86	-24.57	
0.060	0.0762		0.20	0.70	0.393	297.51	295.54	-3118.15	-37.89	
0.0010	0.0013									15.954
0.0018	0.0023									7.007
0.0029	0.0036									3.894
0.0043	0.0054									1.573
0.0061	0.0078									-2.202
0.0078	0.0098									-8.686
0.0088	0.0112									-13.886
0.0094	0.0119									-15.790
0.0098	0.0123									-16.281
0.0108	0.0137									-14.984
0.0122	0.0154									-10.770
0.0139	0.0175									-7.147
0.0161	0.0203									-5.981
0.0187	0.0237									-7.052
0.0213	0.0269									-9.361
0.0234	0.0295									-13.058
0.0250	0.0315									-19.234
0.0262	0.0331									-26.136
0.0270	0.0342									-28.275
0.0273	0.0346									-28.302
0.0284	0.0359									-24.424
0.0297	0.0376									-16.402
0.0315	0.0398									-9.177
0.0337	0.0425									-6.211
0.0363	0.0459									-9.493
0.0389	0.0492									-16.717
0.0410	0.0517									-25.158
0.0425	0.0538									-34.873
0.0438	0.0553									-43.220
0.0446	0.0564									-44.081
0.0449	0.0568									-43.329
0.0460	0.0581									-35.769
0.0473	0.0598									-23.327
0.0491	0.0620									-12.714
0.0513	0.0648									-7.578
0.0539	0.0681									-10.602
0.0565	0.0714									-18.762
0.0585	0.0740									-28.083
0.0601	0.0760									-38.470

APPENDIX D
PARAMETRIC RESULTS

D.1 Introduction

Chapter 4 presented sample results from the investigative and full parametric analysis. The present Appendix will present complete data results.

D.2 Investigative Parametric

The conditions used in the investigative parametric have been described in Chapter 4. The analysis was performed using the model described in Chapter 2. Tables 4-1 and 4-2 show the numerical model conditions. Fluid properties and miscellaneous model parameters are given in Table 4-3.

Average and local heat flux rates have been presented for the glass region located between the midpoint of the 5th and 6th slats, to the midpoint of the 12th and 13th slats. This vertical section includes 7 blind slats, and 0.16 m of glass. Local convective and radiative heat flux rates are given in Figs. D-1 through D-7 where slat positions are shown in gray and positive flux is from the plate to the air.

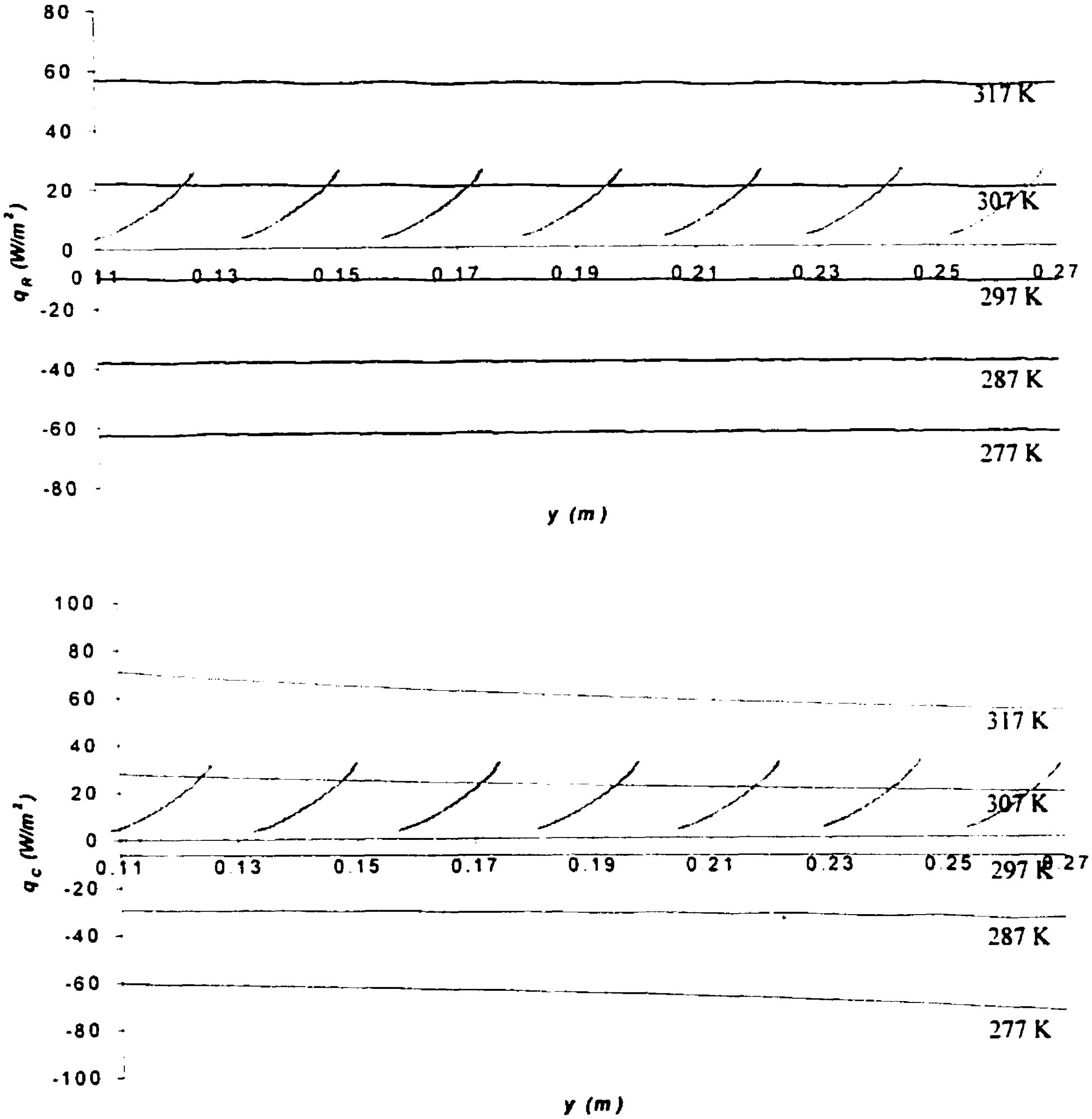

Figure D-1: Local convective and radiative heat flux in the center-of-glass region with changing glass temperature ($\phi = -45°$, $b = 30$ mm, $\varepsilon_b = \varepsilon_p = 0.6$, $q_b = 60$ W/m^2). Slat positions are shown in gray.

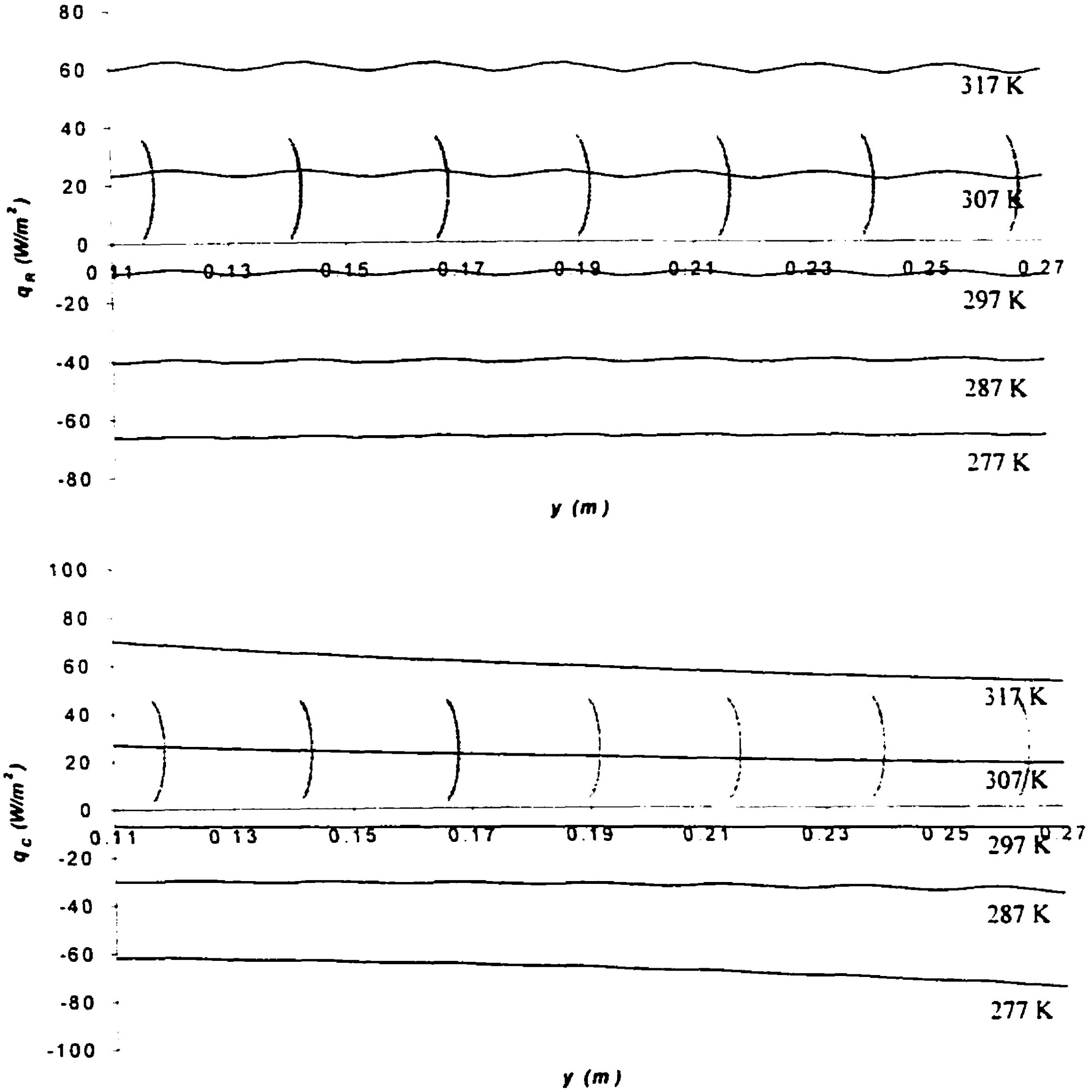

Figure D-2: Local convective and radiative heat flux in the center-of-glass region with changing glass temperature ($\phi = 0^\circ$, $b = 30$ mm, $\varepsilon_b = \varepsilon_p = 0.6$, $q_b = 60$ W/m^2). Slat positions are shown in gray.

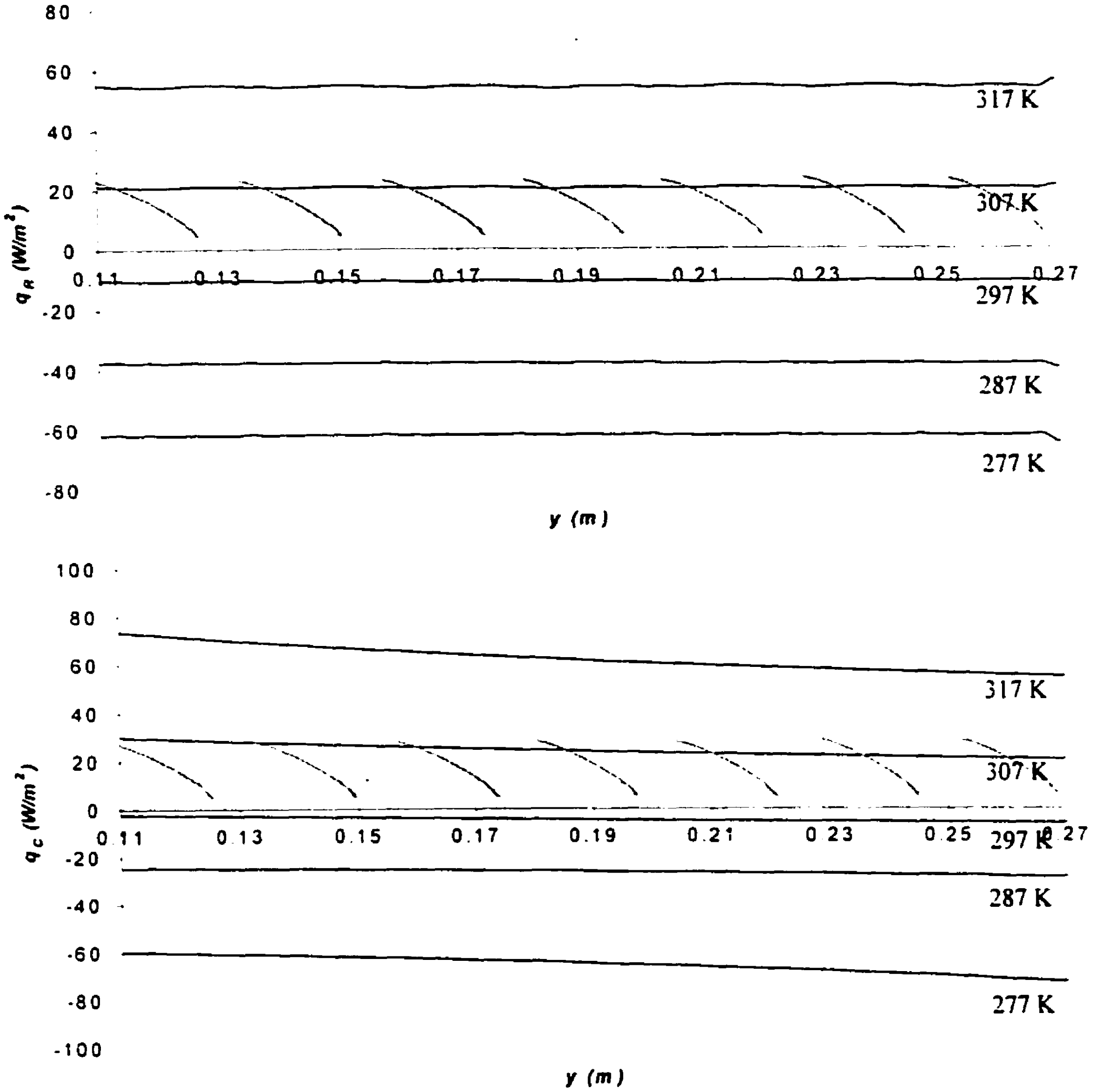

Figure D-3: Local convective and radiative heat flux in the center-of-glass region with changing glass temperature ($\phi = 45^\circ$, b = 30 mm, $\varepsilon_b = \varepsilon_p = 0.6$, q_b = 60 W/m^2). Slat positions are shown in gray.

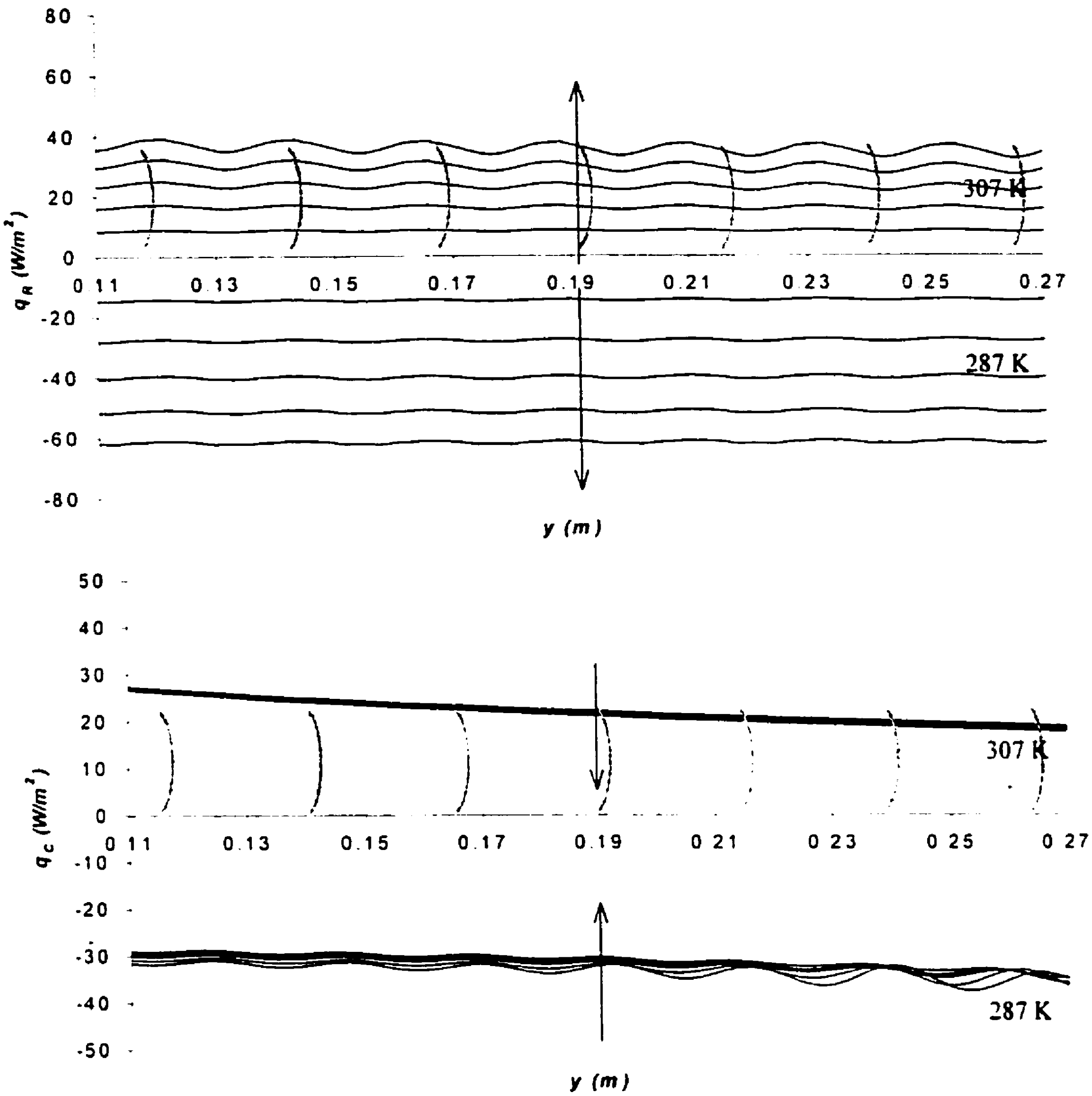

Figure D-4: Local convective and radiative heat flux in the center-of-glass region with changing plate emissivity and glass temperature ($\phi = 0^\circ$, $T_p = 287$ K, 307 K, $b = 30$ mm, $\varepsilon_b = 0.6$, $q_b = 60$ W/m^2). Slat positions are shown in gray. Arrows indicate direction of increasing plate emissivity.

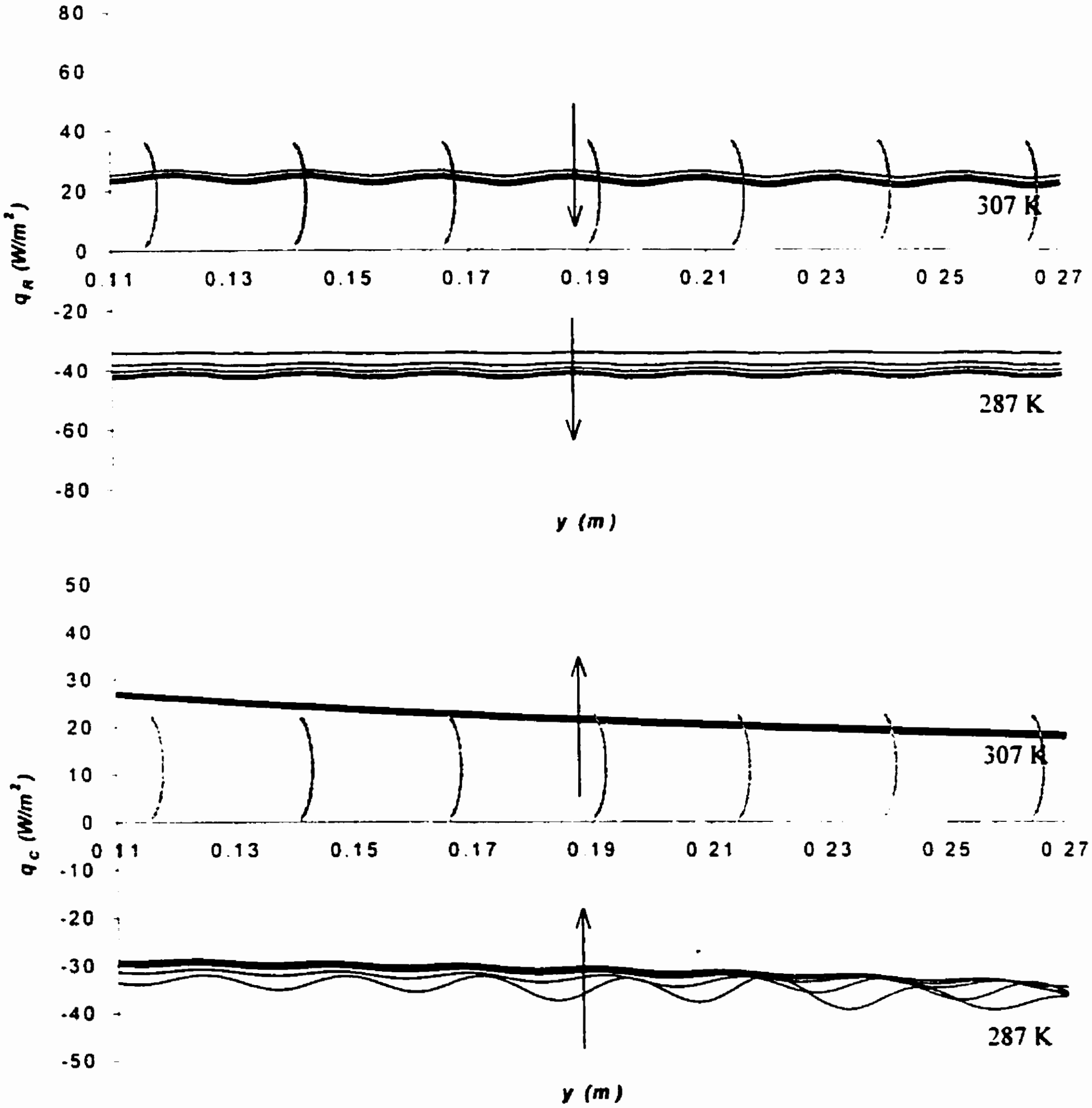

Figure D-5: Local convective and radiative heat flux in the center-of-glass region with changing blind emissivity and glass temperature ($\phi = 0°$, $T_p = 287$ K, 307 K, $b = 30$ mm, $\varepsilon_p = 0.6$, $q_b = 60$ W/m^2). Slat positions are shown in gray. Arrows indicate direction of increasing blind emissivity.

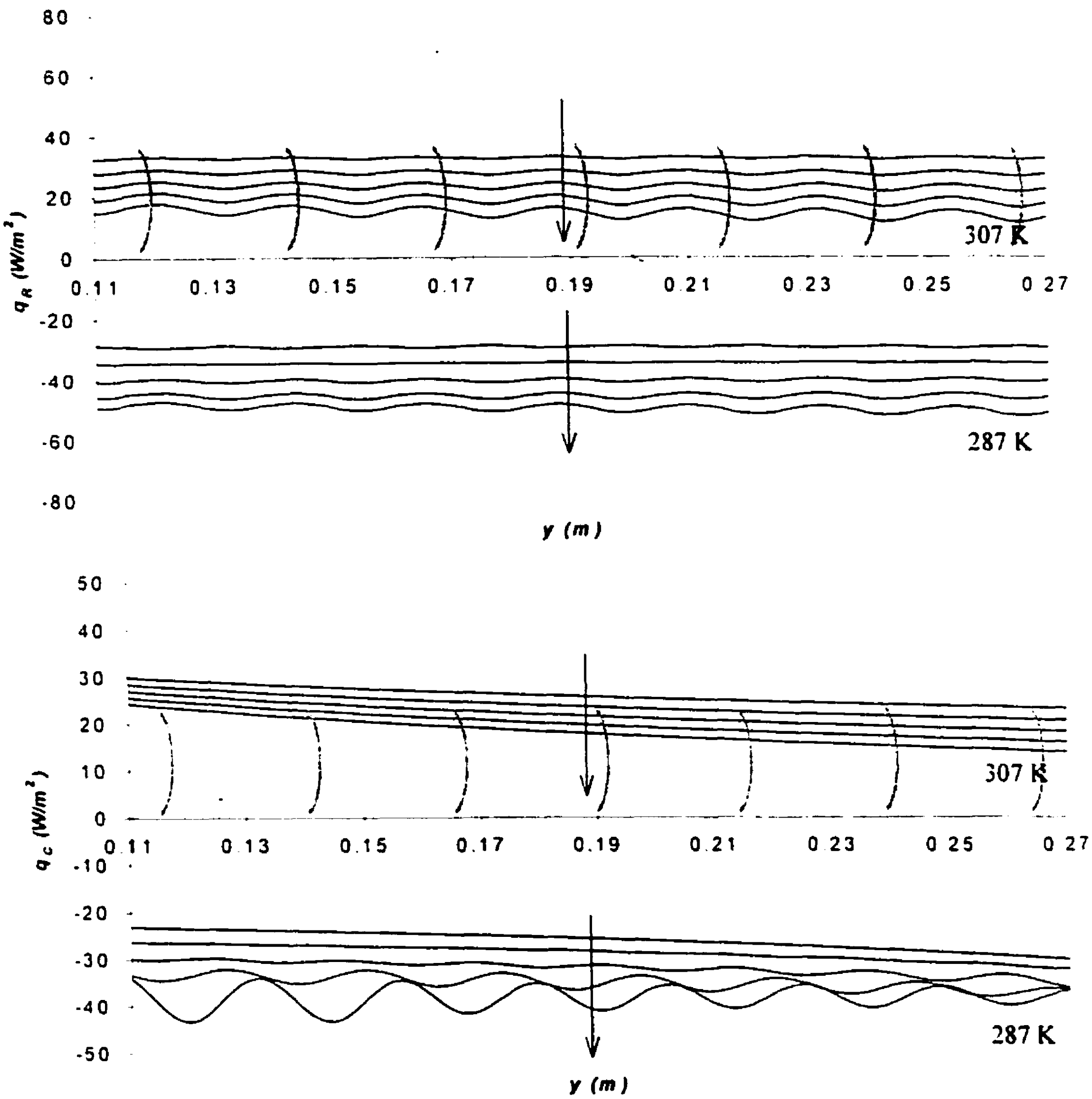

Figure D-6: Local convective and radiative heat flux in the center-of-glass region with changing absorbed solar flux and glass temperature (ϕ = 0°, T_p = 287 K, 307 K, b = 30 mm, $\varepsilon_b = \varepsilon_p$ = 0.6). Slat positions are shown in gray. Arrows indicate direction of increasing absorbed solar flux.

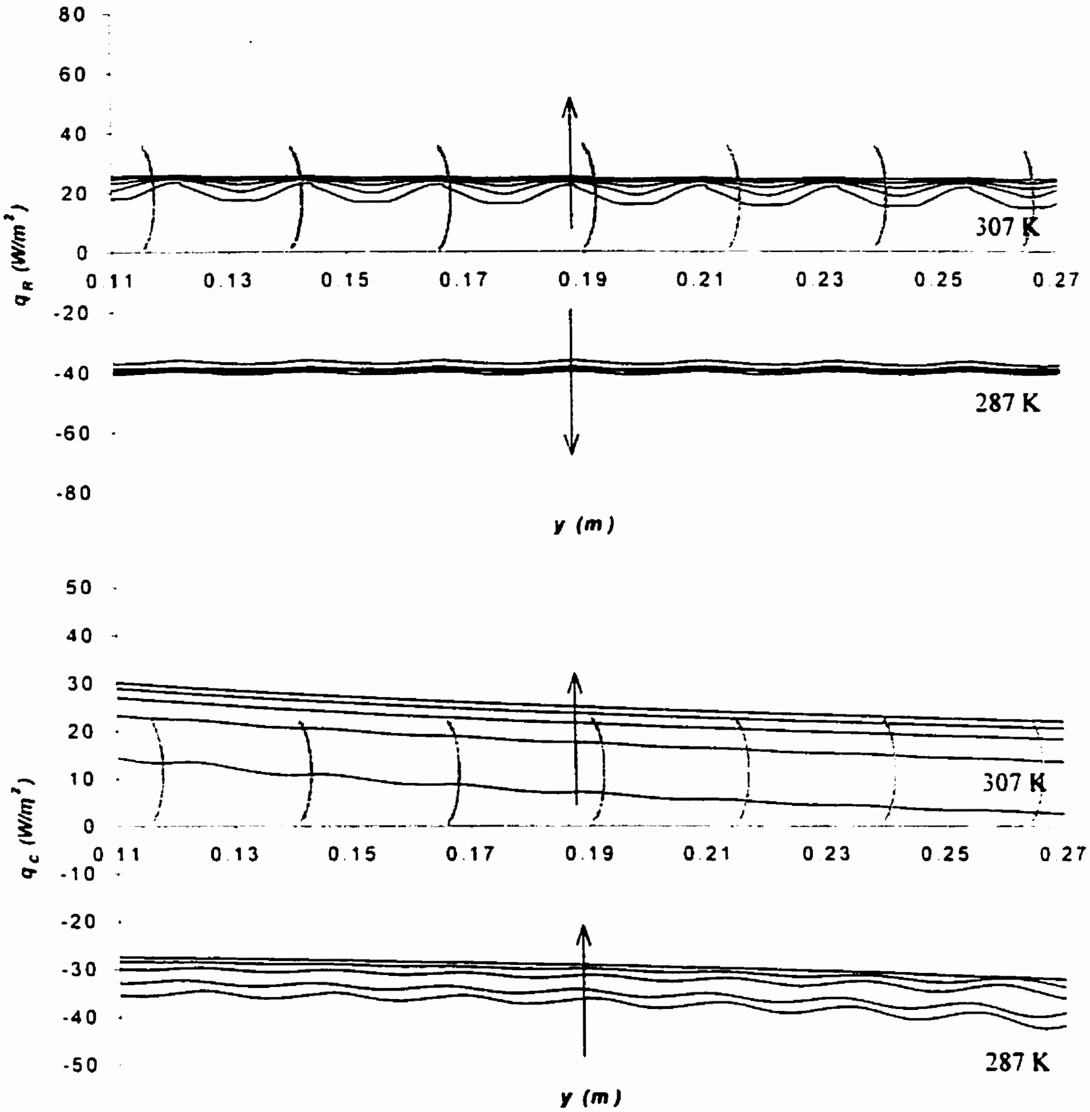

Figure D-7: Local convective and radiative heat flux in the center-of-glass region with changing blind position and glass temperature ($\phi = 0°$, T_p = 287 K, 307 K, $\varepsilon_b = \varepsilon_p = 0.6$, $q_b = 60$ W/m^2). Slat positions are shown in gray. Arrows indicate direction of increasing nominal blind spacing.

D.3 Full Parametric

Heat flux rates at the plate were determined in conjunction with the three level factorial design (Montgomery and Runger 1999) that has been described in Chapter 4. The factorial design allows the first and second order effects of the variables to be estimated in addition to the effects of parameter interaction. The full three-level factorial parametric series. The analysis was performed using the model described in Chapter 2. Table 4-9 shows the numerical model conditions. Fluid properties and miscellaneous model parameters are given in Table 4-3. Complete test results are presented in Tables D-1 through D-3.

The analysis of the experimental series has been described in Chapter 4. Three forms of the coded model have been examined. These include the blind angle in the forms ϕ or $\sin\phi$, $\cos\phi$, and $n = b - w\cos\phi/2$. The results of all the data fits are presented here. Contrary to the results presented in Chapter 4, the data presented in Tables D-4 through D-6 are in coded form, and have not been combined into a total flux variable. Figures D-8 through D-10 show the measured verses predicted comparison.

Table D-1: Heat flux at inside glass surface for all parametric cases where $b = 20$ mm.

T_p (°C)	ε_b	ε_p	q_b (W/m^2)	-45 slat		0 slat		45 slat	
				q_C (W/m^2)	q_R (W/m^2)	q_C (W/m^2)	q_R (W/m^2)	q_C (W/m^2)	q_R (W/m^2)
10	0.30	0.30	25	-44.37	-21.07	-42.70	-21.56	-43.92	-21.32
10	0.30	0.30	75	-58.08	-25.36	-60.66	-25.19	-55.40	-25.32
10	0.30	0.30	125	-75.02	-29.78	-88.27	-27.68	-75.23	-28.88
10	0.30	0.57	25	-42.96	-34.94	-41.30	-38.07	-42.98	-35.33
10	0.30	0.57	75	-56.14	-42.24	-58.39	-44.50	-53.61	-42.10
10	0.30	0.57	125	-72.21	-49.49	-84.29	-49.18	-72.25	-48.21
10	0.30	0.84	25	-41.95	-45.68	-40.11	-52.42	-42.25	-46.17
10	0.30	0.84	75	-54.67	-55.37	-56.48	-61.28	-52.30	-55.14
10	0.30	0.84	125	-70.46	-64.75	-81.05	-68.10	-69.88	-63.34
10	0.60	0.30	25	-42.82	-22.34	-41.57	-21.93	-42.81	-22.73
10	0.60	0.30	75	-54.05	-27.93	-56.12	-26.71	-51.38	-28.06
10	0.60	0.30	125	-67.66	-33.43	-77.47	-30.64	-65.74	-33.14
10	0.60	0.57	25	-41.02	-38.36	-39.68	-39.25	-41.51	-38.97
10	0.60	0.57	75	-51.41	-48.16	-53.06	-47.76	-49.12	-48.32
10	0.60	0.57	125	-63.88	-57.68	-72.18	-55.46	-61.41	-57.29
10	0.60	0.84	25	-39.61	-51.61	-38.01	-54.72	-40.48	-52.41
10	0.60	0.84	75	-49.25	-64.87	-50.42	-66.44	-47.38	-65.04
10	0.60	0.84	125	-60.89	-77.80	-67.84	-77.87	-58.16	-77.32
10	0.90	0.30	25	-42.10	-23.12	-41.03	-22.13	-42.27	-23.61
10	0.90	0.30	75	-52.04	-29.19	-53.92	-27.41	-49.52	-29.52
10	0.90	0.30	125	-63.77	-35.15	-72.24	-32.17	-61.02	-35.25
10	0.90	0.57	25	-40.09	-40.73	-38.88	-39.93	-40.79	-41.60
10	0.90	0.57	75	-49.03	-51.55	-50.48	-49.37	-47.04	-52.14
10	0.90	0.57	125	-59.57	-62.16	-66.49	-58.68	-56.49	-62.48
10	0.90	0.84	25	-38.41	-56.03	-36.95	-56.10	-39.52	-57.29
10	0.90	0.84	75	-46.44	-70.80	-47.49	-69.12	-45.10	-71.63
10	0.90	0.84	125	-56.06	-85.72	-61.85	-82.79	-53.09	-86.18
24	0.30	0.30	25	-7.70	-2.77	-8.71	-2.17	-6.47	-2.60
24	0.30	0.30	75	-21.26	-7.40	-24.88	-6.14	-16.28	-6.58
24	0.30	0.30	125	-33.33	-11.82	-41.41	-10.07	-24.64	-10.24
24	0.30	0.57	25	-7.56	-4.64	-8.63	-3.85	-6.38	-4.34
24	0.30	0.57	75	-20.89	-12.39	-24.51	-10.81	-16.06	-11.00
24	0.30	0.57	125	-32.81	-19.79	-40.81	-17.74	-24.34	-17.12
24	0.30	0.84	25	-7.45	-6.13	-8.56	-5.31	-6.31	-5.71
24	0.30	0.84	75	-20.60	-16.32	-24.19	-14.86	-15.89	-14.46
24	0.30	0.84	125	-32.40	-26.07	-40.31	-24.38	-24.10	-22.52
24	0.60	0.30	25	-6.03	-3.33	-7.02	-2.69	-5.19	-3.24
24	0.60	0.30	75	-17.86	-9.32	-20.46	-7.81	-13.88	-8.64
24	0.60	0.30	125	-28.77	-15.12	-34.73	-12.98	-21.48	-13.67
24	0.60	0.57	25	-5.77	-5.77	-6.86	-4.84	-4.99	-5.61
24	0.60	0.57	75	-17.13	-16.13	-19.77	-13.96	-13.42	-14.94
24	0.60	0.57	125	-27.75	-26.19	-33.58	-23.20	-20.84	-23.70
24	0.60	0.84	25	-5.55	-7.82	-6.70	-6.78	-4.82	-7.58
24	0.60	0.84	75	-16.52	-21.81	-19.15	-19.42	-13.02	-20.22
24	0.60	0.84	125	-26.88	-35.46	-32.58	-32.29	-20.28	-32.12
24	0.90	0.30	25	-5.15	-3.45	-6.22	-2.89	-4.51	-3.45
24	0.90	0.30	75	-15.86	-9.94	-18.27	-8.53	-12.50	-9.46
24	0.90	0.30	125	-26.03	-16.28	-31.27	-14.27	-19.61	-15.13
24	0.90	0.57	25	-4.84	-6.12	-5.99	-5.26	-4.25	-6.12
24	0.90	0.57	75	-14.95	-17.59	-17.42	-15.37	-11.87	-16.80
24	0.90	0.57	125	-24.71	-28.88	-29.81	-25.73	-18.74	-26.95
24	0.90	0.84	25	-4.57	-8.47	-5.79	-7.44	-4.02	-8.45
24	0.90	0.84	75	-14.13	-24.26	-16.68	-21.56	-11.31	-23.23
24	0.90	0.84	125	-23.52	-39.90	-28.46	-36.01	-17.94	-37.38
38	0.30	0.30	25	33.37	19.54	29.54	21.27	36.27	20.34
38	0.30	0.30	75	24.74	15.49	17.52	17.84	29.86	16.85
38	0.30	0.30	125	16.22	11.36	5.45	14.28	23.81	13.40
38	0.30	0.57	25	32.35	32.39	28.22	37.53	35.53	33.79
38	0.30	0.57	75	23.94	25.67	16.44	31.51	29.30	28.02
38	0.30	0.57	125	15.60	18.77	4.59	25.25	23.37	22.29

38	0.30	0.84	25	31.55	42.30	27.08	51.66	34.95	44.21
38	0.30	0.84	75	23.30	33.49	15.51	43.42	28.86	36.69
38	0.30	0.84	125	15.10	24.42	3.84	34.83	23.03	29.19
38	0.60	0.30	25	33.82	19.89	30.52	20.74	36.51	20.86
38	0.60	0.30	75	26.30	14.66	20.14	16.24	30.96	16.19
38	0.60	0.30	125	18.75	9.28	9.62	11.55	25.61	11.49
38	0.60	0.57	25	32.40	34.10	28.77	37.04	35.45	35.88
38	0.60	0.57	75	25.22	25.12	18.78	29.03	30.17	27.89
38	0.60	0.57	125	17.97	15.82	8.61	20.66	25.04	19.81
38	0.60	0.84	25	31.21	45.75	27.22	51.51	34.57	48.30
38	0.60	0.84	75	24.30	33.66	17.56	40.41	29.51	37.58
38	0.60	0.84	125	17.30	21.11	7.70	28.79	24.56	26.69
38	0.90	0.30	25	34.16	20.44	31.05	20.56	36.67	21.48
38	0.90	0.30	75	27.31	14.77	21.55	15.57	31.62	16.28
38	0.90	0.30	125	20.36	8.90	11.86	10.34	26.70	11.02
38	0.90	0.57	25	32.53	35.93	29.09	36.98	35.42	37.94
38	0.90	0.57	75	26.07	25.94	20.05	28.01	30.70	28.82
38	0.90	0.57	125	19.49	15.56	10.79	18.61	26.05	19.51
38	0.90	0.84	25	31.10	49.23	27.31	51.74	34.33	52.26
38	0.90	0.84	75	24.97	35.50	18.69	39.21	29.88	39.74
38	0.90	0.84	125	18.70	21.19	9.83	26.05	25.46	26.90

Table D-2: Heat flux at inside glass surface for all parametric cases where b = 30 mm.

T_p (°C)	ε_b	ε_p	q_b (W/m^2)	-45 slat		0 slat		45 slat	
				q_C (W/m^2)	q_R (W/m^2)	q_C (W/m^2)	q_R (W/m^2)	q_C (W/m^2)	q_R (W/m^2)
10	0.30	0.30	25	-43.09	-21.91	-43.68	-23.13	-42.62	-21.75
10	0.30	0.30	75	-49.56	-25.41	-50.00	-26.66	-45.57	-25.09
10	0.30	0.30	125	-55.45	-28.56	-55.69	-29.86	-48.06	-28.10
10	0.30	0.57	25	-42.48	-36.62	-43.06	-40.79	-42.34	-36.17
10	0.30	0.57	75	-48.75	-42.73	-49.35	-47.15	-45.15	-42.00
10	0.30	0.57	125	-54.64	-48.12	-55.24	-52.75	-48.29	-47.33
10	0.30	0.84	25	-42.07	-48.13	-42.59	-56.12	-42.14	-47.35
10	0.30	0.84	75	-48.05	-56.45	-48.78	-64.95	-44.70	-55.27
10	0.30	0.84	125	-53.92	-63.68	-54.58	-73.01	-49.97	-62.31
10	0.60	0.30	25	-42.36	-23.38	-42.92	-23.97	-42.23	-23.19
10	0.60	0.30	75	-47.77	-28.19	-48.25	-28.68	-44.55	-27.93
10	0.60	0.30	125	-53.20	-32.52	-53.67	-33.15	-47.29	-32.17
10	0.60	0.57	25	-41.75	-40.36	-42.24	-42.89	-41.86	-39.90
10	0.60	0.57	75	-46.44	-49.10	-47.06	-51.48	-44.22	-48.46
10	0.60	0.57	125	-52.02	-56.92	-52.22	-59.51	-46.54	-56.01
10	0.60	0.84	25	-41.36	-54.56	-41.72	-59.79	-41.59	-53.84
10	0.60	0.84	75	-45.32	-66.66	-46.31	-71.70	-43.51	-65.66
10	0.60	0.84	125	-51.53	-77.86	-51.21	-83.22	-46.90	-75.93
10	0.90	0.30	25	-42.05	-24.23	-42.59	-24.40	-42.04	-24.09
10	0.90	0.30	75	-46.77	-29.59	-47.12	-29.68	-44.39	-29.45
10	0.90	0.30	125	-52.02	-34.51	-52.01	-34.66	-46.77	-34.28
10	0.90	0.57	25	-41.45	-42.88	-41.88	-44.06	-41.65	-42.62
10	0.90	0.57	75	-45.18	-52.76	-46.25	-53.57	-43.48	-52.50
10	0.90	0.57	125	-50.67	-62.06	-50.62	-62.89	-45.79	-61.42
10	0.90	0.84	25	-41.01	-59.28	-41.27	-61.95	-41.35	-59.02
10	0.90	0.84	75	-43.81	-73.00	-45.07	-75.08	-42.86	-72.66
10	0.90	0.84	125	-49.00	-87.42	-49.40	-88.65	-45.23	-85.50
24	0.30	0.30	25	-4.29	-2.28	-4.70	-2.03	-2.95	-2.14
24	0.30	0.30	75	-9.66	-5.46	-10.92	-5.07	-5.55	-5.31
24	0.30	0.30	125	-14.28	-8.45	-16.33	-8.03	-7.04	-8.37
24	0.30	0.57	25	-4.22	-3.85	-4.68	-3.60	-2.93	-3.59
24	0.30	0.57	75	-9.55	-9.23	-10.84	-8.99	-5.52	-8.92
24	0.30	0.57	125	-14.14	-14.28	-16.23	-14.23	-7.00	-14.06
24	0.30	0.84	25	-4.17	-5.11	-4.66	-5.01	-2.91	-4.75
24	0.30	0.84	75	-9.47	-12.25	-10.78	-12.43	-5.49	-11.78
24	0.30	0.84	125	-14.04	-18.96	-16.13	-19.64	-6.97	-18.56
24	0.60	0.30	25	-3.71	-2.91	-4.00	-2.61	-2.53	-2.74
24	0.60	0.30	75	-8.69	-7.25	-9.68	-6.74	-5.08	-7.09
24	0.60	0.30	125	-12.98	-11.35	-14.62	-10.76	-6.59	-11.31
24	0.60	0.57	25	-3.58	-5.10	-3.94	-4.72	-2.48	-4.78
24	0.60	0.57	75	-8.48	-12.71	-9.53	-12.16	-5.00	-12.37
24	0.60	0.57	125	-12.71	-19.92	-14.41	-19.41	-6.50	-19.74
24	0.60	0.84	25	-3.47	-6.97	-3.88	-6.65	-2.43	-6.52
24	0.60	0.84	75	-8.30	-17.40	-9.39	-17.07	-4.92	-16.85
24	0.60	0.84	125	-12.47	-27.28	-14.21	-27.24	-6.42	-26.91
24	0.90	0.30	25	-3.35	-3.12	-3.61	-2.84	-2.27	-2.95
24	0.90	0.30	75	-8.07	-7.97	-8.97	-7.51	-4.78	-7.86
24	0.90	0.30	125	-12.15	-12.58	-13.64	-12.07	-6.30	-12.64
24	0.90	0.57	25	-3.19	-5.60	-3.59	-5.17	-2.20	-5.29
24	0.90	0.57	75	-7.79	-14.35	-8.75	-13.68	-4.66	-14.10
24	0.90	0.57	125	-11.78	-22.67	-13.34	-22.01	-6.16	-22.70
24	0.90	0.84	25	-3.04	-7.83	-3.44	-7.40	-2.13	-7.38
24	0.90	0.84	75	-7.53	-20.08	-8.55	-19.37	-4.54	-19.68
24	0.90	0.84	125	-11.44	-31.78	-13.07	-31.19	-6.03	-31.71
38	0.30	0.30	25	39.76	21.13	39.39	23.02	40.54	21.06
38	0.30	0.30	75	36.95	18.15	36.05	20.12	39.26	18.05
38	0.30	0.30	125	34.10	15.26	32.75	17.24	38.31	15.09
38	0.30	0.57	25	39.45	35.46	39.04	40.68	40.39	35.16
38	0.30	0.57	75	36.69	30.51	35.76	35.61	39.16	30.17
38	0.30	0.57	125	33.88	25.66	32.51	30.51	38.25	25.22

38	0.30	0.84	25	39.20	46.78	38.72	56.05	40.26	46.19
38	0.30	0.84	75	36.48	40.29	35.50	49.10	39.08	39.67
38	0.30	0.84	125	33.70	33.90	32.29	42.10	38.20	33.16
38	0.60	0.30	25	39.82	21.79	39.51	23.03	40.59	21.78
38	0.60	0.30	75	37.34	17.78	36.57	19.13	39.44	17.70
38	0.60	0.30	125	34.79	13.83	33.64	15.20	38.55	13.62
38	0.60	0.57	25	39.37	37.89	39.01	41.30	40.35	37.71
38	0.60	0.57	75	36.97	31.00	36.17	34.36	39.29	30.71
38	0.60	0.57	125	34.49	24.14	33.32	27.33	38.46	23.64
38	0.60	0.84	25	38.99	51.50	38.57	57.64	40.16	51.05
38	0.60	0.84	75	36.65	42.21	35.81	48.03	39.16	41.62
38	0.60	0.84	125	34.23	32.89	33.02	38.22	38.38	32.06
38	0.90	0.30	25	39.89	22.42	39.58	23.11	40.62	22.50
38	0.90	0.30	75	37.62	17.96	36.87	18.72	39.55	17.92
38	0.90	0.30	125	35.26	13.54	34.16	14.27	38.70	13.31
38	0.90	0.57	25	39.37	40.01	39.02	41.81	40.34	40.04
38	0.90	0.57	75	37.19	32.15	36.42	33.93	39.37	31.97
38	0.90	0.57	125	34.92	24.26	33.80	25.89	38.59	23.77
38	0.90	0.84	25	38.89	55.61	38.50	58.82	40.10	55.53
38	0.90	0.84	75	36.80	44.79	36.00	47.81	39.22	44.41
38	0.90	0.84	125	34.61	33.83	33.47	36.50	38.49	33.02

Table D-3: Heat flux at inside glass surface for all parametric cases where b = 40 mm.

T_p (°C)	ε_h	ε_p	q_b (W/m^2)	-45 slat		0 slat		45 slat	
				q_C (W/m^2)	q_R (W/m^2)	q_C (W/m^2)	q_R (W/m^2)	q_C (W/m^2)	q_R (W/m^2)
10	0.30	0.30	25	-42.02	-21.92	-42.16	-23.15	-41.46	-21.73
10	0.30	0.30	75	-45.61	-24.63	-45.38	-25.79	-43.45	-24.59
10	0.30	0.30	125	-48.61	-27.20	-48.16	-28.38	-45.24	-27.37
10	0.30	0.57	25	-41.62	-36.96	-41.85	-41.04	-41.32	-36.47
10	0.30	0.57	75	-45.20	-41.70	-45.06	-45.84	-43.23	-41.38
10	0.30	0.57	125	-48.40	-46.10	-48.21	-50.50	-45.09	-46.23
10	0.30	0.84	25	-41.42	-48.90	-41.67	-56.63	-41.30	-48.05
10	0.30	0.84	75	-44.82	-55.38	-44.75	-63.40	-43.08	-54.69
10	0.30	0.84	125	-48.16	-61.29	-47.98	-69.86	-45.06	-61.10
10	0.60	0.30	25	-41.57	-23.43	-41.81	-24.09	-41.33	-23.29
10	0.60	0.30	75	-44.76	-27.21	-44.61	-27.77	-42.90	-27.28
10	0.60	0.30	125	-47.79	-30.77	-47.59	-31.42	-44.75	-31.20
10	0.60	0.57	25	-41.47	-40.72	-41.68	-43.29	-41.58	-40.34
10	0.60	0.57	75	-44.03	-47.82	-44.05	-50.19	-42.45	-47.63
10	0.60	0.57	125	-46.98	-54.24	-46.67	-56.84	-44.06	-54.57
10	0.60	0.84	25	-41.68	-55.20	-41.83	-60.37	-41.71	-54.55
10	0.60	0.84	75	-43.39	-65.46	-43.54	-70.48	-42.12	-64.84
10	0.60	0.84	125	-46.47	-74.46	-46.47	-79.89	-43.62	-74.32
10	0.90	0.30	25	-41.42	-24.30	-41.70	-24.57	-41.39	-24.25
10	0.90	0.30	75	-44.25	-28.60	-44.18	-28.78	-42.50	-28.80
10	0.90	0.30	125	-46.96	-32.66	-46.54	-32.89	-43.79	-33.22
10	0.90	0.57	25	-41.62	-43.17	-41.77	-44.47	-41.68	-43.03
10	0.90	0.57	75	-43.35	-51.56	-43.50	-52.54	-42.12	-51.66
10	0.90	0.57	125	-46.32	-59.09	-46.44	-60.14	-43.44	-59.78
10	0.90	0.84	25	-41.76	-59.91	-41.73	-62.67	-41.79	-59.85
10	0.90	0.84	75	-42.50	-72.16	-42.87	-74.46	-41.61	-72.05
10	0.90	0.84	125	-45.44	-82.98	-45.55	-85.36	-43.42	-83.60
24	0.30	0.30	25	-2.50	-1.83	-2.68	-1.69	-1.17	-1.89
24	0.30	0.30	75	-5.83	-4.43	-6.03	-4.20	-1.55	-4.83
24	0.30	0.30	125	-8.88	-6.89	-8.91	-6.65	-1.56	-7.74
24	0.30	0.57	25	-2.48	-3.12	-2.68	-3.03	-1.17	-3.19
24	0.30	0.57	75	-5.79	-7.52	-6.01	-7.49	-1.54	-8.16
24	0.30	0.57	125	-8.82	-11.71	-8.88	-11.85	-1.55	-13.07
24	0.30	0.84	25	-2.46	-4.15	-2.67	-4.21	-1.17	-4.24
24	0.30	0.84	75	-5.76	-10.03	-5.99	-10.40	-1.54	-10.82
24	0.30	0.84	125	-8.77	-15.60	-8.85	-16.44	-1.55	-17.33
24	0.60	0.30	25	-2.18	-2.39	-2.34	-2.24	-1.07	-2.46
24	0.60	0.30	75	-5.21	-5.98	-5.39	-5.72	-1.53	-6.49
24	0.60	0.30	125	-7.99	-9.41	-8.02	-9.13	-1.59	-10.51
24	0.60	0.57	25	-2.13	-4.21	-2.32	-4.09	-1.06	-4.32
24	0.60	0.57	75	-5.12	-10.55	-5.34	-10.40	-1.52	-11.38
24	0.60	0.57	125	-7.86	-16.61	-7.94	-16.58	-1.58	-18.42
24	0.60	0.84	25	-2.09	-5.78	-2.30	-5.80	-1.05	-5.91
24	0.60	0.84	75	-5.05	-14.51	-5.29	-14.68	-1.51	-15.56
24	0.60	0.84	125	-7.76	-22.87	-7.87	-23.39	-1.57	-25.18
24	0.90	0.30	25	-1.98	-2.60	-2.14	-2.50	-1.01	-2.69
24	0.90	0.30	75	-4.81	-6.66	-5.01	-6.48	-1.51	-7.24
24	0.90	0.30	125	-7.40	-10.55	-7.48	-10.38	-1.60	-11.78
24	0.90	0.57	25	-1.91	-4.69	-2.11	-4.61	-0.99	-4.84
24	0.90	0.57	75	-4.69	-12.06	-4.93	-11.90	-1.49	-13.04
24	0.90	0.57	125	-7.24	-19.14	-7.37	-19.07	-1.59	-21.23
24	0.90	0.84	25	-1.85	-6.58	-2.09	-6.61	-0.97	-6.80
24	0.90	0.84	75	-4.58	-16.98	-4.86	-16.97	-1.47	-18.26
24	0.90	0.84	125	-7.08	-26.98	-7.26	-27.19	-1.58	-29.75
38	0.30	0.30	25	41.56	21.73	41.35	23.38	42.02	21.46
38	0.30	0.30	75	40.78	19.20	40.11	20.92	42.17	18.70
38	0.30	0.30	125	39.95	16.75	38.82	18.46	42.47	15.92
38	0.30	0.57	25	41.47	36.70	41.24	41.47	42.02	36.02
38	0.30	0.57	75	40.71	32.47	40.01	37.13	42.19	31.39
38	0.30	0.57	125	39.89	28.34	38.73	32.77	42.49	26.73

38	0.30	0.84	25	41.40	48.66	41.14	57.28	42.02	47.50
38	0.30	0.84	75	40.65	43.10	39.93	51.31	42.21	41.41
38	0.30	0.84	125	39.83	37.62	38.66	45.29	42.51	35.25
38	0.60	0.30	25	41.57	22.44	41.39	23.44	42.01	22.18
38	0.60	0.30	75	40.89	18.99	40.31	20.06	42.12	18.40
38	0.60	0.30	125	40.16	15.60	39.17	16.66	42.36	14.57
38	0.60	0.57	25	41.45	39.32	41.23	42.24	42.01	38.61
38	0.60	0.57	75	40.79	33.36	40.17	36.20	42.15	32.07
38	0.60	0.57	125	40.07	27.42	39.05	30.07	42.39	25.39
38	0.60	0.84	25	41.34	53.79	41.09	59.22	42.02	52.48
38	0.60	0.84	75	40.69	45.70	40.04	50.79	42.17	43.62
38	0.60	0.84	125	39.99	37.60	38.94	42.19	42.41	34.53
38	0.90	0.30	25	41.58	23.08	41.41	23.53	42.01	22.88
38	0.90	0.30	75	40.97	19.20	40.43	19.69	42.09	18.62
38	0.90	0.30	125	40.29	15.37	39.38	15.81	42.30	14.28
38	0.90	0.57	25	41.44	41.53	41.23	42.84	42.01	40.95
38	0.90	0.57	75	40.84	34.67	40.27	35.90	42.12	33.38
38	0.90	0.57	125	40.19	27.78	39.25	28.82	42.33	25.60
38	0.90	0.84	25	41.31	58.18	41.06	60.61	42.02	57.04
38	0.90	0.84	75	40.73	48.67	40.12	50.85	42.15	46.54
38	0.90	0.84	125	40.10	39.05	39.12	40.82	42.36	35.69

Table D-4: Estimated model parameters and quality of fit indicators for parametric case using cosϕ. Parameters are presented in coded form. 99% confidence interval of parameters are in brackets. Note that b is in mm, T is in °C.

	Convection (W/m^2)	Radiation (W/m^2)
Constant	-9.48 ± 0.63	-11.94 ± 0.51
b	8.19 ± 0.51	1.60 ± 0.24
T_{gi}	40.48 ± 0.51	40.57 ± 0.41
ε_b	1.25 ± 0.29	-2.24 ± 0.24
ε_{gi}		-3.84 ± 0.24
q_b	-6.83 ± 0.51	-7.18 ± 0.24
$cos\phi$	3.25 ± 0.51	-0.649 ± 0.41
b^2	-3.38 ± 0.51	
bT_{gi}	1.64 ± 0.36	1.73 ± 0.29
$b\varepsilon_b$	-1.18 ± 0.36	
$b\varepsilon_{gi}$		0.62 ± 0.29
bq_b	4.55 ± 0.36	1.12 ± 0.29
$bcos\phi$	-2.37 ± 0.62	
T_{gi}^2	2.75 ± 0.51	3.77 ± 0.41
$T_{gi}\,\varepsilon_b$	-0.76 ± 0.36	2.37 ± 0.29
$T_{gi}\,\varepsilon_p$	-0.80 ± 0.36	15.81 ± 0.29
$T_{gi}\,q_b$	1.61 ± 0.36	0.38 ± 0.29
$T_{gi}\,cos\phi$	1.04 ± 0.62	-2.68 ± 0.51
ε_b^2		0.78 ± 0.41
$\varepsilon_b\varepsilon_{gi}$		-1.09 ± 0.29
$\varepsilon_b q_b$	0.84 ± 0.36	-1.66 ± 0.29
$\varepsilon_b cos\phi$		
ε_{gi}^2		
$\varepsilon_{gi}\,q_b$		-2.99 ± 0.29
$\varepsilon_{gi}\,cos\phi$		
q_b^2		
$q_b cos\phi$	2.34 ± 0.62	
σ	2.50	2.04
$MSR/MSE > F_{P-1,N-P,0.01}$	8242>1.98 ∴ no evidence of lack of fit	11469>1.94 ∴ no evidence of lack of fit
R^2	0.995 ∴ strong fit	0.996 ∴ strong fit

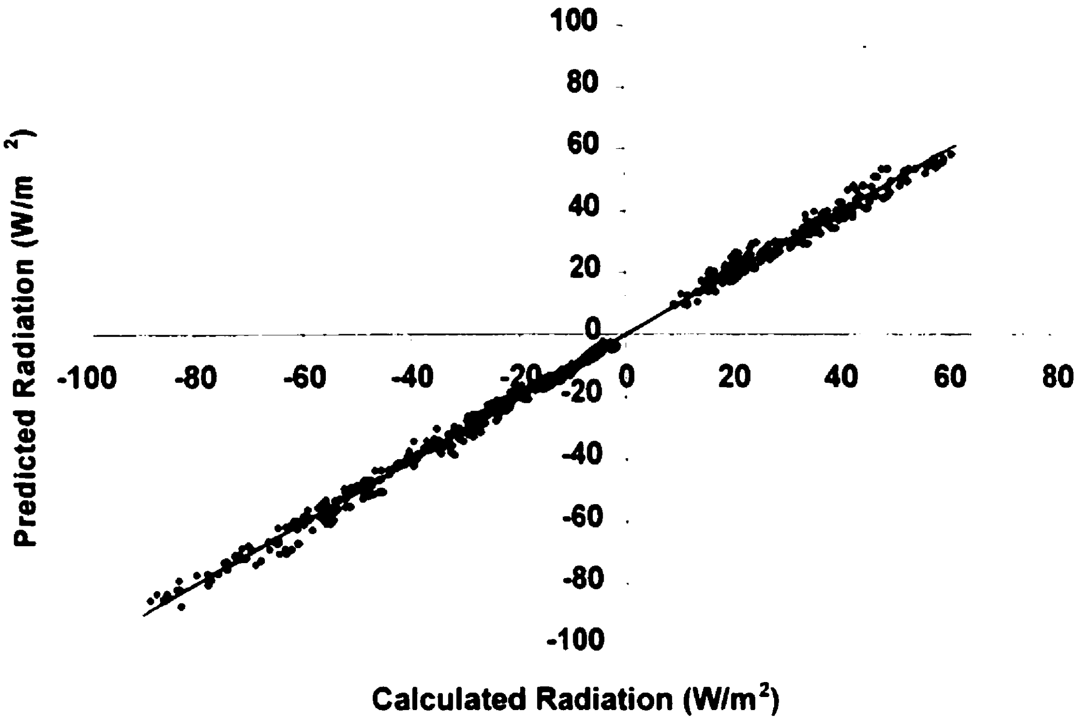

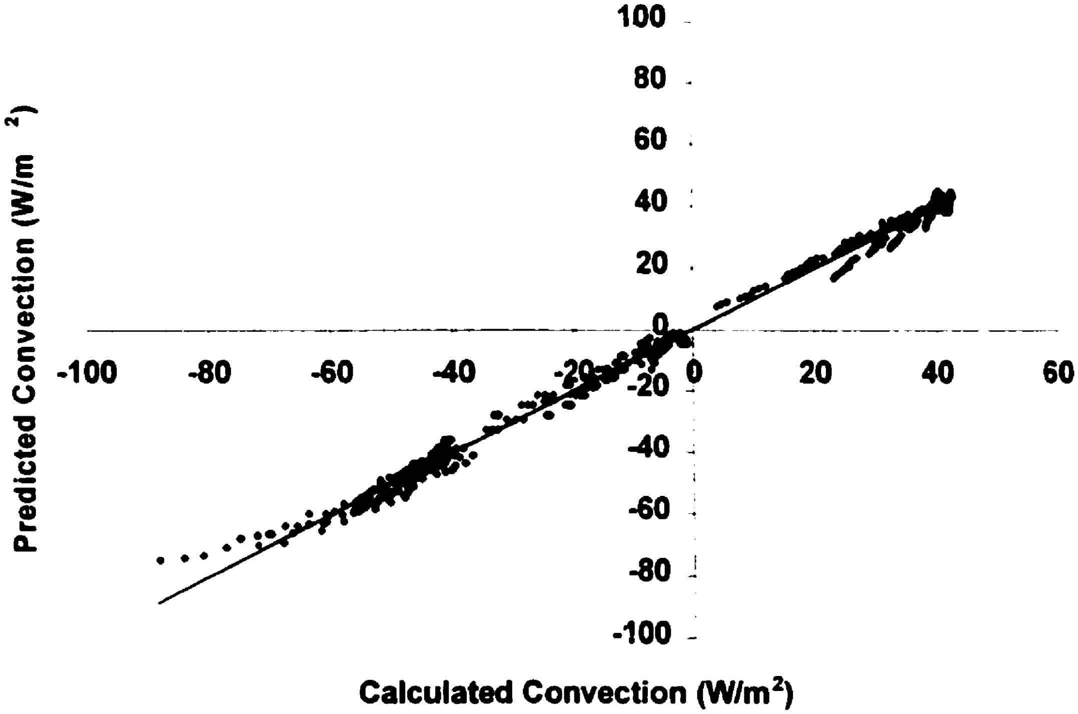

Figure D-8: Predicted verses calculated heat flux for case of cosϕ.

Table D-5: Estimated model parameters and quality of fit indicators for parametric case using ϕ and sinϕ. Parameters are presented in coded form. 99% confidence interval of parameters are in brackets. Note that b is in mm, T is in °C.

	Convection (W/m^2)	Radiation (W/m^2)
Constant	-9.48 ± 0.63	-11.94 ± 0.57
b	6.61 ± 0.29	1.60 ± 0.27
T_{gi}	41.17 ± 0.29	38.79 ± 0.27
ε_b	1.25 ± 0.29	-2.24 ± 0.27
ε_{gi}	0.32 ± 0.29	-3.84 ± 0.27
q_b	-5.27 ± 0.29	-7.18 ± 0.27
$sin\phi$, ϕ	1.43 ± 0.29	-
b^2	-3.38 ± 0.50	
bT_{gi}	1.64 ± 0.36	1.72 ± 0.32
$b\varepsilon_b$	-1.18 ± 0.36	
$b\varepsilon_{gi}$		0.62 ± 0.32
bq_b	4.55 ± 0.36	1.12 ± 0.32
$b\ sin\phi$, $b\phi$		-0.49 ± 0.32
T_{gi}^2	2.75 ± 0.50	3.77 ± 0.46
$T_{gi}\ \varepsilon_b$	-0.76 ± 0.36	2.36 ± 0.32
$T_{gi}\ \varepsilon_p$	-0.80 ± 0.36	15.81 ± 0.32
$T_{gi}\ q_b$	1.61 ± 0.36	0.38 ± 0.32
$T_{gi}sin\phi$, $T_{gi}\phi$		
ε_b^2		0.78 ± 0.46
$\varepsilon_b\varepsilon_{gi}$		-1.09 ± 0.32
$\varepsilon_b q_b$	0.84 ± 0.36	-1.66 ± 0.32
$\varepsilon_b sin\phi$, $\varepsilon_b\phi$		
ε_{gi}^2		
$\varepsilon_{gi}\ q_b$		-2.99 ± 0.32
$\varepsilon_{gi}sin\phi$, $\varepsilon_{gi}\phi$		
q_b^2		
$q_b sin\phi$, $q_b\phi$	1.00 ± 0.36	
$sin^2\phi$, ϕ^2	3.25 ± 0.50	-0.65 ± 0.46
σ	2.59	2.27
$MSR/MSE > F_{P-1,N-P,0.01}$	8324>1.99 ∴ no evidence of lack of fit	9264>1.94 ∴ no evidence of lack of fit
R^2	0.995 ∴ strong fit	0.996 ∴ strong fit

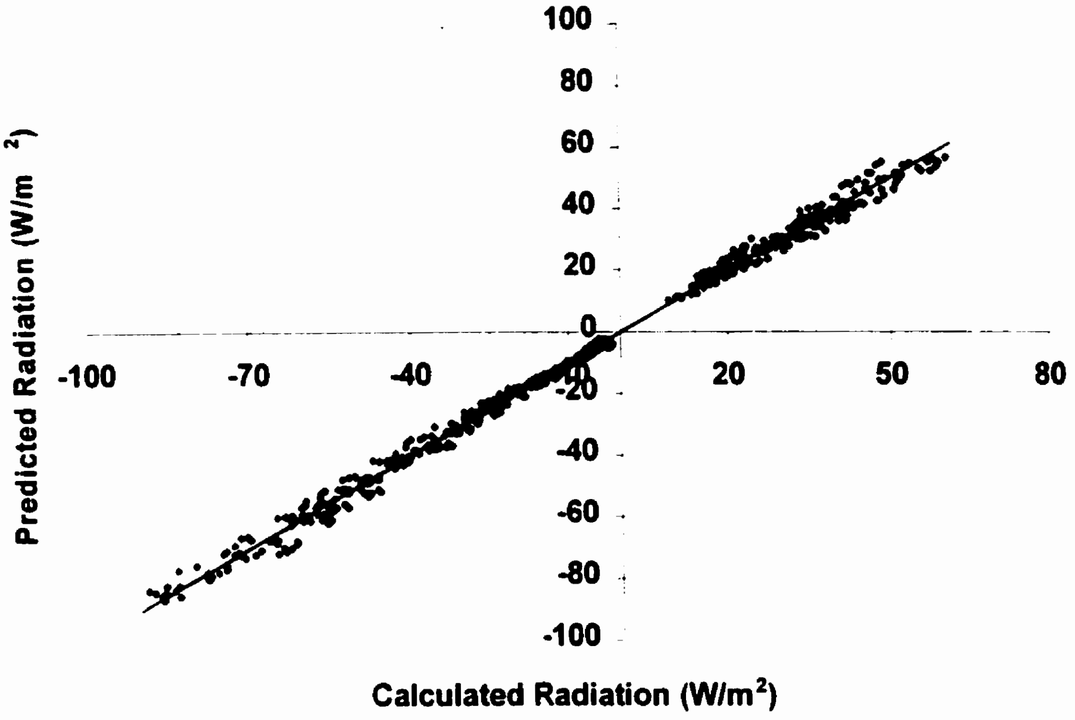

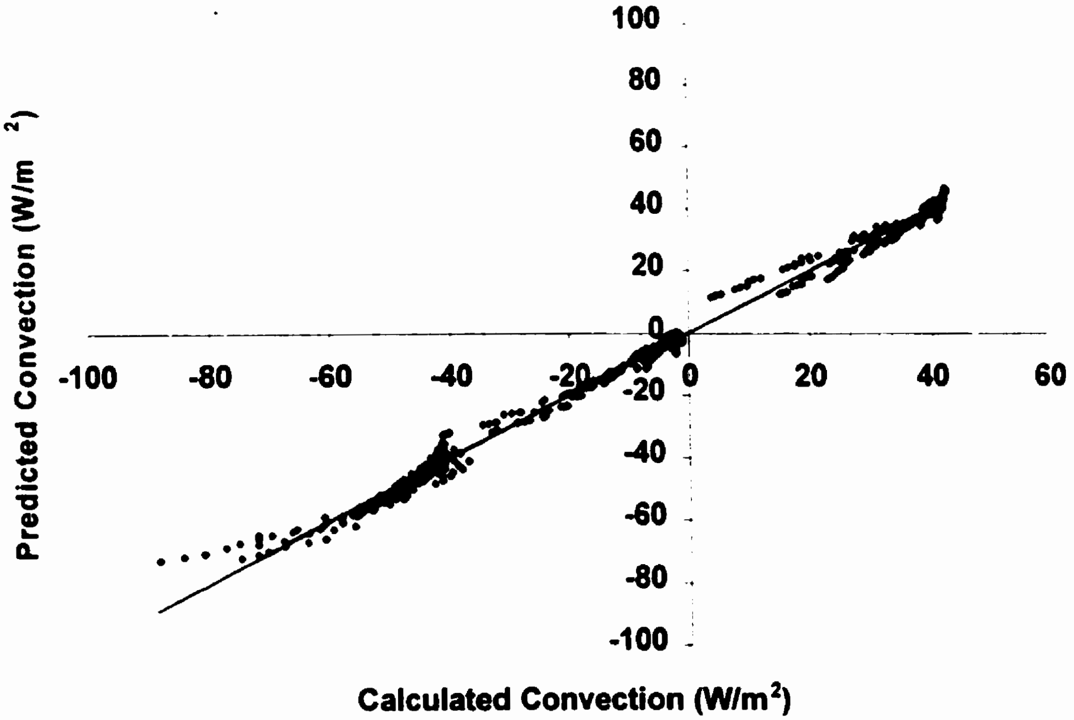

Figure D-9: Predicted verses calculated heat flux for case of ϕ and sinϕ.

Table D-6: Estimated model parameters and quality of fit indicators for parametric case using *n*. Parameters are presented in coded form. 99% confidence interval of parameters are in brackets. Note that *b* is in mm, *T* is in °C.

	Convection (W/m^2)	Radiation (W/m^2)
Constant	-7.66 ± 0.51	-12.46 ± 0.53
n	8.43 ± 0.35	1.73 ± 0.34
T_{gi}	41.07 ± 0.29	38.70 ± 0.29
ε_b	1.33 ± 0.29	-2.24 ± 0.29
ε_{gi}	0.32 ± 0.29	-3.88 ± 0.29
q_b	-5.55 ± 0.29	-7.25 ± 0.29
n^2	-4.71 ± 0.61	
nT_{gi}	2.00 ± 0.42	1.58 ± 0.41
$n\varepsilon_b$	-1.40 ± 0.42	
$n\varepsilon_{gi}$		0.69 ± 0.41
nq_b	5.49 ± 0.42	1.24 ± 0.41
T_{gi}^2	2.75 ± 0.51	3.77 ± 0.50
$T_{gi}\ \varepsilon_b$	-0.76 ± 0.36	2.36 ± 0.35
$T_{gi}\ \varepsilon_p$	-0.80 ± 0.36	15.81 ± 0.35
$T_{gi}\ q_b$	1.61 ± 0.36	0.38 ± 0.35
ε_b^2		0.78 ± 0.50
$\varepsilon_b\varepsilon_{gi}$		-1.09 ± 0.35
$\varepsilon_b q_b$	0.84 ± 0.36	-1.66 ± 0.35
ε_{gi}^2		
$\varepsilon_{gi}\ q_b$		-2.99 ± 0.35
q_b^2		
σ	2.51	2.48
MSR/MSE > $F_{P-1,N-P,0.01}$	9920>2.04 ∴ no evidence of lack of fit	8713>1.98 ∴ no evidence of lack of fit
R^2	0.995 ∴ strong fit	0.995 ∴ strong fit

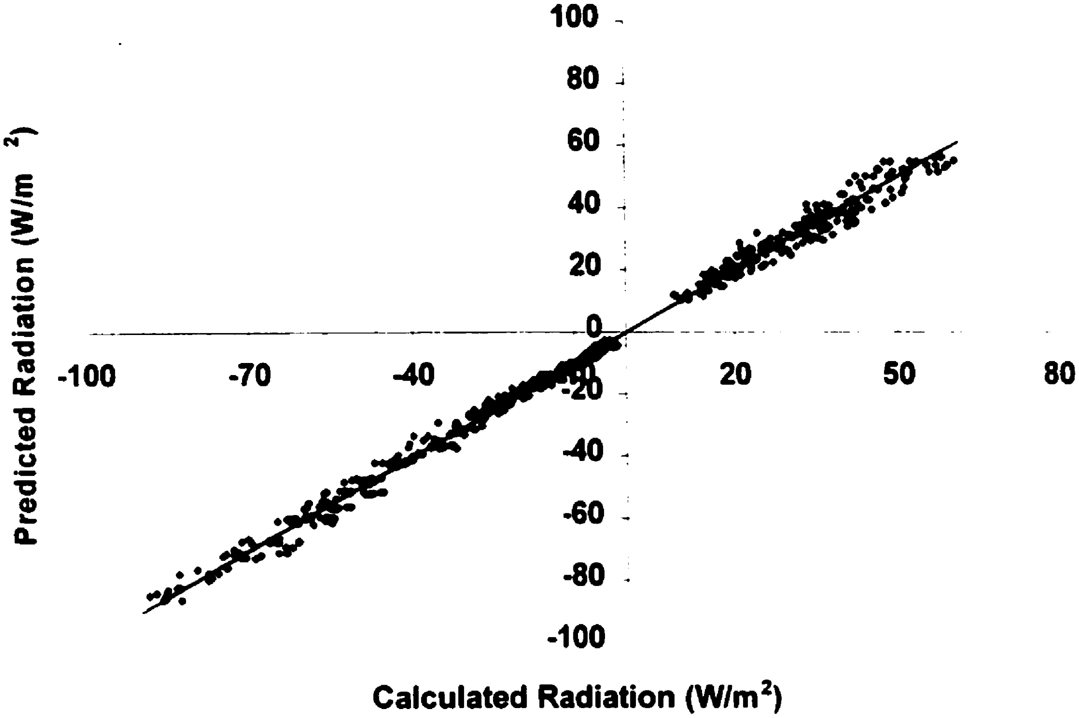

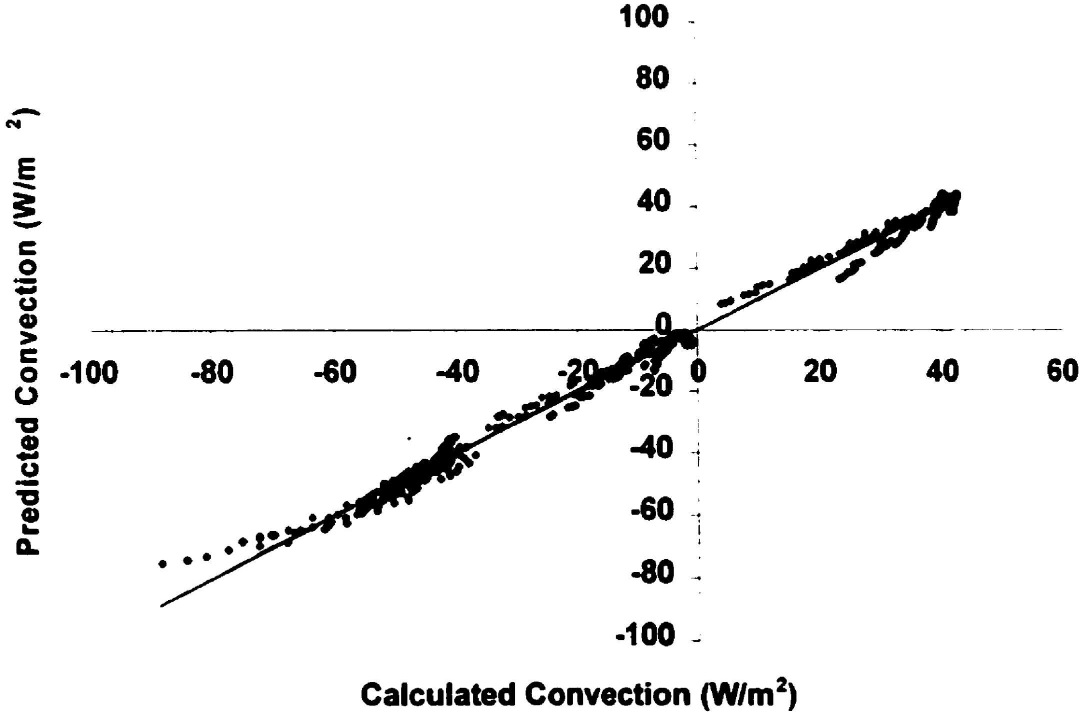

Figure D-10: Predicted verses calculated heat flux for case of *n*.

APPENDIX E
U-FACTOR AND *SHGC*: MEASUREMENT AND PREDICTION

E.1 Introduction

Chapter 5 presents a comparison of *SHGC* predicted using the results of the full parametric analysis to *SHGC* measured experimentally using a solar calorimeter. In the present Appendix, a description of solar calorimetry and how it was used to determine *U*-factor and *SHGC* is presented. A sample calculation using the method provided in Chapter 5 has also been included.

E.2 Experimental Procedure

E.2.1 Calorimetry

Testing was performed using Queen's Solar Calorimeter located at Queen's University (Figs. E-1 and E-2). A full description of the calorimeter and its systems can be found in Harrison and Collins (1999).

To calculate the energy input into a calorimeter due to energy flow through a glazing system, careful metering of the input and output energy flows is required. This includes energy removed by the flow loop, energy added by any internal fans and pumps, and losses through the calorimeter walls. Energy input, Q_{input}, is then calorimetrically determined by

$$Q_{input} = Q_{flow} - Q_{fan} - Q_{pump} + Q_{walls} + Q_{mask} \qquad \text{(E.1)}$$

where Q_{flow}, Q_{fan}, Q_{pump}, Q_{walls}, and Q_{mask} denote: the energy removed by the calorimeter flow loop; the electrical power supplied to the calorimeter's internal fan and pump; and heat lost through the walls and mask, respectively. The energy balance of the calorimeter is presented in Fig. E-3.

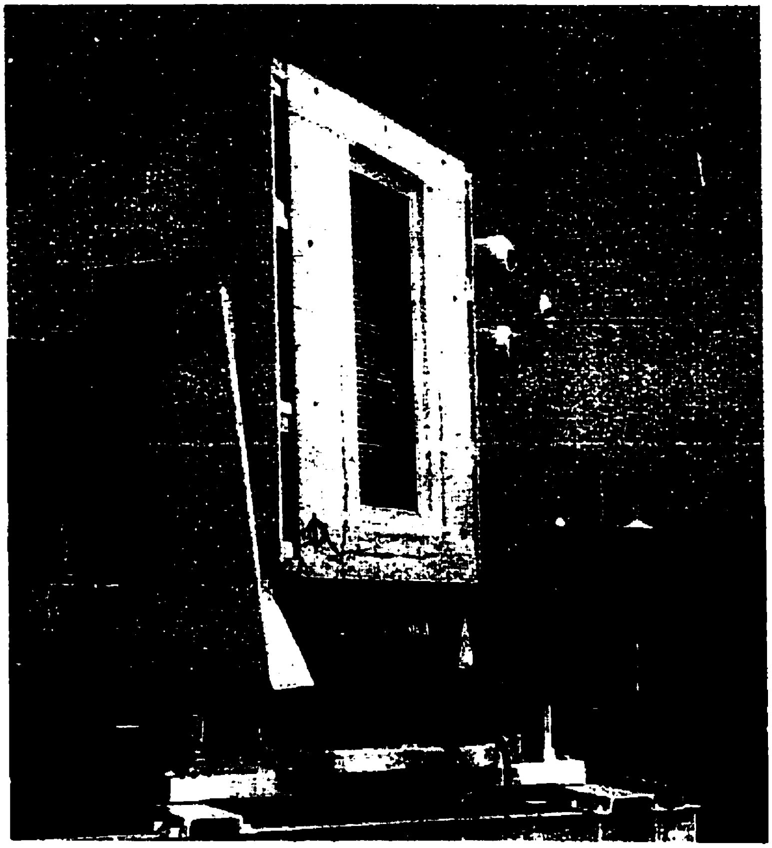

Figure E-1: Queen's University Solar Calorimeter in operation.

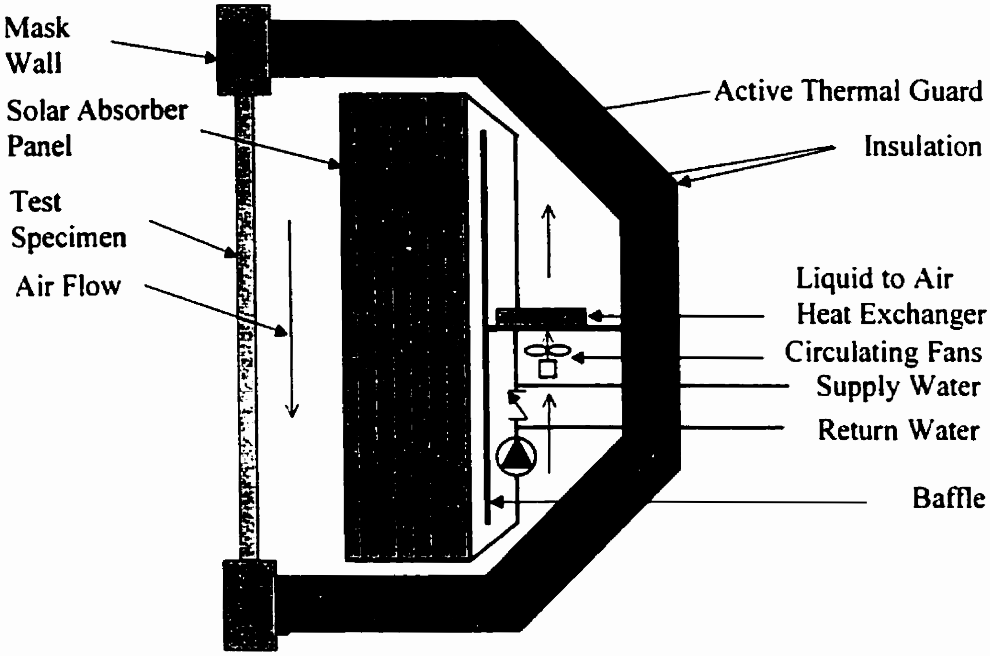

Figure E-2: Queen's Solar Calorimeter. Cross-sectional schematic.

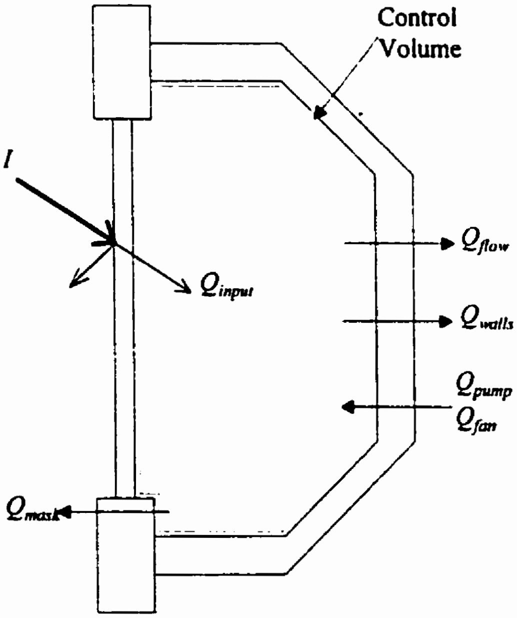

Figure E-3: Calorimeter energy balance for standard test procedures.

The instantaneous energy flow rate through a glazing system is calculated as the difference between the gain due to solar radiation, and the heat loss due to the interior/exterior temperature difference

$$Q_{input} = F \cdot I \cdot A_{fen} - U \cdot A_{fen}(\Delta T_{i,o}) \qquad \text{(E.2)}$$

where Q_{input} is the combined solar and thermal gains per unit area of the window system. U represents the windows overall heat transfer coefficient, and $\Delta T_{i,o}$ is the temperature difference across the window. U is determined in the absence of sunlight (I = 0), and F is determined in the absence of an interior exterior temperature gradient ($\Delta T_{i,o}$ = 0).

The efficiency of a glazing system can be described as the ratio of instantaneous gain to incident solar radiation.

$$\eta = Q_{input} \cdot \left(A_{fen} \cdot I\right)^{-1} \qquad \text{(E.3)}$$

It has been shown that the time averaged thermal efficiency, η, can be graphically represented in the same manner as the instantaneous efficiency curve (Harrison and Barakat 1983). Therefore, for a series of tests, a plot of thermal efficiency verses $\Delta T/I$ can be developed. By using a linear regression on these points, the window system can be characterized: the slope represents the systems U-factor, and the y-axis intercept is the solar heat gain coefficient. An example instantaneous efficiency curve has been presented in Fig. E-4.

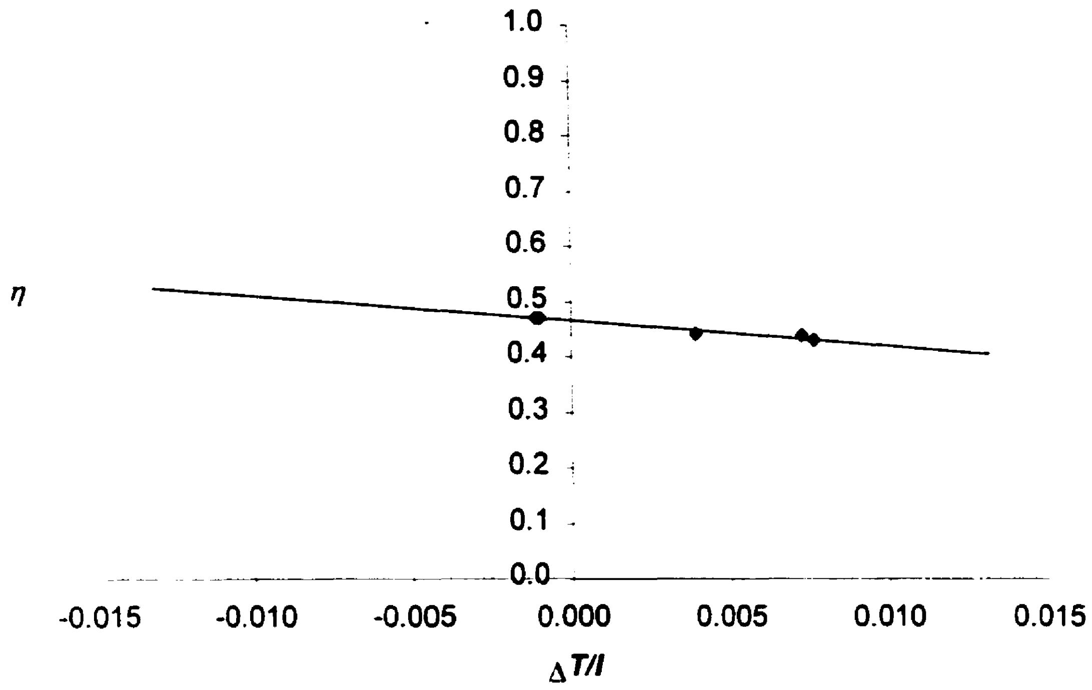

Figure E-4: Example of thermal efficiency verses *ΔT/I*. The slope represents the *U*-factor, and the *y*-intercept is the solar heat gain coefficient.

While this method assumes the thermal and solar characteristics of a window system are uncoupled, it is the only method currently available for the experimental determination of window thermal and solar performance. Calorimeter facilities which can control the indoor temperature, produce a $\Delta T = 0$ situation where all metered energy is *SHG*. Calorimetric facilities which do no actively control the internal temperature will instead produce the plot shown in Fig. E-4. In either case, it is assumed that the *SHGC* and *U*-factor are uncoupled, and the relation between η and $\Delta T/I$ is linear.

E.2.2 Experimental Series

Calorimetric experiments were performed for a number of conditions. At each of 30 ° and 45° solar incident angles, two commercially available blinds installed at a nominal distance of b = 30 mm were examined at 0, -45, and 45 degree slat angles. One blind had a white enameled surface while the other (an identical product) was painted flat black. The radiative properties of the blind material used in the experiment were measured at the University of Waterloo using a Gier Dunkle MS-251 Solar Reflectometer and a Gier Dunkle Db-100 Infrared Reflectometer. They were found to have a solar absorptance of 0.32 and 0.90, and hemispherical emissivities of 0.75 and 0.89 for the white and black blinds respectively (Wright 1997). The window was composed of two 3 mm lites of clear glass with a 13 mm air gap. The optical properties of that glass were determined at 30° and 45° solar incident angles from Rubin (1984). Glass emissivity was 0.84 for all surfaces, with a thermal resistance of 0.0031 $K{\cdot}m^2/W$ for each lite. The results of the calorimetric tests are presented in Table E-1 along with the total irradiation and the direct and diffuse fractions measured during each experiment.

Calorimeter tests were performed based on the method described by Harrison and Collins (1999), with few exceptions. Azimuth tracking with some altitude adjustment was used to maintain solar incident angles. Care was taken not to tilt the calorimeter more than 10° from vertical.

E.2.3 Experimental Results

SHGC and *U*-factor were determined based on the total area of the fenestration system (including the frame). The *SHGC* results have been corrected to the glass *SHGC* assuming no *SHG* through the frame, and using the glass area only for calculations, i.e., A_{fen} and A_g are 0.720 and 0.473 m respectively. $SHGC_{COG} = 0.720 \cdot SHGC_{fen}/0.473$. Sufficient data was not collected to determine the glass from the total *U*-factor using the frame and edge-of-glass *U*-factors. As such, this comparison could not be performed. Experimental results are presented in Table E-1. Uncertainty was determined using the method presented by Harrison and Dubrous (1993). The direct and diffuse fraction are also given in Table E-1. The value quoted are the average fraction for the test points used in the test sequence, i.e., multiple tests were needed to determine the *SHGC* and *U*-factor, all of which had a unique direct and diffuse fraction. This data was required as input for the mathematical comparison. The standard deviation was no greater than 0.06 for any given test sequence. Complete data analysis is available from the Queen's University Solar Calorimetry Laboratory.

Table E-1: Calorimetric results of solar performance for a window and shade system with b = 30 mm. Fenestration is double glazed clear 3 mm glass (both lites). Measured *SHGC* uncertainty is ±0.02. *U*-factor uncertainty is ±1.4 W/m²K.

Test	$SHGC_{fen}$	$SHGC_{COG}$	I (W/m^2)	I_D/I, I_d/I,
No Blind	0.47	0.72	1044	0.80 , 0.20
White, 30° incidence, 0° slat angle	0.39	0.59	883	0.78 , 0.22
White, 45° incidence, 0° slat angle	0.37	0.56	720	0.76 , 0.24
White, 30° incidence, 45° slat angle	0.30	0.46	825	0.78 , 0.22
White, 45° incidence, 45° slat angle	0.29	0.44	732	0.69 , 0.31
Black, 30° incidence, 0° slat angle	0.43	0.66	931	0.82 , 0.18
Black, 45° incidence, 0° slat angle	NA	NA	NA	NA
Black, 30° incidence, 45° slat angle	0.42	0.64	915	0.78 , 0.22
Black, 45° incidence, 45° slat angle	0.42	0.64	795	0.78 , 0.22

E.3 Sample *U*-Factor and *SHGC* Prediction

Although the calculation of *SHGC* and *U*-factor was the logical next step in the progression of this research, important parts of the analysis are still missing. A reliable method of predicting blind layer optical properties needs to be developed, and experimental data needs to be produced to provide a comprehensive basis for validating calculated values of *SHGC* and *U*-factor. A preliminary comparison, however, was possible.

Layer specific optical properties were determined from Rubin (1984) for the glass and Parmalee et al. (1952, 1953b) for the blind. The glass layer was homogenous, and therefore layer specific properties were the same as the directional material properties. The blind layer properties were based on the blind material properties and the solar angle of incidence using predictor equations produced by Parmalee et al. (1952, 1953b). Those equations provide different values for sky and ground diffuse, and it was necessary to find the sky/ground diffuse split. For the basis of this comparison, it was assumed to be 50/50 due to the location of the calorimeter, which has a good view of Lake Ontario, a stone roof, and the glass facade of a neighboring building, and a very small view of surrounding greenery. All blind layer properties have been presented in Table E-2.

Table E-2: Layer specific optical properties used in data analysis. For the current investigation, optical properties apply to both sides of each glazing.

Slat Absor	Slat Angle	Solar Incid	Direct Parmelee and Aubele (1952)			Diffuse (sky/ground) Parmelee and Vild (1953)			
α_b	ϕ	ψ	τ_D	α_D	ρ_D	τ_d	α_d	ρ_d	ε
0.32	0	30	0.50	0.32	0.18	0.51/0.51	0.29/0.29	0.20/0.20	0.75
0.32	0	45	0.25	0.45	0.30	0.51/0.51	0.29/0.29	0.20/0.20	0.75
0.32	45	30	0.12	0.39	0.49	0.13/0.60	0.38/0.16	0.49/0.24	0.75
0.32	45	45	0.10	0.37	0.53	0.13/0.60	0.38/0.16	0.49/0.24	0.75
0.90	0	30	0.32	0.66	0.02	0.37/0.37	0.61/0.61	0.02/0.02	0.89
0.90	0	45	0.02	0.94	0.04	0.37/0.37	0.61/0.61	0.02/0.02	0.89
0.90	45	30	0.01	0.93	0.06	0.02/0.50	0.92/0.46	0.06/0.04	0.89
0.90	45	45	0.01	0.93	0.06	0.02/0.50	0.92/0.46	0.06/0.04	0.89

Layer	τ	α	ρ	ε
Clear Glass at 30° Solar Incidence, both sides	0.83	0.09	0.08	0.84
Clear Glass at 45° Solar Incidence, both sides	0.81	0.10	0.09	0.84

E.3.1 Sample *U*-Factor Calculation

The calculation of *U*-factor was performed for comparison to the same window and shading device that was tested experimentally. Specifically, the case examined was

$$b = 30 \text{ mm}$$
$$\phi = 45^\circ$$
$$\varepsilon_b = 0.76,\ \varepsilon_{g1} = \varepsilon_{g2} = 0.84$$
$$q_b = 0 \text{ W/m}$$
$$T_o = 40^\circ\text{C},\ T_i = 24^\circ\text{C}$$

Other system properties are presented in Tables E-1 and E-2. The numerical analysis was performed for a room temperature of 24°C, therefore the analysis must be biased so that condition remains, i.e., if the desired interior and external temperatures are 22 and 40 °C respectively, 24 and 42 °C should be used. If the results are uncoupled, this bias will have no effect.

To calculate the *U*-factor of a window and shade system it was necessary to iterate on the glass temperatures. To begin, it was assumed that the inner and outer glass temperatures were 28 °C and 38 °C respectively.

The air-space heat transfer coefficient was determined from Table 4 in Chapter 29 of the ASHRAE HOF (2001). Using an average cavity temperature (33°C) and cavity temperature difference (10°C), air space thickness (13 mm) and effective cavity emissivity (ε_S), h_S became 6.0 W/m^2·K where

$$\varepsilon_s = \frac{1}{\left(1/\varepsilon_2\right)+\left(1/\varepsilon_3\right)-1} = \frac{1}{\left(1/0.84\right)+\left(1/0.84\right)-1} = 0.72 \qquad \text{(E.4)}$$

The subscripts 2 and 3 denote the surface numbered from the exterior surface of the outdoor glazing. The exterior air film coefficient, h_O, was assumed to be 22.7 W/m^2·K as per ASHRAE summer design conditions (ASHRAE 2001).

The interior heat transfer coefficient was solved using the flux equation in Table 4-11, 4-12, or 4-13, and the interior glass temperature. Using an estimated inside glass temperature of T_{g2} = 28°C (and b=30 mm, ϕ = 45°, ε_b = 0.76, ε_{g2} = 0.84, q_b = 0 W/m^2), the heat flux was 26 W/m^2 into the room. Therefore, the interior radiative and convective heat transfer coefficient, h_i became

$$h_i = \frac{q_i}{(T_{gi} - T_i)} = \frac{26}{(28-24)} = 6.5 \text{ W/m}^2\text{K} \qquad \text{(E.5)}$$

and the system *U*-factor was

$$U = \frac{1}{1/h_o + R_{go} + 1/h_s + R_{gi} + 1/h_i} \qquad \text{(E.6)}$$

$$= \frac{1}{1/_{22.7} + 0.0031 + 1/_{6.0} + 0.0031 + 1/_{6.5}} = 2.70 \text{ W/m}^2\text{K}$$

Because there was no solar flux, the heat flux at the indoor surface was also the heat flux through the window. In this case, for the whole window, the heat flux was

$$U(T_o - T_i) = 2.70(40 - 24) = 43.15 \text{ W/m}^2 \qquad \text{(E.7)}$$

Compared to $q_i = 26$ W/m^2, it was obvious that another iteration was required.

Recalculate the glass temperatures

$$T_{go} = T_o - \frac{q}{h_o} = 40 - \frac{43.15}{22.7} = 38.10\,^{\circ}\text{C} \qquad \text{(E.8)}$$

$$T_{gi} = T_i + \frac{q}{h_i} = 24 + \frac{43.15}{6.5} = 30.64\,^{\circ}\text{C} \qquad \text{(E.9)}$$

Using these new temperatures, the process was repeated until $q = q_i$ and the predicted glass temperatures converged. For this example, convergence occured with

$$U = 2.77 \text{ W/m}^2\text{K}$$
$$T_{gi} = 30.63^{\circ}\text{C}$$
$$T_{go} = 38.05^{\circ}\text{C}$$
$$q = 44.24 \text{ W/m}^2$$

E.3.2 Sample *SHGC* Calculation

The calculation of *SHGC* was performed for comparison to the same window and shading device that was tested experimentally. Specifically, the case examined was

b=30 mm
$\phi = 45^{\circ}$, $\psi = 45^{\circ}$
$\varepsilon_b = 0.76$, $\varepsilon_{g1} = \varepsilon_{g2} = 0.84$
$I = 732$ W/m2, $I_D/I = 0.69$
$T_o = 24^{\circ}$C, $T_i = 24^{\circ}$C

Other system properties were presented in Tables E-1 and E-2. As before, the numerical analysis was performed for a room temperature of 24°C, therefore the analysis must also be performed at that temperature.

To begin, it was necessary to first estimate the absorption in the glasses and blind for a solar incidence angle of 45 deg. Using layer specific optical properties estimated from Parmelee and Aubele (1952), an optical balance could be used to find the effective absorption of each layer (Farber et al. 1963). Considering one inter-reflection, for the exterior glass

$$\alpha_{go} = \alpha_1 + \frac{\tau_{go}\rho_3\alpha_2}{(1-\rho_2\rho_3)} + \tau_{go}\tau_{gi}^2\rho_5\alpha_2 \tag{E.11}$$

the interior glass was

$$\alpha_{gi} = \frac{\tau_{go}\alpha_3}{(1-\rho_2\rho_3)} + \tau_{go}\tau_{gi}\rho_5\alpha_4(1+\rho_4\rho_5+\tau_{gi}\rho_2) \tag{E.12}$$

and, the blind absorption was

$$\alpha_b = \alpha_5\tau_{go}\tau_{gi}(1+\rho_3\rho_2)(1+\rho_5\rho_4) \tag{E.13}$$

Each of these effective absorptions must be solved using the layer specific values in Table E-2 for direct and diffuse irradiation. For the given system, $\alpha_{go,D} = 0.136$, $\alpha_{go,d} = 0.126$, $\alpha_{gi,D} = 0.118$, $\alpha_{gi,d} = 0.106$, $\alpha_{b,D} = 0.256$, $\alpha_{b,d} = 0.184$. The solar radiation absorbed then depends on the direct and diffuse levels. During this calorimeter test, the direct radiation was measured at 505 W/m^2 while the diffuse was 227 W/m^2. Therefore

$$I\alpha_{go} = I_D\alpha_{go,D} + I_d\alpha_{go,d} = 505\cdot 0.136 + 227\cdot 0.126 = 97.2\ \text{W/m}^2 \tag{E.14}$$

$$I\alpha_{gi} = I_D\alpha_{gi,D} + I_d\alpha_{gi,d} = 505\cdot 0.118 + 227\cdot 0.106 = 83.7\ \text{W/m}^2 \tag{E.15}$$

$$I\alpha_b = I_D\alpha_{b,D} + I_d\alpha_{b,d} = 505 \cdot 0.256 + 227 \cdot 0.184 = 171.3\ \text{W/m}^2 \qquad \text{(E.16)}$$

To determine the solar heat gain coefficient, it was necessary to iterate based on the interior glass temperature. For this analysis, it was assumed that T_{gi} = 40°C. The interior heat transfer coefficient was solved using the flux equation in Tables 4-11, 4-12, or 4-13. For b = 30 mm, ϕ = 45°, ε_b = 0.76, ε_{gi} = 0.84, $q_b = I\alpha_b$ = 171.3 W/m^2, T_{gi} = 40°C, the heat flux is 69.20 W/m^2 into the room. The air-space heat transfer coefficient, h_s, was determined from Table 4 in Chapter 29 of the ASHRAE HOF (2001) to be 6.0 W/m^{2}K. By performing an energy balance at the interior glazing, the exterior glazing temperature could be estimated by

$$q_s = q_i - I\alpha_{gi} = 69.20 - 83.7 = -14.50\ \text{W/m}^2 \qquad \text{(E.17)}$$

$$T_{go} = T_{gi} + \frac{q_s}{h_s} = 40 + \frac{-14.50}{6} = 37.6\,^\circ\text{C} \qquad \text{(E.18)}$$

The heat flux at the outdoor glazing could now be calculated by two methods: by the energy balance, and by using the exterior air film coefficient (h_o = 22.7 W/m^2·K).

$$q_o = q_s - I\alpha_{go} = -14.50 - 97.2 = -111.70\ \text{W/m}^2 \qquad \text{(E.19)}$$

$$q_o = h_o\left(T_o - T_{go}\right) = 22.7(24 - 37.6) = -308.72\ \text{W/m}^2 \qquad \text{(E.20)}$$

The initial guess of T_{gi} was not very good. It was necessary to reduce the exterior glazing temperature and increase the heat flux by decreasing the interior glass temperature.

At T_{gi} = 36.8°C, q_o converges at -138 W/m^2. Checking h_s as before, produces a value of 5.9 W/m^{2}K. Adjusting and obtaining convergence again, the convergence solution does not change, and T_{gi} = 36.8°C and q_o = -138W/m^2.

The solar heat gain coefficient can be obtained by performing an energy balance on the outer glazing and adding the transmitted portion of radiation.

$$N_{sys}\alpha = \frac{(q_o + \sum I\alpha)}{I_D + I_d} = \frac{(-138 + 97.2 + 83.7 + 171.3)}{732} = 0.29 \qquad \text{(E.21)}$$

$$\tau = \tau_o(\tau_i + \rho_3\rho_2\tau_i)(\tau_b + \rho_5\rho_4\tau_b) \qquad \text{(E.22)}$$

Equation (E.22) was solved using both direct and diffuse properties. So that $\tau_D = 0.07$, and $\tau_d = 0.41$. The solar heat gain coefficient was then

$$SHGC = \frac{\tau_D I_D + \tau_d I_d}{I_D + I_d} + N_{sys}\alpha = \frac{0.07 \cdot 505 + 0.25 \cdot 227}{732} + 0.29 = 0.42 \qquad \text{(E.23)}$$

E.3.3 Results

A comparison of calorimetric and numerically determined solar heat gain and *U*-factor data have been presented in Table E-3.

Table E-3: Comparison of measured and predicted solar heat gain coefficients.

α_b	ϕ (deg)	ψ (deg)	*U* (W/m·K)	τ_{sys}	$N\alpha_{sys}$	Predicted *SHGC*	Measured *SHGC*
no blind	no blind	45	[a]2.87 [b](2.84)	0.66	0.07	[a]0.73	0.71±0.02
0.32	0	30	2.81	0.35	0.26	0.61	0.59±0.02
0.32	0	45	2.81	0.21	0.32	0.53	0.56±0.02
0.32	45	30	2.77	0.13	0.31	0.44	0.46±0.02
0.32	45	45	2.77	0.13	0.29	0.42	0.44±0.02
0.90	0	30	2.82	0.23	0.45	0.68	0.66±0.02
0.90	0	45	2.82	0.06	0.57	0.63	NA[c]
0.90	45	30	2.78	0.05	0.60	0.65	0.64±0.02
0.90	45	45	2.78	0.04	0.58	0.63	0.64±0.02

[a] results predicted using standard ASHRAE calculations (ASHRAE HOF 2001)

[b] U_{cog} as reported by CSA tests (CSA 1992)

[c] Test not performed